

NOV 29 2004

Final Report  
on

**Liquid-Propellant Rocket Engine Injector Dynamics and  
Combustion Processes at Supercritical Conditions**

for  
AFOSR Contract/Grant F49620-01-1-0114

Prepared by

Vigor Yang  
Department of Mechanical Engineering  
The Pennsylvania State University  
104 Research Building East  
University Park, PA 16802

Submitted to:

Air Force Office of Scientific Research  
4015 Wilson Boulevard, Room 713  
Arlington, VA 22203-1954

November 2004

**DISTRIBUTION STATEMENT A**  
Approved for Public Release  
Distribution Unlimited

20050112 015

# REPORT DOCUMENTATION PAGE

AFRL-SR-AR-TR-05-

Public reporting burden for this collection of information is estimated to average 1 hour per response, including the time for reviewing instructions needed, and completing and reviewing this collection of information. Send comments regarding this burden estimate or any other aspect of this burden to Department of Defense, Washington Headquarters Services, Directorate for Information Operations and Reports (0704-01-4302). Respondents should be aware that notwithstanding any other provision of law, no person shall be subject to any penalty for failing to comply with a valid OMB control number. PLEASE DO NOT RETURN YOUR FORM TO THE ABOVE ADDRESS.

*0001*

1. REPORT DATE (DD-MM-YYYY) 01/05/2001		2. REPORT TYPE Final Technical Report		3. DATES COVERED (From - To) 12/15/2000-5/31/2004	
4. TITLE AND SUBTITLE  Liquid-Propellant Rocket Engine Injector Dynamics and Combustion Processes at Supercritical Conditions		5a. CONTRACT NUMBER <b>5b. GRANT NUMBER</b> F49620-01-1-0114 <b>5c. PROGRAM ELEMENT NUMBER</b>			
6. AUTHOR(S)  Vigor Yang		<b>5d. PROJECT NUMBER</b> <b>5e. TASK NUMBER</b> <b>5f. WORK UNIT NUMBER</b>			
7. PERFORMING ORGANIZATION NAME(S) AND ADDRESS(ES)  The Pennsylvania State University 104 Research Building East University Park, PA 16802		<b>8. PERFORMING ORGANIZATION REPORT NUMBER</b>			
9. SPONSORING / MONITORING AGENCY NAME(S) AND ADDRESS(ES)  Dr. Mitat A. Birkan Air Force Office of Scientific Research 4015 Wilson Boulevard, Room 713 Arlington, VA 22203-1954		<b>10. SPONSOR/MONITOR'S ACRONYM(S)</b> <b>AFOSR</b>			
		<b>11. SPONSOR/MONITOR'S REPORT NUMBER(S)</b>			
12. DISTRIBUTION / AVAILABILITY STATEMENT  Approved for public release; distribution unlimited.					
13. SUPPLEMENTARY NOTES					
14. ABSTRACT  The present AFOSR project focuses on the theoretical modeling and numerical simulation of liquid-propellant rocket engine injector flow and combustion dynamics. Emphasis is placed on cryogenic propellants in both shear and swirl co-axial injectors at supercritical conditions. The formulation is based on the full conservation equations in three dimensions, and accommodates variable properties and finite-rate chemical kinetics. Full account is taken of various high-pressure phenomena such as thermodynamic non-idealities and transport anomalies commonly observed in the transcritical regime. Furthermore, an efficient numerical framework utilizing state-of-the-art computer software and hardware technologies is implemented, such that sweeping calculations can be conducted within a realistic time frame. Various fundamental physicochemical mechanisms associated with cryogenic propellant injection, mixing, and combustion are studied systematically. Results have not only enhanced basic understanding of the subject problem, but also established a quantitative basis to identify and prioritize the key design parameters and flow variables that exert strong influences on the injector behavior in different environments.					
15. SUBJECT TERMS  supercritical fluid injection, mixing, and combustion; liquid rocket engines, injectors					
16. SECURITY CLASSIFICATION OF:  a. REPORT unclassified			17. LIMITATION OF ABSTRACT  UU	18. NUMBER OF PAGES	19a. NAME OF RESPONSIBLE PERSON 211
b. ABSTRACT unclassified					19b. TELEPHONE NUMBER (include area code) (814) 863-1502
Standard Form 298 (Rev. 8-98) Prescribed by ANSI Std. Z39.18					

The present AFOSR project focuses on the theoretical modeling and numerical simulation of liquid-propellant rocket engine injector flow and combustion dynamics. Emphasis is placed on cryogenic propellants in both shear and swirl co-axial injectors at supercritical conditions. The formulation is based on the full conservation equations in three dimensions, and accommodates variable properties and finite-rate chemical kinetics. Full account is taken of various high-pressure phenomena such as thermodynamic non-idealities and transport anomalies commonly observed in the transcritical regime. Furthermore, an efficient numerical framework utilizing state-of-the-art computer software and hardware technologies is implemented, such that sweeping calculations can be conducted within a realistic time frame. Various fundamental physiochemical mechanisms associated with cryogenic propellant injection, mixing, and combustion are studied systematically. The work covers the following three specific topical areas:

- injection of liquid nitrogen into supercritical nitrogen environments
- injection of liquid oxygen through simplex swirl injectors under supercritical conditions
- flow and flame dynamics of shear co-axial injectors with liquid oxygen and methane

Results have not only enhanced basic understanding of the subject problem, but also established a quantitative basis to identify and prioritize the key design parameters and flow variables that exert strong influences on the injector behavior in different environments.

## ABSTRACT

The present research focuses on the modeling and simulation of cryogenic fluid injection and mixing processes under supercritical conditions. The objectives are: 1) to establish a unified theoretical framework that accommodates full conservation laws, turbulence closure, and real-fluid thermodynamics and transport phenomena; 2) to systematically investigate underlying physiochemical mechanisms at near- and super-critical conditions, and 3) to construct a quantitative basis for identifying and prioritizing key design parameters and flow variables that exert strong influence on the injector behavior in different environments.

A theoretical formulation is based on full conservation laws and includes real-fluid thermodynamics and transport phenomena over the entire temperature and pressure regimes of concern. Thermodynamic properties, such as enthalpy, internal energy, and heat capacity, are directly calculated from fundamental thermodynamics theories and a modified Soave-Redlich-Kwong (SRK) equation of state. Transport properties, such as viscosity and thermal conductivity, are estimated with an extended corresponding-state principle. Mass diffusivity is obtained by the Takahashi method calibrated for high-pressure conditions. Turbulence closure is achieved using a large-eddy-simulation (LES) technique, in which large energy-carrying structures are computed explicitly and the effect of small-scale motions on the resolved scales is modeled. A modified Smagorinsky model extended to compressible flows is used to treat small-scale motions. The resultant governing equations are calculated numerically using a preconditioned, density-based finite volume method along with a dual time-stepping integration algorithm. All of the numerical relations, including the Jacobian matrices and eigenvalues, are derived based on fundamental thermodynamics theories that can accommodate any equation of state. The resultant algorithm has been proven to be robust and efficient. Further numerical efficiency is achieved by utilizing a

parallel computation scheme that involves the message-passing interface (MPI) library and multi-block treatment.

The theoretical model and numerical scheme were first validated against experimental data of cryogenic nitrogen fluid injection under supercritical conditions. Both two- and three-dimensional simulations were conducted. Reasonably good agreement was obtained in terms of the mean density distribution and the jet spreading angle. The jet dynamics was largely dictated by the local thermodynamic state through its influence on the fluid thermophysical properties. When the fluid temperature transited across the inflection point on an isobaric density-temperature curve, the resultant rapid property variations might qualitatively modify the jet behavior compared with its counterpart at low pressure. An increase in the ambient pressure resulted in an earlier transition of the jet into the self-similar region.

Efforts were also applied to examine the flow and flame dynamics of a shear coaxial injector using liquid oxygen and methane. Emphasis was placed on the effects of momentum flux ratio on the near-field flow evolution. An increase in momentum flux ratio enhanced the turbulent mixing between two streams, and gave rise to a shorter liquid oxygen jet core. Finally, the behavior of liquid oxygen injection through a swirl injector was investigated. The influences of various injector geometric parameters and flow conditions on the injector performance were identified. The flow development inside the injector could be divided into the developing, steady, and acceleration regimes. Results from a parametric study indicated that both the dense fluid film thickness and the spray cone angle were strongly influenced by the swirling strength of the injected fluid, which was determined by the injector geometrical constant. Those parameters, however, did not rely heavily on the mass flowrate. Therefore, a larger oxidizer swirl element with greater mass flowrate than that of the shear coaxial injector still could obtain the required intraelement mixing efficiency.

## TABLE OF CONTENTS

LIST OF FIGURES.....	7
LIST OF TABLES .....	12
Chapter 1 Introduction .....	1
1.1 Motivation and Objectives .....	1
1.2 Review of Relevant Literature.....	5
1.2.1 Supercritical Fluid .....	5
1.2.2 Experimental Study on High-Pressure Cryogenic Fluid Injection and Mixing.....	6
1.2.3 Experimental Study on High-Pressure Cryogenic Propellants Combustion... 11	11
1.2.4 Theoretical and Experimental Study on Swirl Coaxial Injector Design..... 17	17
1.2.5 Numerical Works on High-Pressure Fluid Mixing and Combustion..... 21	21
1.2.6 Work Scope and Method of Approach .....	23
Chapter 2 Theoretical Formulation and Property Evaluation.....	27
2.1 Governing Equations .....	27
2.2 Turbulence Closure: Large-Eddy-Simulation .....	29
2.2.1 Filtering Operations.....	32
2.2.2 Filtered Governing Equations.....	33
2.2.3 Subgrid-Scale Models.....	36
2.2.3.1 Algebraic Smagorinsky Model .....	36
2.2.3.2 Dynamic Smagorinsky Model .....	38
2.3 Equation of State .....	40
2.3.1 Modified Soave-Redlich-Kwong (SRK) Equation of State.....	40
2.3.2 Benedict-Webb-Rubin (BWR) Equation of State.....	42
2.4 Thermodynamic Properties .....	44
2.4.1 Partial Molar and Partial Density Properties .....	45
2.4.2 Critical Point of Fluid Mixture .....	49
2.5 Transport Properties .....	51
2.5.1 Corresponding States Theories .....	51
2.5.2 Mixing Rules for Mixtures .....	53
2.5.3 Viscosity of Mixtures .....	55
2.5.4 Thermal Conductivity of Mixtures .....	56
2.5.5 Binary Mass Diffusivity .....	57
Chapter 3 Numerical Methodology.....	60
3.1 Basic Approach .....	60
3.2 Three-Dimensional Cartesian System .....	61
3.3 A Unified Preconditioning Scheme for General Fluid Mixtures.....	62
3.3.1 Important Thermodynamic Relationships .....	64
3.3.2 Preconditioning Matrix.....	69
3.3.3 Convergence Optimization .....	71

3.3.3.1 Inviscid Preconditioning Factor.....	73
3.3.3.2 Unsteady Preconditioning Factor.....	74
3.3.3.3 Viscous Preconditioning Factor.....	75
3.4 Spatial Discretization: Finite Volume Approach.....	77
3.4.1 Finite Volume Approach .....	77
3.4.2 Evaluation of Inviscid Fluxes .....	81
3.4.3 Evaluation of Viscous and SGS Fluxes .....	83
3.4.4 Evaluation of Artificial Dissipation.....	84
3.5 Temporal Discretization .....	86
3.6 Boundary Conditions.....	89
3.6.1 Characteristic Boundary Conditions.....	89
3.7 Parallel Implementation.....	93
3.7.1 Parallel Architecture .....	93
3.7.2 Beowulf Cluster Parallel Computers .....	95
3.7.3 Domain Decomposition .....	96
 Chapter 4 Two-Dimensional Analysis of Supercritical Cryogenic Fluid Injection .....	98
4.1 Problem Description.....	98
4.2 Computational Domain and Grid System.....	99
4.3 Boundary Conditions.....	102
4.4 Results and Discussion .....	102
4.4.1 Instantaneous Flowfield.....	104
4.4.2 Effect of Density Stratification .....	105
4.4.3 Shear-Layer Instability .....	108
4.4.4 Vortical Dynamics.....	110
4.4.5 Mean Flow Properties.....	112
4.5 Summary .....	114
 Chapter 5 Three-Dimensional Analysis of Supercritical Cryogenic Fluid Injection .....	127
5.1 Problem Description.....	127
5.2 Thermophysical Properties.....	128
5.3 Results and Discussion .....	130
5.3.1 Instantaneous Flow Visualization.....	130
5.3.2 Vortical Dynamics.....	136
5.3.3 Shear-Layer Instability and Jet Prefer Mode .....	139
5.3.4 Mean and Turbulent Properties .....	142
5.3.5 Proper Orthogonal Decomposition Analysis .....	152
5.4 Summary .....	156
 Chapter 6 High-pressure LOX and Methane Mixing.....	158
6.1 Problem Description.....	158
6.2 Presentation of Results .....	163
6.2.1 Instantaneous Flow Dynamics.....	163
6.2.2 Spectral Analysis .....	168
6.2.3 Statistical Data Analysis .....	175
6.3 Discussion .....	180

Chapter 7 High-Pressure LOX Swirl Injection .....	182
7.1 Problem Description.....	182
7.2 Simulation Results.....	185
7.2.1 Flow Structures.....	187
7.2.2 Effects of Important Design Parameters on the Swirl Injector Performance..	195
7.2.2.1 Mass Flowrate.....	195
7.2.2.2 Slit Position.....	199
7.2.2.3 LOX Post Length.....	201
7.2.2.4 Geometric Characteristic Number .....	202
7.3 A Viscous Correction on Classical Swirl Injector Theory .....	205
7.4 Summary .....	209
Chapter 8 Summary and Recommendations .....	210
8.1 Summary .....	210
8.2 Recommendation for Future work.....	212
Bibliography.....	214
Appendix A Properties of the Favre Average (Based on Reynolds Average) .....	224
Appendix B Thermodynamic Relationship.....	225
Appendix C Derivative Expressions in Soave-Redlich-Kwong Equation of State .....	230
Appendix D Jacobian Matrices .....	232
D.1 Jacobian of Primitive Variables.....	232
D.2 Convective Flux Jacobians .....	233
D.3 Chemical Source Jacobian.....	236

## LIST OF FIGURES

Fig. 1.1: Schematic diagram illustrating the basic phenomena associated with injection and combustion of LOX and GH <sub>2</sub> at sub- and supercritical chamber pressures (adopted from Oefelein and Yang, 1998).....	2
Fig. 1.2: P-T phase diagram of a pure propellant and the operating conditions of different combustion devices.....	6
Fig. 1.3: Transition of jet boundary from liquid-jet like to gas-jet-like appearance.....	8
Fig. 1.4: Near Injector region of a liquid-oxygen-gaseous-hydrogen shear-coaxial injector, a) flame; and b) corresponding flowfield. Oxygen and hydrogen velocities are 30 and 300 m/s, respectively. The injection temperatures are 100 and 300 K for oxygen and hydrogen streams, respectively, and the chamber pressure is 4.5 MPa (Adopted from Mayer and Tamura, 1996). .....	14
Fig. 1.5: Schematic of flame-holding mechanism.....	16
Fig. 1.6: Schematic of swirl coaxial injector.....	18
Fig. 2.1: Concepts of DNS, LES and RANS (adopted from Wang, 2002). .....	30
Fig. 2.2: Molar volume of a mixture as function of composition at fixed pressure and temperature.....	46
Fig. 2.3: T-V phase diagram of multi-component mixture with different compositions ( $x_1=0.4, 0.6$ ).....	50
Fig. 3.1: Contours of the condition number as a function of the Mach number squared and the preconditioning factor.....	73
Fig. 3.2: Schematic of three-dimensional adjacent cells .....	78
Fig. 3.3: Schematic diagram of the stencil used in evaluating inviscid flux terms in the $x - y$ plane.....	82
Fig. 3.4: Schematic diagram for a three-dimensional auxiliary cell.....	83
Fig. 3.5: Multiple instruction multiple data (MIMD) architecture (adopted from Apte, 2000).....	95
Fig. 3.6: Schematic of a two-dimensional sub-domain with ghost cells (adopted from Wang, 2002) .....	97
Fig. 4.1: Schematic of fluid jet.....	99
Fig. 4.2: Grid system employed in the computation (at one-fourth of the original grid density).....	100

Fig. 4.3: Effect of grid resolution on radial distributions of mean axial velocity, turbulent kinetic energy, compressibility factor, and viscosity at different axial locations ( $p_{\infty} = 4.3 \text{ MPa}$ , $T_{\infty} = 300 \text{ K}$ , $u_{\text{inj}} = 15 \text{ m/s}$ , $T_{\text{inj}} = 120 \text{ K}$ , $D_{\text{inj}} = 254 \mu\text{m}$ ). ....	101
Fig. 4.4: Density and constant-pressure specific heat of nitrogen as the functions of temperature and pressure.....	116
Fig. 4.5: Effect of pressure on density, density gradient, temperature and vorticity fields ( $T_{\infty} = 300 \text{ K}$ , $u_{\text{inj}} = 15 \text{ m/s}$ , $T_{\text{inj}} = 120 \text{ K}$ , $D_{\text{inj}} = 254 \mu\text{m}$ , $t = 1.55 \text{ ms}$ ). ....	117
Fig. 4.6: Time evolution of jet surface structures ( $p_{\infty} = 9.3 \text{ MPa}$ , $T_{\infty} = 300 \text{ K}$ , $u_{\text{inj}} = 15 \text{ m/s}$ , $T_{\text{inj}} = 120 \text{ K}$ , $D_{\text{inj}} = 254 \mu\text{m}$ ). ....	118
Fig. 4.7: Power spectral densities of velocity fluctuations at different radial locations with $x/D_{\text{inj}} = 16$ ( $p_{\infty} = 9.3 \text{ MPa}$ , $T_{\infty} = 300 \text{ K}$ , $u_{\text{inj}} = 15 \text{ m/s}$ , $T_{\text{inj}} = 120 \text{ K}$ , $D_{\text{inj}} = 254 \mu\text{m}$ ). ....	119
Fig. 4.8: Effect of pressure on power spectral densities of radial velocity fluctuations at two different axial locations with $r/D_{\text{inj}} = 0.5$ .....	120
Fig. 4.9: Spatial growth rate as function of Strouhal number at different pressures.....	121
Fig. 4.10: Vorticity budgets at different ambient pressures ( $T_{\infty} = 300 \text{ K}$ , $u_{\text{inj}} = 15 \text{ m/s}$ , $T_{\text{inj}} = 120 \text{ K}$ , $D_{\text{inj}} = 254 \mu\text{m}$ , $t = 1.55 \text{ ms}$ ). ....	122
Fig. 4.11: Effect of pressure on normalized density distribution in radial direction.....	123
Fig. 4.12: Effect of pressure on normalized velocity distribution in radial direction.....	124
Fig. 4.13: Effect of pressure on normalized density, normalized temperature, and compressibility factor along jet centerline. ....	125
Fig. 4.14: Radial distributions of mean thermophysical properties at $x/D_{\text{inj}} = 10$ .....	126
Fig. 5.1: Thermo-physical properties of nitrogen as functions of pressure and temperature.....	130
Fig. 5.2: Effect of pressure on vorticity magnitude, temperature, and density-gradient fields ( $T_{\infty} = 300 \text{ K}$ , $u_{\text{inj}} = 15 \text{ m/s}$ , $T_{\text{inj}} = 120 \text{ K}$ , $D_{\text{inj}} = 254 \mu\text{m}$ , $t^* = 80$ ). ....	132
Fig. 5.3: Effect of pressure on specific heat, thermal diffusivity, kinematic viscosity, and compressibility factor fields ( $T_{\infty} = 300 \text{ K}$ , $u_{\text{inj}} = 15 \text{ m/s}$ , $T_{\text{inj}} = 120 \text{ K}$ , $D_{\text{inj}} = 254 \mu\text{m}$ , $t^* = 88$ ). ....	133
Fig. 5.4: Large coherent structures visualized by the instantaneous iso-surface of dilatation magnitude at a threshold corresponding to 15% of the maxima ( $p_{\infty} = 6.9 \text{ MPa}$ , $T_{\infty} = 300 \text{ K}$ , $u_{\text{inj}} = 15 \text{ m/s}$ , $T_{\text{inj}} = 120 \text{ K}$ , $D_{\text{inj}} = 254 \mu\text{m}$ ). ....	135

Fig. 5.5: Spatial averaged vorticity magnitude and azimuthal vorticity budgets at two different axial locations ( $p_{\infty} = 6.9 \text{ MPa}$ , $T_{\infty} = 300 \text{ K}$ , $u_{\text{inj}} = 15 \text{ m/s}$ , $T_{\text{inj}} = 120 \text{ K}$ , $D_{\text{inj}} = 254 \mu\text{m}$ , $t^* = 88$ ).....	137
Fig. 5.6: Spatial averaged vorticity magnitude and azimuthal vorticity budgets at two different axial locations ( $p_{\infty} = 9.3 \text{ MPa}$ , $T_{\infty} = 300 \text{ K}$ , $u_{\text{inj}} = 15 \text{ m/s}$ , $T_{\text{inj}} = 120 \text{ K}$ , $D_{\text{inj}} = 254 \mu\text{m}$ , $t^* = 88$ ).....	139
Fig. 5.7: Power spectral densities of pressure fluctuations at different axial locations with $r/D_{\text{inj}} = 0.5$ ( $p_{\infty} = 6.9 \text{ MPa}$ , $T_{\infty} = 300 \text{ K}$ , $u_{\text{inj}} = 15 \text{ m/s}$ , $T_{\text{inj}} = 120 \text{ K}$ , $D_{\text{inj}} = 254 \mu\text{m}$ )....	140
Fig. 5.8: Power spectral densities of pressure fluctuations at different axial locations with $r/D_{\text{inj}} = 0.5$ ( $p_{\infty} = 9.3 \text{ MPa}$ , $T_{\infty} = 300 \text{ K}$ , $u_{\text{inj}} = 15 \text{ m/s}$ , $T_{\text{inj}} = 120 \text{ K}$ , $D_{\text{inj}} = 254 \mu\text{m}$ )....	141
Fig. 5.9: Effect of pressure on the normalized temperature, velocity, density along jet centerline and the FWHM distributions ( $T_{\infty} = 300 \text{ K}$ , $u_{\text{inj}} = 15 \text{ m/s}$ , $T_{\text{inj}} = 120 \text{ K}$ , $D_{\text{inj}} = 254 \mu\text{m}$ ).....	144
Fig. 5.10: Effect of initial density ratio on velocity decay, a) velocity decay, b) velocity decay normalized using the pseudo-similarity laws suggests by Chen and Rodi (1980). .....	145
Fig. 5.11: The normalized density distributions in radial direction at different axial locations ( $T_{\infty} = 300 \text{ K}$ , $u_{\text{inj}} = 15 \text{ m/s}$ , $T_{\text{inj}} = 120 \text{ K}$ , $D_{\text{inj}} = 254 \mu\text{m}$ ).....	146
Fig. 5.12: Tangent of the jet visual spreading angle versus the ambience to injectant density ratio.....	148
Fig. 5.13: The normalized velocity distributions in radial direction at the axial location $x/D_{\text{inj}} = 35$ ( $T_{\infty} = 300 \text{ K}$ , $u_{\text{inj}} = 15 \text{ m/s}$ , $T_{\text{inj}} = 120 \text{ K}$ , $D_{\text{inj}} = 254 \mu\text{m}$ ).....	149
Fig. 5.14: The normalized Reynolds stress components distributions in radial direction averaged among the region $30 < x/D_{\text{inj}} < 35$ ( $T_{\infty} = 300 \text{ K}$ , $u_{\text{inj}} = 15 \text{ m/s}$ , $T_{\text{inj}} = 120 \text{ K}$ , $D_{\text{inj}} = 254 \mu\text{m}$ ). ....	150
Fig. 5.15: The normalized turbulence intensity distributions along jet centerline ( $T_{\infty} = 300 \text{ K}$ , $u_{\text{inj}} = 15 \text{ m/s}$ , $T_{\text{inj}} = 120 \text{ K}$ , $D_{\text{inj}} = 254 \mu\text{m}$ ).....	151
Fig. 5.16: Energies of POD modes in the near field ( $T_{\infty} = 300 \text{ K}$ , $u_{\text{inj}} = 15 \text{ m/s}$ , $T_{\text{inj}} = 120 \text{ K}$ , $D_{\text{inj}} = 254 \mu\text{m}$ ).....	153
Fig. 5.17: Most energetic pressure POD modes visualized with iso-surfaces of pressure ( $p_{\infty} = 6.9 \text{ MPa}$ , $T_{\infty} = 300 \text{ K}$ , $u_{\text{inj}} = 15 \text{ m/s}$ , $T_{\text{inj}} = 120 \text{ K}$ , $D_{\text{inj}} = 254 \mu\text{m}$ ). ....	154
Fig. 5.18: Most energetic pressure POD modes visualized with iso-surfaces of pressure ( $p_{\infty} = 9.3 \text{ MPa}$ , $T_{\infty} = 300 \text{ K}$ , $u_{\text{inj}} = 15 \text{ m/s}$ , $T_{\text{inj}} = 120 \text{ K}$ , $D_{\text{inj}} = 254 \mu\text{m}$ ). ....	155

Fig. 6.1: Schematic of shear co-axial injector employed in the simulation.....	159
Fig. 6.2: Thermo-physical properties of methane as functions of pressure and temperature.....	160
Fig. 6.3: Thermo-physical properties of oxygen as functions of pressure and temperature....	160
Fig. 6.4: Grid system employed in the simulation (at one-fourth original grid density).....	162
Fig. 6.5: Snapshots of oxygen mass fraction and vorticity fields of co-axial injection of LOX and methane at conditions 1 and 2 in Table 6.2 .....	164
Fig. 6.6: Mass fraction, density, vorticity, and velocity vector fields in the region near the LOX post for Cases 1 and 2 in Table 6.2 .....	165
Fig. 6.7: Time evolution of vorticity field over one cycle of vortex pairing of Case 1 in Table 6.2 .....	167
Fig. 6.8: Frequency spectra of the radial velocity oscillations along the inner shear-layer, Case 1 in Table 6.2 .....	169
Fig. 6.9: Frequency spectra of the radial velocity oscillations along the outer shear-layer, Case 1 in Table 6.2 .....	170
Fig. 6.10: Frequency spectra of the radial velocity oscillations along the inner shear-layer, Case 2 in Table 6.2 .....	173
Fig. 6.11: Frequency spectra of the radial velocity oscillations along the outer shear-layer, Case 2 in Table 6.2 .....	174
Fig. 6.12: Time averaged axial velocity, turbulent kinetic energy (TKE), and oxygen mass fraction fields of Cases 1 and 2 in Table 6.2 .....	175
Fig. 6.13: Comparison of the radial distributions of the time averaged density, oxygen mass fraction, axial velocity, and turbulent kinetic energy at the different axial locations for Cases 1 and 2 in Table 6.2 .....	177
Fig. 6.14: Time-averaged velocity vector distributions near the LOX post of Cases 1 and 2 in Table 6.2.....	178
Fig. 6.15: Comparison of axial distributions of the time-averaged density, oxygen mass fraction, axial velocity, and turbulent kinetic energy along the centerline of the inner streams.....	179
Fig. 6.16: Schematic of the shear coaxial injection of LOX and methane at supercritical conditions.....	181
Fig. 7.1: Schematic of simplex swirl injector employed in the present study, 1-injector casing; 2-vortex chamber; 3-discharge nozzle, 4-tangential passages. ....	183

Fig. 7.2: Schematic of 2D axi-symmetric grid system at one-third of the original grid density .....	184
Fig. 7.3: Mean density and velocity components fields ( $p_{\infty} = 10 \text{ MPa}$ , $T_{\text{inj}} = 120 \text{ K}$ , $T_{\infty} = 300 \text{ K}$ , $\dot{m} = 0.2 \text{ kg/s}$ , $K = 3.2$ ).....	188
Fig. 7.4: Radial distributions of mean velocity components, temperature, density, and compressibility factor at various axial locations ( $\dot{m} = 0.2 \text{ kg/s}$ , $K = 3.2$ ). ....	190
Fig. 7.5: The dense fluid film thickness along the injector inner wall ( $p_{\infty} = 10 \text{ MPa}$ , $T_{\text{inj}} = 120 \text{ K}$ , $T_{\infty} = 300 \text{ K}$ , $\dot{m} = 0.2 \text{ kg/s}$ , $K = 3.2$ ). ....	191
Fig. 7.6: Temporal evolution of temperature field over one cycle of the dominant vortex shedding process ( $p_{\infty} = 10 \text{ MPa}$ , $T_{\text{inj}} = 120 \text{ K}$ , $T_{\infty} = 300 \text{ K}$ , $\dot{m} = 0.2 \text{ kg/s}$ , $K = 3.2$ ).....	193
Fig. 7.7: Power spectral densities of the pressure fluctuations at six different axial locations ( $p_{\infty} = 10 \text{ MPa}$ , $T_{\text{inj}} = 120 \text{ K}$ , $T_{\infty} = 300 \text{ K}$ , $\dot{m} = 0.2 \text{ kg/s}$ , $K = 3.2$ ). ....	194
Fig. 7.8: Effect of mass flowrate on the film thickness.....	195
Fig. 7.9: Effect of mass flowrate on the temperature fields. ....	197
Fig. 7.10: Effect of mass flowrate on the power spectral density of the pressure oscillations.....	198
Fig. 7.11: Effect of slit position on the film thickness. ....	199
Fig. 7.12: Effect of slit position on the pseudo streamline patterns near the head end. ....	200
Fig. 7.13: Comparison of liquid film thickness predicted from different theoretical models and the simulation results.....	202
Fig. 7.14: Effect of the swirl strength on the film thickness. ....	203
Fig. 7.15: Effect of swirl strength on the pseudo streamline patterns. ....	204
Fig. 7.16: The power spectral density of pressure oscillations at different axial locations( $p_{\infty} = 10 \text{ MPa}$ , $T_{\text{inj}} = 120 \text{ K}$ , $T_{\infty} = 300 \text{ K}$ , $\dot{m} = 0.2 \text{ kg/s}$ , $K = 4.2$ ). ....	205
Fig. 7.17: Schematic of displacement effect in a swirl injector. ....	207

## LIST OF TABLES

Table 1.1 Engine Operation Conditions and Critical Properties of Fuels .....	1
Table 2.1: Coefficients of $A_n$ .....	43
Table 2.2: Semi-empirical Constants Based on Methane.....	43
Table 2.3: Coefficients for Shape Factor Correlations.....	53
Table 4.1: Simulation Conditions.....	103
Table 4.2: Conditional averaged temperatures (K) in regions with $ \nabla \rho  >$ cutoff value.....	105
Table 4.3: Temperatures at inflection points on isobaric $\rho - T$ curves at different pressures .....	106
Table 5.1: Simulation Conditions.....	128
Table 5.2: Temperatures at inflection points on isobaric $\rho - T$ curves at different pressures .....	134
Table 5.3: Conditional averaged temperatures (K) in regions with $ \nabla \rho  >$ cutoff value.....	134
Table 5.4: Physical parameters of the experiments used for comparison. ....	143
Table 6.1: The critical points of methane and oxygen. ....	159
Table 6.2: Simulation conditions for the analysis of high-pressure LOX/methane injection and mixing process. Subscript 1 denotes the oxygen stream, and subscript 2 denotes the methane stream.....	161
Table 6.3: The predicted initial vortex shedding frequency ( $f_1$ ) and its first sub-harmonics ( $f_2$ ) of each shear-layer in Case 1.....	171
Table 6.4: The predicted initial vortex shedding frequency ( $f_1$ ) and its first sub-harmonics ( $f_2$ ) of each shear-layer in Case 2. ....	172
Table 7.1: Geometric parameters of the studied swirl injector .....	183
Table 7.2: Test Conditions* .....	186
Table 7.3: Effect of mass flowrate on dense fluid film thickness and spray cone angle.....	196
Table 7.4: Effect of slit position on film thickness and spray cone angle.....	201

Table 7.5: Effect of LOX post length on the dense fluid film thickness and spray cone angle. .... 202

Table 7.6: Effect of swirl strength on the dense fluid film thickness and spray cone angle. .. 204



## Chapter 1

### Introduction

#### 1.1 Motivation and Objectives

Cryogenic propellants mixing and combustion in supercritical environments have long been matters of serious practical concern in combustion science and technology, mainly due to the necessity of developing high-pressure combustion devices, such as liquid-propellant rocket, gas turbine, and diesel engines. Cryogenic fuels and/or oxidizers are usually delivered to combustion chambers at their subcritical state, which then undergo a sequence of vaporization, mixing, ignition, and combustion processes at pressure and temperature levels well above the thermodynamic critical points of the fluids (see Table 1.1). Under these conditions, cryogenic propellants may heat up and experience a thermodynamic state transition into the supercritical regime. The mixing and combustion processes exhibit many features distinct from those in an atmospheric environment, thereby rendering conventional approaches developed for low-pressure applications invalid.

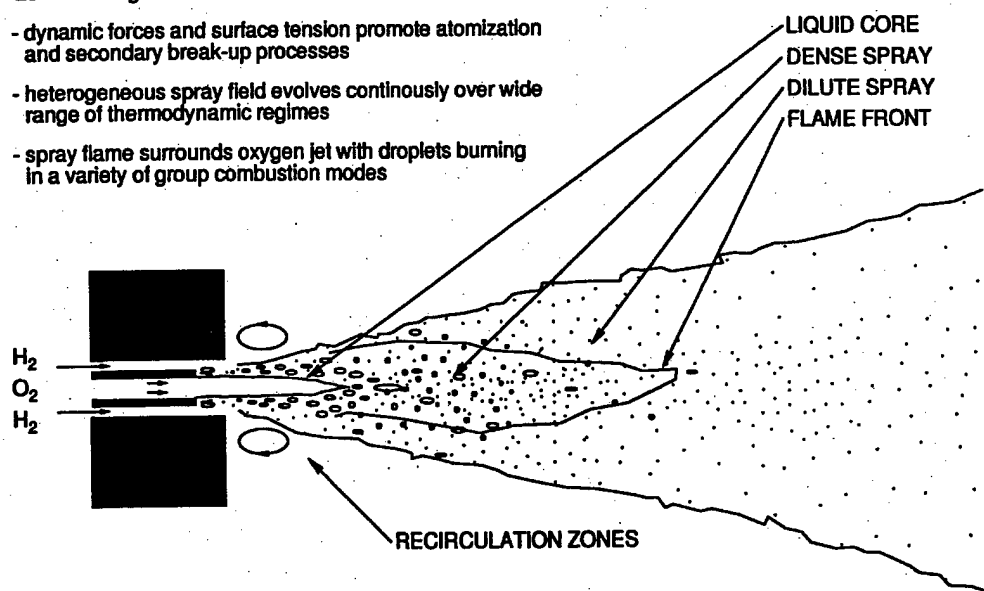
Table 1.1 Engine Operation Conditions and Critical Properties of Fuels

Engines/Combustors	Fuels	Operation Conditions	Critical Properties of Fuel
Space Shuttle Main Engine	Oxygen Hydrogen	225 atm 13 atm, 33.2 K	49.7 atm, 154.6K ~30 atm, ~650K
Diesel Engine	Diesel Oil	> 50 atm	

Under supercritical pressures, the sharp distinction between liquid and gas phases vanishes due to the diminishment of surface tension and enthalpy of vaporization, and questions

- "Low" Heating Rates

- dynamic forces and surface tension promote atomization and secondary break-up processes
- heterogeneous spray field evolves continuously over wide range of thermodynamic regimes
- spray flame surrounds oxygen jet with droplets burning in a variety of group combustion modes



- "High" Heating Rates

- diminished intermolecular forces promote diffusion processes prior to atomization
- injected jet vaporizes forming continuous fluid in presence of exceedingly large interfacial gradients
- diffusion flame resides within annular post wake separating oxygen jet from outer hydrogen flow

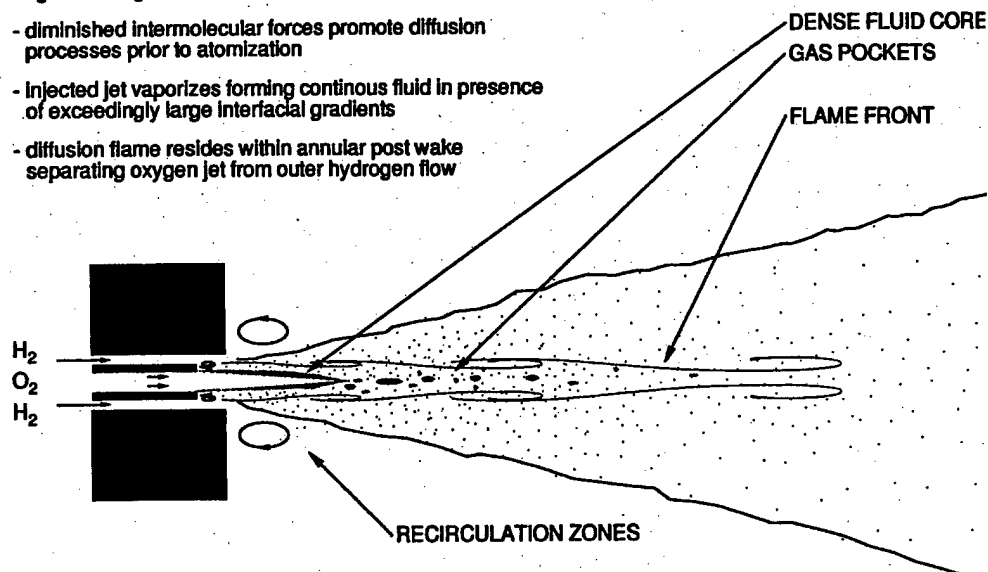


Fig. 1.1: Schematic diagram illustrating the basic phenomena associated with injection and combustion of LOX and GH<sub>2</sub> at sub- and supercritical chamber pressures (adopted from Oefelein and Yang, 1998).

arise with respect to phenomenologically correct characterization of propellant injection, mixing, and combustion processes. Figure 1.1 schematically compares the basic phenomena of a liquid-oxygen-gaseous-hydrogen (LOX/GH<sub>2</sub>) shear-coaxial injector element operated at low and high pressures (Oefelein and Yang, 1998). At subcritical chamber pressures, injected liquid jets undergo the classical cascade of processes associated with atomization. For this situation, dynamic forces and surface tension promote the formation of a heterogeneous spray that evolves continuously over a wide range of thermophysical regimes. Spray flames form and are lifted away from the injector faceplate in a manner consistent with the combustion mechanism exhibited by local droplet clusters. When chamber pressures approach or exceed the critical value of a particular propellant, the injected fluid jets undergo a “transcritical” change of state as the interfacial fluid temperatures rise above the saturation or critical temperature of the local mixture. For this situation, diminishment of intermolecular forces promotes diffusion dominated processes prior to atomization and respective jets vaporize, forming a continuous fluid in the presence of exceedingly large gradients. Well-mixed diffusion flames evolve and are anchored by small but intensive recirculation zones generated by the shear-layers imposed by adjacent propellant streams. These flames produce wakes that extend far downstream.

Simulating high-pressure phenomena described above inherently poses a variety of challenges which involve all of the classical closure problems and a unique set of problems imposed by thermodynamic non-idealities and transport anomalies. First, from the classical point of view, reacting, multiphase flow introduces the complicating factors of chemical kinetics, highly nonlinear source terms, and a variety of subgrid-scale (sgs) velocity and scalar-mixing interactions. Second, thermodynamic and transport anomalies may occur during the temperature transition across the critical value, especially when the pressure approaches the critical point, a phenomenon commonly referred to as near-critical enhancement (Levett Senger, 1991). As a result, compressibility effects (i.e., volumetric changes induced by pressure variations) and

variable inertial effects (i.e., volumetric changes induced by heat addition and/or variable composition) play an important role in dictating the flow evolution. Third, the fluid properties and their spatial gradients vary continuously throughout the entire field. The resultant coupling dynamics becomes transient between the injected and the surrounding fluids, and involves an array of physicochemical processes with widely disparate time and length scales. Fourth, the flow Reynolds number increases dramatically with pressure. For oxygen and hydrogen, an increase in pressure from 1 to 100 atmospheres results in a reduction of the corresponding kinematic viscosity by a factor of two orders of magnitude. Based on the Kolmogorov universal equilibrium theory, the Kolmogorov and Taylor microscales may decrease by 1.5 and 1.0 orders of magnitude, respectively. These reductions of the characteristic scales of turbulent motions have a direct impact to the flow evolution and the numerical grid density required to resolve key processes. Finally, exceedingly large density gradients emerge during high-pressure injection and mixing. At 100 atmospheres, the density ratio associated with a 100 K oxygen jet and a 300 K gaseous hydrogen stream (a typical operating condition in liquid rocket engine) is approximately 144. In a shear-coaxial element, this change occurs over an interval smaller than the thickness of the annular post, which is on the order of 0.1 mm. Resolving a gradient of such size numerically requires the use of extremely dense grids. Comprehensive reviews of the state of knowledge on supercritical mixing and combustion were recently given by Yang (2000) and Bellan (2000).

The complexity of the problem outlined above is numerically demanding, and a variety of uncertainties exist with regard to the closure. This dissertation represents one of the attempts to address key issues related to modeling and understanding unsteady fluid dynamic and physicochemical processes at supercritical conditions. The objectives are as follows: 1) to provide insight with respect to many uncertainties associated with modeling turbulent, chemical reacting, real-fluid mixture at high-pressure; 2) to establish a unified theoretical framework which could accommodate full conservation laws, turbulence closure, real-fluid thermodynamics,

and transport anomalous; 3) to systematically investigate the fundamental flow dynamics and physiochemical processes at near and supercritical conditions; 4) to found a quantitative basis for identifying and prioritizing the key design parameters and flow variables that exert strong influence on the injector behavior in different environments.

## 1.2 Review of Relevant Literature

### 1.2.1 Supercritical Fluid

According to classical thermodynamic theory (Prausnitz et al., 1986), a fluid is in its supercritical state when both the temperature and pressure exceed the critical values (see Fig. 1.2). Because surface tension and enthalpy of vaporization that manifest the liquid/gas boundary become zero, there is no longer the possibility of a two-phase region, but instead a single phase exists. The general term for the substance is fluid. In this regime, fluid exhibits salient features distinguishing itself from both gas and liquid.

At near- and supercritical conditions, fluid properties possess liquid-like density, gas-like diffusivity, and pressure-dependent solubility. Surface tension and enthalpy of vaporization vanish, and isothermal compressibility and specific heat increase significantly. In addition, fluid properties and their gradient vary continuously. Those non-idealities become even more exacerbated when fluid state approaches the critical condition. In the vicinity of the critical point, the thermophysical properties of fluids exhibit anomalous variations and are very sensitive to both temperature and pressure, a phenomenon commonly referred to as near critical enhancement (Levelt Senger, 1991). Those phenomena, coupled with intense chemical reaction and turbulence, have significant impacts on the operational dynamics of a given combustion system.

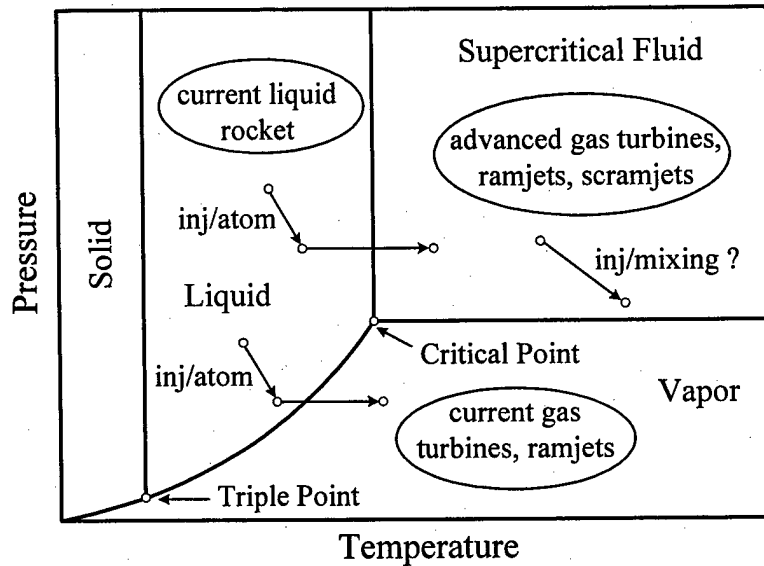


Fig. 1.2: P-T phase diagram of a pure propellant and the operating conditions of different combustion devices.

### 1.2.2 Experimental Study on High-Pressure Cryogenic Fluid Injection and Mixing

High-pressure cryogenic propellants combustion in liquid rocket engines poses various technological and scientific difficulties, including injection optimization, ignition, flame stabilization, and combustion instabilities. The whole process is so complex that its mechanism cannot be thoroughly understood without extensive theoretical and experimental works conducted on simplified configurations and under well-controlled conditions. In this subsection, the experimental works on high-pressure fluid injection and mixing are first reviewed.

Experimental investigation into supercritical fluid jet dynamics dates back to 1971. Newman and Brzustowski (1971) studied the injection of CO<sub>2</sub> fluid with an inlet temperature of 295K into a chamber filled with CO<sub>2</sub> and N<sub>2</sub> mixtures at near critical conditions. The critical temperature and pressure of CO<sub>2</sub> are 304 K and 73 atm, respectively, and those of N<sub>2</sub> are 126 K and 34 atm, respectively. The chamber temperature and pressure were preconditioned in the

range of 295-330 K and 62-90 atm, respectively, and the CO<sub>2</sub> mass fraction varied from 0 to 50%. The shadowgraph visualization technique was employed to investigate the jet flow evolution and its interaction with the surrounding fluid. Results indicated that over the pressure range considered, the jet surface structure and spray formation were suppressed with increasing temperature and CO<sub>2</sub> concentration in the chamber, mainly due to the diminished surface tension and enhanced CO<sub>2</sub> evaporation at near and above the critical temperature. Droplets were observed around the jet boundary, but their sizes decreased with an increase in the ambient temperature. The jet could be globally treated as a variable-density, single-phase turbulent submerged jet at both subcritical and supercritical pressures when the ambient temperature remained supercritical.

Motivated by the development of high-pressure cryogenic-propellant rocket engines, extensive experimental studies have been conducted to provide direct insight into supercritical fluid injection and mixing. The work included injection of liquid nitrogen and co-injection of liquid nitrogen and gaseous helium into gaseous nitrogen environments over a wide range of pressures (Chehroudi et al., 2003).

Chehroudi et al. (1999, 2000, 2002a, 2002b) studied the injection of liquid nitrogen initially at a subcritical temperature into an environment at a fixed supercritical temperature (300 K) and various pressures ranging from sub- to supercritical values (7.8 to 93 atm). Shadowgraph image, fractal analysis, and Raman scattering measurement were employed to examine the structures of the jet and the shear-layer between the injected and ambient fluids. The results based on the flow visualization confirmed the findings by Newman and Brzustowski. Drastic changes in jet surface phenomena took place across the critical pressure. Ligaments and droplets formed at subcritical pressures, but disappeared at supercritical conditions, due to the prevalence of turbulent motions and vanishment of surface tension, as shown in Fig. 1.3. Fractal analysis

indicated that the jet surface topology at supercritical pressure bears a strong resemblance to its gaseous counterpart. The fractal dimension, however, dropped rapidly to a value close to that of liquid spray as the pressure reduced below the critical point.

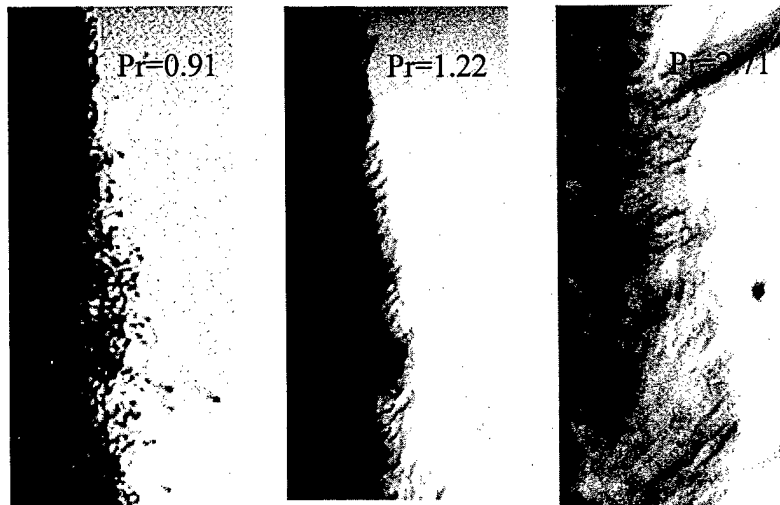


Fig. 1.3: Transition of jet boundary from liquid-jet like to gas-jet-like appearance.

To quantitatively characterize high-pressure cryogenic jet, its initial growth rate was measured and compared with the results of a large number of other flows, including atomized liquid sprays, turbulent incompressible gaseous jets, supersonic jets, and incompressible variable density jets/mixing layers covering over four-order of magnitude in the density ratio of injected to ambient flows (Chehroudi et al., 2002a). The growth rate of supercritical jet agreed well with that of the incompressible, variable density, gaseous mixing layers at low pressures. This was the first time a quantitative parameter was defined and used to demonstrate the similarity between these two flows beyond their physical appearance. Since the fluid jet exhibited distinct features at sub- and supercritical pressures, a unified model for the initial growth rate of jet, which could consider both the droplet gasification at low pressure and the interfacial bulge

formation/separation at high-pressure, was proposed (Chehroudi et al. 2002b). Its prediction showed good agreement with the measured data.

Systematical cold flow experiments were conducted by Mayer and his colleagues at DLR of Germany (Mayer et al., 1996, 1998, 2000). The injections of liquid nitrogen into gaseous nitrogen/helium environment with and without co-flow gas helium were preformed. The chamber pressure varied from 10 to 60 atmospheres, and its temperature was fixed at 300 K. The injection temperature of nitrogen reached as low as 90 K, whereas that of gaseous helium ranged from 100 to 370 K. Similar changes in the jet surface structures were observed in shadowgraph images as pressure increased from sub- to super-critical values. Due to the fade of surface tension, the atomization mechanism changed to shear-layer instability, and the mixing of the injected dense nitrogen fluid with the helium co-flow or ambient gas behaved like a variable density, turbulent shear-layer at near- and supercritical conditions. Since mixing was strongly related to the large-scale vortices within the shear-layer, their length scales were quantitatively measured based on the flashlight photography and high-speed cinematography (Branam and Mayer, 2003). For pure nitrogen injection at a near critical temperature (123 K), the length scales in radial direction were two to three times greater than the radial ones near the injector exit due to the strong density gradient around the jet surface. This asymmetry decayed as the fluid was convected downstream, and it also became unpronounced when the injection temperature exceeded the critical value. It was also indicated that the resolved scales were comparable in magnitude to the Taylor micro scale in turbulent flow.

The spontaneous Raman Scattering technique was first employed to qualitatively measure the species distributions in high-pressure experiments (Anderson et al., 1995). Then, it was applied to investigate the density and temperature distributions of supercritical nitrogen jets (Oschwald and Schik, 1999; Branam and Mayer, 2003). In general, the normalized density

profiles in the downstream indicated a tendency towards the self-similarity solution observed for classical constant- and variable-density single-phase fluid jets at low pressures. This, again, confirmed their similarities. The centerline density and temperature distributions of cryogenic jet at a near critical pressure (40 atm) were acquired by Oschwald and Schick. They noted that the density decay became faster as the fluid temperature increased from sub- to supercritical values. The temperature, however, remained a relatively flat profile even far downstream. This was attributed to the anomalous thermophysical property variations near the critical point of nitrogen. Those quantitative measurement conducted at high-pressure provided indispensable basis for CFD model validation.

Chehroudi et al. (2002c, 2004) studied the effects of acoustic waves on single the nitrogen jet and the coaxial injection of liquid nitrogen and gaseous nitrogen over a wide range of chamber pressures. The strength of the acoustic wave was up to 180 dB, and the resonant frequencies of the assembly were at 2700 and 4800 Hz. The influence was substantial at subcritical conditions but became unnoticeable as pressure increased and exceeded the critical point. The phenomenon may be attributed to the formation of high-frequency vortices in the shear-layer and the weaker characteristic acoustic impedances of injected fluid under supercritical pressure. In addition, the co-axial subcritical jets at higher velocity ratios were more apt to be influenced. Since the sensitivity of coaxial jet to the external acoustic oscillations might correspond to the causes of combustion instability in liquid rocket engine, the acoustic impedance of the central jet and the fuel/oxidizer momentum ratio were proposed as the key parameters to physically characterize different operating conditions.

### 1.2.3 Experimental Study on High-Pressure Cryogenic Propellants Combustion

Typical applications of cryogenic propellants combustion in rocket engine have been illustrated in Fig. 1.1. Reactants are introduced into the combustion chamber through coaxial injectors. Liquid oxygen (LOX) generally is delivered through the inner tube at low speed, while gaseous hydrogen ( $\text{GH}_2$ ) is fed through the outer annular duct.

At a subcritical pressure, atomization starts at the confluence of the liquid and gaseous streams. The liquid core diminishes progressively as the spray is formed. The initial ligaments are torn away from the LOX jet by the hydrogen stream, which finally experience a secondary atomization and break into finer droplets because their sizes are too large to sustain the shearing stresses associated with the velocity difference between the two streams. The atomization quality is determined by two important parameters (Candel et al., 1998). The momentum ratio between the two streams controls the stripping of the liquid core and determines its length, whereas the sizes of the droplets after secondary breakup are sensitive to the Weber number ( $\text{We}$ ) defined based their diameter. When the Reynolds numbers of the two streams are sufficiently large, the droplets vaporize, and gaseous oxygen reacts with hydrogen in a highly turbulent flowfield.

The three characteristic time scales associated with vaporization, mixing, and combustion could be used to define two Damkhöler numbers: the chemical reaction Damkhöler number that compares the mixing time with the chemical time

$$Da_c = \frac{\text{Mixing Time}}{\text{Chemical Reaction Time}} \quad (1.1)$$

and the vaporization Damkhöler number, which is the ratio of the mixing to vaporization times

$$Da_v = \frac{\text{Mixing Time}}{\text{Vaporization Time}} \quad (1.2)$$

Snyder et al. (1997) estimated the magnitude of these numbers for a shear-coaxial injector at elevated chamber pressure. The chemical Damköhler number is always greater than unity, whereas the vaporization Damköhler number is generally lower than unity. Therefore, vaporization of LOX droplets controls the combustion process at subcritical pressure. If the droplets are too large, they may escape the combustion chamber without being fully vaporized. The greater chemical reaction Damköhler number indicates that combustion occurs only in thin reactive zones and that the regime of combustion is of the flamelet type.

When chamber pressure is near or above the critical points of the injected propellants, surface tension and enthalpy of vaporization diminish. The vanishment of intermolecular forces promotes diffusion dominated processes, and the injected fluid forms a continuous flow regime in the presence of exceedingly large gradients. The magnitude of the LOX jet gasification rate is at least one order greater than that of the vaporization at lower pressure (Delplanque and Sirignano, 1994). Furthermore, the Reynolds number increases with pressure leading to faster small-scale mixing. These two effects combine to suggest that large-scale turbulent mixing becomes the slowest and therefore is the most influential process.

Candel et al. (1998) and Herding et al. (1998) carried out extensive experiments on the jet flame formed from a single coaxial injector at elevated chamber pressure (5-10 atm) over a wide range of mass and momentum ratios. The injection temperature of hydrogen was fixed at 289 K, and that of oxygen was around 100 K. Several important diagnostic techniques were developed. Flow visualization was achieved through emission images of OH radicals. The intensive reaction zone (flame) was simultaneously localized by planar Laser-Induced Fluorescence (LIF) of OH and O<sub>2</sub>. The interface between gas and liquid and the breakup length of LOX jet were measured by the Elastic Light Scattering (ELS) technique. Quantitive temperature measurement was measured using the Coherent Anti-Stokes Raman Spectroscopy (CARS). The mean flame surface structures deduced from the Abel Transformation of the averaged OH emission image

were compared with that measured by the OH-LIF images. Good agreement was obtained. The mean flame began at the LOX post tip, which was initially a thin, nearly cylindrical surface around the inner jet and expanded downstream into a thick shell surrounding the LOX spray. The initial expansion angle increased with increasing momentum ratio. Further downstream, the mean flame became annular. The inner and outer diameters of the flame volume slowly decreased with axial distance as the oxygen convected in the central region was being consumed. Statistics of flame location obtained from O<sub>2</sub>-LIF showed that the wrinkling and flapping of the flame were smaller near the injector and increased downstream. In addition, the large temperature fluctuations at the near injector region were detected by the CARS spectrum of H<sub>2</sub>, which indicated the presence of an unsteady mixing layer between oxygen jet and hydrogen flow.

Flame stabilization is a crucial issue in a propulsion system. In liquid-propellant rocket engines, it is achieved by recessing the LOX post with respect to the injector face plate. The detailed mechanisms of recess on cryogenic flame stabilization were investigated by Kendrick et al. (1999) at an elevated pressure (10 atm). The injection temperatures of LOX and gaseous hydrogen were approximately 100 K and 297 K, respectively. The momentum ratio between the annular and inner streams varied from 6.5 to 14.5. The flowfield was visualized by the OH emission image. When the LOX post was recessed, the flame was stabilized inside the injector, and its expansion angle was augmented. The thickness of the flame brush and the size of the reaction zone were also enhanced. The recess effect was more substantial at lower momentum ratio. A simple one dimensional model was constructed to explain the observed phenomena. Since the flame developed inside the injector, it produced hot gases which occupied a certain fraction of the available duct area. As a result, the annular hydrogen stream was accelerated, and the gas to liquid momentum ratio was enhanced. The strengthened momentum ratio, in turn, led to a faster breakup of the liquid core and a correspondingly enlarged flame blooming angle.

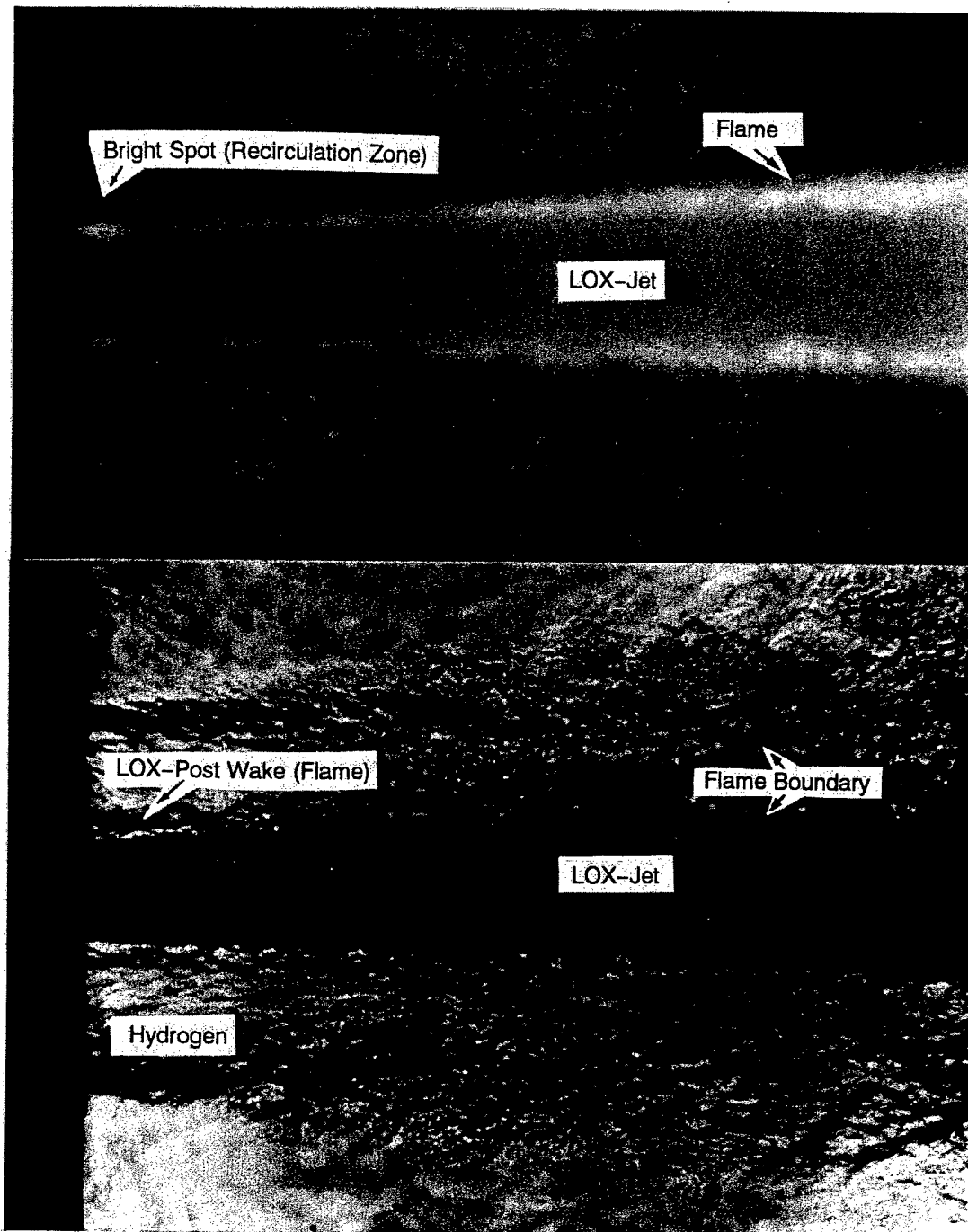


Fig. 1.4: Near Injector region of a liquid-oxygen-gaseous-hydrogen shear-coaxial injector, a) flame; and b) corresponding flowfield. Oxygen and hydrogen velocities are 30 and 300 m/s, respectively. The injection temperatures are 100 and 300 K for oxygen and hydrogen streams, respectively, and the chamber pressure is 4.5 MPa (Adopted from Mayer and Tamura, 1996).

Combustion of LOX and GH<sub>2</sub> at both sub- and supercritical chamber pressure (5 to 70 atm) was investigated by Juniper et al. (2000). The injection temperatures of LOX and GH<sub>2</sub> were 80 K and 280 K, respectively. The gas to liquid momentum ratio ranged from 6 to 14.5. At subcritical pressures, ligaments and droplets appeared at the edge of the LOX jet. However, they were no longer evident at 70 atmospheres, where the dense oxygen was in the form of pocket with indistinguishable boundary. The atomization and vaporization was inhibited. Although the flame still attached to the LOX post tip at supercritical pressures, the initial expansion angle was reduced and became less dependent on the momentum ratio. The combustion was dominant by the large-scale turbulent mixing, which was associated with the velocity ratio of two streams. To retain the same momentum ratio at higher pressure, the velocity ratio was reduced, which caused the turbulent mixing to diminish and the flame to narrow.

Another notable and important work on high-pressure combustion was conducted by Mayer and his colleagues (Mayer and Tamura, 1996; Mayer et al., 2001; Ivancic and Mayer, 2002). Subscale shear-coaxial injectors with and without recess were employed. The hot firing test conditions covered a wide range of pressure (10-100 atm). The injection velocity of LOX was 10-30 m/s, and the temperature was 100 K. The velocity of GH<sub>2</sub> stream was fixed at 300 m/s, and its temperature varied from 150 to 300 K. Those conditions were comparable to the operating state of a liquid rocket engine. The flow visualization was achieved by shadowgraph imaging. The most important results of their work were presented in Fig. 1.4. A LOX post wake flame and its interaction with the H<sub>2</sub>/O<sub>2</sub> shear-layer were clearly observed. The flame always attached instantaneously to the LOX post after ignition. A bright flame spot observed close to the LOX post tip suggested that a well-mixed flame with strong radiation was anchored in an intensive recirculation zone. This flow pattern could be observed over the entire range of test conditions for injector with and without recess, and even for a LOX post tip thickness of 0.3 mm.

The flame anchoring mechanism was illustrated in Fig. 1.5. Several small recirculation eddies were generated in the vicinity of the LOX-post tip, which consisted of partly preburned hydrogen rich gas. As the evaporating LOX mixed and reacted with the hydrogen gas in these eddies, the hot product again mixed with hydrogen stream and circulated back. Since the flow velocities in this region were so low, stationary combustion was possible.

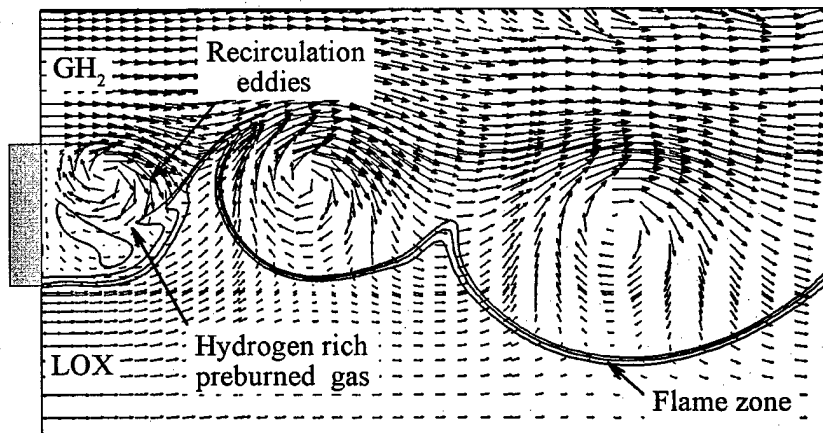


Fig. 1.5: Schematic of flame-holding mechanism.

Ignition poses many problems to launch vehicles. For example, an accidentally high pressure peak generated due to the ignition delay may trigger combustion instabilities with the risk of a serious damage of the combustor. The transient ignition of a cryogenic GH<sub>2</sub>/LOX system was recently investigated by Gurliat et al. (2003). A subscale shear-coaxial injector without recess was employed. Both the hydrogen and oxygen streams were delivered to the chamber at 77 K. The combustion was triggered by the intensive energy input from a pulsed laser at a certain axial location downstream of the faceplate. The detailed temporal behavior of the ignition was available for first time through high-speed Schlieren image. The process could be characterized into four different phases. The primary ignition phase began at the time of energy deposition. During this phase, the flame front was convected downstream by the flow and expanded in the shear-layer. After the flame reached the edge of the shear-layer, the flame

propagation phase started, where its front propagated upstream through the recirculation zone and consumed the premixed propellants. After reaching the faceplate and depleting all premixed propellants in the recirculation zone, it had to move downstream away from the injector until it achieved a maximum distance in the flame lift-off phase. The flame was finally anchored by the wake region near the faceplate. The existence of those steps during the ignition was also confirmed by the chamber pressure history; however, the time scale of each phase may vary depending on different operating conditions.

#### **1.2.4 Theoretical and Experimental Study on Swirl Coaxial Injector Design**

Figure 1.6 schematically shows the configuration of a typical swirl coaxial injector widely employed in contemporary liquid-propellant rocket injection systems for liquid/liquid and gas/liquid mixtures. Liquid oxygen is introduced tangentially into the center post, and then forms a swirling film attached to the tube due to centrifugal force. A hollow gas core exists in the center region in accordance with the conservation of angular momentum. The film exits the post in the form of a thin sheet and impinges on the surrounding fuel stream. The swirl atomization process basically involves two mechanisms: disintegration of the liquid sheet as it swirls and stretches; and sheet breaks up due to the interaction with the surrounding coaxial flow.

Compared with jet injector, a liquid swirl injector distinguishes itself in many aspects (Bazarov et al., 2004). First, for the same pressure drop and liquid flowrate, the average median diameter of droplet is 2.2 to 2.5-fold smaller than that of jet injectors. This advantage prevails for high flowrates and abates when counter pressure (i.e., the sum of the combustion chamber pressure and the centrifugal pressure created by liquid swirling motion) grows. Second, swirl injectors are not so sensitive to manufacturing errors such as deviation from the prescribed

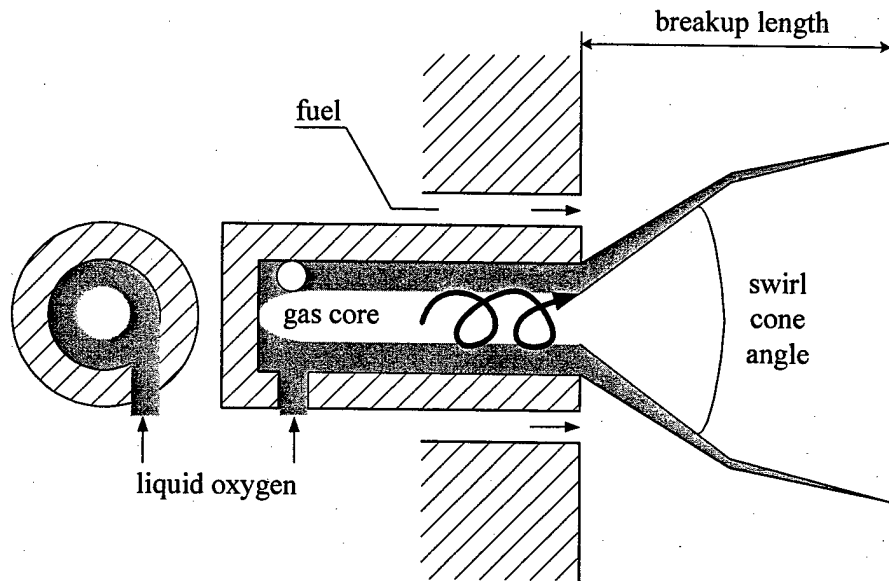


Fig. 1.6: Schematic of swirl coaxial injector.

diameter and surface misalignment. In addition, the flow passage areas of swirl injectors are much larger than those of jet injectors with the same flowrates and, consequently, they are less susceptible to choking or cavitation. Thirdly, the central post of rocket swirl injector features large aspect ratios (i.e. L/D up to 20) owing to propellant supply manifolding considerations. The viscous loss along the wall exerts significant influence on the flow evolution and consequently alters the spray distribution and atomization.

The fundamentals of inviscid swirl injector theory were established more than 60 years ago by Abramovich in 1944 and independently by Taylor in 1947. The up-to-date discussion of the classical theory and the injector design criterion, which was particularly easy of implementation, were presented by Bazarov et al. (2004) and Bayvel and Orzechowski (1993). Besides the theoretical analysis, a series of experiments were conducted to provide an essential reference frame of swirl injector design, especially for liquid rocket applications.

Hulka et al. (1991, 1993, 1993) conducted a series of cold-flow studies using water and inert gases as propellant simulants to characterize several liquid rocket swirl injector elements.

There were three basic types of tests, including still photography of free oxidizer sprays, mass and mixture ratio distribution measurements of water only and water/nitrogen sprays, and the Rupe mixing efficiency measurement at atmospheric pressure using water and a sucrose solution over a broad range of mixture and velocity ratios. Rupe mixing efficiency,  $Em$ , is calculated as a summation of the mass weighted mixture ratio over the number of collected samples

$$Em = 1 - \sum_{i=1}^N X_{fi} \frac{R_o - R_i}{R_o} - \sum_{i=1}^N X_{oi} \frac{R_o - R_i}{R_o - 1} \quad (1.3)$$

where,  $N$  is the number of collected samples,  $X_{oi}$  is the mass fraction of an oxidizer rich sample,  $X_{fi}$  is the mass fraction of a fuel rich sample,  $R_o$  is the overall oxidizer mass fraction, and  $R_i$  is the oxidizer mass fraction of a sample. A broad range of fuel/oxidizer mixture and velocity ratios was studied. Results indicated that the mixing efficiency could be greatly increased by increasing the oxidizer initial spreading angle, which was achieved by reducing the tangential inlet area or increasing the central post-exit diameter. The oxidizer mass flowrate had insignificant influence on the single element mixing efficiency, suggesting a larger oxidizer swirl element with a mass flowrate greater than that of a shear-coaxial injector could still obtain better intraelement mixing efficiency.

Rahman et al. (1995) visualized water/air spray injection at room conditions. The instantaneous shadowgraph indicated that in the absence of gas flow, a hollow conical liquid sheet was formed at the injector exit. The cone angle was effectively fixed by the injector geometry, whereas the breakup point of the liquid sheet became closer to the injector exit as the mass flowrate increased. Due to the viscous loss, the conical sheet angle decreased with the increase in the aspect ratio of the post length to the diameter.

A similar cold flow test with water/nitrogen as injectants was studied by Sasaki et al. (1997), with particular attention paid to the effect of the central post recess distance. In a recessed injector, because the liquid sheet generated by the swirl motion impinged on the outer wall of the annular fuel passage, its spray angle narrowed with a deformed pattern. The liquid sheet, which blocked the annular passage, was blown off in the shape of a mushroom and with a screaming sound known as self-pulsation phenomena. The effect of recesses on the spray characteristics of a swirl coaxial injector was also studied by Han et al. (2003). Water and kerosene were employed as simulants for oxidizer and fuel, respectively. With the use of phase Doppler particle analyzer (PDPA) and mechanical patternator, the median droplet size, spray angle, and breakup length were measured. Their results indicated that an optimal recess length existed to obtain a maximum mixing efficiency.

The dynamic characteristics of the swirl injector were thoroughly studied by Bazarov and Yang (1998). The overall response function of the swirl injector could be represented in terms of the transfer characteristics of each individual element (tangential passage, vortex chamber, and discharge nozzle) and analyzed independently, and then combined together. The resultant amplitude-phase characteristics were very complicated; however, they guided the designers to obtain any desired pulsation characteristics by either suppressing or amplifying flow oscillations. Based on this work, it becomes possible to control the engine combustion dynamics by changing the injector dynamics alone without modifying the other parts of the combustion devices. In addition, various mechanisms for driving self-pulsations in both liquid and gas-liquid injectors were analyzed and discussed in detail. The self-pulsation boundary at different operating conditions was also illustrated. Those results are very useful to the engineering design.

Most of the existing studies were conducted at low pressures, and thus did not simulate many of the important scaling parameters of the liquid rocket swirl injectors. Based on the cold flow experiments conducted at a moderate pressure (3.84MPa), Cox (1988) noted the importance

of performing high-pressure experiments to match both the gas/liquid density and velocity ratios in real conditions. Recently, Strakey et al. (2001) studied the characteristics of a swirl coaxial gas-liquid injector over a wide range of gas/liquid momentum ratios from 0 to 100 at elevated chamber pressure (2.97MPa) using water and helium/nitrogen as propellant simulants. For high momentum ratio, the spray spreading angle was much less than that reported in previous studies at one-atmosphere pressure. However, compared with the shear-coaxial injector, the swirl spray did exhibit a smaller overall droplet size.

Besides cold flow testing, a number of hot-fire experiments were conducted for single- or multi-elements swirl injectors at both moderate (i.e., 2.6-3.5 MPa) and high chamber pressure (i.e., 10.3 MPa) (Tamura et al., 1997; Elm, 1991). The C\* efficiency was found to increase with increasing mixture ratio. A major factor contributing to this phenomenon is the increased swirl cone angle as the fuel/oxidizer momentum ratio decreases. More details can be found in the cited works.

### **1.2.5 Numerical Works on High-Pressure Fluid Mixing and Combustion**

Parallel to experimental studies, attempts were made both theoretically and numerically to explore the underlying mechanisms of high-pressure fluid injection and combustion.

The most comprehensive numerical models were established by Oefelein and Yang (1998). They modeled two-dimensional mixing and combustion of oxygen and hydrogen streams at supercritical conditions by means of a large-eddy-simulation technique. The formulation accommodated real-fluid thermodynamics and transport phenomena. All the thermophysical properties were evaluated directly from fundamental thermodynamics theories over the entire fluid states of concern. Furthermore, a unified treatment of numerical algorithms based on general fluid thermodynamics was established to improve computational accuracy and efficiency

(Meng and Yang, 2003). The results indicated that the density gradient dominated the evolution of the mixing layer and the mass diffusion rate greatly diminished near the critical point.

The dominance of density gradient was observed in the direct numerical simulation (DNS) conducted by Bellan and colleagues (Miller et al., 2000, Okong'o and Bellan, 2002, Okong'o et al., 2002), where the temporal evolutions of heptane/nitrogen and oxygen/hydrogen mixing layers at supercritical conditions were treated, and several important characteristics of high-pressure transitional mixing processes were identified. Because emerging turbulent eddies were damped by strong density stratification, the layer was considerably more stable than a corresponding gaseous one at standard pressure. During the entire evolution process, energy dissipation due to both the species-flux and heat-flux effects was dominant, whereas the viscous effect appeared minimal. This suggested that turbulent models for supercritical fluids should primarily focus on duplicating the species mass flux rather than the typical momentum flux.

Ivancic and Mayer (2002), Branam et al.(2003), and Barata et al. (2003) simulated cryogenic fluid injection and combustion at both sub- and supercritical pressures. The two-dimensional steady calculations were performed, which included the  $k - \varepsilon$  turbulence model and real gas properties evaluation for the injected cryogenic fluid. Since the treated processes were inherently transient, their drastic steady state assumption might yield inaccurate results and could not exhibit the distinct features of high-pressure real-fluid dynamics.

The extinction limits of the flame generated around the LOX jet boundary were theoretically studied by Juniper et al.(2003). A one-dimensional counterflow diffusion flame model was constructed. The results indicated that the flame was very stable in the near injector region. It could not be extinct by strain rate, even for a very low hydrogen stream temperature. Since the typical strain rates encountered in rocket engine were insufficient to punch a hole in the flame, the edge of this diffusion flame sheet should be stabilized behind the lip of the LOX post. Following this suggestion, a two-dimensional simulation was performed to investigate the flame

stabilization mechanism behind a step over a liquid reactant surface (Juniper and Candel, 2003). It was reported that the most influential parameter regarding flame stabilization was the height of the step with respect to the flame thickness. If the flame was thicker than the step, it could not remain in the recirculation zone behind the step and was readily blown off.

### 1.2.6 Work Scope and Method of Approach

The present study investigates the high-pressure cryogenic fluid injection and mixing dynamics by means of large-eddy-simulation. The flow evolution under consideration is extremely complicated, involving thermodynamic nonidealities, transport anomaly, and high Reynolds number turbulent flow. A variety of uncertainties exist with regard to the closure problem. To address these difficulties in a manner consistent with current experimental efforts, this research focuses on detailed representations of fluid dynamic and thermophysical processes in the simplified configurations and well controlled experimental conditions. The approach follows three fundamental steps: 1) the development of a generalized theoretical framework with the accurate property evaluation schemes and closure methodologies; 2) the implementation of an efficient and robust numerical algorithm for general fluid mixture, in which the real-fluid thermodynamics are treated consistently with full account of pressure effects; 3) the systematic investigation of a series of cases associated with trans- and supercritical injection and mixing dynamics. These steps are carried out in Chapters 2 through 7, respectively, with relevant conclusions and recommendations presented in Chapter 8.

Chapter 2 presents a generalized theoretical framework that accommodates high-pressure real fluid thermodynamics, transport anomalies, and turbulence. The governing equations are obtained using convolution integrals to filter out the small-scale dynamics from the resolved-scales over a defined set of spatial and temporal intervals. The subgrid-scale (sgs) terms are

modeled using a compressible-flow version of the Smagorinsky model suggested by Erlebacher et al. (1992). Thermodynamic properties, including enthalpy, internal energy, heat capacity, and their related partial density properties, are directly calculated by means of fundamental thermodynamic theories (1999) and a modified Soave-Redlich-Kwong (SRK) equation of state that is reasonably accurate and easy for implementation (Graboski and Daubert, 1978a, 1978b). Transport properties, such as viscosity and thermal conductivity, are estimated with an extended corresponding state principle with a 32-term Benedict-Webb-Rubin (BWR) equation of state (Ely and Hanley, 1981, 1983).

In Chapter 3, the governing system is discretized using a preconditioned, density-based, finite-volume methodology. The basic formulations are derived using fundamental thermodynamic theories, in which the definition of partial mass and partial density properties are introduced. This framework takes full account of thermodynamic nonidealities and transport anomalies and accommodates any arbitrary equation of state. The developed equations are coupled with the preconditioning scheme, which renders the numerical algorithm capable of solving all-Mach number fluid flows at any fluid state (2003). Second order dual-time stepping integration with the convergence acceleration techniques developed by Choi and Merkel (1993) and Buelow et al. (1994) are adopted for temporal discretization. Spatial discretization employs the fourth-order accurate flux differencing methodologies developed by Rai and Chakravarthy (1994). A fourth-order scalar dissipation with a total-variation-diminish (TVD) switch developed by Swanson and Turkel (1992) and Jorgenson and Turkel (1993) is implemented to ensure computational stability and to prevent numerical oscillations in regions with steep gradients. A multiblock domain decomposition technique, along with static load balance, is used to facilitate the application of efficient parallel computation with message passing interfaces at the domain boundaries.

Chapters 4, 5, 6, and 7 present a series of case studies. In Chapters 4 and 5, injections of cryogenic nitrogen fluid initially at a subcritical temperature into a supercritical environment, in which both the pressure and temperature exceed the thermodynamic critical point, are investigated over a broad range of ambient pressures. The unique processes, which have substantial influence on the supercritical jet dynamics, are identified and analyzed in detail. The results are compared with experimental data to establish the accuracy and credibility of the numerical method.

The validated model is applied in Chapter 6 to examine key phenomena associated with high-pressure injection and mixing of LOX and methane. Emphasis is placed on the thermophysical processes and transport which occur in the vicinity of the splitter plate and the impact of the different injection conditions. The simulation is conducted on a fixed pressure of 100 atmospheres, with the injection temperature selected to produce an optimal matrix of sub- and transcritical conditions. Results highlight the effect of the velocity ratio on the shear-layer dynamics, the dominating effect of the density gradient, and the influence of the injection temperature on the flow evolution.

Swirl injection of high-pressure cryogenic oxygen into a supercritical gaseous oxygen environment is studied in Chapter 7. The influences of various geometric parameters and operation conditions, including mass flowrate, tangential slit position, injector post length, and swirl strength, on the injector dynamics and performance are investigated systematically. Both the internal flow dynamics and the external mixing process are explored. The distinct features between high- and low-pressure swirl injections are identified. To help understand the physical phenomena involved, a theoretical model is established. Its predictions are consistent with the simulation results.

Finally, the conclusions of the present research and recommendations for future work are summarized in Chapter 8.

## Chapter 2

### Theoretical Formulation and Property Evaluation

#### 2.1 Governing Equations

The theoretical formulation is based on the full conservation equations of mass, momentum, energy, and species concentration in Cartesian coordinates

$$\frac{\partial \rho}{\partial t} + \frac{\partial (\rho u_i)}{\partial x_i} = 0 \quad (2.1)$$

$$\frac{\partial (\rho u_i)}{\partial t} + \frac{\partial (\rho u_i u_j)}{\partial x_j} = -\frac{\partial p}{\partial x_i} + \frac{\partial \tau_{ij}}{\partial x_j} \quad (2.2)$$

$$\frac{\partial \rho E}{\partial t} + \frac{\partial [(\rho E + p)u_i]}{\partial x_i} = -\frac{\partial q_i}{\partial x_i} + \frac{\partial (u_i \tau_{ij})}{\partial x_j} \quad (2.3)$$

$$\frac{\partial \rho Y_k}{\partial t} + \frac{\partial (\rho Y_k u_j)}{\partial x_j} = \dot{\omega}_k - \frac{\partial (\rho Y_k U_{k,j})}{\partial x_j}, \quad k = 1, \dots, N-1 \quad (2.4)$$

where  $i$ ,  $j$ , and  $k$  are the spatial coordinate index, the dummy index to spatial coordinate, and the species index, respectively.  $N$  is the total number of species.  $Y_k$  and  $U_{k,j}$  represent mass fraction and diffusion velocities of species  $k$ , respectively. The viscous stress tensor  $\tau_{ij}$  for a Newtonian fluid (with Stokes assumption) and the heat flux vector  $q_j$  are defined as

$$\tau_{ij} = \mu \left( \frac{\partial u_i}{\partial x_j} + \frac{\partial u_j}{\partial x_i} - \frac{2}{3} \delta_{ij} \frac{\partial u_l}{\partial x_l} \right) \quad (2.5)$$

$$q_j = -\lambda \frac{\partial T}{\partial x_j} + \rho \sum_{k=1}^N \hat{h}_k Y_k U_{k,j} \quad (2.6)$$

where  $\mu$  and  $\lambda$  are the coefficients of viscosity and thermal conductivity, respectively. In the present work, viscosity and thermal conductivity are estimated with an extended-corresponding-state-principle with a 32-term Benedict-Webb-Rubin (BWR) equation of state. The specific total energy  $E$  is given by

$$E = e + \frac{u_j u_i}{2} \quad (2.7)$$

The specific internal energy,  $e$ , is obtained as

$$e = h - \frac{p}{\rho} \quad (2.8)$$

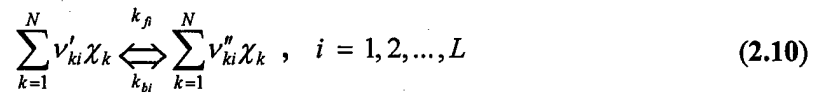
The specific enthalpy of mixture,  $h$ , containing contributions from its constituent species, can be written as

$$h = \sum_{k=1}^N Y_k \hat{h}_k \quad (2.9)$$

where  $\hat{h}_k$  is partial mass enthalpy of species  $k$ , which will be defined in the following sections.

The formulation is closed by a modified Soave-Redlich-Kwong (SRK) equation of state for real fluid mixture.

To obtain the expression for the chemical reaction source term, consider an  $L$ -step reaction mechanism with  $N$  species, which can be written as



where  $v'_{ki}$  and  $v''_{ki}$  are the stoichiometric coefficients on the reactants and products side for species  $k$  in the  $i^{\text{th}}$  reaction.  $\chi_k$  represents the chemical formula of species  $k$ .  $k_{fi}$  and  $k_{bi}$  are the

reaction rate constants of the forward and backward reactions, respectively. They may take the following form

$$k_i(T) = A_i T^b \exp(-E_i / R_u T) \quad (2.11)$$

where  $A$ ,  $b$ , and  $E_i$  are empirical parameters and  $E_i$  represents the activation energy of reaction  $i$ .

The following relationship expresses the net production rate  $\dot{\omega}_k$  of each species in a multi-step mechanism

$$\dot{\omega}_k = W_k \sum_{i=1}^L (v''_{ki} - v'_{ki}) \left[ k_{fi} \prod_{k=1}^N [\chi_k]^{v'_{ki}} - k_{bi} \prod_{k=1}^N [\chi_k]^{v''_{ki}} \right], \quad k = 1, 2, \dots, N \quad (2.12)$$

where  $W_k$  and  $[\chi_k]$  represent the molecular weight and molar concentration of species  $k$ . Note that the expression for the net production rate, Eq. 2.12, is valid only for elementary reactions. Since some researchers may use a global kinetic mechanism, the exponents for molar concentrations may differ from their stoichiometric coefficients.

## 2.2 Turbulence Closure: Large-Eddy-Simulation

Turbulence remains a challenge in fluid mechanics research due to its strong nonlinear behavior, although this topic has been studied for more than one hundred years. Numerical simulation of turbulent motions can be classified into three categories, as illustrated in Fig. 2.1.

The most straightforward method is direct numerical simulation (DNS). Given sufficient computing resources, the equations governing flow evolution can be solved without any model, and the entire spectrum of turbulence scales is resolved explicitly. DNS is the most accurate tool for studying turbulence; however, the computational burden of DNS for solving most practical engineering problems is far beyond the current computer capabilities.

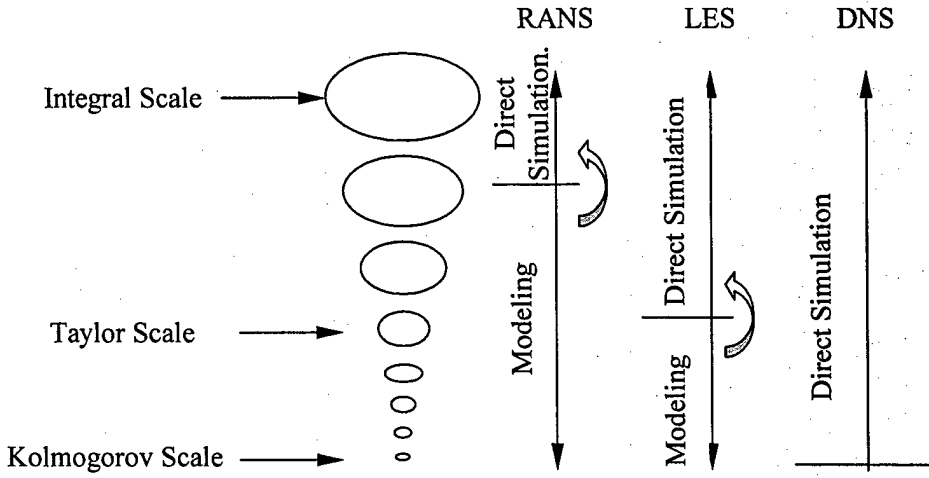


Fig. 2.1: Concepts of DNS, LES and RANS (adopted from Wang, 2002).

The Reynolds-averaged Navier-Stokes equations (RANS) have been used for most engineering applications. The computational cost for RANS models is much less than that for DNS because of its lower grid resolution requirement. However, owing to the distinctive behavior between large- and small-scale turbulent motions, it is impossible to achieve a universal model that can cover all turbulent flows (Piomelli, 1999).

Large-eddy-simulation (LES) (Deardorff, 1970; Pope, 2000) is an intermediate approach between the two aforementioned methods. The largest scales, which contain most energy, are directly simulated. On the other hand, smaller scales, i.e., subgrid scales, are modeled. This method is based on the assumption that small-scale flow evolution tends to be more homogeneous than large-scale flow motions. The inhomogeneity of flow properties decreases with decreasing scales, and eventually disappears at the Kolmogorov scales, i.e., dissipation scales (Batchelor, 1953; Brasseur, 2002). In principle, the grid size of LES should fall in the inertial range.

Subgrid-scale (SGS) modeling is the core of LES. Because the dissipation scales, i.e., Kolmogorov scales, of turbulent flows are not resolved, the main role of SGS models is to transfer energy from resolved scales to unresolved scales through the energy cascade. In other words, the effects of unresolved scales on resolved scales must be modeled. Several SGS models have been developed since the late 1980s, most of which are based on the eddy-viscosity model. Commonly used SGS models include the Smagorinsky eddy viscosity model, dynamic eddy viscosity model, and similarity and mixed model.

The Smagorinsky SGS model (Smagorinsky, 1963) is widely used because of its simplicity. It predicts fairly accurately from the global dissipation point of view when the integral scales are well resolved. This model, however, has obvious drawbacks because the coefficients are positive constants in its standard form. As a result, the model is too dissipative to predict the SGS stresses in laminar regions or in the viscosity sub-layers of boundary layers, where the SGS stresses should vanish. It cannot predict the backscatter phenomena in the near-wall region either. These drawbacks can be avoided by introducing *ad hoc* modifications, such as the van Driest damping (van Driest, 1956) and an intermittency function (Piomelli et al., 1990). The van Driest damping function corrects the behavior in the near-wall region and the intermittency function eliminates the SGS stress in the laminar flow region. These *ad hoc* adjustments require empirical functions.

To avoid the empirical coefficients in the Smagorinsky model, a dynamic eddy viscosity model (Germano et al., 1991) was proposed, which represented a significant progress in subgrid-scale modeling. In the dynamic model, both a test and an LES filters are used, instead of just an LES filter as in the Smagorinsky model. The coefficients of the dynamic model are assumed to be constant in both filters and are computed dynamically during the calculation. The dynamic model yields good predictions of the average subgrid-scale stresses at the local level.

A weakness of the eddy viscosity model is that the principal axis of the strain-rate and SGS stress tensors are aligned. A scale-similar model was introduced by Bardina et al.(1980) to avoid this problem. A dynamic model, including a scale-similar part, was applied by Zang et al.(1993). These models are based on the recognition that the most active subgrid-scales are generally those close to the cutoff wavenumber, and that the scales with which they interact most are also near the cutoff wavenumber. Meneveau et al. (2000) stated that the mixed models are superior, on the whole, to simple eddy viscosity models.

Another promising approach to the LES subgrid-scale modeling is the Monotonically Integrated LES (MILES), which solves the unfiltered Navier-Stokes equations using high-resolution monotone algorithms. In this approach implicit tensorial (anisotropic) SGS models, provided by intrinsic non-linear high-frequency filters built into the convection discretization, are coupled naturally with the resolvable scales of the flow. The MILES approach provides an attractive alternative when seeking improved LES for inhomogeneous (inherently anisotropic) high Reynolds number turbulent flows (Fureby and Grinstein, 1999; 2002; Grinstein et al., 2002).

### **2.2.1 Filtering Operations**

In a large-eddy-simulation, filtering operations are used to separate the large-scale from the small-scale turbulent motions. A filtered (or resolved, or large-scale) variable is defined as

$$\bar{f}(\mathbf{x}) = \int_{\infty} f(\mathbf{x})G_f(\mathbf{x} - \mathbf{x}')d\mathbf{x}' \quad (2.13)$$

where  $G_f$  is the filter function and  $\int_{\infty} G_f(\mathbf{x})d\mathbf{x} = 1$ . Leonard (1974) indicated that if  $G_f$  is only a

function of  $\mathbf{x} - \mathbf{x}'$ , differentiation and the filtering operation could commute each other. The most commonly used filter functions are the Top-hat, Gaussian, and Cutoff filters.

The Top-hat filter is popularly employed in physical space and is defined as

$$G_f(\mathbf{x}) = \begin{cases} 1/\Delta & \text{if } |\mathbf{x}| \leq \Delta/2 \\ 0 & \text{otherwise} \end{cases} \quad (2.14)$$

In a finite volume method, the cell-averaged variables are defined at each cell as

$$\bar{f} = \frac{1}{\Delta V} \int_{\Delta V} f(\mathbf{x}) d\mathbf{x} \quad (2.15)$$

Thus, the cell average in the finite volume method, which will be implemented in the current study, belongs to the Top-hat filter. The Gaussian filter is also defined in physical space. The Gaussian filter function is the Gaussian distribution with zero mean and variance  $\sigma^2 = \Delta^2 / 12$

$$G_f(\mathbf{x}) = \sqrt{\frac{6}{\pi \Delta^2}} \exp\left(-\frac{6|\mathbf{x}|^2}{\Delta^2}\right) \quad (2.16)$$

The Cutoff filter is a Top-hat filter in the spectral space

$$\hat{G}_f(\mathbf{k}) = \begin{cases} 1 & \text{if } |\mathbf{k}| \leq \pi/\Delta \\ 0 & \text{otherwise} \end{cases} \quad (2.17)$$

A detailed description of properties of various filters can be found in textbook (Pope, 2000).

## 2.2.2 Filtered Governing Equations

Any instantaneous variable ( $f$ ) can be defined as the sum of a Favre-averaged filtered scale ( $\tilde{f}$ ) and a sub-grid scale ( $f''$ )

$$f = \tilde{f} + f'' \quad (2.18)$$

where

$$\tilde{f} = \frac{\overline{\rho f}}{\overline{\rho}} \quad (2.19)$$

Favre-averaging is used here to simplify the governing equations and to account for the variable density effects. However,  $\overline{\rho f g} \neq \overline{\rho} \tilde{f} \tilde{g} + \overline{\rho f' g'}$  for filtering operations in LES, which is different from the Reynolds average (see Appendix A).

The filtered Favre-averaged Navier-Stokes equations for mass, momentum, energy and species concentration can be written as

$$\frac{\partial \overline{\rho}}{\partial t} + \frac{\partial \overline{\rho u_i}}{\partial x_i} = 0 \quad (2.20)$$

$$\frac{\partial \overline{\rho u_i}}{\partial t} + \frac{\partial (\overline{\rho u_i} \tilde{u}_j + \overline{p} \delta_{ij})}{\partial x_j} = \frac{\partial (\tilde{\tau}_{ij} - \tau_{ij}^{sgs})}{\partial x_j} \quad (2.21)$$

$$\frac{\partial \overline{\rho E}}{\partial t} + \frac{\partial ((\overline{\rho E} + \overline{p}) \tilde{u}_i)}{\partial x_i} = \frac{\partial}{\partial x_i} (\tilde{u}_j \tilde{\tau}_{ij} + \lambda \frac{\partial \tilde{T}}{\partial x_i} - H_i^{sgs} + \sigma_i^{sgs}) \quad (2.22)$$

$$\frac{\partial \overline{\rho Y_k}}{\partial t} + \frac{\partial (\overline{\rho u_j} \tilde{Y}_k)}{\partial x_j} = \frac{\partial}{\partial x_j} (\overline{\rho} \tilde{U}_{k,j} \tilde{Y}_k - \Phi_{k,j}^{sgs} - \Theta_{k,j}^{sgs}) + \bar{\omega}_k \quad (2.23)$$

The unclosed sub-grid terms are:

$$\tau_{ij}^{sgs} = (\overline{\rho u_i u_j} - \overline{\rho u_i} \overline{u_j}) \quad (2.24)$$

$$H_i^{sgs} = (\overline{\rho E u_i} - \overline{\rho E} \overline{u_i}) + (\overline{p u_i} - \overline{p} \overline{u_i}) \quad (2.25)$$

$$\sigma_{ij}^{sgs} = (\overline{u_j \tau_{ij}} - \overline{u_j} \overline{\tau_{ij}}) \quad (2.26)$$

$$\Phi_{k,j}^{sgs} = (\overline{\rho Y_k u_j} - \overline{\rho Y_k} \overline{u_j}) \quad (2.27)$$

$$\Theta_{k,j}^{sgs} = (\overline{\rho Y_k U_{k,j}} - \overline{\rho Y_k} \overline{U_{k,j}}) \quad (2.28)$$

The SGS stresses term  $\tau_{ij}^{sgs}$ , SGS energy fluxes term  $H_i^{sgs}$  and SGS species fluxes  $\Phi_{k,j}^{sgs}$  result from filtering these convective terms. The SGS viscous work term,  $\sigma_{ij}^{sgs}$ , comes from correlations of the velocity field with the viscous stress tensor, and the SGS species diffusive fluxes term,  $\Theta_{k,j}^{sgs}$ , comes from correlations of the velocity field with the species mass fractions with the diffusion velocities. The filtered species mass production rate,  $\dot{\omega}_k$ , is also unclosed. The modeling of these SGS terms is discussed in detail in the following subsections.

In addition to the conservation equations, the equation of state must be filtered. Filtering the equation of state gives us

$$\bar{p} = R_u \tilde{Z} \bar{\rho} \tilde{T} + R_u (\tilde{Z} \bar{\rho}'' \bar{T}'' + \bar{\rho} \bar{Z}'' \bar{T}'' + \tilde{T} \bar{Z}'' \bar{\rho}'') \quad (2.29)$$

where  $Z$  is the compressibility factor. For ideal gas without heat release, the high order correlations in the filtered equation of state can be neglected (Calhoon and Menon, 1996). This may be not true for high-pressure real-fluid mixture. However, due to the difficulty and uncertainty in modeling those correlations, they are neglected without any justification in the current study.

The filtered total energy  $\tilde{E}$  can be approximated as

$$\tilde{E} = \tilde{h} - \frac{\tilde{p}}{\bar{\rho}} + \frac{\tilde{u}_k^2}{2} + k^{sgs} = \tilde{\psi} + \int_{p_0}^p \left[ \frac{1}{\rho} + \frac{T}{\rho^2} \left( \frac{\partial \rho}{\partial T} \right)_p \right] dp - \frac{\tilde{p}}{\bar{\rho}} + \frac{\tilde{u}_k^2}{2} + k^{sgs} \quad (2.30)$$

where  $\psi = \sum_1^N Y_k h_k^0$  and  $k^{sgs} = \tau_{kk}^{sgs} / 2\bar{\rho} = \frac{1}{2} (\bar{\rho} u_k u_k / \bar{\rho} - \tilde{u}_k^2)$ .

### 2.2.3 Subgrid-Scale Models

The SGS modeling is the core of LES. Because small eddies dissipate most of the energy and are unresolved, SGS models are introduced to allow for the transfer of energy from larger to smaller scales and to mimic the drain of energy associated with the energy cascade. Most of the SGS models are based on an eddy-viscosity type model. In these models, the SGS stress  $\tau_{ij}^{sgs}$  is related to the large-scale strain-rate tensor  $\tilde{S}_{ij}$  as follows

$$\tau_{ij}^{sgs} - \frac{\delta_{ij}}{3} \tau_{kk}^{sgs} = -2\nu_t \tilde{S}_{ij} \quad (2.31)$$

where  $\nu_t$  is the eddy viscosity and  $\tilde{S}_{ij} = \frac{1}{2} \left( \frac{\partial \tilde{u}_j}{\partial x_i} + \frac{\partial \tilde{u}_i}{\partial x_j} \right)$

#### 2.2.3.1 Algebraic Smagorinsky Model

In this kind of model, the eddy viscosity  $\nu_t$  is obtained algebraically to avoid solving additional equations. Usually the equilibrium hypothesis is made to simplify the problem and to obtain an algebraic model. The equilibrium hypothesis assumes that small-scale motions, which have shorter time scales than the large, energy-carrying eddies, can adjust more rapidly to perturbations and recover equilibrium nearly instantaneously. Under this assumption, a balance exists between the SGS kinetic energy production term and the viscous dissipation term:  $-\tau_{ij} \bar{S}_{ij} = \varepsilon_v$ . The Smagorinsky model based on the equilibrium hypothesis can be written as

$$\nu_t = (C_s \Delta)^2 |\tilde{S}| \quad (2.32)$$

where  $\Delta$  is the filter width and  $|\tilde{S}| = (2\tilde{S}_{ij}\tilde{S}_{ij})^{1/2}$ . The coefficient  $C_s$  can be determined from the isotropic turbulence decay or a *prioric* test. Erlebacher et al. (1992) extended the above model to include flow compressibility effects

$$\tau_{ij}^{sgs} = -2\nu_t \bar{\rho} (\tilde{S}_{ij} - \frac{\tilde{S}_{kk}\delta_{ij}}{3}) + \frac{2}{3} \bar{\rho} k^{sgs} \delta_{ij} \quad (2.33)$$

where  $\nu_t$  is the eddy viscosity.

$$\nu_t = C_R (\Delta D)^2 |\tilde{S}| \quad (2.34)$$

$$k^{sgs} = C_I (\Delta D)^2 \tilde{S}_{ij} \tilde{S}_{ij} \quad (2.35)$$

where the dimensionless quantities  $C_R$  and  $C_I$  represent the compressible Smagorinsky constants. The Van-Driest damping function ( $D$ ) is used to take into account the inhomogeneities near the wall (Moin and Kim, 1982), and is expressed as

$$D = 1 - \exp(1 - (y^+)^3 / 26^3) \quad (2.36)$$

where  $y^+ = y u_t / \nu$  and  $u_t$  is friction velocity.

The subgrid energy fluxes term  $H_j^{sgs}$  is modeled as

$$H_j^{sgs} = -\bar{\rho} \frac{\nu_t}{Pr_t} \left( \frac{\partial \tilde{h}}{\partial x_j} + \tilde{u}_i \frac{\partial \tilde{u}_i}{\partial x_j} + \frac{1}{2} \frac{\partial k^{sgs}}{\partial x_j} \right) \quad (2.37)$$

where  $Pr_t$  represents the turbulent Prandtl number, a standard value 0.7 is used. The SGS viscous work term,  $\sigma_{ij}^{sgs}$ , is neglected due to its small contribution to the total energy equation.

The convective species flux term is usually approximated as

$$\Phi_{k,i}^{sgs} = -\bar{\rho} \frac{\nu_t}{Sc_t} \frac{\partial \tilde{Y}_k}{\partial x_i} \quad (2.38)$$

where  $Sc_t$  is the turbulent Schmidt number. However, the use of the gradient transport assumption for reactive species is questionable. The SGS species diffusive fluxes term,  $\Theta_{k,j}^{sgs}$ , usually is also neglected.

The algebraic Smagorinsky type model described above is the most widely used model in LES. However, as pointed out by Moin et al. (1991), its limitations are as follows. First, the optimal model constant must be changed for a different class of flows. The model does not have the correct limiting behavior near a wall. The SGS stress does not vanish in laminar flow and the model is found to be very dissipative in the laminar/transition region. The model does not account for the backscatter of energy from small to large scale, which has been shown to be of importance in the transition region.

### 2.2.3.2 Dynamic Smagorinsky Model

The dynamic model introduced by Germano et al. (1991) overcomes many of the aforementioned deficiencies in algebraic models. The dynamic model uses the assumption of scale invariance by applying the coefficient measured from the resolved scales to the SGS range. It calculates the model coefficients dynamically as a function of position from the information already contained in the resolved velocity field during the simulation (rather than treating it as an adjustable parameter as in the standard Smagorinsky model). The dynamic model uses resolved-scale information at the grid-filter level and a coarser test-filter  $\hat{G}_f$  with characteristic  $\hat{\Delta} > \Delta$  (typically,  $\hat{\Delta} = 2\Delta$ ) in order to compute the model parameters  $C_R$  and  $C_I$  as a function of space and time (Germano et al., 1991). Formally, the dynamical procedure is based on the Germano identity (Germano, 1992)

$$L_{ij} = T_{ij} - \langle \tau_{ij}^{sgs} \rangle \quad (2.39)$$

where  $L_{ij} = \langle \tilde{\rho} \tilde{u}_i \tilde{u}_j \rangle - \langle \bar{\rho} \rangle \tilde{\tilde{u}}_i \tilde{\tilde{u}}_j$  and  $T_{ij} = \langle \tilde{\rho} u_i u_j \rangle - \langle \bar{\rho} \rangle \tilde{\tilde{u}}_i \tilde{\tilde{u}}_j$ . Here a Favre-filtered variable under a test-filter is defined as  $\tilde{f} = \langle \tilde{\rho} f \rangle / \langle \bar{\rho} \rangle$ . The brackets  $\langle \cdot \rangle$  denote the averaging operation based on the test filter. The following expressions can be derived for the dynamic evaluation of  $C_R$  and  $C_I$  using the least square minimization approach of Lilly (1992) for the momentum SGS stress tensor.

$$C_R = \frac{\langle L_{ij} M_{ij} \rangle}{\langle M_{kl} M_{kl} \rangle} - \frac{1}{3} \frac{\langle L_{mm} M_{mm} \rangle}{\langle M_{kl} M_{kl} \rangle} \quad (2.40)$$

$$C_I = \frac{\langle L_{kk} \rangle}{\langle \beta - \langle \alpha \rangle \rangle} \quad (2.41)$$

The forms of  $M_{ij}$ ,  $\beta$  and  $\alpha$  are given as follows

$$M_{ij} = \beta_{ij} - \langle \alpha_{ij} \rangle \quad (2.42)$$

$$\beta_{ij} = -2\hat{\Delta}^2 \langle \bar{\rho} \rangle |\tilde{\tilde{S}}| (\tilde{\tilde{S}}_{ij} - \frac{\delta_{ij}}{3} \tilde{\tilde{S}}_{kk}); \alpha_{ij} = -2\Delta^2 \bar{\rho} |\tilde{\tilde{S}}| (\tilde{\tilde{S}}_{ij} - \frac{\delta_{ij}}{3} \tilde{\tilde{S}}_{kk}) \quad (2.43)$$

$$\beta = 2 \langle \bar{\rho} \rangle \hat{\Delta}^2 |\tilde{\tilde{S}}|^2; \alpha = 2 \bar{\rho} \Delta^2 |\tilde{\tilde{S}}|^2 \quad (2.44)$$

The same idea for modeling the SGS turbulent stress can be employed to dynamically calculate the turbulent Prandtl number and Schmidt number in Eq. 2.37 and Eq. 2.38.

We implemented the algebraic Smagorinsky model in the current study although it may not be the best SGS model. There are two reasons: first, the best SGS model for real-fluid flows is still unknown; and second, the grid requirement for other models such as the dynamical model is normally stricter than the algebraic Smagorinsky model due to its double filters, both of which are required to be located in the inertial range.

## 2.3 Equation of State

In order to evaluate thermophysical properties for real-fluid mixture, an equation of state capable of handling real fluid behavior at high-pressure and low-temperature regime is required. The most common equation of state utilized for calculating high-pressure fluid properties is the cubic equations of state, which includes Redlich-Kwong, Peng-Robinson, and the modified Soave-Redlich-Kwong (SRK) equations of state. The modified SRK equation of state, which is capable of handling the quantum gas behavior of hydrogen, is adopted here for the calculation of thermodynamic properties and derivation of numerical relationships. The consistent treatment of thermodynamic properties using one equation of state produces an efficient numerical algorithm. A more complicated Benedict-Webb-Rubin (BWR) equation of state, combined with the extended corresponding states theory, is utilized for estimating transport properties, as suggested by Ely and Hanly (1981, 1983). Both the modified SRK and the BWR equations of state are capable of representing liquid phase behavior. The BWR equation of state can be applied over broader temperature and pressure ranges, but the SRK equation of state is easier to apply, especially for deriving the thermodynamic differential relationships.

### 2.3.1 Modified Soave-Redlich-Kwong (SRK) Equation of State

The modified SRK equation of state is considered to be both simple and fairly accurate, which takes the following form (Graboski and Daubert, 1978a, 1978b)

$$p = \frac{\rho R_u T}{(W - b\rho)} - \frac{a\alpha}{W} \frac{\rho^2}{(W + b\rho)} \quad (2.45)$$

where  $R_u$  is the universal gas constant. The parameters 'a' and 'b' account for the effects of the attractive and repulsive forces between molecules, respectively. ' $\alpha$ ' is the third parameter, which

is a function of temperature and acentric factor. For mixtures, they are calculated from the following mixing rules

$$\alpha a = \sum_{i=1}^N \sum_{j=1}^N x_i x_j \alpha_{ij} a_{ij} \quad (2.46)$$

$$b = \sum_{i=1}^N x_i b_i \quad (2.47)$$

The cross parameter  $\alpha_{ij} a_{ij}$  in Eq.2.46 is given by

$$\alpha_{ij} a_{ij} = \sum_{i=1}^N \sum_{j=1}^N \sqrt{\alpha_i \alpha_j a_i a_j} (1 - \kappa_{ij}) \quad (2.48)$$

where  $x_i$  is the mole fraction of species  $i$ .  $\kappa_{ij}$  is the binary interaction coefficient, which can be calculated from a known data set (Graboski and Daubert, 1978a, 1978b). The constants  $a_i, b_i$  can be determined from the following universal relationships

$$a_i = 0.42747 \frac{R_u^2 T_{ci}^2}{p_{ci}} \quad (2.49)$$

$$b_i = 0.08664 \frac{R_u T_{ci}}{p_{ci}} \quad (2.50)$$

The third parameter for species  $i$  is given as

$$\alpha_i = [1 + S_i (1 - \sqrt{T_n})]^2 \quad (2.51)$$

where  $T_{ci}$ ,  $p_{ci}$ , are the critical temperature and pressure for species  $i$ .  $T_n$  is the reduced temperature for species  $i$ , and  $S_i$  is another variable. These parameters are given by the following formulas

$$T_n = \frac{T}{T_{ci}} \quad (2.52)$$

$$S_i = 0.48508 + 1.5517\omega_i - 0.15613\omega_i^2 \quad (2.53)$$

Equations 2.51 and 2.53 are not capable of accurately correlating hydrogen systems due to its quantum gas behavior. A modified expression of  $\alpha$  for hydrogen is further established (Graboski and Daubert, 1978a, 1978b)

$$\alpha_{H_2} = 1.202 \exp(-0.30228T_c) \quad (2.54)$$

This correlation is expected to be accurate for hydrogen at reduced temperatures greater than about 2.5 (the critical temperature of hydrogen is 33.2K). No mixture of technical interests lies below this temperature. When Eq. 2.54 is used, the binary interaction coefficients  $\kappa_{ij}$  involving hydrogen species should be set to 0.

### 2.3.2 Benedict-Webb-Rubin (BWR) Equation of State

The BWR equation of state of methane is presented here, which is proposed by Jacobsen and Stewart (1973) based on very broad ranges of experimental data to ensure the proper extrapolation to low-temperature and high-pressure regions. Its expression is

$$p = \sum_{n=1}^9 A_n(T) \rho^n + \sum_{n=10}^{15} A_n(T) \rho^{2n-17} e^{-\gamma\rho^2} \quad (2.55)$$

where the 15 coefficients  $A_n$  are given in Table 2.1, which are functions of temperature. The 32 semi-empirical Constants of Ns are list in Table 2.2. The units for pressure, density, and temperature are given in bar, mol/liter, and K. The stain-rate  $\gamma$  is  $0.0096 \text{ (mol/liter)}^2$ .

Table 2.1: Coefficients of  $A_n$ 

$A_1 = R_U T$	$A_9 = N_{19}/T^2$
$A_2 = N_1 T + N_2 T^{1/2} + N_3 + N_4/T + N_5/T^2$	$A_{10} = N_{20}/T^2 + N_{21}/T^3$
$A_3 = N_6 T + N_7 + N_8/T + N_9/T^2$	$A_{11} = N_{22}/T^2 + N_{23}/T^4$
$A_4 = N_{10} T + N_{11} + N_{12}/T$	$A_{12} = N_{24}/T^2 + N_{25}/T^3$
$A_5 = N_{13}$	$A_{13} = N_{26}/T^2 + N_{27}/T^4$
$A_6 = N_{14}/T + N_{15}/T^2$	$A_{14} = N_{28}/T^2 + N_{29}/T^3$
$A_7 = N_{16}/T$	$A_{15} = N_{30}/T^2 + N_{31}/T^3 + N_{32}/T^4$
$A_8 = N_{17}/T + N_{18}/T^2$	

Table 2.2: Semi-empirical Constants Based on Methane

$N_1 = -1.184347314485E-2$	$N_{17} = 1.071143181503E-5$
$N_2 = 7.540377272657E-1$	$N_{18} = -9.290851745353E-3$
$N_3 = -1.225769717554E+1$	$N_{19} = 1.610140169312E-4$
$N_4 = 6.260681393432E+2$	$N_{20} = 3.469830970789E+4$
$N_5 = -3.490654409121E+4$	$N_{21} = -1.370878559048E+6$
$N_6 = 5.301046385532E-4$	$N_{22} = 1.790105676252E+2$
$N_7 = -2.875764479978E-1$	$N_{23} = 1.615880743238E+6$
$N_8 = 5.011947936427E+1$	$N_{24} = 6.265306650288E-1$
$N_9 = -2.821562800903E+4$	$N_{25} = 1.820173769533E+1$
$N_{10} = -2.064957753744E+5$	$N_{26} = 1.449888505811E-3$
$N_{11} = 1.285951844828E-2$	$N_{27} = -3.159999123798E+1$
$N_{12} = -1.106266656726E+0$	$N_{28} = -5.290335668451E-6$
$N_{13} = 3.060813353408E-4$	$N_{29} = 1.694350244152E-3$
$N_{14} = -3.174982181302E-3$	$N_{30} = 8.612049038886E-9$
$N_{15} = 5.191608004779E+0$	$N_{31} = -2.598235689063E-6$
$N_{16} = -3.074944210271E-4$	$N_{32} = 3.153374374912E-5$

## 2.4 Thermodynamic Properties

In order to solve the conservation equations, additional relationships relating thermodynamic properties to temperature and, in high-pressure cases, pressure, are required. The thermodynamic properties to be evaluated are density, internal energy, enthalpy, entropy, partial molar enthalpy, and chemical potential of each species. These properties can be derived directly from fundamental thermodynamic relationships

$$e(T, \rho) = e_0(T) + \int_{\rho_0}^{\rho} \left[ \frac{p}{\rho^2} - \frac{T}{\rho^2} \left( \frac{\partial p}{\partial T} \right)_\rho \right] d\rho \quad (2.56)$$

$$h(T, p) = h_0(T) + \int_{p_0}^p \left[ \frac{1}{\rho} + \frac{T}{\rho^2} \left( \frac{\partial \rho}{\partial T} \right)_P \right] dp \quad (2.57)$$

$$s(T, \rho) = s_0(T, \rho_0) - \int_{\rho_0}^{\rho} \left[ \frac{1}{\rho^2} \left( \frac{\partial p}{\partial T} \right)_\rho \right] d\rho \quad (2.58)$$

$$C_P(T, \rho) = C_{V0}(T) - \int_{\rho_0}^{\rho} \left[ \frac{T}{\rho^2} \left( \frac{\partial^2 p}{\partial T^2} \right)_\rho \right] d\rho + \frac{T}{\rho^2} \left( \frac{\partial p}{\partial T} \right)_\rho^2 / \left( \frac{\partial p}{\partial \rho} \right)_T \quad (2.59)$$

where the  $e, h, s, C_P, C_V$  are internal energy, enthalpy, entropy, constant-pressure heat capacity, and constant-volume heat capacity, respectively. The subscript 0 refers to an ideal state at a low pressure and integral terms are the departure functions. All the partial derivatives in these relations are calculated based on the modified Soave-Redlich-Kwong equation of state, and they are

$$\left( \frac{\partial p}{\partial T} \right)_{\rho_j} = \frac{\rho R_u}{(M_w - b\rho)} - \frac{1}{M_w} \left[ \frac{\partial}{\partial T} (a\alpha) \right]_{\rho, Y_i} \frac{\rho^2}{(M_w + b\rho)} \quad (2.60)$$

$$\left( \frac{\partial p}{\partial \rho} \right)_{T, Y_i} = \frac{M_w R_u T}{(M_w - b\rho)^2} - \frac{a\alpha}{M_w} \frac{\rho(2M_w + b\rho)}{(M_w + b\rho)^2} \quad (2.61)$$

$$\left( \frac{\partial p}{\partial \rho_i} \right)_{T, \rho_j \neq i} = \frac{M_w R_u T}{M_{w_i} (M_w - b\rho)^2} [M_w + \rho(b_i - b)] - \frac{2\rho \sum_j x_j a_{ij} \alpha_{ij}}{M_{w_i} (M_w + b\rho)} + \frac{a \alpha \rho^2 b_i}{M_{w_i} (M_w + b\rho)^2} \quad (2.62)$$

where the derivative  $\frac{\partial}{\partial T} (a\alpha)$  is given in Appendix C.

#### 2.4.1 Partial Molar and Partial Density Properties

At standard pressure, gas mixtures behave ideally, where the mixture properties are simply the molar-weighted sum of the properties of each component. High-pressure fluid mixtures, however, do not obey Raoult's law (Moran and Shapiro, 1999). Their properties, such as total volume, internal energy, enthalpy, and Gibbs free energy, depend on both the temperature, pressure, and composition. If any of the above properties are denoted by  $F(x_1, x_2, \dots, p, T)$ , then the partial molar property  $\bar{F}_i$  is defined as

$$\bar{F}_i = (\partial F / \partial x_i)_{p, T, x_{j \neq i}} \quad (2.63)$$

For a binary mixture, the partial molar properties in terms of the mole fraction of the first component ( $x_1$ ) is

$$\begin{aligned} \bar{F}_1 &= (\partial F / \partial x_1)_{p, T} \\ \bar{F}_2 &= F - x_1 (\partial F / \partial x_1)_{p, T} \end{aligned} \quad (2.64)$$

Figure 2.2 shows a plot of the volume of one molar mixture as a function of  $x_1$ . The partial molar volume,  $\bar{V}_1$  and  $\bar{V}_2$ , at a given mole fraction  $x_1^*$  are obtained by drawing a tangent to the volume curve at  $x_1^*$  and reading off the intercepts of the tangent with the vertical axis at

$x_1 = 0.1$ . The plot also shows the excess volume  $V^E$ , defined as the difference between the actual volume and the molar fraction-averaged volume of the two pure components at the same pressure and temperature.

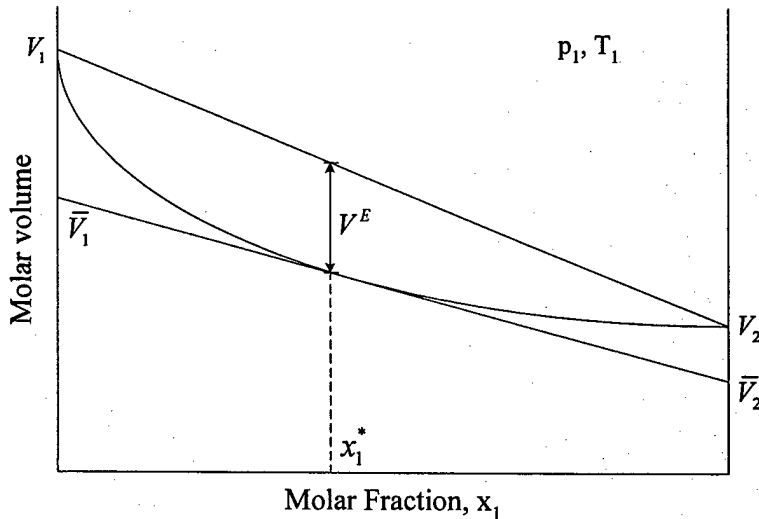


Fig. 2.2: Molar volume of a mixture as function of composition at fixed pressure and temperature.

As being demonstrated in the early works regarding high-pressure droplet vaporization and combustion (Manrique and Borman, 1969; Hsieh et al., 1991), in order to find faithful results, the properties of each component in a non-ideal mixture have to be calculated based on the partial molar properties. In a general CFD code, all flow properties are derived in a mass or density based manner, which rends the evaluation of partial molar properties inconvenient. Thus, the concepts of partial mass and partial density properties were recently established by Lafon et al. (1995) and Meng (2000). According to fundamental thermodynamics, any thermodynamic property  $\phi$  in a mixture is a function of temperature, pressure, and masses of the constituent species

$$m\phi = m\phi(T, p, m_i) \quad (2.65)$$

Therefore, the partial mass property is defined as

$$\hat{\phi}_i = \left( \frac{\partial m\phi}{\partial m_i} \right)_{T,p,m_{j \neq i}} \quad (2.66)$$

where  $i, j = 1, \dots, N$ , and  $\phi$  refers to any proper thermodynamic property per unit mass of a mixture, such as enthalpy and internal energy.

In fluid mechanics, density is more convenient to use instead of mass. Therefore, it is better to define the mixture thermodynamic properties per unit volume

$$\rho\phi = \rho\phi(T, \rho_i) \quad (2.67)$$

This leads naturally to the definition of the partial density property  $\hat{\phi}_i$

$$\hat{\phi}_i = \left( \frac{\partial \rho\phi}{\partial \rho_i} \right)_{T,\rho_{j \neq i}} \quad (2.68)$$

According to this definition, the partial density internal energy, enthalpy, and entropy are expressed as

$$\hat{e}_i = \left( \frac{\partial \rho e}{\partial \rho_i} \right)_{T,\rho_{j \neq i}} \quad (2.69)$$

$$\hat{h}_i = \left( \frac{\partial \rho h}{\partial \rho_i} \right)_{T,\rho_{j \neq i}} \quad (2.70)$$

$$\hat{s}_i = \left( \frac{\partial \rho s}{\partial \rho_i} \right)_{T,\rho_{j \neq i}} \quad (2.71)$$

where calculations of  $\hat{e}_i$ ,  $\hat{h}_i$  and  $\hat{s}_i$  require the thermodynamic relations presented in Eq. 2.56 to 2.60, and the SRK equation of state. In addition, a relationship between the partial density property and the partial mass property is derived as

$$\hat{\phi}_i = \hat{\phi}_i + \rho \left( \frac{\partial \phi}{\partial p} \right)_{T,Y_j} \left( \frac{\partial p}{\partial \rho_i} \right)_{T,\rho_{j \neq i}} \quad (2.72)$$

Utilizing fundamental thermodynamic theories, including Euler equation and Gibbs-Duhem relation, the following relationship regarding chemical potential of each species, which is required for the treatment of thermodynamic phase equilibrium, can be derived

$$\mu_i = \hat{f}_i = \hat{e}_i - T\hat{s}_i \quad (2.73)$$

The details for calculating thermodynamic properties are presented in Appendix B. As a specific example, the partial density internal energy and enthalpy of species  $i$ ,  $\hat{e}_i$  and  $\hat{h}_i$ , are derived here. According to the definition presented in Eq. 2.69, we first need to derive an expression for the internal energy  $e$ . Using Eq. 2.56 and the derivative expressions presented in Appendix B, the following relation is found

$$e(T, \rho) = e_0(T) + \frac{T^2}{bM_w} \left( \frac{\partial a\alpha/T}{\partial T} \right)_{\rho, Y_i} \ln \left( 1 + \frac{b\rho}{M_w} \right) \quad (2.74)$$

where the expression of  $\frac{\partial a\alpha/T}{\partial T}$  is presented in Appendix C.

Based on the definition, the partial density internal energy  $\hat{e}_i$  can be expressed as

$$\begin{aligned} \hat{e}_i &= e_{i,0} + \frac{2}{bM_{wi}} \left[ \sum_j x_j \left( T \frac{\partial}{\partial T} (a_{ij}\alpha_{ij}) - a_{ij}\alpha_{ij} \right) \right] \ln \left( 1 + \frac{b\rho}{M_w} \right) \\ &\quad + \frac{b_i}{bM_{wi}} \left[ T \frac{\partial}{\partial T} (a\alpha) - a\alpha \right] \left[ \frac{\rho}{M_w + b\rho} - \frac{1}{b} \ln \left( 1 + \frac{b\rho}{M_w} \right) \right] \end{aligned} \quad (2.75)$$

Utilizing Eq. 2.75, the expression for the internal energy, Eq. 2.74, can be related to the partial density internal energy

$$e = \sum_i Y_i \hat{e}_i - \frac{1}{M_w} \left[ T \frac{\partial}{\partial T} (a\alpha) - a\alpha \right] \frac{\rho}{M_w + b\rho} \quad (2.76)$$

According to thermodynamics

$$\rho h = \rho e + p \quad (2.77)$$

Following the definition for the partial density property, the expression for partial density enthalpy can be found by taking derivative of the partial density of species  $i$  at both sides of the Eq. 2.77 and keeping temperature and all the other partial densities constant

$$\left( \frac{\partial ph}{\partial \rho_i} \right)_{T, \rho_j \neq i} = \left( \frac{\partial pe}{\partial \rho_i} \right)_{T, \rho_j \neq i} + \left( \frac{\partial p}{\partial \rho_i} \right)_{T, \rho_j \neq i} \quad (2.78)$$

It is recognized that Eq. 2.78 is equivalent to Eq. 2.79

$$\hat{h}_i = \hat{e}_i + \left( \frac{\partial p}{\partial \rho_i} \right)_{T, \rho_j \neq i} \quad (2.79)$$

Substituting Eq. 2.72 into Eq. 2.79, and taking use of the fundamental expressions of enthalpy, which are available in any thermodynamics textbook, the following relationship regarding the partial mass enthalpy,  $\hat{h}_i$ , can be derived

$$\hat{h}_i = \hat{e}_i + \frac{T}{\rho} \left( \frac{\partial p}{\partial T} \right)_{\rho_j} \left( \frac{\partial p}{\partial \rho_i} \right)_{T, \rho_j \neq i} \quad (2.80)$$

#### 2.4.2 Critical Point of Fluid Mixture

The thermodynamic critical point of a pure fluid is fixed and corresponds to the maximum temperature and pressure where the vapor-liquid equilibrium (VLE) with two distinct phases can coexist. However, when the system consists of more than one component, the critical temperature and pressure are functions of the composition (as shown in Fig. 2.3). Since a fluid mixture reaches a stability limit at the critical point, the Gibbs criteria should be satisfied to guarantee a concave distribution of the Helmholtz free energy as its composition varies. Due to

the different physical criteria for criticality in a pure fluid and a mixture, the properties that diverge strongly in pure fluids near the critical region only diverge weakly in mixtures.

In general, the Gibbs Criteria requires the two determinants defined below equal zero at the critical point of mixture

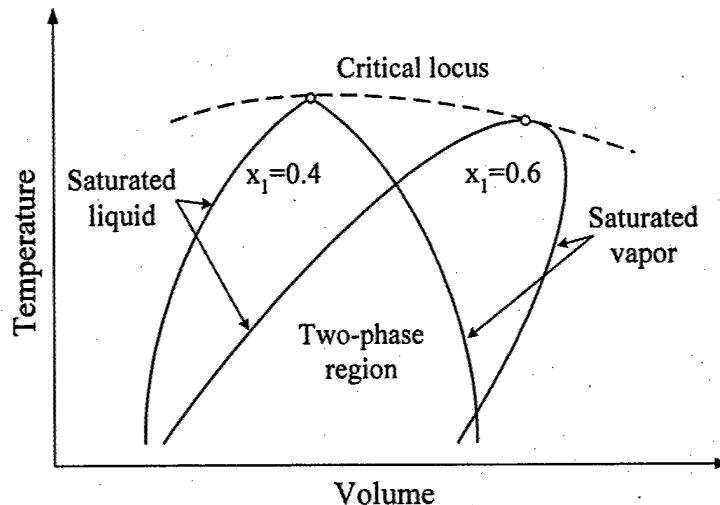


Fig. 2.3: T-V phase diagram of multi-component mixture with different compositions ( $x_1=0.4, 0.6$ ).

$$L = \begin{vmatrix} A_{11} & A_{12} & \cdots & A_{1n} \\ A_{21} & A_{22} & \cdots & A_{2n} \\ \vdots & \vdots & \ddots & \vdots \\ A_{n1} & A_{n2} & \cdots & A_{nn} \end{vmatrix} = 0 \quad (2.81)$$

and

$$M = \begin{vmatrix} A_{11} & A_{12} & \cdots & \cdots & A_{1n} \\ A_{21} & A_{22} & \cdots & \cdots & A_{2n} \\ \vdots & \vdots & \vdots & \vdots & \vdots \\ A_{n-1,1} & A_{n-1,2} & \cdots & \cdots & A_{n-1,n} \\ \frac{\partial L}{\partial N_1} & \frac{\partial L}{\partial N_2} & \cdots & \cdots & \frac{\partial L}{\partial N_n} \end{vmatrix} = 0 \quad (2.82)$$

where  $A$  is the Helmholtz free energy, and  $A_{ij} = \left(\frac{\partial^2 A}{\partial N_i \partial N_j}\right)_{T,V}$ .

With a proper equation of state, the above equations can be solved simultaneously to find the critical temperature and volume. The critical pressure of mixture is then determined based on the pre-specified  $P - V - T$  relationship.

## 2.5 Transport Properties

Transport properties to be evaluated include viscosity, thermal conductivity and binary mass diffusivity. Accurate estimations of these properties are very important for high-pressure fluid mixing and combustion computation, since they determine not only the flow dynamics, but also the heat and mass transfer rates. As proved in the literature, pressure effects have to be taken into account to accurately estimate these properties.

### 2.5.1 Corresponding States Theories

The law of corresponding state, which was originally proposed by van der Waals in 1873, expresses that the equilibrium properties of different fluids can be related to their critical properties in a universal way. For example, if pressure, temperature, and volume are related to their critical properties, the PVT function relating the reduced pressure, temperature, and volume becomes identical for all substances. The reduced property is defined as

$$p_r = p / p_c, T_r = T / T_c, V_r = V / V_c \quad (2.83)$$

The corresponding states theory also holds for other properties, including viscosity, and thermal conductivity. Based on the corresponding states argument, a property of any fluid can be

estimated by relating to its counterpart of a reference substance, whose property can be easily determined (Ely and Hanly, 1981).

$$\eta_x(T, \rho) = \eta_0(T_0, \rho_0) F_\eta \quad (2.84)$$

where the subscript x refers to the fluid of interest, 0 to the reference fluid

$$F_\eta = \left( \frac{Mw_x}{Mw_0} \right)^{1/2} f_{x,0}^{1/2} h_{x,0}^{-2/3} \quad (2.85)$$

Here,  $Mw$  is the molecular weight.  $T_0$  and  $\rho_0$  of the reference fluid are calculated by

$$\begin{aligned} T_0 &= T / f_{x,0} \\ \rho_0 &= \rho h_{x,0} \end{aligned} \quad (2.86)$$

In general corresponding states theory, the parameters  $f_{x,0}$  and  $h_{x,0}$  is the ratio of the critical temperature and volume. However, the range of its applicability can be broadened considerably by introducing the extended corresponding states (EXCST) model, where the equivalent parameters of  $f_{x,0}$  and  $h_{x,0}$  become

$$f_{x,0} = (T_{c,x} / T_{c,0}) \theta(T_{r,x}, V_{r,x}, \omega_x) \quad (2.87)$$

$$h_{x,0} = (V_{c,x} / V_{c,0}) \phi(T_{r,x}, V_{r,x}, \omega_x) \quad (2.88)$$

In Eq. 2.87 and Eq. 2.88,  $\theta$  and  $\phi$  are the so-called shape factors, which are functions of Pitzer's acentric factor  $\omega_x$  and the reduced temperature and volume. These functions can be calculated by the following correlations

$$\theta(T_{r,x}, V_{r,x}, \omega_x) = 1 + (\omega_x - \omega_0) F(T_{r,x}, V_{r,x}) \quad (2.89)$$

$$\phi(T_{r,x}, V_{r,x}, \omega_x) = [1 + (\omega_x - \omega_0) G(T_{r,x}, V_{r,x})] Z_{c,0} / Z_{c,x} \quad (2.90)$$

where Z is the compressibility factor.

$$F(T_{r,x}, V_{r,x}) = a_1 + b_1 \ln T_x^+ + (c_1 + d_1 / T_x^+) (V_x^+ - 0.5) \quad (2.91)$$

$$G(T_{r,x}, V_{r,x}) = a_2 (V_x^+ + b_2) + c_2 (V_x^+ + d_2) \ln T_x^+ \quad (2.92)$$

and where

$$T_x^+ = \min[2, \max(T_{r,x}, 0.5)] \quad (2.93)$$

$$V_x^+ = \min[2, \max(V_{r,x}, 0.5)] \quad (2.94)$$

The coefficients in Eq. 2.91 and Eq. 2.92 are listed in Table 2.3

Table 2.3: Coefficients for Shape Factor Correlations

Coefficients in Eq. 2.91	Coefficients in Eq. 2.92
$a_1=0.090569$	$a_1=0.394901$
$b_1=-0.862762$	$b_1=-1.023545$
$c_1=0.316636$	$c_1=-0.932813$
$d_1=-0.465684$	$d_1=-0.754639$

The extended corresponding states theory will be utilized with appropriate mixing rules to estimate the transport properties of mixtures.

### 2.5.2 Mixing Rules for Mixtures

In order to apply the corresponding states theory to a mixture, the variables of that mixture have to be calculated from the corresponding parameters of its components using appropriate mixing rules.

Typically, the mixing rule expresses a mixture parameter  $Q_m$  in terms of composition and pure component parameters according to

$$Q_m = \sum_i \sum_j x_i x_j Q_{ij} \quad (2.95)$$

where  $x_i$  and  $x_j$  are the molar fractions of compounds  $i$  and  $j$ , respectively. The interaction term  $Q_{ij}$  is calculated from composition properties  $Q_i$  and  $Q_j$  based on a combining rule. The simplest combining rule is either arithmetic average or geometric mean, in which the double summation in Eq. 2.95 is reduced

$$Q_{ij} = \frac{Q_i + Q_j}{2} \quad \text{and} \quad Q_m = \sum_i x_i Q_i \quad (2.96)$$

$$Q_{ij} = (Q_i Q_j)^{1/2} \quad \text{and} \quad Q_m = (\sum_i x_i Q_i^{1/2})^2 \quad (2.97)$$

To improve performance, it is customary to include a binary interaction parameters  $k_{ij}$  into the expressions for  $Q_{ij}$ . One possibility could be

$$Q_{ij} = \frac{k_{ij}(Q_i + Q_j)}{2} \quad (2.98)$$

The value of  $k_{ii}$  is unity, and values of  $k_{ij}$  for all possible binary pairs should be determined by regressing experimental data. The partial molar properties are very sensitive to the values of  $k_{ij}$ .

The theory of mixing rules is discussed elsewhere (Reid et al., 1986) and will not be treated deeply here. The following mixing rules are defined for calculating transport properties (Ely and Hanly, 1981)

$$h_{x,0} = \sum_i \sum_j x_i x_j h_{ij,0} \quad (2.99)$$

$$f_{x,0} = h_{x,0}^{-1} \sum_i \sum_j x_i x_j f_{ij,0} h_{ij,0} \quad (2.100)$$

The molecular weight of the mixture can be found by

$$Mw_x^{1/2} = h_{x,0}^{-4/3} f_{x,0}^{-1/2} \sum_i \sum_j x_i x_j h_{ij,0}^{4/3} f_{ij,0}^{1/2} Mw_{ij,0}^{1/2} \quad (2.101)$$

where the indexes, i and j, represent the species components in the mixture. The following combining rules are chosen

$$f_{ij,0} = (f_{i,0} f_{j,0})^{1/2} (1 - \kappa_{ij}) \quad (2.102)$$

$$h_{ij,0} = \frac{1}{8} (h_{i,0}^{1/3} + h_{j,0}^{1/3})^3 (1 - l_{ij}) \quad (2.103)$$

$$Mw_{ij} = 2Mw_i Mw_j / (Mw_i + Mw_j) \quad (2.104)$$

where the variables,  $\kappa_{ij}$ , and  $l_{ij}$ , are the binary interaction parameters with values close to zero, which are set to zero for estimating transport properties.

### 2.5.3 Viscosity of Mixtures

The extended corresponding states one fluid model (Ely and Hanly, 1981) is applied here for estimating the viscosity of a mixture. The basic idea is straightforward. First, it is assumed that the viscosity of a single-phase mixture is equated to that of a hypothetical pure fluid

$$\mu_{mix}(T, \rho) = \mu_x(T, \rho) \quad (2.105)$$

where the subscripts, mix and x, refer to the mixture and the hypothetical pure fluid, respectively.

The corresponding states theory for transport properties is then used to evaluate the viscosity of the hypothetical pure fluid with respect to a given reference fluid

$$\mu_x(T, \rho) = \mu_0(T_0, \rho_0) F_\mu \quad (2.106)$$

where the subscript, 0, refers to the reference fluid

$$F_\mu = \left( \frac{Mw_x}{Mw_0} \right)^{1/2} f_{x,0}^{1/2} h_{x,0}^{-2/3} \quad (2.107)$$

The variables,  $f_{x,0}$ ,  $h_{x,0}$ , and  $Mw_x$  are then evaluated by the extended corresponding states (EXCST) theory and the mixing rules.

Methane is chosen as the reference fluid, because of the existence of its PVT and viscosity data over the entire range of fluid states. The date fitted methane viscosity correlation is

$$\mu_0(\rho_0, T_0) = \mu_0^{(1)}(T_0) + \mu_0^{(2)}(T_0)\rho_0 + \Delta\mu_0(\rho_0, T_0)X_\mu \quad (2.108)$$

where the first two terms represent the dilute gas and first density correction, respectively, while the last term is a remainder which dominates in high-density region. The factor,  $X_\mu$ , is a correction of the possible non-correspondence of viscosity. The details about this correlation can be found in the paper of Ely and Hanly (1981).

#### 2.5.4 Thermal Conductivity of Mixtures

Estimating the thermal conductivity of a mixture is more complicated, since it is affected by two factors, one arising from the transfer of energy from pure collision or translation effect,  $\lambda'$ , and another from the transfer of energy via the internal degree of freedom,  $\lambda''$  (Ely and Hanly, 1983). The latter term is, in general, independent of density. Therefore, only the collision or translation part is evaluated using the extended corresponding states one fluid model, which takes the same procedure as that for estimating the viscosity of a mixture. First, the thermal conductivity of a mixture is equated to that of a hypothetical pure fluid as

$$\lambda'_{mix}(\rho, T) = \lambda'_x(\rho, T) \quad (2.109)$$

The corresponding states theory is then applied to calculate the thermal conductivity of the hypothetical pure fluid via

$$\lambda'_x(T, \rho) = \lambda'_0(T_0, \rho_0)F_\lambda X_\lambda \quad (2.110)$$

where  $F_\lambda$  takes the same form as in Eq. 2.107, whose calculation requires the extended corresponding states theory and the mixing rules, and  $X_\lambda$  is the correction term for non-correspondence.

Finally, the thermal conductivity of a mixture can be expressed as

$$\lambda_{mix}(\rho, T) = \lambda'_0(\rho_0, T_0)F_\lambda X_\lambda + \lambda''_{mix}(T) \quad (2.111)$$

In Eq. 2.111 the thermal conductivity of the reference fluid, methane, is evaluated via an empirical correlation. The second term in Eq. 2.111, which is related to internal degree of freedom, can be calculated via the modified Eucken correlation with mixing rules (Ely and Hanly, 1983), which are

$$\frac{\lambda''_i M w_i}{\mu_i^g} = 1.32(C_{p,i}^g - \frac{5R_u}{2}) \quad (2.112)$$

and

$$\lambda''_{mix}(T) = \sum_i \sum_j x_i x_j \lambda''_{ij} \quad (2.113)$$

$$(\lambda''_{ij})^{-1} = 2[(\lambda''_i)^{-1} + (\lambda''_j)^{-1}] \quad (2.114)$$

where the indexes, i and j, refer to the components in the mixture,  $\mu_i^g$  is the dilute gas viscosity of component i,  $C_{p,i}^g$  is the ideal gas heat capacity of component i, and  $R_u$  is the universal gas constant.

### 2.5.5 Binary Mass Diffusivity

Evaluation Binary mass diffusivity presents more challenge than viscosity and thermal conductivity because of the following two reasons. 1. There are only limited experimental data

existent for binary mass diffusivity at high pressures, which results in few estimation methods. 2. There is no satisfactory liquid state theory available for calculating binary mass diffusivity in the liquid phase.

In this work, the binary mass diffusivity in gaseous phase at low pressure is evaluated using empirical correlation of Fuller et al., which is recommended by Reid et al. (1986). It takes the following form

$$D_{ij} = \frac{0.00143T^{1.75}}{pMw_{ij}^{1/2}[(\Sigma_v)_i^{1/3} + (\Sigma_v)_j^{1/3}]^2} \quad (2.115)$$

where  $D_{ij}$  is binary mass diffusivity,  $\text{cm}^2/\text{s}$

T is temperature, K

p is pressure, bar

$Mw_{ij}$  is the combined molecular weight, as expressed in Eq. 2.104

and  $\Sigma_v$  is found for each component by summing atomic diffusion volumes, which is tabulated in Reid et al. (1986, Table 11-1).

High-pressure effect on binary mass diffusivity is evaluated by the method proposed by Takahashi (1974), which is based on a simple corresponding state method

$$\frac{D_{ij}p}{(D_{ij}p)^+} = f(T_r, p_r) \quad (2.116)$$

where the superscript + indicates the low-pressure values given by Eq. 2.115. The function  $f(T_r, P_r)$  represents a scaling factor of pressure based on the reduced temperature and pressure, which is tabulated by Takahashi and also shown in Reid et al. (1986, Fig. 11-3). In order to calculate the reduced parameters, the following combining rules for pseudocritical properties of a mixture are used

$$T_c = x_i T_{c,i} + x_j T_{c,j} \quad (2.117)$$

$$p_c = x_i p_{c,i} + x_j p_{c,j} \quad (2.118)$$

The binary mass diffusivities in liquids are evaluated by the method of Tyn and Calus, as recommended by Reid et al. (1987). For a binary mixture of solute i in solvent j, it is

$$D_{ij} = 8.93 \times 10^{-8} \left( \frac{V_i}{V_j^2} \right)^{1/6} \left( \frac{P_j}{P_i} \right)^{0.6} \frac{T}{\mu_j} \quad (2.119)$$

where V is the molar volume at the normal boiling temperature, cm<sup>3</sup>/mol

T is temperature, K

$\mu_j$  is the viscosity of solvent, cP

$P_i$  and  $P_j$  are parachors for the solute and solvent, and the calculation methods are given in Reid et al. (1986).

There is no correlation currently available for estimating the pressure effect on binary mass diffusivity in liquid phase.

## **Chapter 3**

### **Numerical Methodology**

Analysis of the fluid dynamic and physico-chemical processes described in Chapter 1 poses a variety of numerical challenges. This chapter outlines the inherent difficulties and the numerical framework selected to handle these problems. The basic algorithm treats three-dimensional flowfield in a time-accurate manner using a unified treatment of general fluid thermodynamics with preconditioned, density-based, finite-volume approach and dual-time stepping integration. A multiblock domain decomposition technique, along with static load balance, is used to facilitate the application of efficient parallel computation with message passing interfaces (MPI) at the domain boundaries.

#### **3.1 Basic Approach**

Present analysis of high-pressure real-fluid mixing and combustion dynamics bears two severe numerical challenges. First, thermodynamic non-idealities and transport anomalies take place as the fluid transits through the transcritical regime. Thus, treating these phenomena in a manner consistent with the intrinsic characteristics of a numerical algorithm presents a major obstacle. Second, the rapid variation of fluid state and wide disparities in the characteristic time and length scales pose the well-known stiffness problem. The stiffness system is resultant from three reasons: 1) ill-conditioned eigenvalues; 2) competing convective and diffusion processes; and 3) pressure singularities in the momentum equation.

The application of time derivative preconditioning techniques (Turkel, 1992; Shuen et al., 1993; Choi and Merkel, 1993; Hsieh and Yang, 1997) coupled with recently developed

methodologies for handling general fluid thermodynamics (Meng and Yang, 2003) has largely negated the difficulties outlined above. The current work employs these methodologies, takes full account of thermodynamic nonidealities and transport anomalies in the whole fluid state of concern and accommodates any arbitrary equation of state. The unified treatment of general fluid thermodynamics based on the partial mass and partial density properties is employed coupling the preconditioning techniques developed by Hsieh and Yang (1997). Temporal discretization is obtained using a second-order accurate dual-time stepping integration. Spatial discretization employs the fourth-order accurate flux differencing methodologies developed by Rai and Chakravarthy (1994). A fourth-order scalar dissipation with a total-variation-diminish (TVD) switch developed by Swanson and Turkel (1992) and Jorgenson and Turkel (1993) is implemented to ensure computational stability and to prevent numerical oscillations in the regions with steep gradients. A multiblock domain decomposition technique, along with static load balance, is used to facilitate the application of efficient parallel computation with message passing interfaces at the domain boundaries.

### 3.2 Three-Dimensional Cartesian System

The three-dimensional, unsteady, density-weighted, filtered forms of the compressible Navier-Stokes equations (without body forces) and species conservation equation can be expressed as

$$\frac{\partial \mathbf{Q}}{\partial t} + \frac{\partial(\mathbf{E} - \mathbf{E}_v)}{\partial x} + \frac{\partial(\mathbf{F} - \mathbf{F}_v)}{\partial y} + \frac{\partial(\mathbf{G} - \mathbf{G}_v)}{\partial z} = \mathbf{H} \quad (3.1)$$

where the vectors  $\mathbf{Q}, \mathbf{E}, \mathbf{F}, \mathbf{G}, \mathbf{E}_v, \mathbf{F}_v, \mathbf{G}_v$ , and  $\mathbf{H}$  are defined as

$$\mathbf{Q} = (\bar{\rho}, \bar{\rho}\tilde{u}, \bar{\rho}\tilde{v}, \bar{\rho}\tilde{w}, \bar{\rho}\tilde{E}, \bar{\rho}\tilde{Y}_1, \dots, \bar{\rho}\tilde{Y}_{N-1})^T \quad (3.2)$$

$$\mathbf{E} = (\bar{\rho}\tilde{u}, \bar{\rho}\tilde{u}^2 + \bar{p}, \bar{\rho}\tilde{u}\tilde{v}, \bar{\rho}\tilde{u}\tilde{w}, (\bar{\rho}\tilde{E} + \bar{p})\tilde{u}, \bar{\rho}\tilde{u}\tilde{Y}_1, \dots, \bar{\rho}\tilde{u}\tilde{Y}_{N-1})^T \quad (3.3)$$

$$\mathbf{F} = (\bar{\rho}\tilde{v}, \bar{\rho}\tilde{u}\tilde{v}, \bar{\rho}\tilde{v}^2 + \bar{p}, \bar{\rho}\tilde{v}\tilde{w}, (\bar{\rho}\tilde{E} + \bar{p})\tilde{v}, \bar{\rho}\tilde{v}\tilde{Y}_1, \dots, \bar{\rho}\tilde{v}\tilde{Y}_{N-1})^T \quad (3.4)$$

$$\mathbf{G} = (\bar{\rho}\tilde{w}, \bar{\rho}\tilde{u}\tilde{w}, \bar{\rho}\tilde{v}\tilde{w}, \bar{\rho}\tilde{w}^2 + \bar{p}, (\bar{\rho}\tilde{E} + \bar{p})\tilde{w}, \bar{\rho}\tilde{w}\tilde{Y}_1, \dots, \bar{\rho}\tilde{w}\tilde{Y}_{N-1})^T \quad (3.5)$$

$$\mathbf{E}_v = (0, \bar{\tau}_{xx} - \tau_{xx}^{sgs}, \bar{\tau}_{xy} - \tau_{xy}^{sgs}, \bar{\tau}_{xz} - \tau_{xz}^{sgs}, \tilde{u}\bar{\tau}_{xx} + \tilde{v}\bar{\tau}_{xy} + \tilde{w}\bar{\tau}_{xz} + \bar{q}_x - H_x^{sgs} + \sigma_x^{sgs}, 0, \dots, 0)^T \quad (3.6)$$

$$\mathbf{F}_v = (0, \bar{\tau}_{xy} - \tau_{xy}^{sgs}, \bar{\tau}_{yy} - \tau_{yy}^{sgs}, \bar{\tau}_{yz} - \tau_{yz}^{sgs}, \tilde{u}\bar{\tau}_{xy} + \tilde{v}\bar{\tau}_{yy} + \tilde{w}\bar{\tau}_{yz} + \bar{q}_y - H_y^{sgs} + \sigma_y^{sgs}, 0, \dots, 0)^T \quad (3.7)$$

$$\mathbf{G}_v = (0, \bar{\tau}_{xz} - \tau_{xz}^{sgs}, \bar{\tau}_{yz} - \tau_{yz}^{sgs}, \bar{\tau}_{zz} - \tau_{zz}^{sgs}, \tilde{u}\bar{\tau}_{xz} + \tilde{v}\bar{\tau}_{yz} + \tilde{w}\bar{\tau}_{zz} + \bar{q}_z - H_z^{sgs} + \sigma_z^{sgs}, 0, \dots, 0)^T \quad (3.8)$$

$$\mathbf{H} = (0, 0, 0, 0, 0, \dot{\omega}_1, \dots, \dot{\omega}_{N-1})^T \quad (3.9)$$

Each nomenclature is defined beforehand and the superscript  $T$  stands for the transpose of the vector.

### 3.3 A Unified Preconditioning Scheme for General Fluid Mixtures

It is well known that time-marching algorithms are efficient for solving the transonic, supersonic, and hypersonic compressible flow problems. However, they encounter convergence difficulties for the low-Mach number flows due to the pressure singularities in the momentum equation and the system stiffness arising from the ill-conditioned eigenvalues.

The first problem can be circumvented easily by introducing pressure decomposition (Choi and Merkel, 1993; Shuen et al., 1993)

$$\bar{p} = \bar{p}_0 + \bar{p}_g \quad (3.10)$$

where  $\bar{p}_0$  is a constant, which is generally chosen as the major part of the pressure. The gauge pressure  $\bar{p}_g$  is the dynamic part, responsible for the velocity-pressure coupling in the momentum equation, and it is the driving force for flow motions. After pressure decomposition, the total pressure inside the momentum is replaced by the gauge pressure.

To solve the system eigenvalue disparities and implement the dual-time stepping procedure, pseudo-time derivatives are added to Eq. 3.1 yielding an equation of the form as

$$\Gamma \frac{\partial Z}{\partial \tau} + \frac{\partial Q}{\partial t} + \frac{\partial(E - E_v)}{\partial x} + \frac{\partial(F - F_v)}{\partial y} + \frac{\partial(G - G_v)}{\partial z} = H \quad (3.11)$$

Here  $\Gamma$  represents the preconditioning matrix and  $\tau$  the pseudo-time variable. By judicious selection of the primitive variable  $Z$  and the preconditioning methodology, convergence in pseudo-time can be optimized for a wide variety of conditions to any desired level of temporal accuracy.

Selection of the primitive variables and the preconditioning matrix is dependent upon two criteria: 1) the eigenvalues must be well conditioned, real, and maintaining their directional characteristics; and 2) diffusion processes must not be reversed. Based on these criteria, the primitive variable vector is defined as

$$Z = (\bar{p}_g, \tilde{u}, \tilde{v}, \tilde{w}, \tilde{T}, \tilde{Y}_1, \dots, \tilde{Y}_{N-1}) \quad (3.12)$$

The choice of pressure  $\bar{p}$  as one of the primitive variables is crucial for two reasons. It singles out the propagation of acoustic waves in the pseudo-time and facilitates the elimination of the pressure singularity problem. The velocity components  $\tilde{u}$ ,  $\tilde{v}$ , and  $\tilde{w}$  are also logical choices since these quantities appear in the diffusion operators. Similarly, the temperature  $\tilde{T}$  and species  $\tilde{Y}_1, \dots, \tilde{Y}_{N-1}$  have been selected because they also appear in the diffusion operators. The choice

of temperature is primarily a matter of convenience. Using this term greatly simplifies the computation of Jacobian matrices and eliminates the need to iteratively solve for temperature as a function of enthalpy.

The preconditioning Jacobian matrix defined in the subsequent sections is derived based on fundamental thermodynamic theories, which is valid over the entire fluid state of concern and can accommodate any arbitrary equation of state. The key thermodynamic relations associated with this approach are listed in the next sub-section.

### 3.3.1 Important Thermodynamic Relationships.

All the relationships required in the numerical algorithm, including Jacobian matrices and fluid properties, are derived using fundamental thermodynamic theories, which can be calculated based on any equation of state. The partial mass and partial density properties of a real fluid mixture, as defined in Chapter 2, are also utilized in the derivations.

First, a thermodynamic relationship correlating pressure as a function of temperature, density, and mass fractions is derived. According to thermodynamics, each intensive property will depend on  $N + 1$  other intensive variables in a mixture. We begin with the following relation

$$p = p(T, \rho_i) \quad (3.13)$$

where  $i = 1, \dots, N$ .

Only the differential form is interested, then it can be expressed as

$$dp = \left( \frac{\partial p}{\partial T} \right)_{\rho_i} dT + \sum_{i=1}^N \left( \frac{\partial p}{\partial \rho_i} \right)_{T, \rho_{j \neq i}} d\rho_i \quad (3.14)$$

Rearrange it, we have the Eq. 3.15

$$dp = \left(\frac{\partial p}{\partial T}\right)_{\rho_i} dT + \sum_{i=1}^{N-1} \left[ \left(\frac{\partial p}{\partial \rho_i}\right)_{T, \rho_{j \neq i}} - \left(\frac{\partial p}{\partial \rho_N}\right)_{T, \rho_{j \neq N}} \right] d\rho_i + \left(\frac{\partial p}{\partial \rho_N}\right)_{T, \rho_{j \neq N}} d\rho \quad (3.15)$$

Since  $\rho_i = \rho Y_i$

$$d\rho_i = Y_i d\rho + \rho dY_i \quad (3.16)$$

Substituting Eq. 3.16 into Eq. 3.15 leads to following expression

$$dp = A_T dT + A_{Y_i} dY_i + A_\rho d\rho \quad (3.17)$$

where

$$A_T = \left(\frac{\partial p}{\partial T}\right)_{\rho_i} \quad (3.18)$$

$$A_{Y_i} = \rho \left[ \left(\frac{\partial p}{\partial \rho_i}\right)_{T, \rho_{j \neq i}} - \left(\frac{\partial p}{\partial \rho_N}\right)_{T, \rho_{j \neq N}} \right] \quad (3.19)$$

$$A_\rho = \left(\frac{\partial p}{\partial \rho}\right)_{T, Y_i} \quad (3.20)$$

A very useful formulation can be derived from Eq. 3.17, which is

$$d\rho = \frac{dp - \left(\frac{\partial p}{\partial T}\right)_{\rho_i} dT - \sum_{i=1}^{N-1} \left[ \left(\frac{\partial p}{\partial \rho_i}\right)_{T, \rho_{j \neq i}} - \left(\frac{\partial p}{\partial \rho_N}\right)_{T, \rho_{j \neq N}} \right] dY_i}{\left(\frac{\partial p}{\partial \rho}\right)_{T, Y_i}} \quad (3.21)$$

Next, a thermodynamic relationship correlating internal energy as a function of pressure, density, and mass fractions is derived. We begin with the following one

$$\rho e = \rho e(T, \rho_i) \quad (3.22)$$

where  $i = 1, \dots, N$ , and  $e$  is the internal energy per unit mass. Its differential form can be written as

$$d\rho e = \rho \left(\frac{\partial e}{\partial T}\right)_{\rho_i} dT + \sum_{i=1}^N \left(\frac{\partial \rho e}{\partial \rho_i}\right)_{T, \rho_{j \neq i}} d\rho_i \quad (3.23)$$

Based on the definition of partial density properties, it is recognized

$$\hat{e}_i = \left( \frac{\partial \rho e}{\partial \rho_i} \right)_{T, \rho_j \neq i} \quad (3.24)$$

which is the partial density internal energy of species  $i$  in the mixture. The first derivative in Eq. 3.23 is the constant volume heat capacity  $C_v$ . Substituting the partial density internal energy of each species into Eq. 3.23 leads to the following expression

$$d\rho e = \rho C_v dT + \sum_{i=1}^N \hat{e}_i d\rho_i \quad (3.25)$$

Inserting Eq. 3.16 into Eq. 3.25

$$d\rho e = \rho C_v dT + \sum_{i=1}^N \hat{e}_i \rho dY_i + \sum_{i=1}^N \hat{e}_i Y_i d\rho \quad (3.26)$$

Since  $d\rho e = \rho de + ed\rho$ , the following expression is easily derived

$$de = C_v dT + \sum_{i=1}^{N-1} (\hat{e}_i - \hat{e}_N) dY_i + \frac{1}{\rho} \left( \sum_{i=1}^N Y_i \hat{e}_i - e \right) d\rho \quad (3.27)$$

Substituting Eq. 3.26 into Eq. 3.27, we can establish Eq. 3.28

$$de = B_T dT + B_p dp + \sum_{i=1}^{N-1} B_{Y_i} dY_i \quad (3.28)$$

where

$$B_T = C_v - \frac{1}{\rho} \left( \sum_{i=1}^N Y_i \hat{e}_i - e \right) \left( \frac{\partial \rho}{\partial p} \right)_{T, Y_i} \left( \frac{\partial p}{\partial T} \right)_{\rho_i} \quad (3.29)$$

$$B_p = \frac{1}{\rho} \left( \sum_{i=1}^N Y_i \hat{e}_i - e \right) \left( \frac{\partial \rho}{\partial p} \right)_{T, Y_i} \quad (3.30)$$

$$B_{Y_i} = \left\{ (\hat{e}_i - \hat{e}_N) - \left( \sum_{i=1}^N Y_i \hat{e}_i - e \right) \cdot \left( \frac{\partial \rho}{\partial p} \right)_{T, Y_i} \cdot \left[ \left( \frac{\partial p}{\partial \rho_i} \right)_{T, \rho_j \neq i} - \left( \frac{\partial p}{\partial \rho_N} \right)_{T, \rho_j \neq N} \right] \right\} \quad (3.31)$$

Based on fundamental thermodynamic theories, the following relation can be easily obtained

$$dh = de + \frac{1}{\rho} dp - \frac{p}{\rho^2} d\rho \quad (3.32)$$

Substituting Eq. 3.28 into Eq. 3.32, the following expression can be derived after some straightforward manipulations

$$dh = D_T dT + D_p dp + \sum_{i=1}^{N-1} D_{Y_i} dY_i \quad (3.33)$$

where

$$D_T = C_v - \frac{1}{\rho} \left( \frac{\partial p}{\partial T} \right)_{\rho_i} \left( \frac{\partial \rho}{\partial p} \right)_{T, Y_i} \left( \sum_{i=1}^N Y_i \hat{e}_i - e - \frac{p}{\rho} \right) \quad (3.34)$$

$$D_p = \frac{1}{\rho} + \frac{1}{\rho} \left( \frac{\partial \rho}{\partial p} \right)_{T, Y_i} \left( \sum_{i=1}^N Y_i \hat{e}_i - e - \frac{p}{\rho} \right) \quad (3.35)$$

$$D_{Y_i} = \hat{e}_i - \hat{e}_N - \left( \frac{\partial \rho}{\partial p} \right)_{T, Y_i} \left( \sum_{i=1}^N Y_i \hat{e}_i - e - \frac{p}{\rho} \right) \left[ \left( \frac{\partial p}{\partial \rho_i} \right)_{T, \rho_{j \neq i}} - \left( \frac{\partial p}{\partial \rho_N} \right)_{T, \rho_{j \neq N}} \right] \quad (3.36)$$

According to the definition in thermodynamics, we recognize that the coefficient  $D_T$  equals to the constant pressure heat capacity  $C_p$  of a mixture,

$$C_p = D_T = C_v - \frac{1}{\rho} \left( \frac{\partial p}{\partial T} \right)_{\rho_i} \left( \frac{\partial \rho}{\partial p} \right)_{T, Y_i} \left( \sum_{i=1}^N Y_i \hat{e}_i - e - \frac{p}{\rho} \right) \quad (3.37)$$

Finally a relationship regarding the speed of sound in the mixture is derived. According to the definition of the speed of sound

$$a^2 = \left( \frac{\partial p}{\partial \rho} \right)_{s, Y_i} \quad (3.38)$$

Based on the Eq. 3.17, the following expression is obtained in a straightforward manner.

$$\left(\frac{\partial p}{\partial \rho}\right)_{s,Y_i} = \left(\frac{\partial p}{\partial T}\right)_{\rho_i} \left(\frac{\partial T}{\partial \rho}\right)_{s,Y_i} + \left(\frac{\partial p}{\partial \rho}\right)_{T,Y_i} \quad (3.39)$$

In thermodynamics, the following relationship exists

$$s = s(T, \rho, Y_i) \quad (3.40)$$

where  $i = 1, \dots, N - 1$ .

After utilizing some fundamental thermodynamic relationships, the following differential form of Eq. 3.40 can be obtained

$$ds = \frac{C_v}{T} dT - \frac{1}{\rho^2} \left(\frac{\partial p}{\partial T}\right)_{\rho_i} d\rho + \sum_{i=1}^{N-1} \left(\frac{\partial s}{\partial Y_i}\right)_{T,\rho,Y_j \neq i} dY_i \quad (3.41)$$

Based on Eq. 3.41, the following expression is further derived

$$\left(\frac{\partial T}{\partial \rho}\right)_{s,Y_i} = \frac{T}{\rho^2} \left(\frac{\partial p}{\partial T}\right)_{\rho_i} / C_v \quad (3.42)$$

Substituting Eq. 3.42 into Eq. 3.39, an expression of the speed of sound in the general fluid mixture is established as

$$a^2 = \left(\frac{\partial p}{\partial \rho}\right)_{s,Y_i} = \frac{C_p}{C_v} \left(\frac{\partial p}{\partial \rho}\right)_{T,Y_i} \quad (3.43)$$

Equations 3.17, 3.28, 3.33, and Eq. 3.43 are the important thermodynamic relationships required in the numerical derivations below.

### 3.3.2 Preconditioning Matrix

With those fundamental thermodynamic relations, the transformation matrix  $T = \frac{\partial Q}{\partial Z}$ ,

$A = \frac{\partial E}{\partial Z}$ ,  $B = \frac{\partial F}{\partial Z}$ ,  $C = \frac{\partial G}{\partial Z}$  are well defined and listed in Appendix B. Each element of the

first column of the matrix T has a common term  $\left(\frac{\partial \rho}{\partial p}\right)_{T, Y_i}$ , which can be expressed as

$$\left(\frac{\partial p}{\partial \rho}\right)_{T, Y_i} = \frac{C_p}{C_v} \left(\frac{\partial p}{\partial \rho}\right)_{s, Y_i} = \frac{\gamma}{a^2} \quad (3.44)$$

The preconditioning matrix are established by simply replacing the speed of sound in this term by a scaling factor  $\beta$ .

$$\Gamma = \begin{pmatrix} \frac{\gamma}{\beta} & 0 & 0 & -\frac{A_T}{A_\rho} & -\frac{A_{Y_1}}{A_\rho} & \dots & -\frac{A_{Y_{N-1}}}{A_\rho} \\ \frac{\gamma \tilde{u}}{\beta} & \bar{\rho} & 0 & 0 & -\frac{A_T \tilde{u}}{A_\rho} & -\frac{A_{Y_1} \tilde{u}}{A_\rho} & \dots & -\frac{A_{Y_{N-1}} \tilde{u}}{A_\rho} \\ \frac{\gamma \tilde{v}}{\beta} & 0 & \bar{\rho} & 0 & -\frac{A_T \tilde{v}}{A_\rho} & -\frac{A_{Y_1} \tilde{v}}{A_\rho} & \dots & -\frac{A_{Y_{N-1}} \tilde{v}}{A_\rho} \\ \frac{\gamma \tilde{w}}{\beta} & 0 & 0 & \bar{\rho} & -\frac{A_T \tilde{w}}{A_\rho} & -\frac{A_{Y_1} \tilde{w}}{A_\rho} & \dots & -\frac{A_{Y_{N-1}} \tilde{w}}{A_\rho} \\ \frac{\gamma \tilde{h}}{\beta} + \left( \sum_{i=1}^N \tilde{Y}_i \tilde{e}_i - e - \frac{p}{\rho} \right) \left( \frac{\partial \rho}{\partial p} \right)_{T, Y_i} & \bar{\rho} \tilde{u} & \bar{\rho} \tilde{v} & \bar{\rho} \tilde{w} & \bar{\rho} B_T - \frac{A_T e}{A_\rho} & \bar{\rho} B_{Y_1} - \frac{A_{Y_1} e}{A_\rho} & \dots & \bar{\rho} B_{Y_{N-1}} - \frac{A_{Y_{N-1}} e}{A_\rho} \\ \frac{\gamma \tilde{Y}_1}{\beta} & 0 & 0 & 0 & -\frac{A_T \tilde{Y}_1}{A_\rho} & \bar{\rho} - \frac{A_{Y_1} \tilde{Y}_1}{A_\rho} & \vdots & -\frac{A_{Y_{N-1}} \tilde{Y}_1}{A_\rho} \\ \vdots & \vdots & \vdots & \vdots & \vdots & \vdots & \ddots & \vdots \\ \frac{\gamma \tilde{Y}_{N-1}}{\beta} & 0 & 0 & 0 & -\frac{A_T \tilde{Y}_{N-1}}{A_\rho} & -\frac{A_{Y_1} \tilde{Y}_{N-1}}{A_\rho} & \dots & \bar{\rho} - \frac{A_{Y_{N-1}} \tilde{Y}_{N-1}}{A_\rho} \end{pmatrix} \quad (3.45)$$

where  $A_T$ ,  $A_{Y_i}$ ,  $B_T$ ,  $B_{Y_i}$  are defined in the previous subsection. The scaling factor  $\beta$  takes the form

$$\beta = \frac{\gamma \epsilon a^2}{1 + (\gamma - 1)\epsilon} \quad (3.46)$$

Here  $\varepsilon$  ( $0 < \varepsilon \leq 1$ ) is the preconditioning factor, which is proportional to the local Mach number  $M^2$  and gives good control of both the inviscid and viscous time scales. In contrast to the form  $\Gamma$  defined by other researchers, all of the off-diagonal terms in Eq. 3.45 have been retained. By keeping these terms, the unaltered system is identically restored as  $\varepsilon \rightarrow 1$ ;

$$\lim_{\varepsilon \rightarrow 1} \Gamma = T \quad (3.47)$$

The criteria employed to select optimal values for  $\varepsilon$  are present in the next subsection.

The system eigenvalues associated with the pseudo-time domain are obtained by taking the determinant of the matrices  $\Gamma^{-1}A$ ,  $\Gamma^{-1}B$ ,  $\Gamma^{-1}C$ . The calculation is straightforward, and the eigenvalues are

$$\lambda = \text{diag}(\lambda_1 \ \lambda_2 \ \tilde{u} \ \tilde{u} \ \tilde{u} \ \dots) \quad (3.48)$$

where  $\lambda_1$  and  $\lambda_2$  represent the rescaled acoustic eigenvalues. These terms are given by

$$\begin{aligned} \lambda_1 &= \frac{1}{2}[U(\varepsilon + 1) + \sqrt{U^2(1 - \varepsilon)^2 + 4\varepsilon a^2}] \\ \lambda_2 &= \frac{1}{2}[U(\varepsilon + 1) - \sqrt{U^2(1 - \varepsilon)^2 + 4\varepsilon a^2}] \end{aligned} \quad (3.49)$$

$U$  represents  $\tilde{u}$ ,  $\tilde{v}$ , and  $\tilde{w}$  in x-, y- and z-direction respectively. As  $\varepsilon \rightarrow 1$ , Eq. 3.49 approaches the values given by the non-preconditioned system. Obviously, all of the eigenvalues are in the same order of magnitude, which proves that the choice of preconditioning matrix  $\Gamma$  and primitive variable vector is appropriate. Furthermore, since all the numerical Jacobians are calculated based on the fundamental thermodynamics theories, those results are independent of equation of state and can be apply to any fluid state of concern without empiricism.

### 3.3.3 Convergence Optimization

Associated with each finite-volume cell are various fundamental time scales which characterize propagation rates of competing convective and diffusive processes in each of the coordinate directions. The convective propagation rates are characterized by the Courant-Friedrichs-Lowy (CFL) numbers

$$CFL_x = \frac{\rho(\lambda_x)\Delta\tau}{\Delta x}, \quad CFL_y = \frac{\rho(\lambda_y)\Delta\tau}{\Delta y}, \quad CFL_z = \frac{\rho(\lambda_z)\Delta\tau}{\Delta z} \quad (3.50)$$

where  $\rho(\lambda_x)$ ,  $\rho(\lambda_y)$ ,  $\rho(\lambda_z)$  are the spectral radii associated with

$$\begin{aligned} \rho(\lambda_x) &= \frac{1}{2} \left[ |u|(1+\varepsilon) + \sqrt{u^2(1-\varepsilon)^2 + 4\varepsilon a^2} \right] \\ \rho(\lambda_y) &= \frac{1}{2} \left[ |v|(1+\varepsilon) + \sqrt{v^2(1-\varepsilon)^2 + 4\varepsilon a^2} \right] \\ \rho(\lambda_z) &= \frac{1}{2} \left[ |w|(1+\varepsilon) + \sqrt{w^2(1-\varepsilon)^2 + 4\varepsilon a^2} \right] \end{aligned} \quad (3.51)$$

The diffusive propagation rates are characterized by the von Neumann numbers

$$VNN_x = \frac{v\Delta\tau}{\Delta x^2}, \quad VNN_y = \frac{v\Delta\tau}{\Delta y^2}, \quad VNN_z = \frac{v\Delta\tau}{\Delta z^2} \quad (3.52)$$

Buelow et al. (1994, 1995) have shown that the maximum CFL number associated with a given cell scales with the grid aspect ratio, whereas the minimum CFL number remains fixed. When source and sink terms are not present, optimum pseudo-time step corresponds to the minimum CFL number. This criteria is enforced in a three-dimensional domain by selecting

$$\Delta\tau = \max\left(\frac{CFL\Delta x}{\rho(\lambda_x)}, \frac{CFL\Delta y}{\rho(\lambda_y)}, \frac{CFL\Delta z}{\rho(\lambda_z)}\right) \quad (3.53)$$

The time step definition given by this equation incorporates the preconditioning factor as a function of the spectral radii given by Eq. 3.51.

The optimal value of the preconditioning factor is dependent upon the local Mach number and the cell Reynolds numbers

$$\text{Re}_x = \frac{\tilde{u}\Delta x}{\nu}, \text{Re}_y = \frac{\tilde{v}\Delta y}{\nu}, \text{Re}_z = \frac{\tilde{w}\Delta z}{\nu} \quad (3.54)$$

the cell Prandtl number  $\text{Pr} = \nu/\alpha$ , the cell Schmidt number  $\text{Sc}_i = \nu/D_{im}$  ( $i = 1, \dots, N$ ), and the physical time step employed in the calculation procedure. If the respective quantities  $\text{Re}$ ,  $\text{RePr}$ ,  $\text{ReSc}$  exceed a value of unity in either of the coordinate direction, convective effects dominant and the conservation equations exhibit a hyperbolic character. For this situation an inviscid criterion must be employed. If  $\text{Re}$ ,  $\text{RePr}$ , and  $\text{ReSc}$  are less than or equal to unity, diffusive effects dominate, a parabolic character is exhibited and a viscous criteria must be employed.

An additional criterion that must be considered when employing the dual-time stepping methodology is the effect of the physical time derivatives on the pseudo-time system. The first term in Eq. 3.11 behaves as a sink in the pseudo-time system with a magnitude that is directly proportional to the pseudo-time step and inversely proportional to the physical time step. It is well known that such terms promote favorable damping characteristics in time-marching schemes and accelerate convergence. Venkateswaran and Merkel (1995) have shown that a limit exists where preconditioning the pseudo-time derivatives negates the favorable damping characteristics induced by these sink terms.

In the current work, the preconditioning factor is selected using the methodologies developed by Choi and Merkel (1993), Buelow et al.(1995), and Venkateswaran and Merkel (1995). Optimal values are specified locally by the relation

$$\epsilon = \min[1, \max(\epsilon_{inv}, \epsilon_{\Delta t}, \epsilon_{vis})] \quad (3.55)$$

The subscripts “inv”, “ $\Delta t$ ”, and “vis” refer to the inviscid, unsteady, and viscous preconditioning factors, respectively. The criteria employed to evaluate these terms are given below.

### 3.3.3.1 Inviscid Preconditioning Factor

Choi and Merkel (1993) have demonstrated that an effective convective criterion which insures that acoustics speeds and flow velocities are the same order of magnitude is obtained when  $\varepsilon$  is assigned a value proportional to the local Mach number. To obtain the correct functional form, it is necessary to examine the characteristic condition number, which is defined as the ratio of the largest to smallest absolute eigenvalue. The optimum condition number is unity.

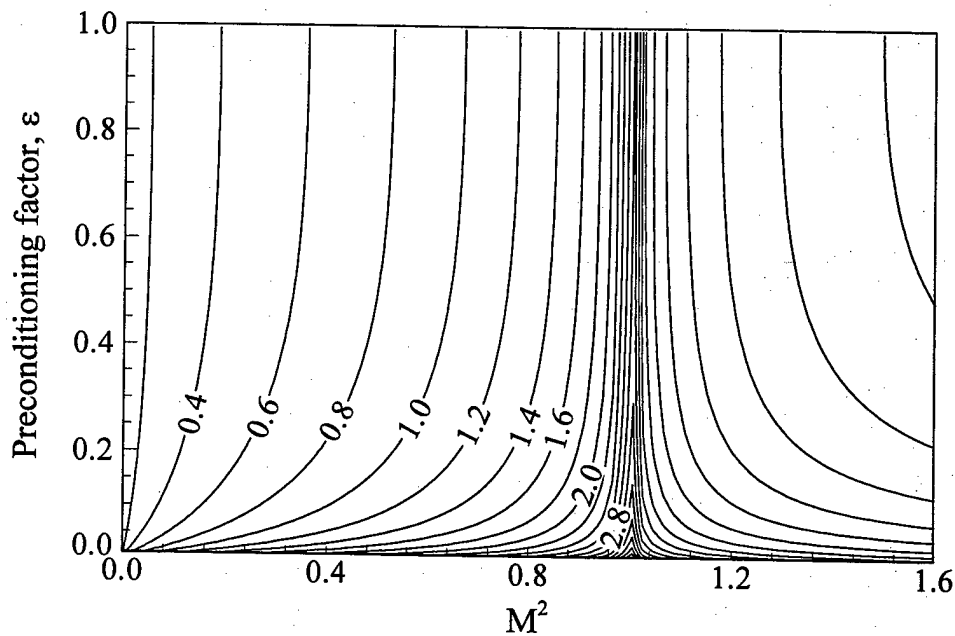


Fig. 3.1: Contours of the condition number as a function of the Mach number squared and the preconditioning factor.

A plot of the condition number associated with Eq. 3.49 is given in Fig. 3.1. Here,  $\log_{10}$  contours are plotted as a function of the Mach number squared and the preconditioning factor  $\varepsilon$ . In the limit as  $M^2 \rightarrow 0$ , a minimum condition number of 2 is obtained, with local minima corresponding to the relation  $\varepsilon = 2M^2$ . To achieve the correct limiting behavior at low Mach numbers, the inviscid criteria for the preconditioning factor is specified as

$$\varepsilon_{inv} = \begin{cases} \varepsilon^2 & M \leq \varepsilon \\ 2M^2 & \varepsilon < M < 1 \\ 1 & M \geq 1 \end{cases} \quad (3.56)$$

The term  $\varepsilon$  is included to avoid singularities in stagnation regions where  $M = 0$ . Typically,  $\varepsilon = 10^{-5}$ . For infinitely large physical CFL numbers (the steady state limit) and in the absence of strong local diffusion processes this choice yields minimal disparities in the system eigenvalues and optimal damping rates. Under these circumstances convergence rates are entirely dependent on the magnitude of the pseudo CFL number.

### 3.3.3.2 Unsteady Preconditioning Factor

Venkateswaran and Merkel (1995) have employed von Neumann stability theory to gain insight into the characteristics of the dual-time system and the effects of the physical CFL number on the numerical attributes of the pseudo-time system. Results demonstrate the effects of small physical time steps on the system eigenvalues. In contrast to the steady state limit described above, the limit of infinitely small physical CFL numbers alters the system eigenvalues such that the choice  $\varepsilon = 1$  renders minimal disparities. This effect is caused by the physical time derivatives which appear as sink terms in the pseudo-time equations.

The trends presented by them indicated that the optimal choice for the unsteady preconditioning factor is bounded by the interval  $\varepsilon_{inv} \leq \varepsilon_{\Delta t} \leq 1$  and inversely related to the value of the local physical CFL number. By examining the eigenvalues and making a series of simplifying assumptions, a factor of the form

$$\varepsilon_{\Delta t} = \frac{1}{a^2} \left[ \left( \frac{l_x}{\pi \Delta t} \right) + \left( \frac{l_y}{\pi \Delta t} \right) \right] + M^2 \quad (3.57)$$

was derived. Here,  $l_x$  and  $l_y$  represent the characteristic dimensions of the computational domain and  $M$  is the Mach number. Equation 3.57 is tuned to damp the low wavenumber modes which are typically the most difficult to treat.

### 3.3.3.3 Viscous Preconditioning Factor

In regions where diffusion processes dominate, the criteria outlined in the last two sections must be modified to account for interactions associated with the parabolic system. Buelow et al. (1994, 1995) have conducted a variety of studies to determine an optimal viscous preconditioning factor for the Navier-Stokes equations. Results from stability analysis indicate that three different requirements must be addressed in order to specify a generalized criterion. For high cell Reynolds numbers ( $Re \gg 1$ ) the acoustic wave speeds should be scaled to the same order of magnitude as the particle speeds, as is accomplished by the inviscid preconditioning factor defined above. For low cell Reynolds numbers ( $Re \ll 1$ ) and high acoustic cell Reynolds numbers ( $Re/M \gg 1$ ) the diffusion rates should be scaled to the same order of magnitude as the acoustic speeds. For low cell Reynolds numbers and low acoustic cell Reynolds numbers the diffusion rates should be scaled to the particle speeds. The only way to satisfy these conditions

simultaneously is to define a viscous preconditioning factor that is dependent on the Fourier wavenumber. Such a definition is not appropriate for implementation in a CFD code.

To overcome the difficulties outlined above, Buelow et al. (1994, 1995) have developed a preconditioning factor based on local length scales which is tuned to damp the low wavenumber modes. This definition requires a priori assumption regarding the orientation of dominate convective and diffusion processes within a given grid configuration and the choice for  $\varepsilon_{vis}$  is somewhat more involved. In three dimensions, there are three possible CFL numbers, and two possible VNN numbers, and six possible values of  $\varepsilon_{vis}$  exist. The most restrictive of the CFL and VNN numbers are usually chosen for stability reasons and these values are the most likely candidates for determining  $\varepsilon_{vis}$ . Some freedom does exist, however, in how  $\varepsilon_{vis}$  is evaluated.

Most grid configurations are stretched such that predominate diffusion processes are resolved in a direction normal to the predominate convective processes. Under these conditions, the rate limiting diffusion processes typically coincide with the maximum von Neumann number in a given cell. To retain the benefits of the time step definition given by Eq. 3.53, this quantity must be optimized with respect to the minimum CFL number. In three-dimensional this achieved by: 1) equating Eq. 3.50 with Eq. 3.52, respectively; 2) solving for respective values of  $\varepsilon$ ; and 3) choosing the largest of the three values obtained. Performing this operation yields an expression of the form

$$\varepsilon_{vis} = \left[ \frac{\tilde{u}^2 \delta_x (\delta_x - 1)}{\tilde{u}^2 \delta_x^2 + a^2}, \frac{\tilde{v}^2 \delta_y (\delta_y - 1)}{\tilde{v}^2 \delta_y^2 + a^2}, \frac{\tilde{w}^2 \delta_z (\delta_z - 1)}{\tilde{w}^2 \delta_z^2 + a^2} \right] \quad (3.58)$$

where

$$\begin{aligned}\delta_x &= \max(\nu, \frac{\nu}{Pr}, \frac{\nu}{Sc_i}) \frac{1}{\tilde{u}} \frac{CFL}{VNN} \\ \delta_y &= \max(\nu, \frac{\nu}{Pr}, \frac{\nu}{Sc_i}) \frac{1}{\tilde{v}} \frac{CFL}{VNN} \\ \delta_z &= \max(\nu, \frac{\nu}{Pr}, \frac{\nu}{Sc_i}) \frac{1}{\tilde{w}} \frac{CFL}{VNN}\end{aligned}\quad (3.59)$$

This equation takes into account the effects of momentum, energy, and mass diffusion processes on the overall convergence rate.

### 3.4 Spatial Discretization: Finite Volume Approach

#### 3.4.1 Finite Volume Approach

The governing equations are solved numerically by means of a finite-volume approach. This method allows for the treatment of arbitrary geometry. To utilize the finite-volume approach, the governing equation is integrated over the control volume  $V$  enclosed by the surface  $S$  in the physical domain as

$$\iiint_V \left( \Gamma \frac{\partial Z}{\partial \tau} + \frac{\partial Q}{\partial t} + \frac{\partial (E - E_v)}{\partial x} + \frac{\partial (F - F_v)}{\partial y} + \frac{\partial (G - G_v)}{\partial z} - H \right) dV = 0 \quad (3.60)$$

Using the Gauss divergence theorem, the integral conservation equation takes the following form for the three-dimensional cell with six surfaces, as shown in Fig. 3.2.

$$\iiint_V (\Gamma \frac{\partial Z}{\partial \tau} + \frac{\partial Q}{\partial t}) dV + \int_{S_\xi} \bar{W} \cdot \vec{n}_\xi dS_\xi + \int_{S_\eta} \bar{W} \cdot \vec{n}_\eta dS_\eta + \int_{S_\zeta} \bar{W} \cdot \vec{n}_\zeta dS_\zeta = \iiint_V H dV \quad (3.61)$$

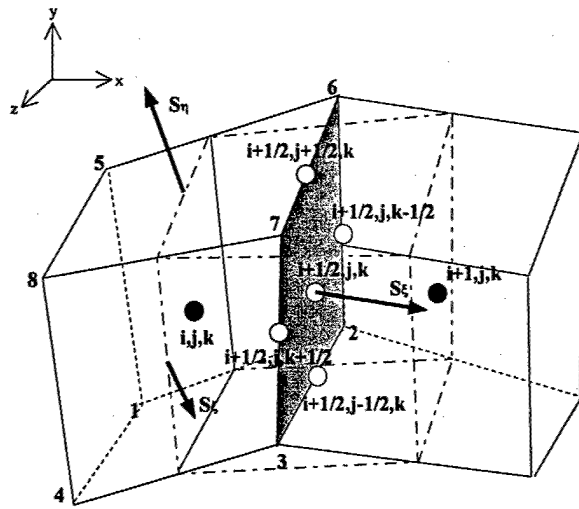


Fig. 3.2: Schematic of three-dimensional adjacent cells

where

$$\vec{W} = (\mathbf{E} - \mathbf{E}_v)\vec{i} + (\mathbf{F} - \mathbf{F}_v)\vec{j} + (\mathbf{G} - \mathbf{G}_v)\vec{k} \quad (3.62)$$

and  $\vec{n}_\xi$ ,  $\vec{n}_\eta$  and  $\vec{n}_\zeta$  are unit normal vectors to the surface in the  $\xi$ ,  $\eta$ -, and  $\zeta$ -directions, respectively. The unit normal vectors are related to cell surface area  $S_\xi$ ,  $S_\eta$ , and  $S_\zeta$  as

$$\begin{aligned} \vec{n}_\xi &= (S_{\xi_x}\vec{i} + S_{\xi_y}\vec{j} + S_{\xi_z}\vec{k})/|\vec{S}_\xi| \\ \vec{n}_\eta &= (S_{\eta_x}\vec{i} + S_{\eta_y}\vec{j} + S_{\eta_z}\vec{k})/|\vec{S}_\eta| \\ \vec{n}_\zeta &= (S_{\zeta_x}\vec{i} + S_{\zeta_y}\vec{j} + S_{\zeta_z}\vec{k})/|\vec{S}_\zeta| \end{aligned} \quad (3.63)$$

The cell surface areas are defined as

$$\begin{aligned}
 \vec{S}_\xi &= \frac{1}{2} (\vec{r}_{72} \times \vec{r}_{36}) = \frac{1}{2} \begin{vmatrix} \vec{i} & \vec{j} & \vec{k} \\ x_2 - x_7 & y_2 - y_7 & z_2 - z_7 \\ x_6 - x_3 & y_6 - y_3 & z_6 - z_3 \end{vmatrix} = S_{\xi x} \vec{i} + S_{\xi y} \vec{j} + S_{\xi z} \vec{k} \\
 \vec{S}_\eta &= \frac{1}{2} (\vec{r}_{86} \times \vec{r}_{75}) = \frac{1}{2} \begin{vmatrix} \vec{i} & \vec{j} & \vec{k} \\ x_6 - x_8 & y_6 - y_8 & z_6 - z_8 \\ x_5 - x_7 & y_5 - y_7 & z_5 - z_7 \end{vmatrix} = S_{\eta x} \vec{i} + S_{\eta y} \vec{j} + S_{\eta z} \vec{k} \\
 \vec{S}_\zeta &= \frac{1}{2} (\vec{r}_{74} \times \vec{r}_{83}) = \frac{1}{2} \begin{vmatrix} \vec{i} & \vec{j} & \vec{k} \\ x_4 - x_7 & y_4 - y_7 & z_4 - z_7 \\ x_3 - x_8 & y_3 - y_8 & z_3 - z_8 \end{vmatrix} = S_{\zeta x} \vec{i} + S_{\zeta y} \vec{j} + S_{\zeta z} \vec{k}
 \end{aligned} \tag{3.64}$$

The magnitude of each surface vector can be obtained by

$$\begin{aligned}
 |\vec{S}_\xi| &= (S_{\xi x}^2 + S_{\xi y}^2 + S_{\xi z}^2)^{1/2} \\
 |\vec{S}_\eta| &= (S_{\eta x}^2 + S_{\eta y}^2 + S_{\eta z}^2)^{1/2} \\
 |\vec{S}_\zeta| &= (S_{\zeta x}^2 + S_{\zeta y}^2 + S_{\zeta z}^2)^{1/2}
 \end{aligned} \tag{3.65}$$

The cell volume  $\Delta V$  associated with each cell can be evaluated using Kordulla and Vinokur (1983) formula

$$\Delta V = \frac{1}{2} \vec{r}_{17} \cdot (\vec{S}_\xi + \vec{S}_\eta + \vec{S}_\zeta) \tag{3.66}$$

We also define cell surface areas per cell volume as

$$\tilde{\vec{S}}_\xi = \vec{S}_\xi / \Delta V, \quad \tilde{\vec{S}}_\eta = \vec{S}_\eta / \Delta V, \quad \tilde{\vec{S}}_\zeta = \vec{S}_\zeta / \Delta V$$

Assuming the increments  $\Delta\xi=\Delta\eta=\Delta\zeta=1$  in the body-fitted coordinate system and substituting Eq. 3.62 and Eq. 3.63 into Eq. 3.61 yields the following governing equation in the general coordinates

$$\left\{ \Gamma \frac{\partial Z}{\partial \tau} + \frac{\partial Q}{\partial t} \right\} + (E_\xi - E_{\xi\nu})_{i-1/2,j,k}^{i+1/2,j,k} + (F_\eta - F_{\eta\nu})_{i,j-1/2,k}^{i,j+1/2,k} + (G_\zeta - G_{\zeta\nu})_{i,j,k-1/2}^{i,j,k+1/2} = H \quad (3.67)$$

where the vectors  $E_\xi, F_\eta, G_\zeta, E_{\xi\nu}, F_{\eta\nu}, G_{\zeta\nu}$  are defined as

$$\begin{aligned} E_\xi &= (\tilde{S}_{\xi x} E + \tilde{S}_{\xi y} F + \tilde{S}_{\xi z} G) & E_{\xi\nu} &= (\tilde{S}_{\xi x} E_\nu + \tilde{S}_{\xi y} F_\nu + \tilde{S}_{\xi z} G_\nu) \\ F_\eta &= (\tilde{S}_{\eta x} E + \tilde{S}_{\eta y} F + \tilde{S}_{\eta z} G) & F_{\eta\nu} &= (\tilde{S}_{\eta x} E_\nu + \tilde{S}_{\eta y} F_\nu + \tilde{S}_{\eta z} G_\nu) \\ G_\zeta &= (\tilde{S}_{\zeta x} E + \tilde{S}_{\zeta y} F + \tilde{S}_{\zeta z} G) & G_{\zeta\nu} &= (\tilde{S}_{\zeta x} E_\nu + \tilde{S}_{\zeta y} F_\nu + \tilde{S}_{\zeta z} G_\nu) \end{aligned} \quad (3.68)$$

The quantities  $E_{\xi,i\pm1/2,j,k}, E_{\xi\nu,i\pm1/2,j,k}, F_{\eta,j,j\pm1/2,k}, F_{\eta\nu,i,j\pm1/2,j,k}, G_{\zeta,i,j,k\pm1/2}$ , and  $G_{\zeta\nu,i,j,k\pm1/2}$  represent the numerical fluxes associated with each cell interface (as shown in Fig. 3.2).  $\tilde{S}$  represents cell surface areas per cell volume. In fact, the above analysis describes the transformation of a quadrilateral cell with a volume  $\Delta V$  in  $x$ - $y$ - $z$  coordinates to a cubic cell with unit volume in the general coordinate (i.e.,  $\xi$ - $\eta$ - $\zeta$  coordinates).

To accelerate convergence, the pseudo-time integration is based on the local time step. The maximum pseudo-time increment  $\Delta\tau$  of each cell can be evaluated by

$$\Delta\tau = \frac{\Delta\tau_\xi \Delta\tau_\eta \Delta\tau_\zeta}{\Delta\tau_\xi + \Delta\tau_\eta + \Delta\tau_\zeta} \quad (3.69)$$

where

$$\begin{aligned} \Delta\tau_\xi &= \frac{CFL \cdot \Delta V}{|\rho(\lambda_x)S_{\xi x} + \rho(\lambda_y)S_{\xi y} + \rho(\lambda_z)S_{\xi z}| / |\vec{S}_\xi|} \\ \Delta\tau_\eta &= \frac{CFL \cdot \Delta V}{|\rho(\lambda_x)S_{\eta x} + \rho(\lambda_y)S_{\eta y} + \rho(\lambda_z)S_{\eta z}| / |\vec{S}_\eta|} \\ \Delta\tau_\zeta &= \frac{CFL \cdot \Delta V}{|\rho(\lambda_x)S_{\zeta x} + \rho(\lambda_y)S_{\zeta y} + \rho(\lambda_z)S_{\zeta z}| / |\vec{S}_\zeta|} \end{aligned}$$

### 3.4.2 Evaluation of Inviscid Fluxes

Different approaches used in evaluating the numerical fluxes lead to different schemes with disparate numerical characteristics. For the central difference scheme, the convective flux at any cell face in the  $\xi$ -direction can be written as

$$\hat{E}_{\xi,i+1/2,j} = \frac{1}{2} [ E_{\xi}(Z^L) + E_{\xi}(Z^R) ] \quad (3.70)$$

where the left and right stencils are used to give the desired accuracy. The above equation corresponds to the stencil illustrated in Fig. 3.3

The superscripts  $L$  and  $R$  represent the left and right cells. Depending on the manner in which these terms are evaluated, a wide variety of central and upwind schemes can be obtained. In the present work, the methodology proposed by Rai and Chakravarthy (1994) is used. Accordingly the numerical flux in Eq. 3.67 is computed as

$$\hat{E}_{\xi,i+1/2,j,k} = \hat{E}_{\xi,i+1/2,j,k} - \phi_{i+1/2,j,k}^{(4)} \left( \frac{\hat{E}_{\xi,i+3/2,j,k} - 2\hat{E}_{\xi,i+1/2,j,k} + \hat{E}_{\xi,i-1/2,j,k}}{24} \right) \quad (3.71)$$

where  $\phi^{(4)}$  is the flux limiter. This term switches the truncation error associated with the flux-difference from fourth-order accuracy when  $\phi^{(4)} = 1$ , to second-order accuracy when  $\phi^{(4)} = 0$ . To evaluate Eq. 3.70 regarding the desired accuracy, the left and right state terms in Eq. 3.71 must be computed using the same or higher order accuracy. These terms are written as follows to facilitate easy switching and make the scheme TVD (total-variation-diminishing).

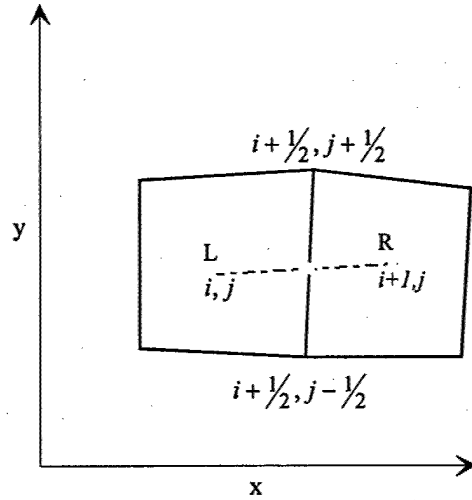


Fig. 3.3: Schematic diagram of the stencil used in evaluating inviscid flux terms in the  $x - y$  plane.

$$Z_{i+1/2,j,k}^L = Z_{i,j,k} + \phi_{i+1/2,j,k}^{(2)} \left( \frac{3\nabla Z_{i+1,j,k} + \nabla Z_{i,j,k}}{8} \right) + \phi_{i+1/2,j,k}^{(4)} \left( \frac{-5\nabla Z_{i+2,j,k} + 7\nabla Z_{i+1,j,k} + \nabla Z_{i,j,k} - 3\nabla Z_{i-1,j,k}}{128} \right) \quad (3.72)$$

$$Z_{i+1/2,j,k}^R = Z_{i,j,k} - \phi_{i+1/2,j,k}^{(2)} \left( \frac{\nabla Z_{i+2,j,k} + 3\nabla Z_{i+1,j,k}}{8} \right) + \phi_{i+1/2,j,k}^{(4)} \left( \frac{3\nabla Z_{i+3,j,k} - \nabla Z_{i+2,j,k} - 7\nabla Z_{i+1,j,k} + 5\nabla Z_{i,j,k}}{128} \right) \quad (3.73)$$

$$\nabla Z_{i,j} = Z_{i,j} - Z_{i-1,j} \quad (3.74)$$

These stencils can be used to get fifth-order accuracy ( $\phi^{(4)} = 1, \phi^{(2)} = 1$ ), third-order accuracy ( $\phi^{(4)} = 0, \phi^{(2)} = 1$ ), and first-order accuracy ( $\phi^{(4)} = 0, \phi^{(2)} = 0$ ), respectively. The present work utilizes second-order overall accuracy for spatial discretization with the exception of close to the physical boundaries. The third-order accurate evaluation of the left and right states is thus employed. The fluxes in  $\eta$ , and  $\zeta$ -directions can be computed in a similar fashion as above.

### 3.4.3 Evaluation of Viscous and SGS Fluxes

A three-dimensional auxiliary cell is shown schematically by the dash-dotted lines in Fig.

**3.4 .** The viscous fluxes need to be evaluated at the center of the cell faces, i.e.,  $i+1/2, j, k$  for the viscous flux in the axial direction. Using the Gauss divergence theorem and applying it to a small control volume  $\Delta V$ , the viscous fluxes can be approximated as

$$\nabla \cdot \vec{f} = \frac{1}{\Delta V} \oint_S \vec{f} \cdot \vec{n} dS \quad (3.75)$$

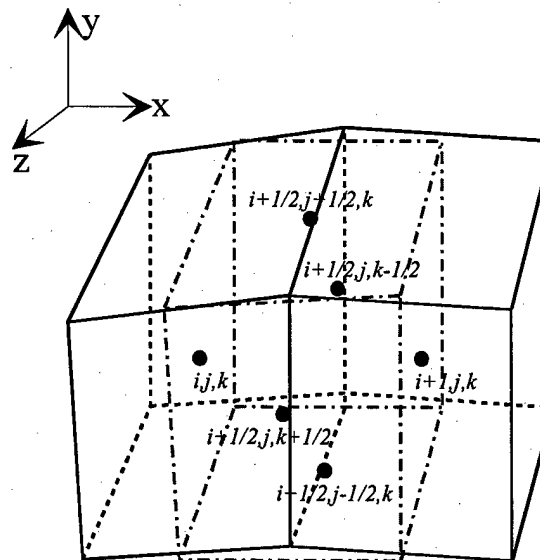


Fig. 3.4: Schematic diagram for a three-dimensional auxiliary cell.

Applying the above formulation to the auxiliary cell at  $(i+1/2, j, k)$  gives

$$\left( \frac{\partial f}{\partial x} \right)_{i+1/2, j, k} = \frac{1}{\Delta V_{i+1/2, j, k}} \left[ f S_{\xi_x} \Big|_{i+1, j, k} - f S_{\xi_x} \Big|_{i, j, k} + f S_{\eta_x} \Big|_{i+1/2, j+1/2, k} \right. \\ \left. - f S_{\eta_x} \Big|_{i+1/2, j-1/2, k} + f S_{\zeta_x} \Big|_{i+1/2, j, k+1/2} - f S_{\zeta_x} \Big|_{i+1/2, j, k-1/2} \right] \quad (3.76)$$

Similarly

$$\left( \frac{\partial f}{\partial y} \right)_{i+1/2,j,k} = \frac{1}{\Delta V_{i+1/2,j,k}} \left[ f S_{\xi y} \Big|_{i+1,j,k} - f S_{\xi y} \Big|_{i,j,k} + f S_{\eta y} \Big|_{i+1/2,j+1/2,k} - f S_{\eta y} \Big|_{i+1/2,j-1/2,k} + f S_{\zeta y} \Big|_{i+1/2,j,k+1/2} - f S_{\zeta y} \Big|_{i+1/2,j,k-1/2} \right] \quad (3.77)$$

$$\left( \frac{\partial f}{\partial z} \right)_{i+1/2,j,k} = \frac{1}{\Delta V_{i+1/2,j,k}} \left[ f S_{\xi z} \Big|_{i+1,j,k} - f S_{\xi z} \Big|_{i,j,k} + f S_{\eta z} \Big|_{i+1/2,j+1/2,k} - f S_{\eta z} \Big|_{i+1/2,j-1/2,k} + f S_{\zeta z} \Big|_{i+1/2,j,k+1/2} - f S_{\zeta z} \Big|_{i+1/2,j,k-1/2} \right] \quad (3.78)$$

Note that  $f$  in the above equations are elements of the viscous flux vectors  $\mathbf{E}_{\xi y}$ ,  $\mathbf{F}_{\eta y}$ , or  $\mathbf{G}_{\zeta y}$ .

Physical variables with one-half indices need to be interpolated from the quantities at the neighboring cell centers and are given as

$$\begin{aligned} f_{i+1/2,j\pm1/2,k} &= \frac{1}{4} (f_{i,j,k} + f_{i+1,j,k} + f_{i+1,j\pm1,k} + f_{i,j\pm1,k}) \\ f_{i+1/2,j,k\pm1/2} &= \frac{1}{4} (f_{i,j,k} + f_{i+1,j,k} + f_{i+1,j,k\pm1} + f_{i,j,k\pm1}) \end{aligned} \quad (3.79)$$

The evaluation of SGS fluxes follows a similar procedure as for the viscous and diffusive fluxes.

### 3.4.4 Evaluation of Artificial Dissipation

Artificial dissipation plays a crucial role in the stability of a numerical scheme based on central differencing. The form of these artificial dissipation terms depends on the order of accuracy of the numerical scheme, and must be higher-order accurate to keep its magnitude minimal. For the present case, the numerical differentiation of the flux vectors is fourth-order accurate in the core region of the computational domain. Accordingly, the artificial dissipation is fourth-order accurate. The accuracy order of the numerical scheme decreases near the physical boundary, and the artificial dissipation also goes to a lower order. The form of numerical dissipation used in the present schemes is quite often a blending of second- and fourth-order

dissipation terms. The second-order terms are used to prevent oscillations near shock waves and in flame zones to prevent spurious oscillations within such thin regions, while the fourth-order terms are important for stability and convergence. The standard dissipation model can be written as

$$\begin{aligned} \mathbf{AD} &= \text{artificial dissipation} \\ &= \mathbf{d}_{i+1/2,j,k} - \mathbf{d}_{i-1/2,j,k} \end{aligned} \quad (3.80)$$

where

$$\mathbf{d}_{i\pm 1/2,j,k} = \frac{\varepsilon_2}{8} \frac{1}{\Delta t} \frac{\partial Z}{\partial \xi} \Big|_{i\pm 1/2,j,k} - \frac{\varepsilon_4}{8} \frac{1}{\Delta t} \frac{\partial^3 Z}{\partial \xi^3} \Big|_{i\pm 1/2,j,k} + \frac{\varepsilon_6}{8} \frac{1}{\Delta t} \frac{\partial^5 Z}{\partial \xi^5} \Big|_{i\pm 1/2,j,k} \quad (3.81)$$

where  $\varepsilon_2, \varepsilon_4, \varepsilon_6$  correspond to the coefficients of the second-, fourth- and sixth-order accurate artificial dissipation terms and in the present formulation,  $\Delta \xi = 1$ .

Even though the standard dissipation model has been proven to be reasonably effective in many cases, there are strong motivations for reducing the numerical dissipation being produced. Also, the standard model has difficulties in hypersonic flow and density stratified supercritical fluid with steep discontinuities as in the present case. A scalar dissipation model was constructed by Swanson and Turkel (1992) and by Jorgenson and Turkel (1993) to overcome the above difficulties. In their model

$$\mathbf{d}_{i+1/2,j,k} = \varepsilon_{i+1/2,j,k}^{(2)} \rho_{i+1/2,j,k}(\lambda) \frac{\partial Z}{\partial \xi} \Big|_{i+1/2,j,k} - \varepsilon_{i+1/2,j,k}^{(4)} \rho_{i+1/2,j,k}(\lambda) \frac{\partial^3 Z}{\partial \xi^3} \Big|_{i+1/2,j,k} \quad (3.82)$$

The modified eigenvalues are given as

$$\tilde{\lambda}_1 = \tilde{\lambda}_2 = \tilde{\lambda}_3 = \tilde{\lambda}_4 = \tilde{\lambda}_5 = \tilde{\lambda}_6 = \rho(\lambda) \quad (3.83)$$

where  $\rho(\lambda)$  is the spectral radius of the flux Jacobian matrix  $\Gamma^{-1} \mathbf{A}$ .

$$\varepsilon_{i+1/2,j,k}^{(2)} = \kappa^{(2)} \max(v_{i-1,j,k}, v_{i,j,k}, v_{i+1,j,k}, v_{i+2,j,k}) \quad (3.84)$$

$$v_{i,j,k} = \left| \frac{p_{i-1,j,k} - 2p_{i,j,k} + p_{i+2,j,k}}{p_{i-1,j,k} + 2p_{i,j,k} + p_{i+1,j,k}} \right| \quad (3.85)$$

$$\varepsilon_{i+1/2,j,k}^{(4)} = \max(0, (\kappa^{(4)} - \varepsilon_{i+1/2,j,k}^{(2)}) ) \quad (3.86)$$

$$\kappa^{(2)} = \frac{1}{4} \sim \frac{1}{2}, \quad \kappa^{(4)} = \frac{1}{64} \sim \frac{1}{32} \quad (3.87)$$

The second-difference dissipation term given in Eq. 3.82 is nonlinear. Its purpose is to introduce an entropy-like condition and to suppress oscillations in the neighborhood of shock discontinuities. This term is small in the smooth portion of the flow field. The switch  $v_{i,j,k}$  is important near discontinuities, since there are large pressure-gradients across them. For high-pressure fluid mixing and combustion, however, this switch is changed to include temperature- or density-gradients, as pressure may still be uniform across the boundary between different fluid layers. The fourth-order term is basically linear and is included to damp high-frequency modes and allow the scheme to approach a steady state. Only this term affects the linear stability of the scheme. Near discontinuities it is reduced to zero.

### 3.5 Temporal Discretization

The physical time derivatives in Eq. 3.67 are evaluated by general backward differencing

$$\frac{\partial Q}{\partial t} = \frac{1}{\Delta t} [a_1 Q^{m+1} - \phi(Q^n, Q^{n-1}, \dots)] \quad (3.88)$$

The coefficient  $a_1$  and function  $\phi$  in Eq. 3.88 can be specified to any level of temporal accuracy desired. In the current work, a three-point backward difference with second-order accuracy is employed. For this situation

$$a_1 = \frac{1}{2}, \quad \phi = \frac{1}{2}(4Q^n - Q^{n-1}) \quad (3.89)$$

The superscripts  $m$  and  $n$  denote iterations within the pseudo-time domain (inner-loop) and physical time domain (outer-loop), respectively. The physical time term  $Q^{m+1}$  can be linearized as

$$Q^{m+1} = Q^m + T\Delta Z^{m+1} \quad (3.90)$$

Substituting Eq. 3.88 and Eq. 3.90 into Eq. 3.67 yields the following discretized system

$$\begin{aligned} & \left\{ \Gamma + \frac{\Delta\tau}{\Delta t} T \right\} \Delta Z + (E_\xi - E_{\xi_v}) \Big|_{i-1/2,j,k}^{i+1/2,j,k} + (F_\eta - F_{\eta_v}) \Big|_{i,j-1/2,k}^{i,j+1/2,k} + \\ & (G_\zeta - G_{\zeta_v}) \Big|_{i,j,k-1/2}^{i,j,k+1/2} = H^{m+1} - \frac{\Delta\tau}{\Delta t} (a_1 Q^m - \phi) \end{aligned} \quad (3.91)$$

A fourth-order Runge-Kutta (RK-4) scheme is used to solve the governing equation 3.91 in the pseudo-time space due to its higher temporal accuracy and relatively larger CFL number (i.e.,  $2\sqrt{2}$  for an Euler calculation using RK-4). A thorough investigation of the stability characteristics of the RK4 method, based on convection of the turbulence energy-spectrum, has been performed by (Apt and Yang, 2001) to establish its creditability and accuracy. Using the four-stage Runge-Kutta scheme, each pseudo-time integration is completed through four consecutive intermediate steps, as given below

$$Z_0 = Z^m$$

$$\begin{aligned} Z_1 &= Z^m + \Delta Z_1, (\Gamma + \frac{\Delta\tau}{\Delta t} T - \Delta\tau D) \Delta Z_1 = \alpha_1 \Delta t \cdot R(Z_0) \\ Z_2 &= Z_1 + \Delta Z_2, (\Gamma + \frac{\Delta\tau}{\Delta t} T - \Delta\tau D) \Delta Z_2 = \alpha_2 \Delta t \cdot R(Z_1) \\ Z_3 &= Z_2 + \Delta Z_3, (\Gamma + \frac{\Delta\tau}{\Delta t} T - \Delta\tau D) \Delta Z_3 = \alpha_3 \Delta t \cdot R(Z_2) \\ Z^{m+1} &= Z_3 + \Delta Z^{m+1}, (\Gamma + \frac{\Delta\tau}{\Delta t} T - \Delta\tau D) \Delta Z^{m+1} = \Delta t \cdot R(Z_3) \end{aligned} \quad (3.92)$$

where

$$\begin{aligned} R(z) &= H^m - \frac{\Delta\tau}{\Delta T} (a_1 Q^m - \phi) - [ (E_\xi - E_{\xi_v}) ]_{i-1/2,j,k}^{i+1/2,j,k} \\ &\quad + (F_\eta - F_{\eta_v})_{i,j-1/2,k}^{i,j+1/2,k} + (G_\zeta - G_{\zeta_v})_{i,j,k-1/2}^{i,j,k+1/2} \end{aligned} \quad (3.93)$$

Superscripts ‘ $m$ ’ and ‘ $m+1$ ’ stand for the solution at the ‘ $m$ th’ and ‘ $m+1$  th’ pseudo-time steps, respectively. The coefficients  $\alpha_1$ ,  $\alpha_2$ , and  $\alpha_3$  can be varied to obtain a variety of schemes with different stability properties. The standard four-stage scheme has the following values (Jameson, 1983)

$$\alpha_1 = \frac{1}{4}, \alpha_2 = \frac{1}{3}, \alpha_3 = \frac{1}{2} \quad (3.94)$$

The iterative solution of given governing equation begins from pseudo-time iteration (inner-loop). At convergence in pseudo-time,  $Q^m = Q^{m+1} = Q^{n+1}$ , the solution is advanced one physical time step (outer-loop).

In order to enhance numerical efficiency and minimize the complexity arising from the irregular shape of the computational mesh, a curvilinear coordinate transformation of the

governing equations is employed so that the grid spacing in the transformed domain is unity. This is equally important for the use of spatial filtering in the LES technique. Non-uniform filter sizes directly violate the assumptions behind the filtering approach. One has to apply the numerical methodology in the body-fitted coordinate system.

### **3.6 Boundary Conditions**

In all cases considered, second-order accurate boundary conditions are implemented. The inlet and exit conditions are specified using the method-of-characteristics (MOC). Inviscid, adiabatic and noncatalytic conditions are imposed at the solid wall. Elsewhere conditions are specified using second order extrapolated values. These conditions produce zero normal gradients with respect to pressure, velocity, temperature, and species mass fraction.

#### **3.6.1 Characteristic Boundary Conditions**

At the inlet and outlet boundary, care must be taken when specifying the numerical boundary conditions. One has to ensure that the unphysical spurious wave reflections are avoided at the boundary and the flow is capable of relaxing to ambient conditions in the prescribed ways, which can be satisfied using the Method-of-Characteristics (MOC) proposed by Poinsot and Lele (1992). In the absence of a significant diffusion processes, the MOC method provides the correct number of conditions that must be specified, as well as conditioned information from the interior domain.

Implementation of the MOC procedure involves diagonalizing the governing system to a quasi one-dimensional characteristic form

$$[S + LM^{-1}\Gamma^{-1}(\Gamma + \frac{\Delta\tau}{\Delta t}T - \Delta\tau D)]\Delta Z = -LM^{-1}\Gamma^{-1} \left\{ (\frac{\partial E}{\partial x} + \frac{\partial F}{\partial y} + \frac{\partial G}{\partial z}) + \tilde{\Omega} + \frac{\Delta\tau}{\Delta t}(a_l Q^m - \phi) - H \right\} \quad (3.95)$$

All of the terms in Eq. 3.95 are evaluated at cell centroids using the finite difference methodology. The term  $\tilde{\Omega}$  is the vector of specified boundary conditions. The term L is a selection matrix that singles out the desired characteristics at respective boundaries. The Jacobian matrix S is defined as  $S = \frac{\partial \tilde{\Omega}}{\partial Z}$ .

In the absence of significant diffusion processes, the MOC procedure dictates the correct number of conditions that must be specified at each boundary and provides well conditioned information from the interior domain. In this study, the conditions imposed at the inlet and exit planes are always subsonic. At the inlet, there is one outgoing characteristic and N+3 conditions must be specified. Here the temperature, velocity, and species concentrations are employed assuming fully-developed turbulent channel flow. These conditions are given by

$$\tilde{\Omega}_{inlet} = \Delta V \begin{pmatrix} 0 \\ \tilde{u} - \tilde{u}_{ref} \\ \tilde{v} - \tilde{v}_{ref} \\ \tilde{w} - \tilde{w}_{ref} \\ \tilde{T} - \tilde{T}_{ref} \\ \tilde{Y}_1 - \tilde{Y}_{1_{ref}} \\ \vdots \\ \tilde{Y}_N - \tilde{Y}_{N-1_{ref}} \end{pmatrix} \quad L_{inlet} = \begin{pmatrix} 1 & 0 & 0 & 0 & 0 & 0 & \cdots & 0 \\ 0 & 0 & 0 & 0 & 0 & 0 & \cdots & 0 \\ 0 & 0 & 0 & 0 & 0 & 0 & \cdots & 0 \\ 0 & 0 & 0 & 0 & 0 & 0 & \cdots & 0 \\ 0 & 0 & 0 & 0 & 0 & 0 & \cdots & 0 \\ 0 & 0 & 0 & 0 & 0 & 0 & \cdots & 0 \\ 0 & 0 & 0 & 0 & 0 & 0 & \cdots & 0 \\ \vdots & \vdots & \vdots & \vdots & \vdots & \vdots & \ddots & \vdots \\ 0 & 0 & 0 & 0 & 0 & 0 & \cdots & 0 \end{pmatrix} \quad (3.96)$$

where  $\tilde{u}_{ref}$ ,  $\tilde{v}_{ref}$ ,  $\tilde{w}_{ref}$ ,  $\tilde{T}_{ref}$ ,  $\tilde{Y}_{1_{ref}}$ , ...,  $\tilde{Y}_{N-1_{ref}}$  represent the specified values of velocity, temperature, and species mass fraction, respectively. At the exit, there are N+3 outgoing characteristics and one condition must be specified. Here a far field pressure condition is

simulated using the methodologies proposed by Rudy and Strikwerda (1980), Poinsot and Lele (1992), and Baum et al. (1994).

To simulate the far field boundary the incoming characteristic given by Eq. 3.95 is modified to provide a nonreflecting outflow condition. The equation of interest is given by the selection matrix

$$L = \begin{pmatrix} 1 & 0 & 0 & 0 & 0 & 0 & \dots & 0 \\ 0 & 0 & 0 & 0 & 0 & 0 & \dots & 0 \\ 0 & 0 & 0 & 0 & 0 & 0 & \dots & 0 \\ 0 & 0 & 0 & 0 & 0 & 0 & \dots & 0 \\ 0 & 0 & 0 & 0 & 0 & 0 & \dots & 0 \\ 0 & 0 & 0 & 0 & 0 & 0 & \dots & 0 \\ 0 & 0 & 0 & 0 & 0 & 0 & \dots & 0 \\ \vdots & \vdots & \vdots & \vdots & \vdots & \vdots & \ddots & \vdots \\ 0 & 0 & 0 & 0 & 0 & 0 & \dots & 0 \end{pmatrix} \quad (3.97)$$

Associate with this equation is the term

$$\Pi_2 = \lambda_2 \left[ \frac{1}{\varepsilon} \frac{u - \lambda_2}{a} \frac{\partial p}{\partial x} - \rho a \frac{\partial u}{\partial x} \right] \quad (3.98)$$

which characterizes the time variation of the normal component of acoustic waves which propagate from an infinitely distant downstream source into the computational domain. The term  $\lambda_2$  is the acoustic eigenvalue given by Eq. 3.49. The terms  $p$  and  $u$  represent the pressure and axial velocity, respectively. Conceptually, a perfectly non-reflecting subsonic outflow condition can be obtained if this term is set equal to zero. Specifying such a condition, however, eliminates the information provided by the acoustic waves and leads to an ill-posed problem. To simulate this information Rudy and Strikwerda (1980), Poinsot and Lele (1992), and Baum, et al. (1994) have proposed that Eq. 3.98 be replaced with the term

$$\Pi_2^k = k(p - p_\infty) \quad (3.99)$$

where  $k$  is a constant that determines the speed with which the average pressure in the computational domain relaxes towards the imposed pressure at infinity  $p_\infty$ . This condition introduces small amplitude acoustic waves using scaling arguments that are based on known quantities at the exit. Rudy and Strikwerda (1980) propose that optimal values of  $k$  are given by Eq. 3.100

$$k = 2 \frac{\sigma}{x_c} \frac{\varepsilon a^2 (1 - \bar{M}^2)}{\sqrt{u(1 - \varepsilon)^2 + 4\varepsilon a^2}} \quad (3.100)$$

The factor presented here has been modified from that given by Rudy and Strikwerda (1980) to accommodate the dual-time preconditioned system. Here  $\bar{M}^2$  represents the maximum Mach number in the computational domain,  $x_c$  is the characteristic axial length of the domain,  $\varepsilon$  is the local preconditioning factor, and  $a$  is the local speed of sound. The term  $\sigma$  is a scaling factor used for optimization. Poinsot and Lele (1992), and Baum, et al. (1994) have shown that values ranging from 0.25 to 0.5 provide the best results. When lower values are specified, solutions tend to drift away from the reference pressure. When larger values are specified, flow oscillations are introduced.

To implement the MOC methodology with the far field pressure condition described above, the  $N+3$  outgoing characteristics are selected and the incoming characteristic is modified by replacing the incoming wave amplitude given by Eq. 3.98. These conditions are given by Eq. 3.101

$$\tilde{\Omega}_{outlet} = \Delta V \begin{pmatrix} p - p_{ref} \\ 0 \\ 0 \\ 0 \\ 0 \\ 0 \\ 0 \\ \vdots \\ 0 \end{pmatrix} \quad L_{outlet} = \begin{pmatrix} 0 & 0 & 0 & 0 & 0 & 0 & \cdots & 0 \\ 0 & 1 & 0 & 0 & 0 & 0 & \cdots & 0 \\ 0 & 0 & 1 & 0 & 0 & 0 & \cdots & 0 \\ 0 & 0 & 0 & 1 & 0 & 0 & \cdots & 0 \\ 0 & 0 & 0 & 0 & 1 & 0 & \cdots & 0 \\ 0 & 0 & 0 & 0 & 0 & 1 & \cdots & 0 \\ \vdots & \vdots & \vdots & \vdots & \vdots & \vdots & \ddots & \vdots \\ 0 & 0 & 0 & 0 & 0 & 0 & \cdots & 1 \end{pmatrix} \quad (3.101)$$

The far field pressure condition has been shown to be effective in reducing reflections at the subsonic exit boundary and is relatively accurate and stable.

### 3.7 Parallel Implementation

#### 3.7.1 Parallel Architecture

Every computer, whether sequential or parallel, operates by executing instructions on data. Depending on whether there is one or several instruction streams and data streams, the computing architecture can be classified into four categories (Flynn, 1972 ).

1. Single Instruction stream, Single Data stream (SISD)
2. Multiple Instruction streams, Single Data stream (MISD)
3. Single Instruction stream, Multiple Data stream (SIMD)
4. Multiple Instruction stream, Multiple Data stream (MIMD)

SISD computers are the standard sequential computer with single processor. In MISD computers, each processor has its own control unit, but they share a common memory. However, MISD machines are seldom used in practice. For SIMD computers, all processors operate under the control of a single instruction stream. TMC CM-200, MasPar, ICL DAP can be regarded as SIMD machines. However, the most widely used computing architecture is the MIMD system,

which is indicated schematically in Fig. 3.5. In this configuration, each processor has its own data set as well as a set of instructions to follow. These processors work independent of each other on these data sets and only communicate at some point during the computation where the data set and the results obtained are shared by two or more processors. MIMD-type computers include IBM SP-2, Cray T3E, CM5 and Beowulf Clustered computers.

For the SIMD or MIMD systems, it is usually necessary to exchange data between processors. This can be done in two ways: 1) shared memory systems, and 2) Distributed memory systems. The shared memory system consists of global address space, which is accessible by all processors and thus memory is shared among these processors. One processor can communicate with other processors by writing into or reading from the global memory. This architecture inherently solves the inter-processor communication problem, but introduces bottleneck problems created from simultaneous access to the memory by more than one processor. In the distributed memory systems, each processor has its own local (or private) memory and the global/shared memory is absent. The processors are connected externally to switches and a network of wires to allow communications among them. The efficiency of these systems is based on the communication time required among these processors, and enjoys several advantages such as hardware compatibility, functionality, and performance. The only drawback of this architecture is the enormous responsibility placed on software programmers. The programmers must provide an efficient scheme to distribute the data and set of instructions, and also explicitly provide the instruction set for communications among the various CPUs. This requires reconstruction of the numerical algorithm and synchronization of the processors for efficient, parallel computing.

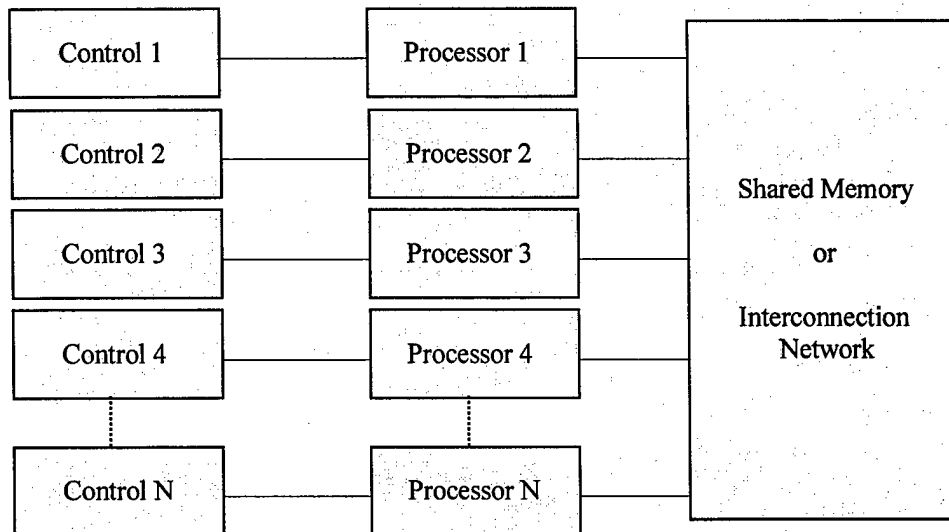


Fig. 3.5: Multiple instruction multiple data (MIMD) architecture (adopted from Apte, 2000)

### 3.7.2 Beowulf Cluster Parallel Computers

A Beowulf system is a multi-computer architecture used for parallel computations. In a Beowulf system, one server computer and many other client computers are connected together via high-speed networks. It is a distributed memory, MIMD system built primarily using commodity hardware components, such as any PC capable of running the free operating system Linux, standard Ethernet adapters, and switches. The first Beowulf system was built by Donald and Becker (1999) and consisted of 16 486DX4-100MHz machines each with 16 MB of memory. The main advantage of a Beowulf system is its high performance/price ratio in comparison with other dedicated MPP systems. Another important characteristic of the Beowulf clusters is compatibility. Changes of hardware, including the node and network system, will not affect the programming model. A Beowulf system also uses commodity software, such as the Linux operating system, Message Passing Interface (MPI), and other available open-source software.

The work conducted for this study was implemented on an in-house Beowulf system, consisting of 500 Pentium II/III processors, a Giga-Bit switch and 100MB fast Ethernet Cards. The operating system was RedHat Linux. The Message Passing Interface (MPI) involves a library of functions and macros that can be used in C, FORTRAN, and C++ Program were used to exchange the information among processors. More detailed information about this Beowulf system can be found in (Wang, 2002).

### 3.7.3 Domain Decomposition

Because the explicit time stepping numerical scheme (RK4) was applied in the current study, only the neighboring data instead of the data from the whole computational domain were required during the calculation of variables in each cell. Since the data dependence is weak, the domain decomposition technique is best suited for this kind of application. It is also commonly implemented in distributed-memory parallel computer systems. In the field of computational fluid dynamics (CFD), it is generally referred to as mesh partitioning, based on the geometric substructure of the computational domain. In the domain-decomposition technique, the physical domain is divided into several sub-domains. Variables in each cell are updated to the next time step simultaneously. In order to calculate the spatial derivatives at the sub-domain boundaries, ghost cells or halo data around the computing cells are introduced. Fig. 3.6 shows an example of a two-dimensional sub-domain with ghost cells. Because the variables in the ghost cell are updated in another sub-domain, message passing is required to synchronize data between different sub-domains. The communication overhead is directly proportional to the volume-to-surface ratio of the grid system in that sub-domain. Maximizing the computation-to-communication ratio leads to higher parallel execution efficiency.

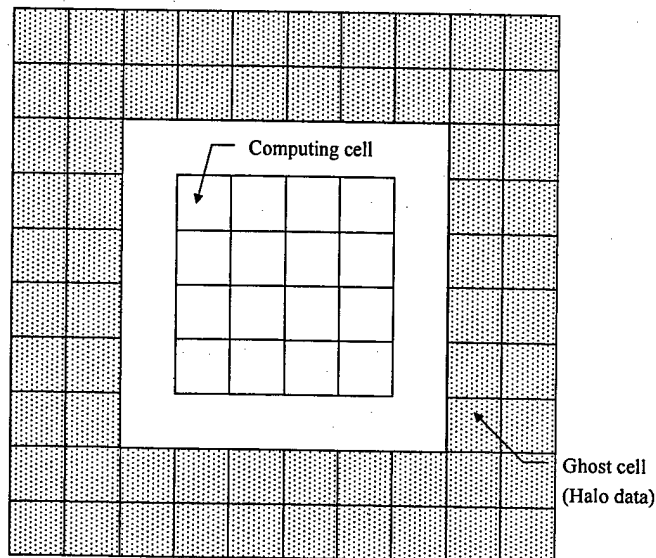


Fig. 3.6: Schematic of a two-dimensional sub-domain with ghost cells (adopted from Wang, 2002)

## Chapter 4

### Two-Dimensional Analysis of Supercritical Cryogenic Fluid Injection

#### 4.1 Problem Description

Substantial efforts have been applied to study fluid jets at low pressures in the past five decades. Three distinct flow regimes were commonly observed in a turbulent jet: a potential core, a transition region, and a fully developed self-similar region, as illustrated in Fig. 4.1. The potential core only contains the injected fluid and reduces in size as the jet mixes with the entrained ambient fluid. The flow properties along the centerline remain nearly constant in this region. Downstream of the potential core, there exists a transition region where turbulent mixing takes place. A fully developed self-similar region is reached further downstream, where the profiles of normalized flow properties collapse into single curves. For an incompressible gas jet, Schetz (1980) stated that the self-similar region appears at approximately  $x/D_{inj} \geq 40$ , whereas other studies (Abramovich, 1963) suggested a different location, as close as  $x/D_{inj} \geq 20$ . If those results, which were obtained at standard pressure and temperature, can be applied to high-pressure real-fluid regime, still need further study.

It is well known that thermodynamic non-idealities and transport anomalous, which occur at high-pressure and low-temperature regime, have significant influence on both the heat and mass transfer, and determine the flow evolution and dynamics in the real-fluid regime. To characterize supercritical fluid jet dynamics, cryogenic nitrogen fluid injection into supercritical gaseous nitrogen through a circular duct, simulating the experiments conducted by Chehroudi et al. (2002a, 2002b), were numerically investigated in this chapter. The model established in the preceding chapters, which could accommodate full conservation laws and real-fluid

thermodynamics and transport phenomena over the entire range of fluid states of concern, is applied. The present analysis allows a detailed investigation into the temporal and spatial evolution of a cryogenic jet. The salient features of supercritical real-fluid jet are well captured.

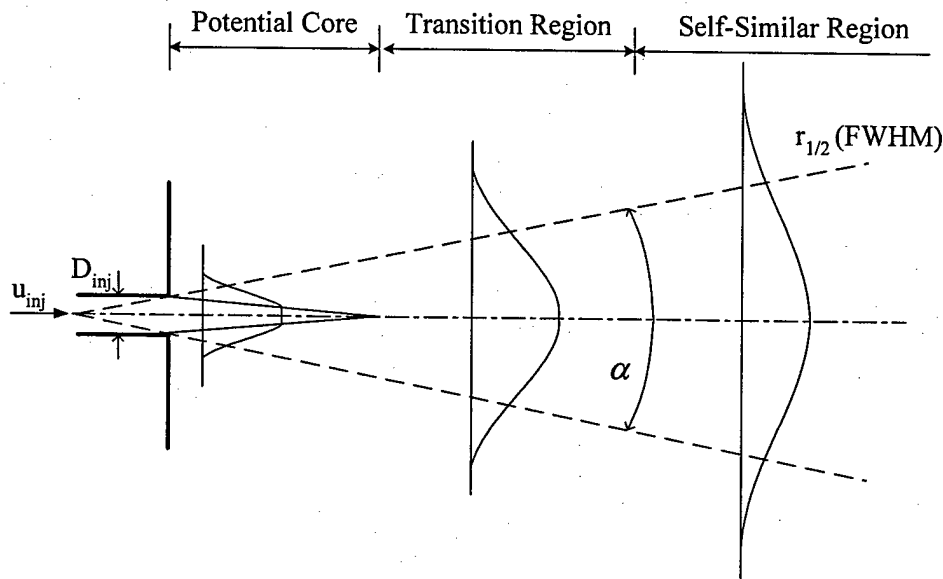


Fig. 4.1: Schematic of fluid jet.

The physical model of concern is shown schematically in Fig. 4.1. Cryogenic nitrogen fluid is injected into supercritical gaseous nitrogen through a circular duct with an inner diameter of 0.254 mm. Because of the enormous computational effort required for calculating the flowfield in the entire three-dimensional regime, only a cylindrical sector with periodic boundary conditions specified in the azimuthal direction is treated herein.

#### 4.2 Computational Domain and Grid System

The computational domain downstream of the injector measures a length of  $40 D_{inj}$  and a radius of  $6 D_{inj}$ . The dimensions are sufficient to minimize the effect of the far-field boundary conditions on the near-injector flow evolution. The entire grid system consists  $225 \times 90$  points

along the axial and radial directions, respectively. The grids are clustered in the shear-layer and near the injector to resolve rapid property variations in those regions. The mean grid size in the near field ( $0 \leq x/D_{inj} \leq 20$ ) falls in the inertial sub-range of the turbulent kinetic energy spectrum, estimated using the Kolmogorov-Obukhov theory. The smallest grid width is  $2 \mu\text{m}$ . For clarity, a system with one-fourth of the original grid density is shown in Fig. 4.2. The computational domain is divided into 45 blocks, with each calculated on a single processor of a distributed-memory parallel computer. The physical time step is  $1 \times 10^{-3}$  ms and the maximum CFL number for the inner-loop pseudo-time integration is 0.7. For each case, simulation was conducted for 12 flow-through times (i.e., 15 ms) to obtain statistically meaningful data.

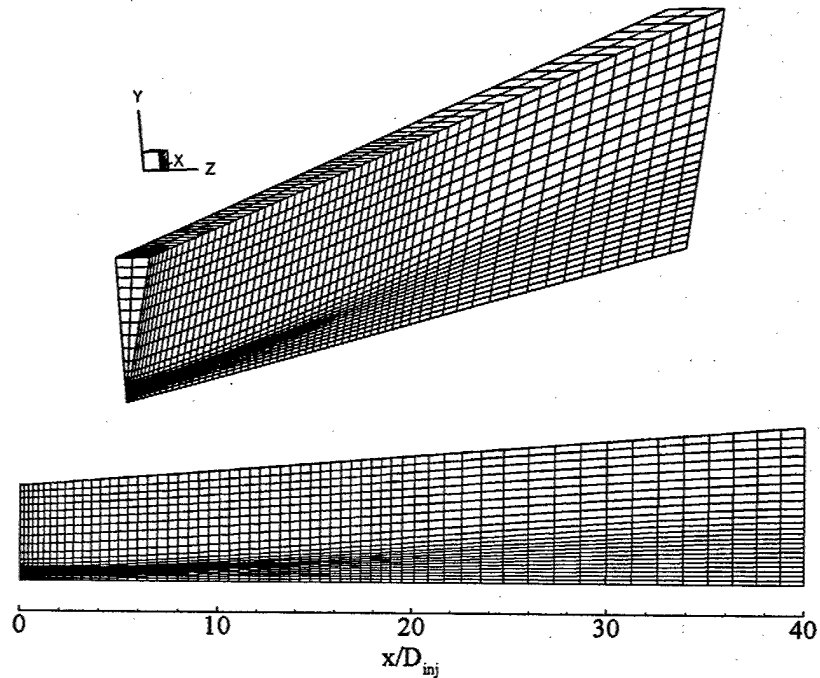


Fig. 4.2: Grid system employed in the computation (at one-fourth of the original grid density).

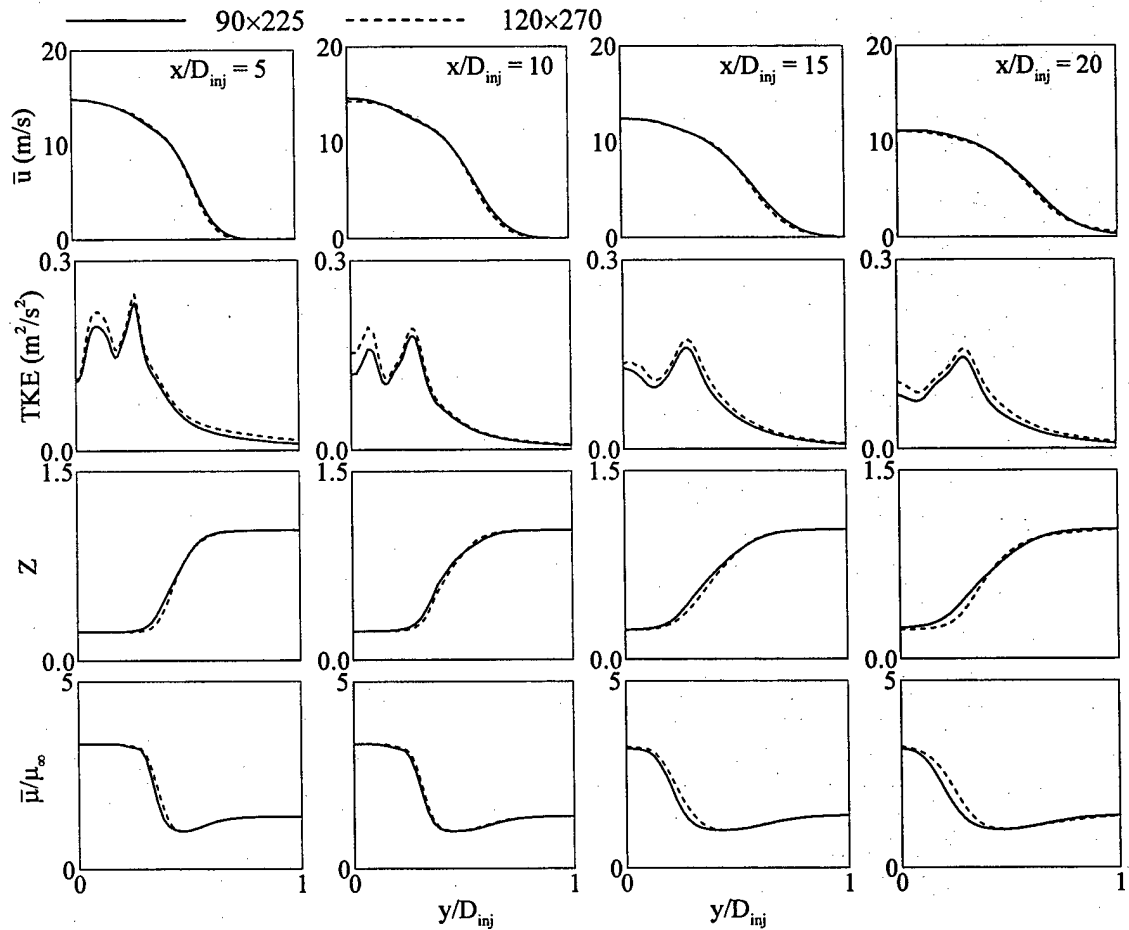


Fig. 4.3: Effect of grid resolution on radial distributions of mean axial velocity, turbulent kinetic energy, compressibility factor, and viscosity at different axial locations ( $p_{\infty} = 4.3 \text{ MPa}$ ,  $T_{\infty} = 300 \text{ K}$ ,  $u_{\text{inj}} = 15 \text{ m/s}$ ,  $T_{\text{inj}} = 120 \text{ K}$ ,  $D_{\text{inj}} = 254 \mu\text{m}$ ).

A grid independence study was performed as part of the validation procedure, in which the same numerical code, configuration, and flow condition (i.e. Case 1 in Table 1) were considered with two different grid resolutions: a fine ( $270 \times 120$ ) and a coarse ( $225 \times 90$ ) mesh. Figure 4.3 shows the radial distributions of the mean axial velocity, turbulent kinetic energy (TKE), compressibility factor Z, and viscosity (normalized by the value of the ambient gas) at different axial locations. Results from the two different grid systems agree well with each other, except for the small deviation of TKE.

### 4.3 Boundary Conditions

At the injector exit, a fully developed turbulent pipe flow is assumed. The mean velocity follows the one-seventh-power law and the temperature is specified with a top-hat profile. The pressure is determined using a one-dimensional approximation to the momentum equation in the axial direction. Turbulence is provided by superimposing broad-band white noise onto the mean velocity profile. The disturbances are generated by a Gaussian random-number generator with an intensity of 12% of the mean quantity. At the downstream boundary, extrapolation of primitive variables from the interior may cause undesired reflection of waves propagating into the computational domain. Thus, the non-reflecting boundary conditions proposed by Poinsot and Lele (1992) are applied, along with the specification of a reference pressure. Because the jet flow is directly exhausted to an ambient condition, the surrounding fluid may be entrained into the computational domain. At the radial boundary, the pressure, temperature, and axial velocity are specified. The conservation law of mass is employed to determine the radial velocity. Finally, the non-slip adiabatic conditions are enforced along the solid walls.

### 4.4 Results and Discussion

The theoretical model and numerical scheme established in the preceding sections were implemented to study the injection and mixing of cryogenic fluid under supercritical conditions. As a specific example, liquid nitrogen at a temperature of 120 K is injected through a circular tube with a diameter of 254  $\mu\text{m}$  into a supercritical nitrogen environment. A turbulent pipe flow with a bulk velocity of 15 m/s is assumed at the injector exit. The ambient temperature remains at 300 K, but the pressure varies from 42 to 93 atm, comparable to the chamber pressures of many operational rocket engines. For reference, the critical temperature and pressure of nitrogen are

126 K and 34 atm, respectively. Three different flow conditions summarized in Table 4.1 are considered, simulating the experiments conducted by Chehroudi and Talley (2002), where the subscripts  $\infty$  and  $inj$  denote the injection and ambient conditions, respectively. The Reynolds number is defined as  $Re = \rho_{inj} u_{inj} D_{inj} / \mu_{inj}$ .

Table 4.1: Simulation Conditions

	Case 1	Case 2	Case 3
$P_\infty$ (MPa)	4.3	6.9	9.3
$T_\infty$ (K)	300	300	300
$\rho_\infty$ (kg/m <sup>3</sup> )	46	77	103
$T_{inj}$ (K)	120	120	120
$\rho_{inj}$ (kg/m <sup>3</sup> )	563	603	626
$u_{inj}$ (m/s)	15	15	15
$\rho_{inj}/\rho_\infty$	12.24	7.83	6.07
Re	48500	44700	42300

Figure 4.4 shows the variations of nitrogen density and constant-pressure specific heat as functions of temperature at four different pressures. Two observations are noted here. First, the density decreases sharply near the critical point as the temperature increases. The effect of density stratification between the jet and the ambient fluid becomes much more substantial for  $p_\infty = 4.3 \text{ MPa}$  compared with the other two cases. Second, the temperature sensitivity of the specific heat depends strongly on pressure. It increases rapidly as the fluid state approaches the critical point, and theoretically becomes infinite exactly at the critical point. This implies that much more thermal energy is needed to heat up the cold fluid jet in Case 1 (i.e.,  $p_\infty = 4.3 \text{ MPa}$ ) than the other two cases when the fluid temperature transits across the near-critical regime. The anomalous variations of fluid volumetric and thermal properties near the critical point and their dependence on pressure have profound influences on fluid jet development at high pressures.

#### 4.4.1 Instantaneous Flowfield

For a constant-density jet, the shear-layer between the jet and the ambient fluid is susceptible to the Kelvin-Helmholz instability and experiences vortex rolling, paring, and breakup. A cryogenic supercritical jet undergoes qualitatively the same process, but with additional mechanisms arising from volume dilation and baroclinic torque.

Figure 4.5 shows snapshots of the density, density-gradient, temperature, and vorticity-magnitude fields at three different ambient pressures. The small vortical structures in the core region result from the imposed turbulent motions at the injector exit. For Case 1, in which the ambient pressure of 4.3 MPa is closer to the critical value, the jet surface is straight near the injector with only tiny instability waves in the downstream region. As the ambient pressure increases, the velocity fluctuation in the radial direction becomes more vigorous. Large-scale instability waves develop in the near-injector region, which then grow up and roll into a succession of ring vortices as the injected fluid moves downstream. The resultant vortical flow motions facilitate the entrainment of the ambient gaseous nitrogen into the cold jet fluid. The initial density-stratification layer is only slightly stretched in Case 1, but severely twisted in higher-pressure cases. As a general trend, the higher the ambient pressure, the stronger vortical motions and radial velocity fluctuations near the jet surface.

It has been established that the evolution and interaction of large coherent structures strongly influence the mixing and entrainment of a shear-layer (Crow and Champagne, 1971).

Figure 4.6 shows the temporal evolution of the jet surface structures of Case 3 ( $p_{\infty} = 9.3 \text{ MPa}$ ). Both the temperature and density fields clearly demonstrate the entrainment of lighter and warmer ambient gaseous nitrogen into the jet flow through vortical motions, along with a series of thread-like entities emerging from the jet surface. The same phenomena were observed in the experiments by Chehroudi and co-workers (2002) under the same flow condition.

#### 4.4.2 Effect of Density Stratification

To explore the formation and influence of the density-stratification layer near the jet boundary, conditional-averaged temperatures over the regions where the density-gradient magnitudes exceed pre-specified cutoff values are determined. The result is listed in Table 4.2, where  $|\nabla \rho|_{\max}$  is the maximum density gradient in the entire field, around  $1.15 \times 10^7 \text{ kg/m}^4$  for Case 3. The conditional fluid temperature decreases with increasing cutoff density-gradient, and approaches the inflection point on the isobaric  $\rho - T$  curve shown in Fig. 4.4. Table 4.3 summarizes the inflection temperatures for the three different pressures considered herein. It is noteworthy that fluid properties usually undergo rapid variations across the temperature inflection point for an isobaric process, and the specific heat reaches its maximum at this point. For example, the density of nitrogen decreases more than three times in Case 1 as the temperature increases from 125 to 135 K. Thus, the formation of the steep density-gradient region is closely related to property variations, which to a large extent are dictated by real-fluid thermodynamics. Turbulent diffusion and mixing tend to introduce warm ambient gases into the cold jet, and subsequently smooth the density-stratification effect. The drastic volume dilation during the mixing process when the temperature transits across the inflection point, however, prevents the entrainment of the surrounding fluid, and thereby facilitates the formation of steep density-gradient regimes.

Table 4.2: Conditional averaged temperatures (K) in regions with  $|\nabla \rho| >$  cutoff value.

Cutoff	Case 1	Case 2	Case 3
$0.1 \cdot  \nabla \rho _{\max}$	131.7	151.0	158.0
$0.2 \cdot  \nabla \rho _{\max}$	131.1	148.0	154.0
$0.3 \cdot  \nabla \rho _{\max}$	130.6	145.5	151.3

Table 4.3: Temperatures at inflection points on isobaric  $\rho - T$  curves at different pressures

	Case 1	Case 2	Case 3
$p_\infty$ (MPa)	4.3	6.9	9.3
T (K)	130.3	142.1	148.6

The effect of density stratification on the evolution of a planar mixing layer was studied by Atsavapranee and Gharib (1997). Because the higher density stratification increasingly inhibits instability-wave growth and vortex paring, the flow topography is considerably simplified, as evidenced in Fig. 4.5. In addition, the total yield of mixed fluid is reduced with high density stratification due to the combined effect of weakened fluid entrainment into the Kelvin-Helmholtz vortices, decreased frequency of vortex paring, and arrest of turbulence during flow restratification.

Figure 4.7 shows the power spectral densities (PSD) of the axial and radial velocity fluctuations at various radial locations of  $r/D_{inj} = 0.6, 0.7$ , and  $0.8$  in the mixing layer for  $p_\infty = 9.3 \text{ MPa}$ . The axial position of  $x/D_{inj} = 16$  is near the end of the potential core, where a sharp density gradient exists at  $r = 0.1 D_{inj}$  (see Fig. 4.5). In the low-frequency regime, in which large-scale structures prevail, the axial velocity fluctuation increases as the density stratification layer is approached. The trend for the radial velocity fluctuation, however, is opposite. The velocity fluctuations in the high-frequency range remain basically insensitive to the radial position. Density stratification exerts a strong influence on large-scale flow motions. It acts like a solid wall in the flow that amplifies the axial turbulent fluctuation but damps the radial one. The same PSD results are also observed for Cases 1 and 2, which are not presented here.

A similar phenomenon was reported by Hannoun et al. (1988) in their experiments on grid-induced shear-free turbulence near a sharp density interface. As a consequence of the strong

anisotropy of the turbulence near the density interface, large eddies of integral length scales become flattened, and the vertical component of the turbulent kinetic energy is transferred to its horizontal quantity. Such an energy redistribution among its spatial components considerably modifies the amount of energy available for fluid mixing at the density interface. Thus, the existence of strong density stratification suppresses radial velocity fluctuations in the flowfield and inhibits the development of instability waves. In the present study, the initial density ratio and the strength of density stratification decrease as the ambient pressure increases, so do their damping effects on the shear-layers. The jet surface is nearly straight in Case 1, with only tiny instability waves developing in the downstream region. The shear-layers, however, are highly twisted in both Cases 2 and 3, as shown in Fig. 4.5.

The frequency spectra of velocity fluctuations shown in Fig. 4.7 do not indicate the standard  $5/3$  law for the turbulent kinetic energy spectrum based on the Kolmogorov theory, which characterizes the inertial subrange. Apte and Yang (2001) mentioned in their two-dimensional simulations of unsteady flow evolution in a porous-walled chamber that the exponent of the wave number in the inertial subrange of the turbulent energy spectrum varies between  $f^{-3}$  and  $f^{-4}$ , with  $f$  being the frequency. Gilbert (1988) proposed that the kinetic energy spectrum can be obtained from spiral vortex distributions within coherent vortices and should follow the  $f^{-11/3}$  law. In this work, the frequency dependence in the inertial subrange lies between  $f^{-5/3}$  and  $f^{-3}$ .

The present two-dimensional large-eddy simulation inherently neglects the vortex stretching mechanism, which is responsible for the transfer of energy from large to small scales through energy cascade and the continuous generation of small-scale vortical structures. Since these structures redistribute and dissipate energy at the smallest scales, the lack of vortex

stretching leads to lower energy-dissipation and turbulence-production rates during the flow evolution. This issue will be addressed in subsequent three-dimensional calculations.

#### 4.4.3 Shear-Layer Instability

To study the vortical dynamics and flow instability in the mixing layer, the power spectral densities of the radial velocity oscillations at two different axial locations are presented in Fig. 4.8. The radial position is fixed at  $r/D_{inj} = 0.5$ . A dominant frequency around 35 kHz, corresponding to the most amplified frequency of the shear layer instability, is observed at an upstream location of  $x/D_{inj} = 8$  for both Cases 2 and 3. This frequency is weakly dependent on the ambient pressure (or the density ratio). When the fluid is convected downstream to  $x/D_{inj} = 18$ , the dominant frequency decreases to 15.9 kHz for Case 2 and 18.6 kHz for Case 3, nearly one half of the value of the most amplified shear instability mode. The vortex pairing process is clearly demonstrated. The situation with Case 1, however, is considerably different. Owing to the low compressibility factor (i.e. 0.21) of the injected fluid and the large density ratio of 12.24, the jet exhibits a liquid-like fluid behavior distinct from the other high-pressure cases. The dominant frequencies become 20 and 10 kHz at  $x/D_{inj} = 8$  and 18, respectively.

The flow instabilities and vortex shedding in constant-density shear layers were reviewed by Schadow and Gutmark (1992). Based on their work, the initial vortex shedding frequency,  $f_1$ , can be scaled with the shear-layer momentum thickness  $\theta_0$  and a characteristic velocity  $\bar{U}$ , normally taken as the average bulk velocity of the two streams. The result yields a non-dimensional frequency or Strouhal number,  $St_i = f_i \theta_0 / \bar{U}$ , which ranges from 0.044 to 0.048 for a planar turbulent shear layer. As the vortices move downstream, they merge together to oscillate at the sub-harmonics of the initial vortex shedding frequency,  $f_i/N$  ( $N = 2, 3, 4, \dots$ ).

Although the above analysis was formulated for planar flows, it can be applied with good accuracy to mixing layers in axisymmetric configurations if the thickness of the shear layer is much smaller than the radius of the injector. In the present work,  $\bar{U} \approx 8 \text{ m/s}$  and the initial momentum thickness  $\theta_0$  estimated for a fully developed turbulent pipe flow is 0.011 mm. If the strouhal number is chosen to be  $St_i = 0.048$ , then the most amplified frequency becomes  $f_1 = 34.9 \text{ kHz}$  and the corresponding second harmonic frequency is 17.5 kHz. Those values agree well with the calculated vortex-shedding frequencies based on the radial velocity oscillations in Cases 2 and 3.

To provide more insight into observed flow phenomena, a linear stability analysis is carried out of the effects of ambient pressure on the fluid jet evolution. The work extends the approaches described by Yu and Monkewitz (1990) and Soteriou and Ghoniem (1995) to include real-fluid thermodynamics. The SRK equation of state is implemented in the formulation. Each dependent variable is decomposed into a base and a perturbation quantity. The former is adopted directly from the present simulation. The latter takes the following general form for a planar jet

$$\hat{\phi}(x, y, t) = \phi(y) \exp\{i(kx - \omega t)\} \quad (4.1)$$

where  $k$  and  $\omega$  are the wave number and frequency, respectively. For a spatial instability problem,  $k$  is a complex variable and its negative imaginary part represents the spatial growth rate. After substitution of the decomposed variables into the conservation laws and linearization of the result, a dispersion equation characterizing the relationship between the wave number and frequency can be derived in terms of pressure fluctuation as follow

$$\frac{d^2 \hat{p}}{dy^2} - \left( \frac{1}{\bar{\rho}} \cdot \frac{d\bar{\rho}}{dy} + \frac{2}{\bar{u} - \omega/k} \frac{d\bar{u}}{dy} \right) \frac{d\hat{p}}{dy} - k^2 \hat{p} = 0 \quad (4.2)$$

The problem now becomes solving Eq. 4.2 for the eigenvalues  $k$  and  $\omega$  subject to appropriate boundary conditions. A complete discussion of the stability analysis is given by Liu et al. (2004).

Figure 4.9 shows the spatial growth rates of the instability waves as a function of the normalized frequency (i.e., the Strouhal number) for the three different pressures considered in the present study. The growth rate of the shear wave decreases with increasing pressure. The strong density stratification in the lower pressure case suppresses the growth of the wave and stabilizes the mixing layer. The theoretically predicted frequencies of the most unstable oscillations are 23.2, 28.8 and 29.6 KHz for Cases 1, 2, and 3, respectively. These values are slightly underestimated for Cases 2 and 3, but overestimated for Case 1. The maximum deviation from the numerical simulation is 15%. The frequency of the most unstable mode exhibits a weak pressure dependence at high pressures. It, however, decreases significantly in the near-critical regime due to the enhanced effect of density stratification and increased mixing-layer momentum thickness.

#### 4.4.4 Vortical Dynamics

As a consequence of the large velocity difference between the jet and ambient flow, a strong shear-layer is generated near the injector, which is then tilted and develops to large structures due to vortex interactions. The vortical dynamics can be best quantified using the transport equation given below

$$\frac{D\boldsymbol{\omega}}{Dt} = (\boldsymbol{\omega} \cdot \nabla) \mathbf{u} - (\nabla \cdot \mathbf{u}) \boldsymbol{\omega} - \nabla \left( \frac{1}{\rho} \right) \times \nabla p + \nabla \times \left( \frac{1}{\rho} \nabla \cdot \boldsymbol{\tau} \right) \quad (4.3)$$

where  $D/Dt$  stands for the substantial derivative. The first term on the right-hand side represents vortex stretching, which vanishes in the present two-dimensional simulation. The second term describes the volume-dilatation effect, and the third term denotes the baroclinic torque produced by the misalignment between the pressure and density gradients. The last term arises from viscous dissipation. For cryogenic fluid injection under supercritical conditions, large volume expansion occurs when the jet is heated by the ambient gas. Thus, both baroclinic torque and volume dilatation may play an important role in determining vorticity transport.

Figure 4.10 shows an instantaneous azimuthal vorticity budget in the radial direction at the axial position of  $x/D_{inj} = 5$  for all the three cases. At this position, the large coherent structures are well developed in Cases 2 and 3. The results are normalized by the bulk velocity ( $u_{inj}$ ) and momentum thickness ( $\theta_0$ ) at the injector exit. The baroclinic torque and viscous dissipation locally rival in magnitude, and have opposite contributions in Eq. 4.3. These two terms attain their maxima in regions with large density gradients in which vigorous mixing between the jet and ambient flows occurs (see Fig. 4.5). In Case 1, much of the vorticity production takes place on the light fluid side. A similar phenomenon was noted by Okong'o and Bellan in their study of a supercritical binary mixing layer. As the ambient pressure increases (or the density ratio decreases), the location with intensive vorticity production slightly shifts toward the dense fluid, but still resides on the ambient gas side, since the radial position of the mixing region also changes. The magnitudes of all the three vorticity production terms increase with increasing ambient pressure due to strengthened vortical motions.

#### 4.4.5 Mean Flow Properties

The mean flow properties are obtained by taking long-time average of the instantaneous quantities over 10 ms (about 8 flow-through times) after the calculated flowfield has reached its stationary state. Figure 4.11 shows the radial distributions of the normalized mean density,  $\rho^+ = (\bar{\rho} - \bar{\rho}_\infty) / (\bar{\rho}_c - \bar{\rho}_\infty)$ , at six different axial locations. The subscript  $c$  refers to the quantity at the centerline. The radial coordinate is normalized by the full width of the radial profile measured where the flow property of concern (i.e., density in the present figure) is one half of its maximum value (FWHM),  $r_{1/2}$ . Similar to incompressible fluid jets, there exist three distinct regions in a cryogenic fluid jet under supercritical conditions: a potential core in the upstream where a flat-hat distribution around the centerline occurs, a transition region, and a fully developed self-similar region. The density profiles at  $x/D_{inj} > 25$  merge to a single distribution for Cases 2 and 3, manifesting the existence of self-similarity in the downstream region. Such a self-similar profile, however, is not observed until  $x/D_{inj} > 30$  for Case 1. The high-pressure condition facilitates the development of the self-similar behavior through its effect on reducing the density ratio of the injected fluid to the ambient flow.

Figure 4.12 shows the normalized axial velocity profiles in the radial direction. Self-similarity is achieved at the same location as that for the density distribution. It occurs at a relatively upstream position as the ambient pressure increases. Compared with the density field, the velocity profile exhibits a narrower distribution, with the jet boundary (defined as the radial position at which  $u = 0.01u_c$ ) situated at  $r/r_{1/2} \approx 2.5$ , a value consistent with the data reported by Branam and Mayer (2003). In addition, no flat-hat profile exists even in the upstream region due to the use of the one-seventh power distribution for a fully developed turbulent pipe flow at the injector exit.

Figure 4.13 presents the axial distributions of the normalized temperature, density and compressibility factor along the centerline for three different pressures. Evidently, the temperature decreases relatively slowly with decreasing pressure in the axial direction. It is well established that when a fluid reaches its thermodynamic critical state, the constant-pressure specific heat becomes infinite and the thermal diffusivity decreases to zero, a phenomenon known as the critical divergence. Because the ambient pressure for Case 1 ( $p_\infty = 4.3 \text{ MPa}$ ) is closer to the critical value, the specific heat increases drastically when the temperature transits across the inflection point on the isobaric  $\rho$ - $T$  curve (see Fig. 4.4). This effect, combined with the lower thermal conductivity, causes a slower increase in temperature along the centerline in Case 1 as the injected fluid moves downstream. The compressibility factor indicates a monotonic decrease with decreasing pressure in the low-temperature regime, and a rapid increase across the inflection point on the isobaric  $\rho$ - $T$  curve. The compressibility factor, thus, increases much more rapidly at a lower pressure, which amounts to a faster decrease in density. Although the centerline temperature varies laggardly in all the three cases, the rapid variation of the compressibility factor causes the density to undergo a fast decrease downstream of the potential core, especially for the case of  $p_\infty = 4.3 \text{ MPa}$ .

The rapid variations of thermophysical properties exert a significant influence on the jet flow evolution. Fig. 4.14 shows the radial distributions of the specific heat, thermal diffusivity, and kinematic viscosity at  $x/D_{inj} = 10$ , a location slightly upstream of the end of the potential core. A spike exists in the specific-heat profile at  $r/r_{1/2} = 0.6$  in Case 1, mainly due to the temperature transition across the inflection point. The same phenomenon is observed for Cases 2 and 3, but with much lower amplitudes. The thermal diffusivity also exercises a large excursion of variation across the temperature inflection point. It increases considerably from the liquid core to the ambient flow by a factor of 14, 7, and 5 in Cases 1, 2, and 3, respectively. A similar

situation occurs with the kinematic viscosity. The intensive change of viscosity in the shear-layer gives rise to another vorticity production mechanism, as shown in Eq. 4.3. These observations, again, highlight the importance of thermophysical properties in dictating the behavior of a supercritical fluid jet.

#### 4.5 Summary

A two-dimensional numerical study has been conducted to investigate cryogenic fluid injection and mixing under supercritical conditions. The model accommodates full conservation laws and real-fluid thermodynamics and transport phenomena over the entire range of fluid states of concern. Turbulent closure is achieved using a large-eddy-simulation technique. The present analysis allows a detailed investigation into the temporal and spatial evolution of a cryogenic jet. The near-field behavior is well captured.

The major results obtained are summarized below.

1. As a result of intensive property variations between the fluid jet and surroundings, a series of large density-gradient regions are formed around the jet surface. These regions act like a solid wall that amplifies the axial flow oscillations but damps the radial ones. The interfacial instability in the shear layer is effectively suppressed, especially for cases with large density ratios. As the ambient pressure increases, the strength of density stratification decreases, so does its damping effect. Thus, the jet expands rapidly with increasing pressure.
2. Various mechanisms dictating vorticity transport are analyzed. The baroclinic torque arising from the density stratification between the injected and ambient flows and viscous dissipation play an important role in determining the flow evolution.
3. The jet dynamics are largely dictated by the local thermodynamic state of the fluid. When the temperature transits across the inflection point in an isobaric process, the rapid property

variations may qualitatively change the jet behavior compared with its counterpart at low pressures. In addition, an increase in the ambient pressure may result in an earlier transition of the jet into the self-similar region.

4. The spatial growth rate of the surface instability wave increases as the ambient pressure increases. The frequency of the most unstable mode exhibits a weak pressure dependence at high pressures. It, however, decreases significantly in the near-critical regime due to the enhanced effect of density stratification and increased mixing-layer momentum thickness. The result agrees well with the linear stability analysis.

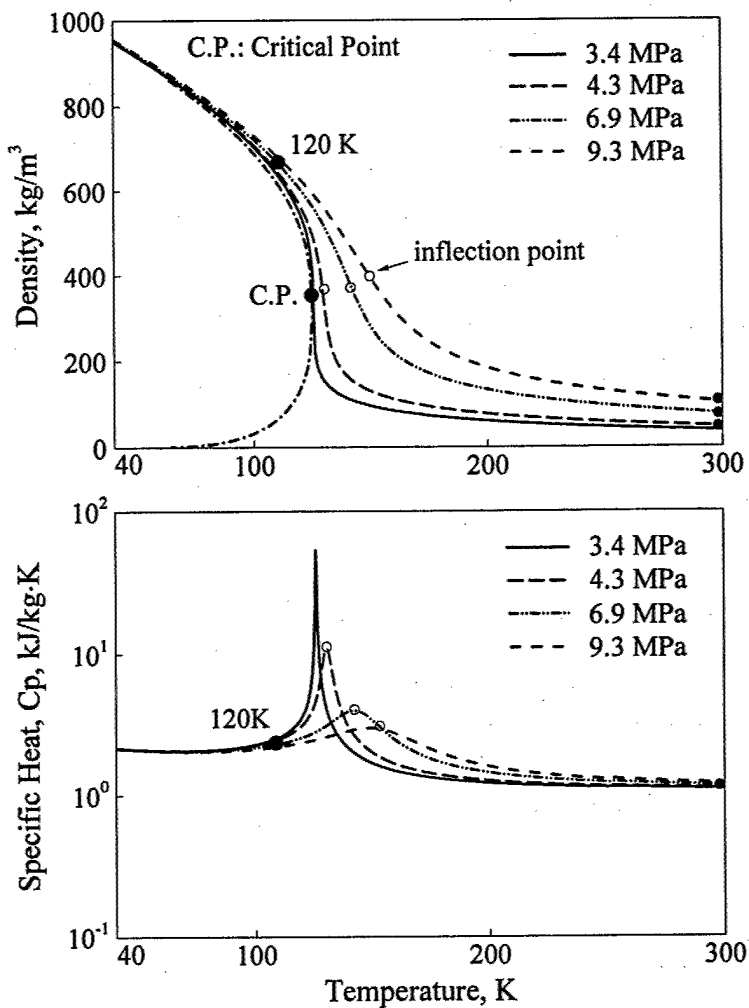


Fig. 4.4: Density and constant-pressure specific heat of nitrogen as the functions of temperature and pressure.

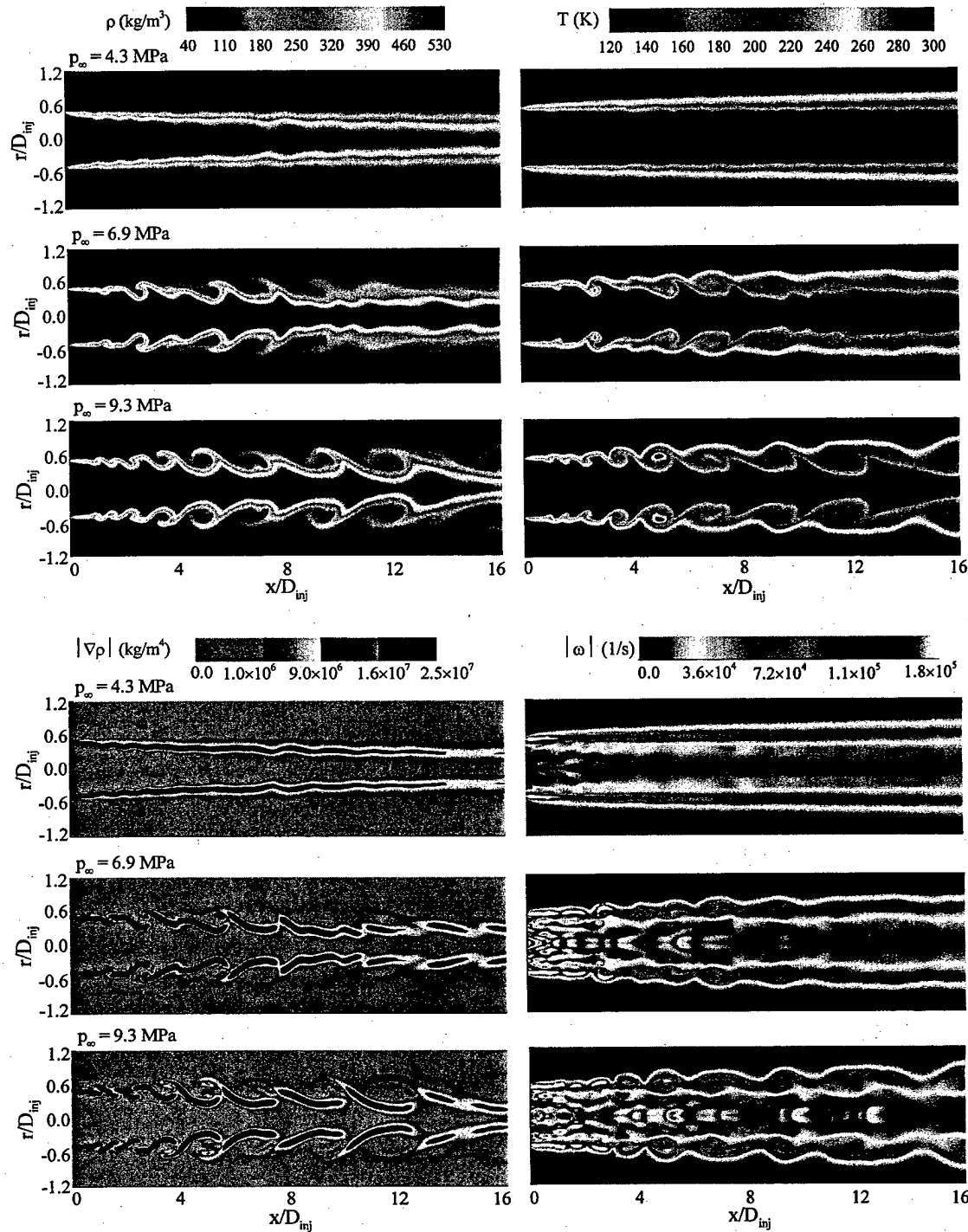


Fig. 4.5: Effect of pressure on density, density gradient, temperature and vorticity fields ( $T_\infty = 300 \text{ K}$ ,  $u_{\text{inj}} = 15 \text{ m/s}$ ,  $T_{\text{inj}} = 120 \text{ K}$ ,  $D_{\text{inj}} = 254 \mu\text{m}$ ,  $t = 1.55 \text{ ms}$ ).

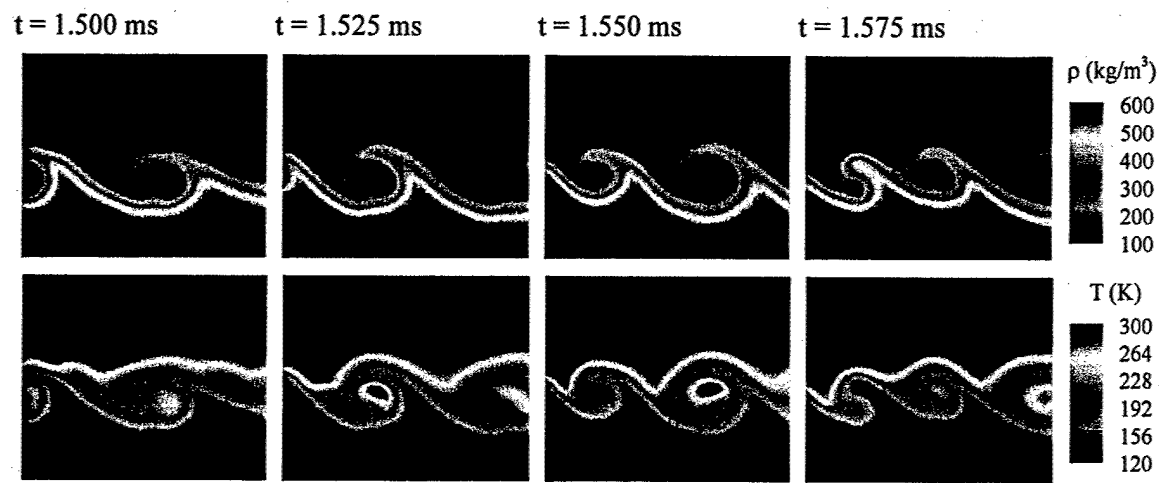


Fig. 4.6: Time evolution of jet surface structures ( $p_\infty = 9.3 \text{ MPa}$ ,  $T_\infty = 300 \text{ K}$ ,  $u_{\text{inj}} = 15 \text{ m/s}$ ,  $T_{\text{inj}} = 120 \text{ K}$ ,  $D_{\text{inj}} = 254 \mu\text{m}$ ).

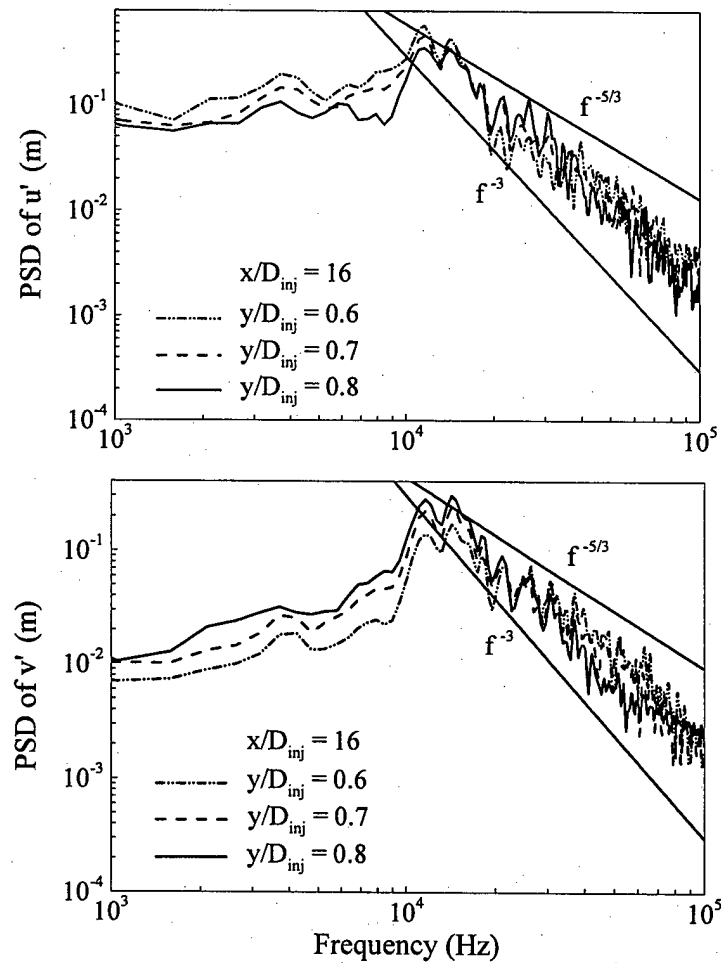


Fig. 4.7: Power spectral densities of velocity fluctuations at different radial locations with  $x/D_{inj} = 16$  ( $p_\infty = 9.3$  MPa,  $T_\infty = 300$  K,  $u_{inj} = 15$  m/s,  $T_{inj} = 120$  K,  $D_{inj} = 254$   $\mu\text{m}$ ).

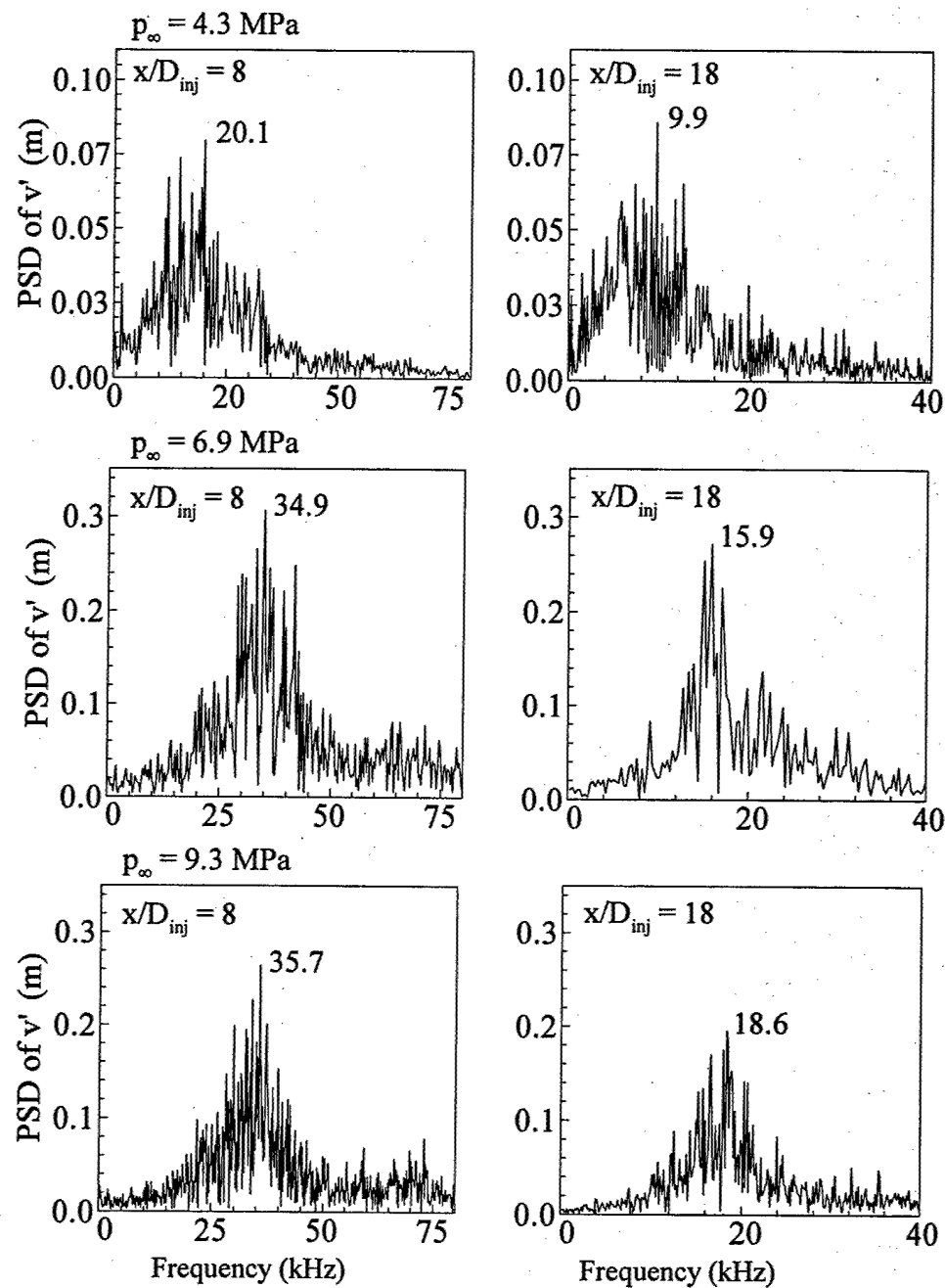


Fig. 4.8: Effect of pressure on power spectral densities of radial velocity fluctuations at two different axial locations with  $r/D_{\text{inj}} = 0.5$ .

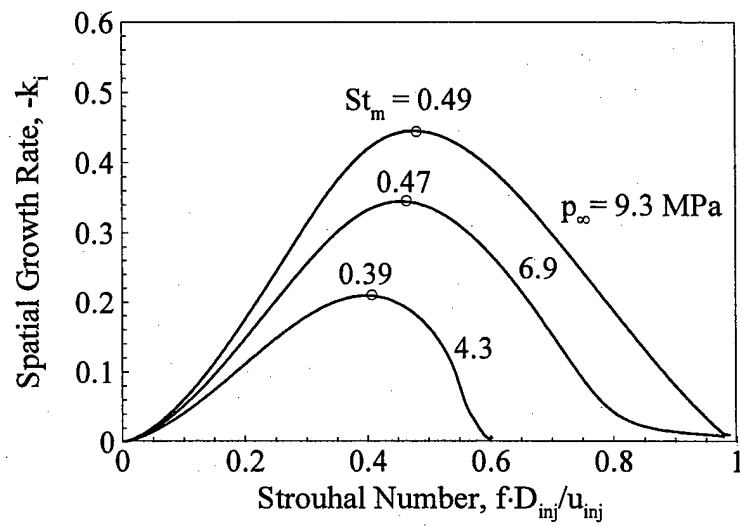


Fig. 4.9: Spatial growth rate as function of Strouhal number at different pressures.

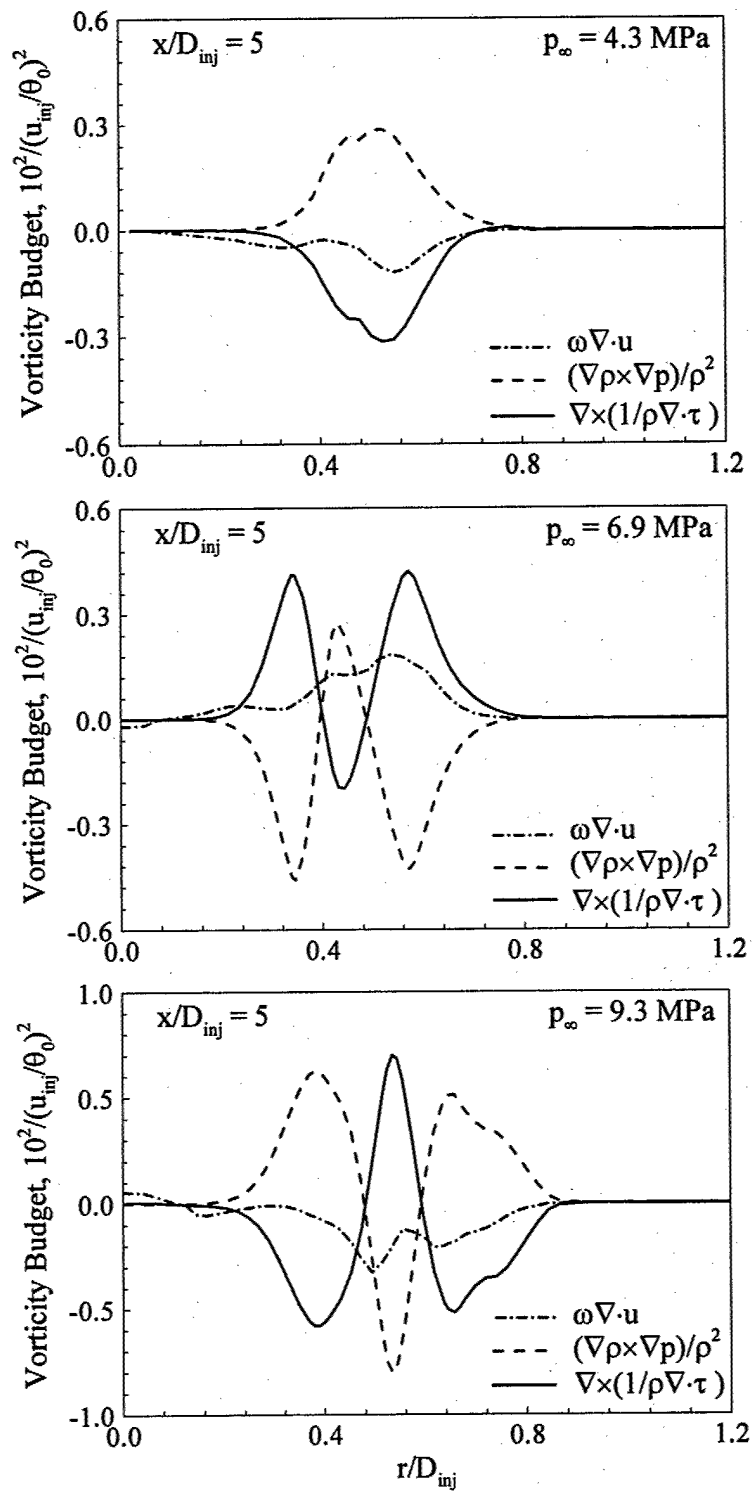


Fig. 4.10: Vorticity budgets at different ambient pressures ( $T_\infty = 300 \text{ K}$ ,  $u_{inj} = 15 \text{ m/s}$ ,  $T_{inj} = 120 \text{ K}$ ,  $D_{inj} = 254 \mu\text{m}$ ,  $t = 1.55 \text{ ms}$ ).

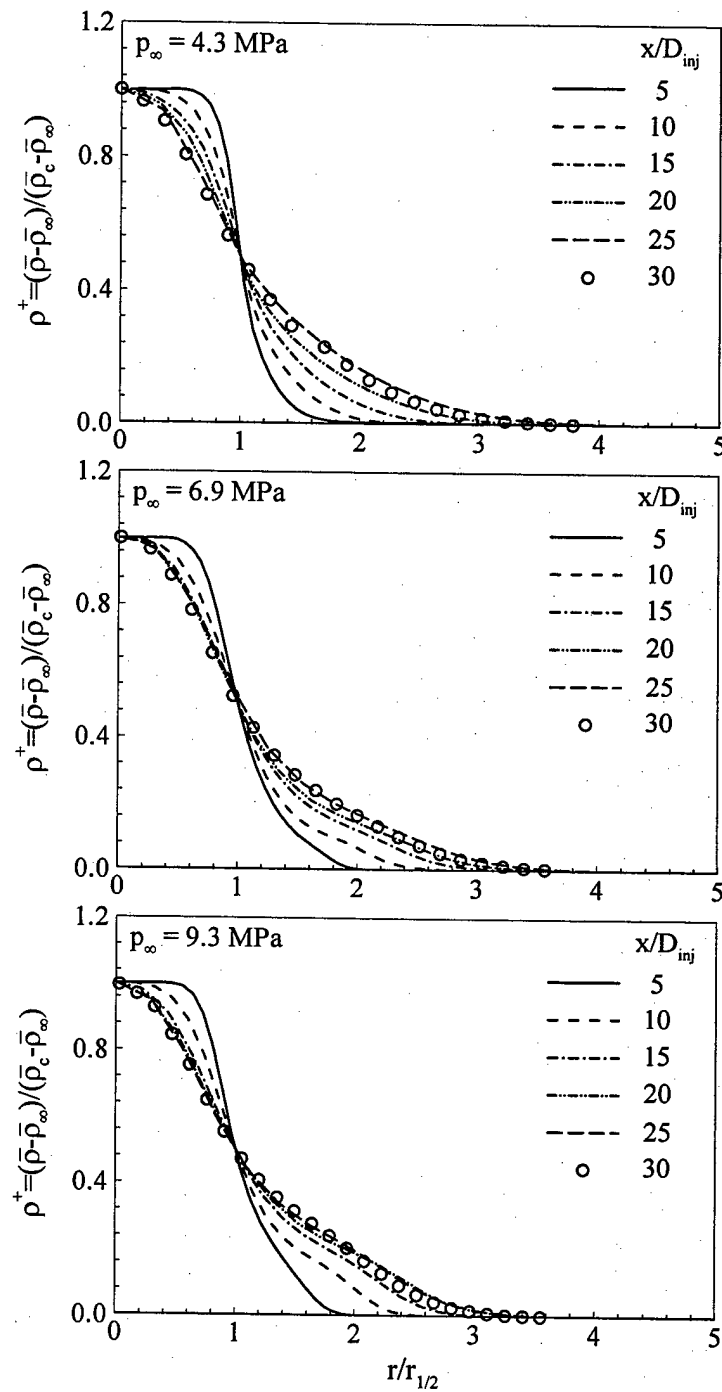


Fig. 4.11: Effect of pressure on normalized density distribution in radial direction.

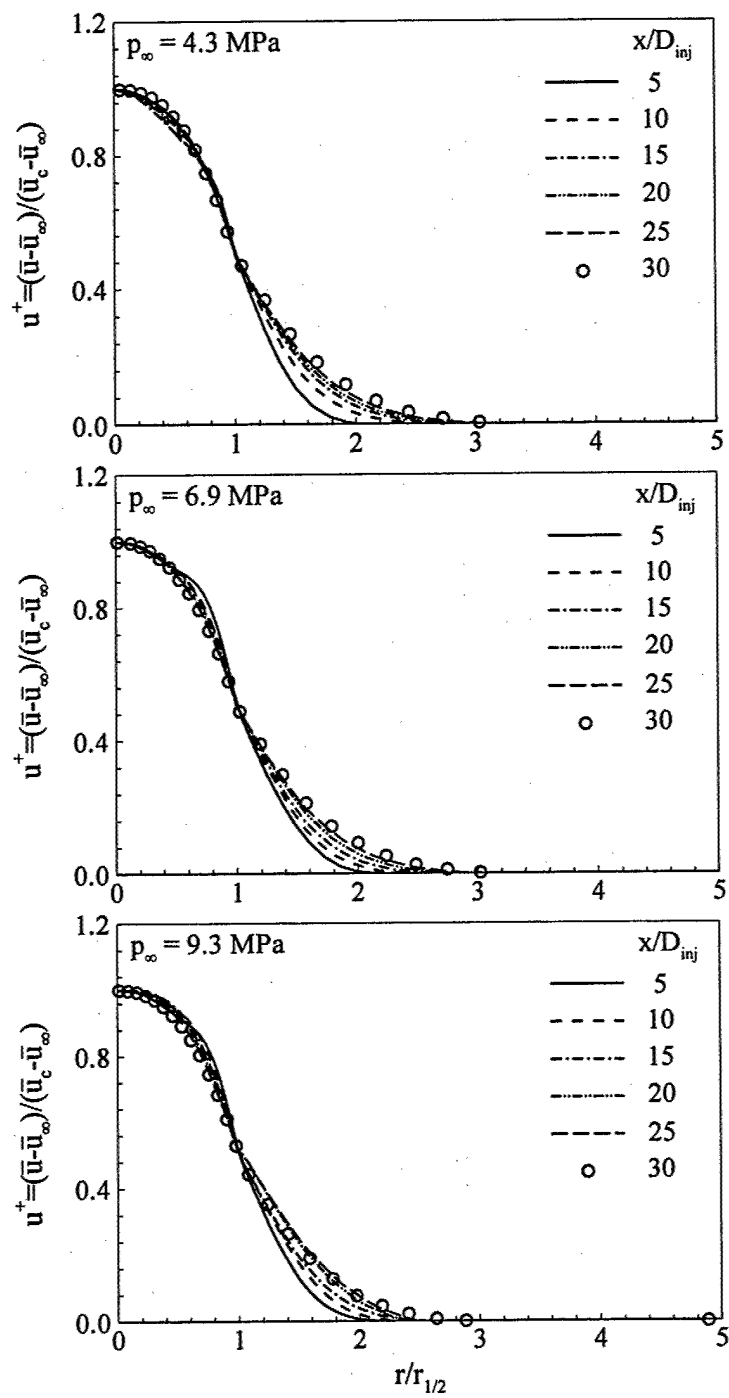


Fig. 4.12: Effect of pressure on normalized velocity distribution in radial direction.

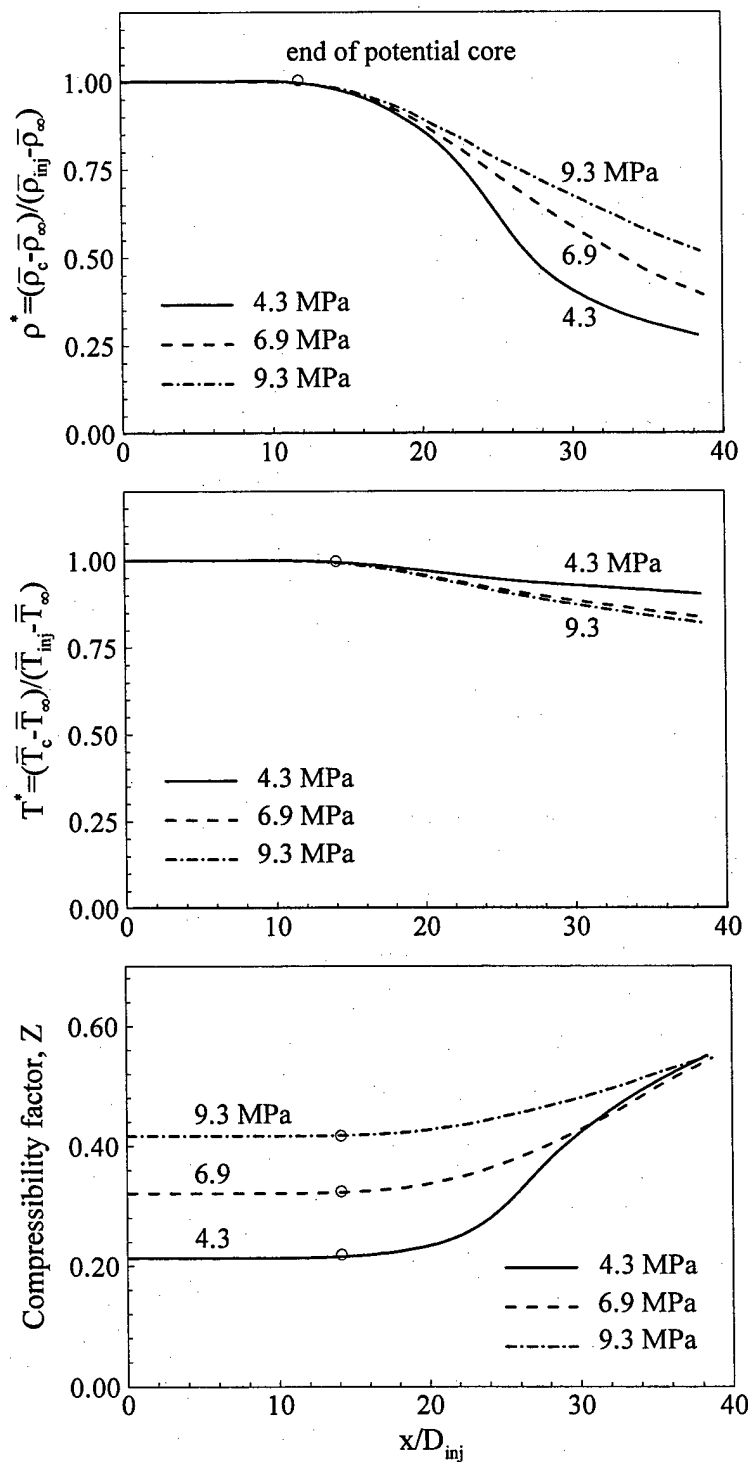


Fig. 4.13: Effect of pressure on normalized density, normalized temperature, and compressibility factor along jet centerline.

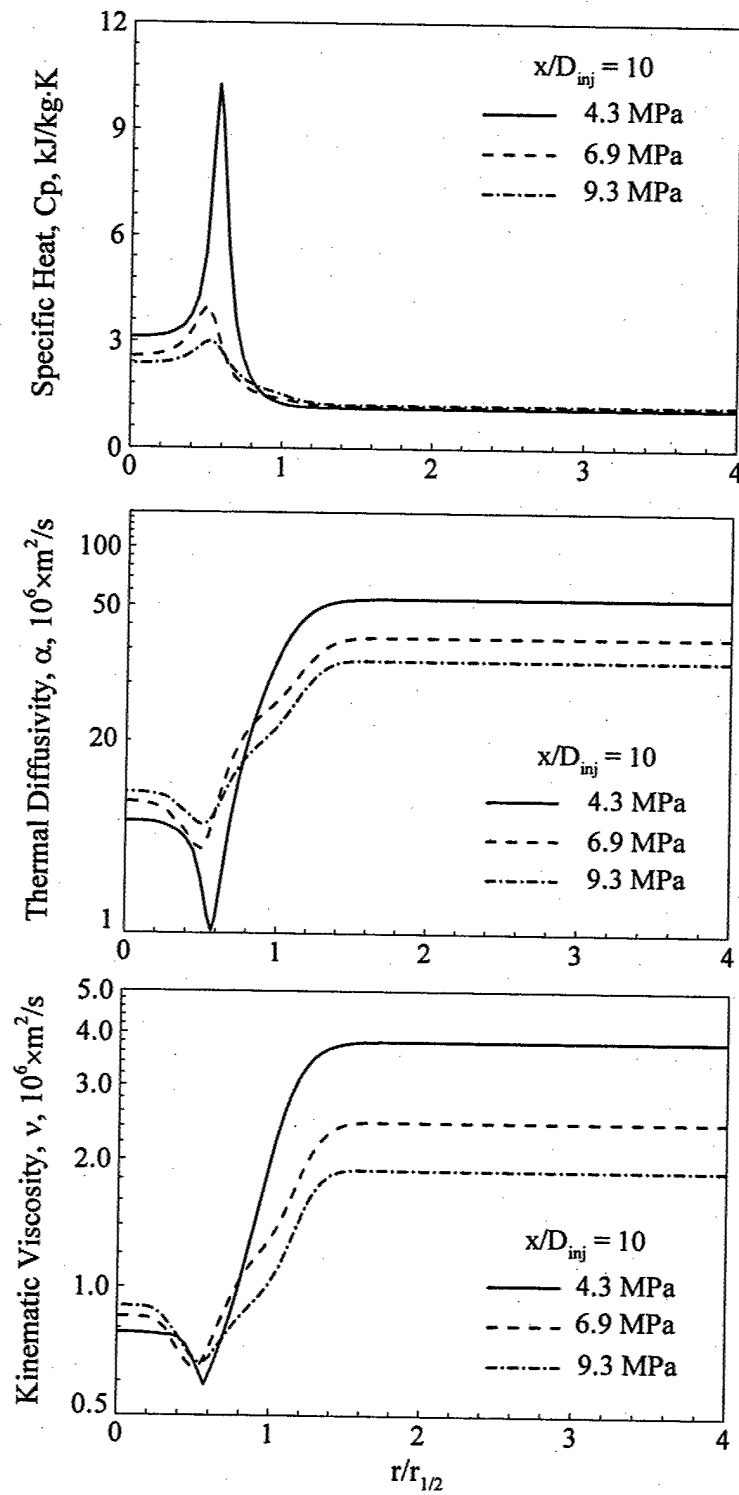


Fig. 4.14: Radial distributions of mean thermophysical properties at  $x/D_{inj} = 10$

## Chapter 5

### Three-Dimensional Analysis of Supercritical Cryogenic Fluid Injection

#### 5.1 Problem Description

Although the two-dimensional large-eddy-simulation carried out in Chapter 4 captures the salient features of high-pressure fluid injection and provides much useful insight into flow dynamics, it inherently neglects the three-dimensional vortex stretching mechanism, which is responsible for the transferring of energy from large to small scales through energy cascade and maintaining the continuous generation of small-scale multidimensional vortical structures. These structures dissipate energy at the smallest scales and provide the primary production and sustaining mechanism associated with near-wall turbulence. The lack of vortex stretching, consequently, leads to the underestimation of velocity decay and turbulence production. The present work attempts to investigate the above-mentioned phenomena by performing a three-dimensional LES. Emphasis is placed on the near field jet dynamics and the effect of real fluid thermodynamics on the jet evolution.

The simulation conditions of Cases 2 and 3 in Chapter 4 are restudied. Liquid nitrogen initially at a subcritical temperature of 120 K is injected through a circular tube with a diameter of 254  $\mu\text{m}$  into a supercritical nitrogen environment. A turbulent pipe flow with a bulk velocity of 15 m/s is assumed at the injector exit. The ambient temperature remains at 300 K, but the pressure varies from 69 to 93 atm, comparable to the chamber pressures of many operational rocket engines. For reference, the critical temperature and pressure of nitrogen are 126 K and 34 atm, respectively. The simulation conditions are summarized in Table 5.1, matching the experiments conducted by Chehroudi and Talley (2002), where the subscripts  $\infty$  and  $\text{inj}$  denote

the injection and ambient conditions, respectively. The Reynolds number is defined as

$$Re = \rho_{inj} u_{inj} D_{inj} / \mu_{inj} .$$

Table 5.1: Simulation Conditions

	$p_\infty$ (MPa)	$T_{inj}$ (K)	$T_\infty$ (K)	$\rho_{inj}$ ( $\text{kg}/\text{m}^3$ )	$\rho_\infty$ ( $\text{kg}/\text{m}^3$ )	$u_{inj}$ (m/s)	$\rho_{inj}/\rho_\infty$	Re
Case 1	6.9	120	300	603	77	15	7.83	44700
Case 2	9.3	120	300	626	103	15	6.07	42300

The computational domain downstream of the injector measures a length of  $40 D_{inj}$  and a mean diameter of  $12 D_{inj}$ . The dimensions are sufficient to minimize the effect of the far-field boundary conditions on the near-injector flow evolution. A three-dimensional grid is generated by rotating the two-dimensional grid with respect to the centerline. The entire grid system consists of  $225 \times 90 \times 72$  points along the axial, radial, and azimuthal direction, respectively. The grids are clustered in the shear-layer and near the injector to resolve rapid property variations in those regions. The mean grid size falls in the inertial sub-range of the turbulent kinetic energy spectrum, estimated using the Kolmogorov-Obukhov theory. The smallest grid width is  $2 \mu\text{m}$ . The computational domain is divided into 54 blocks, with each calculated on a single processor of a distributed-memory parallel computer. The physical time step is  $1 \times 10^{-3}$  ms, and the maximum CFL number for the inner-loop pseudo-time integration is 0.7. For each case, simulation is conducted for 12 flow-through times (i.e., 15 ms) to obtain statistically meaningful data. Each computation takes around 10000CPU-processor hours.

## 5.2 Thermophysical Properties

The non-ideal variations of thermo-physical properties, such as enthalpy, internal energy, and heat capacity, have direct impact on the fluid jets evolution. Figure 5.1 shows the effects of

temperature on the density, specific heat, thermal diffusivity, and kinematic viscosity of nitrogen in the temperature range of 40–1000 K at five different pressures of 1, 10, 33.4, 100, 200 atmospheres. The key trends over the range of pressures and temperatures of interest are illustrated in those figures. At 750 K and above, nitrogen exhibits ideal gas behavior, and the pressure effect is negligible. As the temperature decreases below 750 K, significant non-idealities are introduced with strong pressure dependence. Firstly, when fluid temperature is across the critical point from sub- to supercritical value, its density decreases sharply. In liquid rocket engines, oxidizer is injected into the combustion chamber at a temperature well below the critical temperature. The resultant severe density variation could give rise to two important impacts on the flowfield. The initial density ratio between the injected and ambient fluid is much greater than its counterparts at low pressure, and the strong density stratification may stabilize the jets. On the other hand, as the injected fluid mixes with the hot ambience in the transition region, its temperature increases and is across the critical point. The accompanied local volume expansion has considerable influence on the fluid jet dynamics. Secondly, the temperature sensitivity of the specific heat depends strongly on pressure. It increases rapidly as fluid state approaches the critical point, and theoretically becomes infinite exactly at the critical point. Meanwhile, the thermal diffusivity also exercises a large excursion of variation in the near critical region. It has been shown that the anomalous variations of those properties tend to distinguish the injected fluid from the environment. Thirdly, the flow Reynolds number increases almost linearly with pressure. For nitrogen, an increase in pressure from 1 to 100 atmospheres results in a reduction of the corresponding kinematic viscosity by a factor of two orders of magnitude. Based on the Kolmogorov universal equilibrium theory, given the same characteristic length and velocity, the Kolmogorov and Taylor microscales may decrease by 1.5 and 1.0 orders of magnitude, respectively. These reductions of characteristic scales of turbulent motions have a

direct impact on the flow evolution and the numerical grid density required resolving key processes.

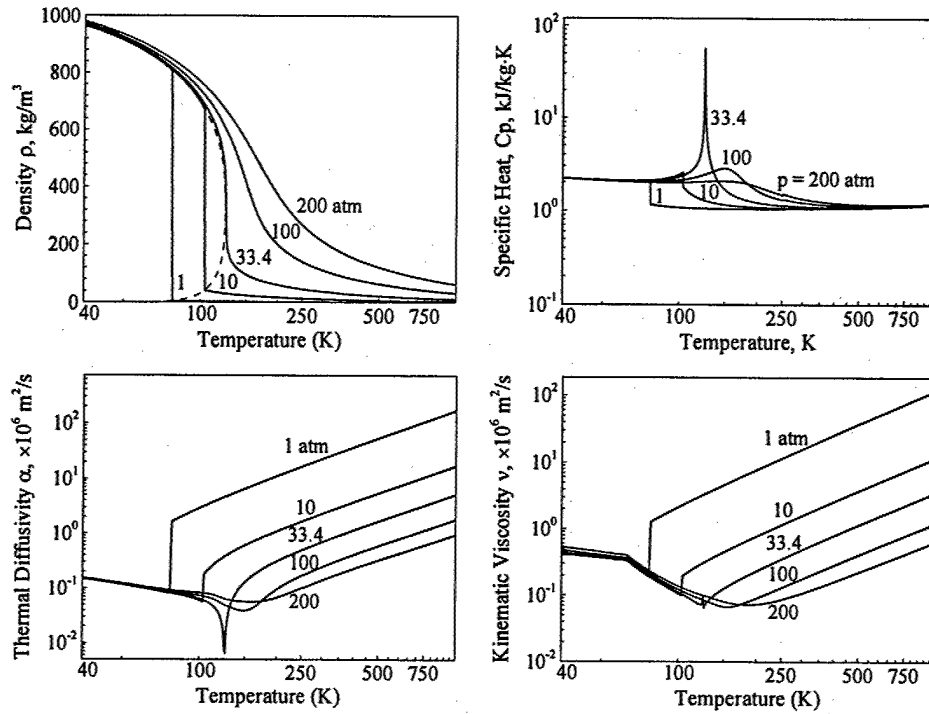


Fig. 5.1: Thermo-physical properties of nitrogen as functions of pressure and temperature.

### 5.3 Results and Discussion

#### 5.3.1 Instantaneous Flow Visualization

Figure 5.2 shows the snapshots of the vorticity, temperature, and density-gradient fields at two different ambient pressures. The small structures in the vorticity field near the injector come from the imposed turbulence at the inlet. For both two cases, the jet surfaces are relatively straight near the injector with only tiny instability waves. As the fluid moves downstream, those waves grow up and roll into a succession of ring vortices. In Case 1 ( $p_\infty = 6.9 \text{ MPa}$ ), vortex

rolling up and paring appear at the axial positions  $x/D_{inj} \approx 5$  and  $x/D_{inj} \approx 9$ , respectively. As a result of vortical motions, the hot irrotational ambient fluid parcel is engulfed into the jet, which is manifested in both the temperature and vorticity fields. The initial density stratification layer is severely twisted, with a string of large density-gradient regions surrounding the cold fluid core. As the pressure increases to  $9.3 \text{ MPa}$ , the stabilization effect of density stratification abates. Therefore, the locations of the vortex rolling and paring shift to the upstream. In addition, the jet spreads wider and its core reduces.

The previous two-dimensional simulation indicated that supercritical jet dynamics is largely dictated by the local fluid state through its influence on the thermophysical properties (Zong et al., 2004). The variations of the constant-pressure specific heat ( $C_p$ ), thermal diffusivity ( $\alpha$ ), kinematic viscosity ( $\nu$ ), and compressibility factor ( $Z$ ) fields are visualized in Fig. 5.3. Those properties are non-dimensionalized by the values of the injected fluid. Although the sharp distinction between liquid and gas phases vanishes due to the diminishment of surface tension and enthalpy of vaporization, the specific heat exhibits an anomaly variation as the fluid temperature transits across the inflection point on the isobaric  $\rho - T$  curve. The temperatures of the inflection points at studied ambient pressures are listed in Table 5.2. It is noteworthy that fluid properties usually undergo rapid variations across this point, where specific heat reaches its maximum, and thermal diffusivity and kinematic viscosity also exercise a large excursion of variation in an isobaric process. The fluid with intense property variations, acting like a boundary, isolates the cold injected fluid from the ambience. Compressibility factor, which measures the departure from ideal behavior, experiences a monotonic increasing from the cold jet to the hot ambience. The largest departure of  $Z$  happens only in the jet core, where it equals to 0.34 and 0.42 for Cases 1 and 2, respectively. As the cold fluid mixes with the hot ambience in the transition region, compressibility factor increases strikingly because of the local volume

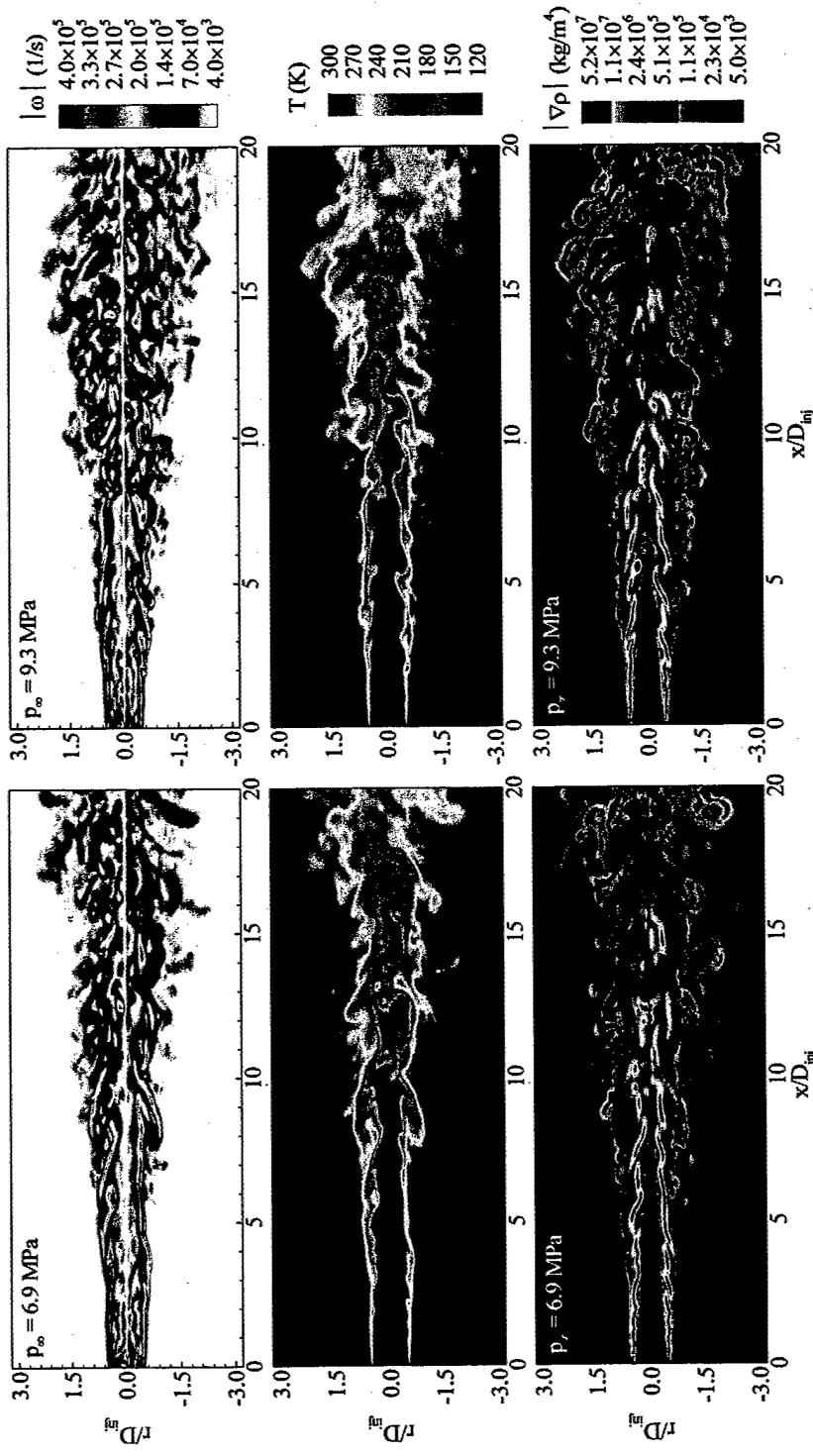


Fig. 5.2: Effect of pressure on vorticity magnitude, temperature, and density-gradient fields ( $\Gamma_\infty = 300$  K,  $u_{inj} = 15$  m/s,  $T_{inj} = 120$  K,  $D_{inj} = 254$   $\mu\text{m}$ ,  $t^* = 80$ ).

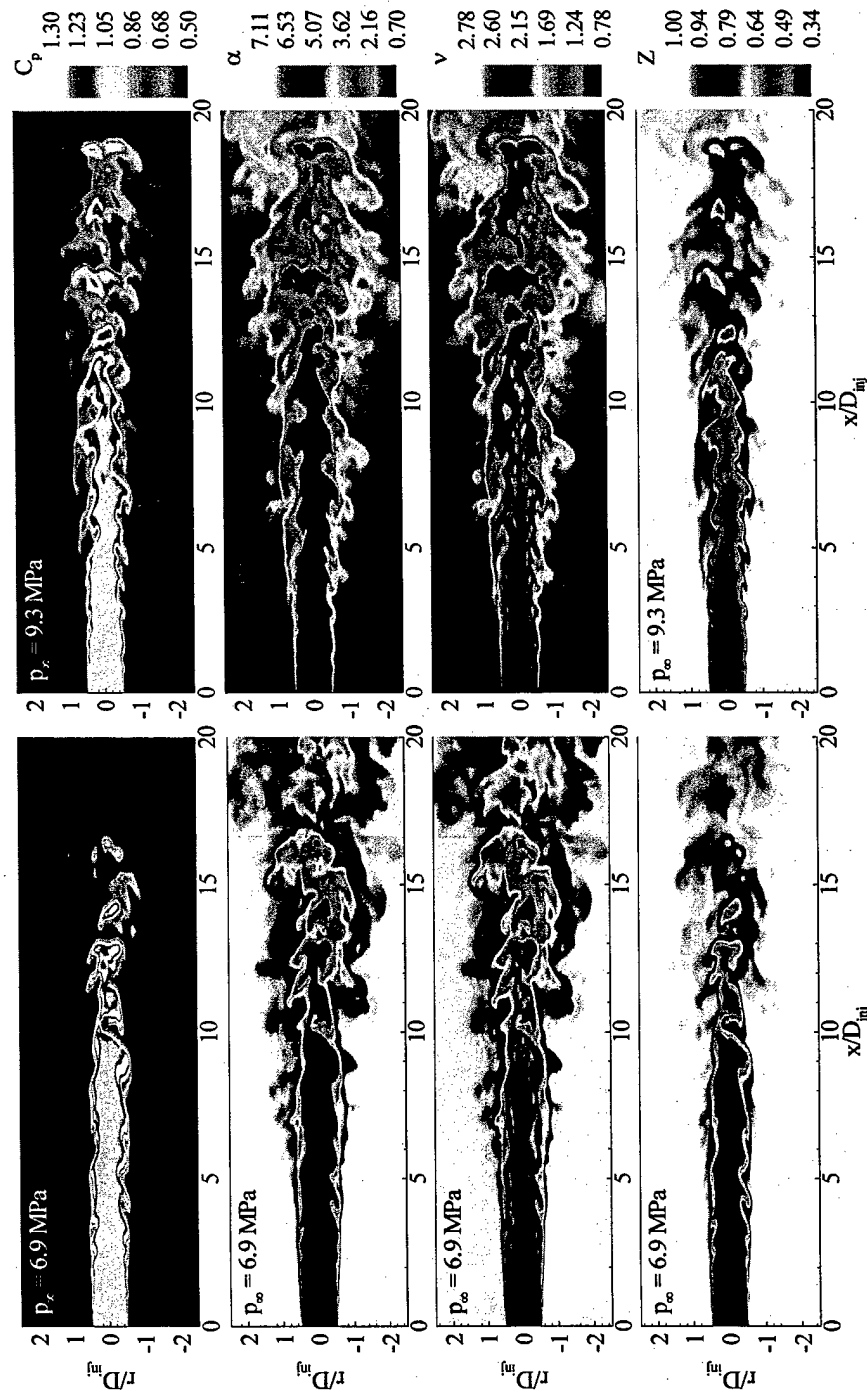


Fig. 5.3: Effect of pressure on specific heat, thermal diffusivity, kinematic viscosity, and compressibility factor fields ( $T_\infty = 300 \text{ K}$ ,  $u_{\text{inj}} = 15 \text{ m/s}$ ,  $T_{\text{inj}} = 120 \text{ K}$ ,  $D_{\text{inj}} = 254 \mu\text{m}$ ,  $t^* = 88$ ).

Table 5.2: Temperatures at inflection points on isobaric  $\rho - T$  curves at different pressures

	Case 1	Case 2
$T$ (K)	142.1	148.6

Table 5.3: Conditional averaged temperatures (K) in regions with  $|\nabla\rho| > \text{cutoff value}$ .

Cutoff	$0.1 \cdot  \nabla\rho _{\max}$	$0.2 \cdot  \nabla\rho _{\max}$	$0.3 \cdot  \nabla\rho _{\max}$
Case 1	150.7	147.6	143.1
Case 2	156.5	153.8	150.4

expansion. Its centerline value approaches 0.9 at the axial position  $x/D_{inj} = 15$  for Case 1, which implies the injected fluid behaves almost ideally.

Presently, the steep density-gradient regions are visually correlated with the fluid layer possessing high specific heat. To explore the mechanism of their formation, the conditional-averaged temperatures over the regions where the density-gradient magnitudes exceed pre-specified cutoff values are determined. The result is listed in Table 5.3, where  $|\nabla\rho|_{\max}$  is the maximum density gradient in the entire field, around  $1.15 \times 10^7 \text{ kg/m}^4$  for Case 2. The value decreases with increasing the cutoff density-gradient, and approaches the inflection point on the isobaric  $\rho - T$  curve. Thus, the formation of the large density-gradient is closely related to property variations, which to a large extent is dictated by real-fluid thermodynamics. Turbulent entrainment and mixing tend to introduce warm ambient gases into the cold jet and, subsequently, smooth the density-stratification. The drastic volume dilation during the mixing, when the temperature transits across the inflection point, however, prevents the entrainment of the surrounding fluid and, thereby, strengthens the stratification. The formation of the large density-gradient is a unique feature in high-pressure fluid injection and mixing. It has been reported by

previous researchers in both the pure fluid injection (Mayer et al., 2000; Zong et al., 2004) and two components mixing layer (Miller et al., 2000; Okong'o et al., 2002).

Density stratification exerts a strong influence on the large-scale flow motions. The large density-gradient acts like a solid wall in the flow that amplifies the axial turbulent fluctuation but damps the radial one (Hannoun et al., 1988; Zong et al., 2004). In addition, density stratification increasingly inhibits instability-wave growth and vortex paring (as shown in Fig. 5.2), which finally results in the reduction of the total yield of mixing (Atsavapranee, 1997).

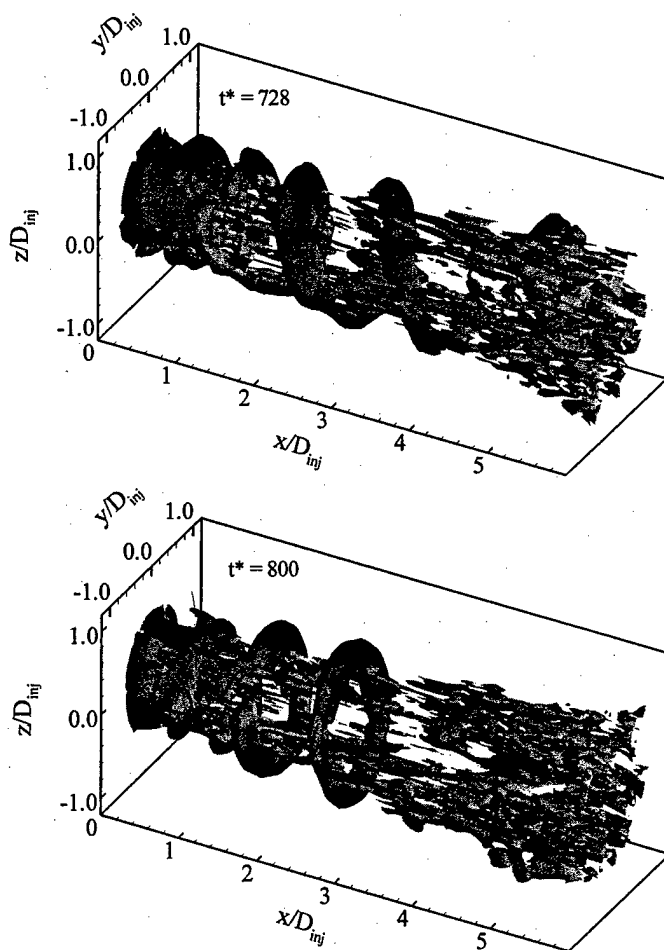


**Fig. 5.4:** Large coherent structures visualized by the instantaneous iso-surface of dilatation magnitude at a threshold corresponding to 15% of the maxima ( $p_\infty = 6.9$  MPa,  $T_\infty = 300$  K,  $u_{inj} = 15$  m/s,  $T_{inj} = 120$  K,  $D_{inj} = 254$   $\mu\text{m}$ ).

The near field three-dimensional flow structures of Case 1 are visualized in Fig. 5.4. Because the flow evolution is inherently coupled with the severe thermal-physical property variations (i.e. local volume expansion), the iso-surface of volume dilatation magnitude is presented instead of the vorticity or velocity fields. Near the injector, the fluid jet possesses intermittent Kelvin-Helmholtz-type shear-layer instability that switches between forming helical structures and discrete rings (Glaze and Frankel, 2003). A qualitative change in the structure of the jet occurs at location  $x/D_{inj} \approx 6$ , where the small scale flow motions are dominant. At the higher pressure (Case 2), the initial instability wave becomes more unstable due to the reducing of density stratification. Although similar coherent structures could also be identified, they are more transient and irregular.

### 5.3.2 Vortical Dynamics

Vortical flow motions play an essential role in turbulence. To identify the major mechanism responsible for vorticity production/destruction at real fluid regime, the vorticity and vorticity-magnitude budgets are examined.

The vorticity transport equation for compressible flow is

$$\frac{D\omega}{Dt} = (\omega \cdot \nabla) u - (\nabla \cdot u)\omega - \nabla\left(\frac{1}{\rho}\right) \times \nabla p + \nabla \times \left(\frac{1}{\rho} \nabla \cdot \tau\right) \quad (5.1)$$

The equivalent equation for the vorticity magnitude follows

$$\frac{D(\omega \cdot \omega)}{Dt} = 2\omega \cdot (\omega \cdot \nabla) u - 2(\nabla \cdot u)\omega \cdot \omega - 2\omega \cdot \nabla\left(\frac{1}{\rho}\right) \times \nabla p + 2\omega \cdot \nabla \times \left(\frac{1}{\rho} \nabla \cdot \tau\right) \quad (5.2)$$

where  $D/Dt$  is the substantial derivative. The first term on the right-hand side of the above equations represents vortex stretching and titling. The second term describes volume-dilatation, and the third term denotes baroclinic torque. The last term arises from viscous dissipation.

Figure 5.5 presents the azimuthal-averaged vorticity magnitude and azimuthal vorticity budgets of Case 1 at the positions slightly upstream of vortex rolling up ( $x/D_{inj} = 2$ ) and downstream of the potential core ( $x/D_{inj} = 10$ ), respectively.

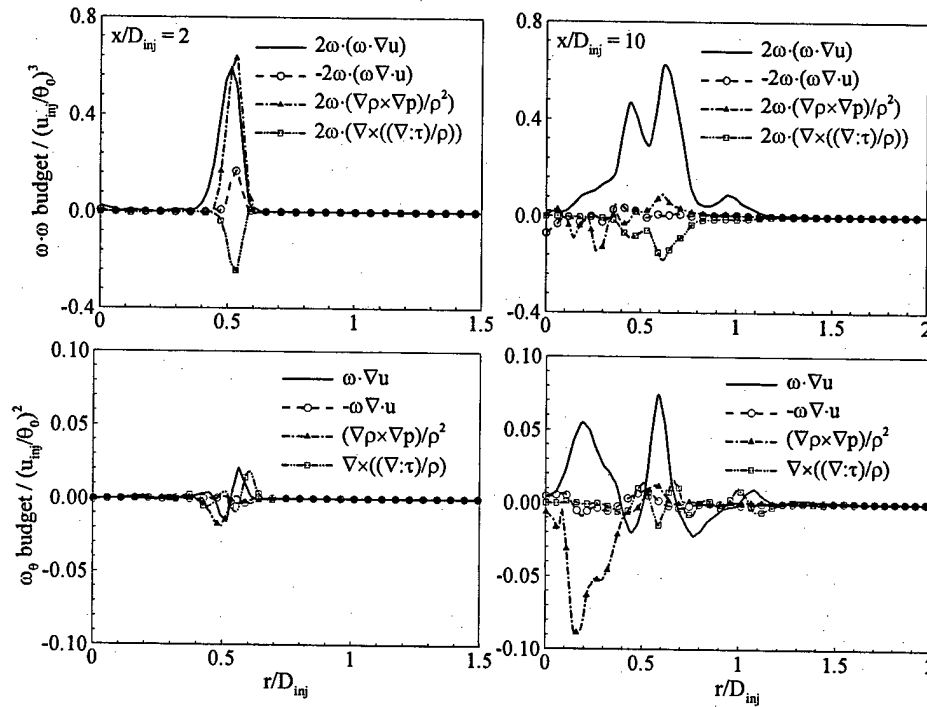


Fig. 5.5: Spatial averaged vorticity magnitude and azimuthal vorticity budgets at two different axial locations ( $p_\infty = 6.9 \text{ MPa}$ ,  $T_\infty = 300 \text{ K}$ ,  $u_{inj} = 15 \text{ m/s}$ ,  $T_{inj} = 120 \text{ K}$ ,  $D_{inj} = 254 \mu\text{m}$ ,  $t^* = 88$ ).

At the axial location  $x/D_{inj} = 2$ , all the terms except viscous dissipation provide positive contributions on the magnitude budget. The baroclinic torque, produced by the misalignment between pressure and density gradients, rivals the stretching and titling term in magnitude, indicating the influence of density stratification on the vorticity production. Similar to that reported by Okong'o et al. (2002), the peaks of baroclinic, volume dilatation, and viscous terms are located in the lighter gaseous nitrogen side. The contribution from vortex stretching and titling, however, is evenly distributed. For the azimuthal vorticity, the baroclinic term plays

important roles on the injected fluid side, whereas stretching and viscous dissipation are dominant in the ambient fluid. The contribution from volume dilatation is small.

As the cold fluid is convected downstream to the axial location  $x/D_{inj} = 10$ , it mixes with the surroundings and is heated. Density stratification abates, and the contributions from baroclinic torque and volume dilatation reduce in the vorticity magnitude field. Viscous dissipation, which is negative and destructs the vorticity magnitude, becomes important. Its magnitude, however, still could not balance the positive contribution from stretching and titling. The culmination of the stretching and tilting term in the transition region implies the production of small scales flow structures. Although baroclinic torque is not the dominant one in the magnitude budget, it provides a significant contribution on the azimuthal vorticity, in which its peak magnitude appears close to the centerline and is greater than that of the vortex stretching. This peak is induced by the existence of a cold fluid parcel at this location.

Figure 5.6 presents the azimuthal-averaged vorticity magnitude and azimuthal vorticity budgets of Case 2 at the same axial locations. At upstream ( $x/D_{inj} = 2$ ), although the baroclinic torque slightly increases because pressure fluctuation enhances with vigorous flow motion, the magnitude of stretching and titling does well exceed it and becomes the dominant one. Similarly, the peaks of all other terms reside in the lighter fluid side, except stretching and titling. The dominance of vortex stretching at an upstream location indicates that density stratification and its damping effect on vertical motions abate. Then, more small-scale turbulent motions could be produced upstream through the stretching mechanism. For the averaged azimuthal vorticity production, the stretching and titling is still greater in magnitude than all other terms. The second one in order of decreasing magnitude is the viscous dissipation.

Since the influence of initial density stratification reduces with the increase of pressure, the injected fluid well mixes with the ambience, resulting in no cold fluid parcels at  $x/D_{inj} = 10$ .

Therefore, the peak of baroclinic torque, which is observed in azimuthal vorticity budget of Case 1, ceases in Case 2. The differences in other terms are moderate.

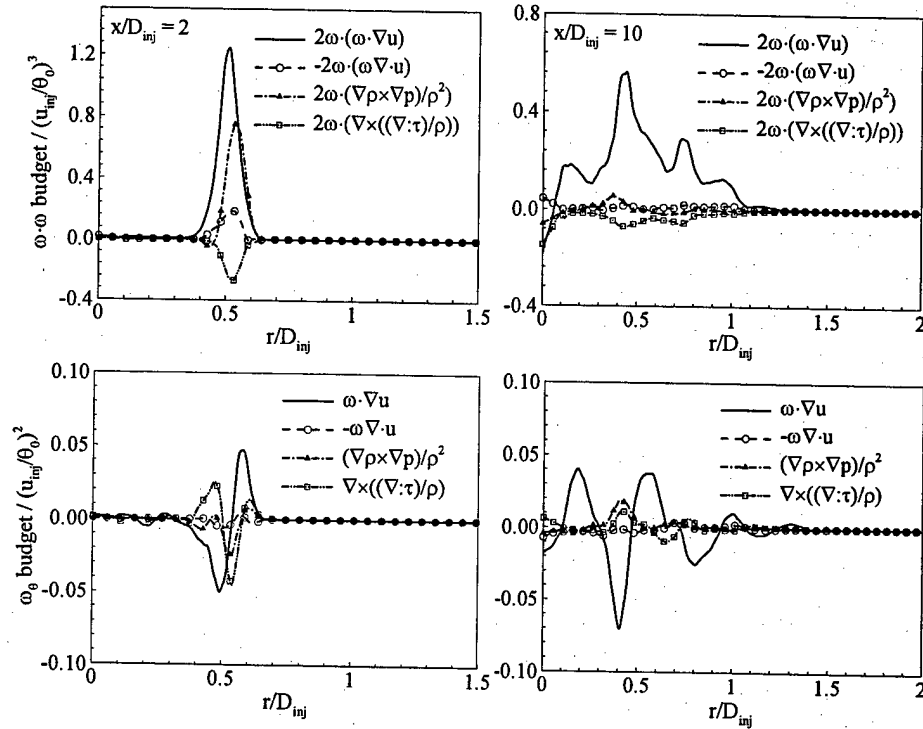


Fig. 5.6: Spatial averaged vorticity magnitude and azimuthal vorticity budgets at two different axial locations ( $p_\infty = 9.3$  MPa,  $T_\infty = 300$  K,  $u_{inj} = 15$  m/s,  $T_{inj} = 120$  K,  $D_{inj} = 254$   $\mu\text{m}$ ,  $t^* = 88$ ).

### 5.3.3 Shear-Layer Instability and Jet Prefer Mode

The power spectral densities of the pressure oscillations at three different axial locations for Case 1 are presented in Fig. 5.7. The radial position is fixed at  $r/D_{inj} = 0.5$ . A dominant frequency of 0.58 is observed at the axial location  $x/D_{inj} = 3$ , corresponding to the initial vortex shedding frequency. As the fluid is convected downstream ( $x/D_{inj} = 6$ ), a peak of 0.29, nearly one half of the initial one, appears. Due to the non-linear interaction of vortices, there are still several intermediate peaks existing between 0.58 and 0.29. The oscillation at the frequency of 0.29

reaches its maximum at  $x/D_{inj} = 9$ , indicating the completion of the first paring. In Case 2, density stratification abates with the increasing of pressure. Therefore, vortex passage frequency after the first paring (0.31) emerges at the upstream location  $x/D_{inj} = 3$  (see Fig. 5.8). This fluctuation becomes the dominant one at  $x/D_{inj} = 6$  and reaches the maximum after the potential core.

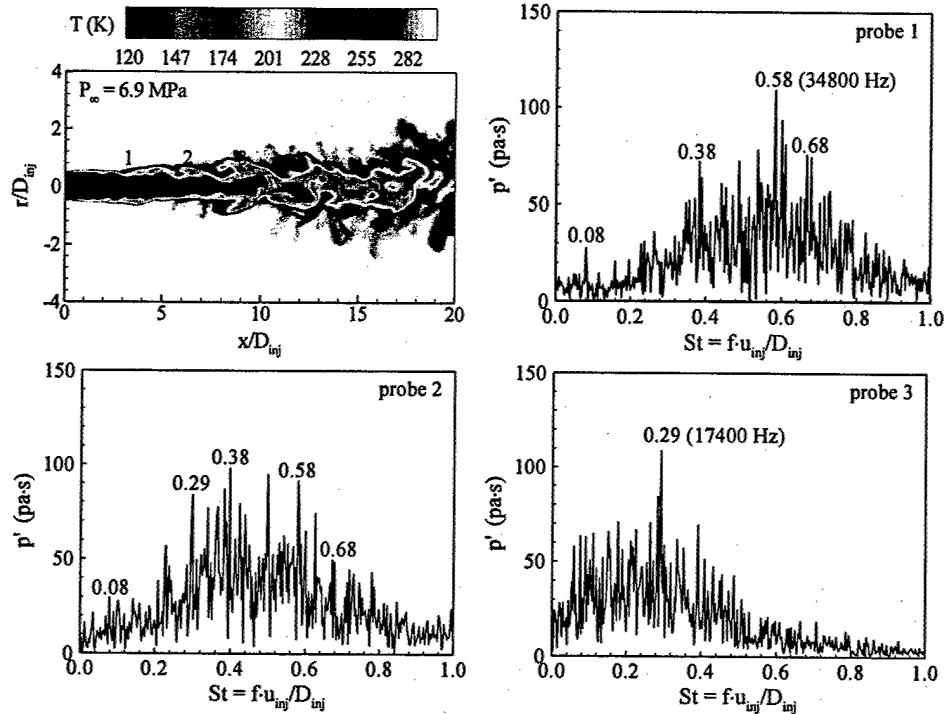


Fig. 5.7: Power spectral densities of pressure fluctuations at different axial locations with  $r/D_{inj} = 0.5$  ( $p_\infty = 6.9$  MPa,  $T_\infty = 300$  K,  $u_{inj} = 15$  m/s,  $T_{inj} = 120$  K,  $D_{inj} = 254$   $\mu$ m).

The flow instabilities and vortex shedding in constant-density shear layers were reviewed by Schadow and Gutmark (1992). Based on their work, the initial vortex shedding frequency,  $f_1$ , can be scaled with the shear-layer momentum thickness  $\theta_0$  and a characteristic velocity  $\bar{U}$ , normally taken as the average bulk velocity of the two streams. The result yields a non-dimensional frequency or Strouhal number,  $St_i = f_i \theta_0 / \bar{U}$ , which ranges from 0.044 to 0.048 for a planar turbulent shear-layer. As the vortices move downstream, they merge together to oscillate at the sub-harmonics of the initial vortex shedding frequency,

$f_1/N$  ( $N = 2, 3, 4, \dots$ ). Although the above analysis was formulated for planar flows, it can be applied with good accuracy to mixing layers in axisymmetric configurations if the thickness of the shear-layer is much smaller than the radius of the injector. In the present work,  $\bar{U} \approx 8 \text{ m/s}$  and the initial momentum thickness  $\theta_0$  estimated for a fully developed turbulent pipe flow is 0.011 mm. If the Strouhal number is chosen to be  $St_i = f_i \theta_0 / \bar{U} = 0.048$ , then the most amplified frequency becomes  $f_1 = 34.9 \text{ kHz}$ , and the corresponding second harmonic frequency is 17.5 kHz. After being normalized with the jet diameter and the injection velocity, they agree well with the vortex-passage frequencies obtained in Cases 1 and 2.

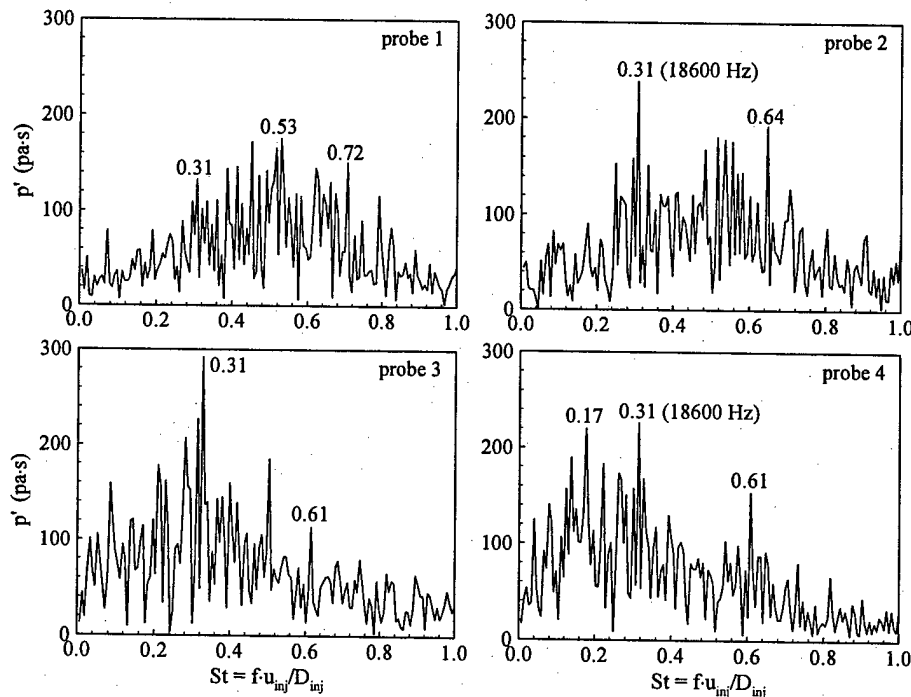


Fig. 5.8: Power spectral densities of pressure fluctuations at different axial locations with  $r/D_{inj} = 0.5$  ( $p_\infty = 9.3 \text{ MPa}$ ,  $T_\infty = 300 \text{ K}$ ,  $u_{inj} = 15 \text{ m/s}$ ,  $T_{inj} = 120 \text{ K}$ ,  $D_{inj} = 254 \mu\text{m}$ ).

Distinct from the most amplified mode of shear-layer instability, jet flow still exhibits a preferred mode or jet-column mode due to the existence of a second length scale, the injector

diameter ( $D_{inj}$ ). Its frequency corresponds to the vortex passage frequency at the end of the potential core. The preferred Strouhal number of circular jets was found to vary between 0.25 and 0.5, which was usually measured in the region between  $x/D_{inj} = 3$  and 5. The scatter in experiments results from the nature of the residual noise presenting in individual facilities (Gutmark and Ho, 1983). For a high-pressure cryogenic jet, both the rolling up and the vortex paring are inhibited by the density stratification, which gives rise to a relatively longer potential core. Therefore, the strong peaks at the Strouhal numbers of 0.29 and 0.31, which reach the maximum at the axial location  $x/D_{inj} = 9$ , represent the jet prefer modes for Cases 1 and 2, respectively. Those values fall into the range being reported.

### 5.3.4 Mean and Turbulent Properties

To validate the present analysis and to characterize high-pressure cryogenic fluid injection, this section presents the mean and turbulence flow properties and compares them with the experimental data regarding the supercritical jet and incompressible turbulent jet with and without density variation. The conditions of the experiments used for comparison are briefly summarized in Table 5.4. The mean flow properties in simulation are obtained by taking the long-time average of the instantaneous quantities over 10 ms (about 8 flow-through times) after the flowfield has reached its stationary state. In addition, an azimuthal average is utilized to augment the statistical samples.

Table 5.4: Physical parameters of the experiments used for comparison.

Source		Re	$x_0 / D_{inj}$	$\rho_{inj} / \rho_\infty$	$p_\infty$ (atm)
Chehroudi et al. (2002a,b)	LN2 into GN2	$4.5 \times 10^4$	-	8.0	69
	LN2 into GN2	$4.0 \times 10^4$	-	6.0	93
Amielh et al. (1996)	Helium into Air	7000	0.2	0.14	1.0
	Air into Air	$2.1 \times 10^4$	2.6	1	1.0
	$\text{CO}_2$ into Air	$3.2 \times 10^4$	2.9	1.4	1.0
Wyganski & Fiedler (1969)	Air into Air	$10^5$	3.0 – 7.0	-	1.0
Panchapakesan & Lumley (1993)	Air into Air	$1.1 \times 10^4$	-	-	1.0
Hussein et al. (1994)	Air into Air	$9.5 \times 10^4$	2.7	-	1.0

Figure 5.9 shows the centerline distributions of the normalized temperature, velocity, density, and the growth of jet half-width based on both the mean velocity and density. In the density and temperature profiles, their values remain unchanged near the injector, indicating the existence of a potential core. The length of the core slightly decreases with elevated pressure in Case 2. After the potential core, the  $z^{-1}$  decay of the jet velocity is observed, where its distribution could be represented as

$$\frac{u_{inj}}{\bar{u}_c} = \frac{1}{B_u} \left[ \frac{x}{D_{inj}} - \frac{x_0}{D_{inj}} \right] \quad (5.3)$$

Here,  $x_0$  is the so-called virtual origin and  $B_u$  is the decay constant. The subscript  $c$  refers to the quantity at the centerline. For the incompressible turbulent jet, a value of  $B_u$  between 5.7 and 6.1 has been suggested. On the same figure, the curve fit ( $x_0 = 2.7$  and  $B_u = 5.9$ ) on the experimental data of Hussein et al. (1994) is shown too. Since the injected fluid is much denser than the ambience, velocity decreases more slowly in the transition region than does its counterpart at standard pressure. Therefore, the curve fits on the present results give a much greater constant around 8.0 and a longer virtual origin. The centerline temperature

experiences a slightly rapid decay but still bears a similar trend as velocity. Because the mixing between the injected and the surrounding fluid is enhanced in the transition region, the cold jet is heated, and its temperature may transits across the inflection point on the constant pressure  $\rho - T$  curve. Since a slight increase in temperature could give rise to a drastic reduction in density near this point, the fluid density diminishes severely after the potential core. At the axial location  $x/D_{inj} = 30$ , there is only a tiny difference between the centerline and the ambient values.

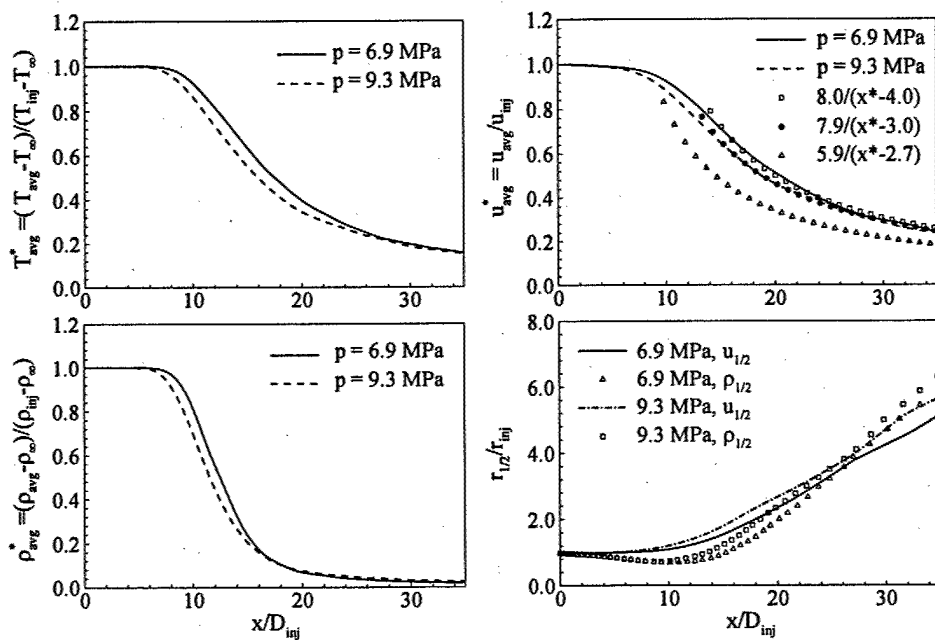


Fig. 5.9: Effect of pressure on the normalized temperature, velocity, density along jet centerline and the FWHM distributions ( $T_\infty = 300 \text{ K}$ ,  $u_{inj} = 15 \text{ m/s}$ ,  $T_{inj} = 120 \text{ K}$ ,  $D_{inj} = 254 \mu\text{m}$ ).

Figure 5.9 also presents the growth of the jet half-width based on the mean velocity and density. The curvatures of that based on velocity decreases at axial location  $x/D_{inj} = 27$  and 30 for Cases 1 and 2, respectively. It implies that the sudden volume expansion of the jet in the transition region is followed by a constant growth downstream. Because the jets are heated, the half-width based on the density reduces and is smaller than unity near the injector. It, then,

spreads readily after the potential core. The half-widths based on both the velocity and density distributions expand as the ambient pressure increases.

Figure 5.10a compares the velocity decays with the data obtained by Amielh et al. (1996) for variable density turbulent jets at standard pressure. Their experimental conditions are listed in Table 5.4. The low-pressure results indicated that density variation exerts a crucial influence on the jet evolution. For instance, the centerline velocity fall-off of the lighter Helium jet is more rapid than that of the Air and CO<sub>2</sub> ones. Although the supercritical jets have greater initial density ratios than the CO<sub>2</sub> jet, their axial velocity decays exhibit similar distributions. It seems the strong initial density stratification of the cryogenic jet has only a moderate effect on the downstream flow evolution.

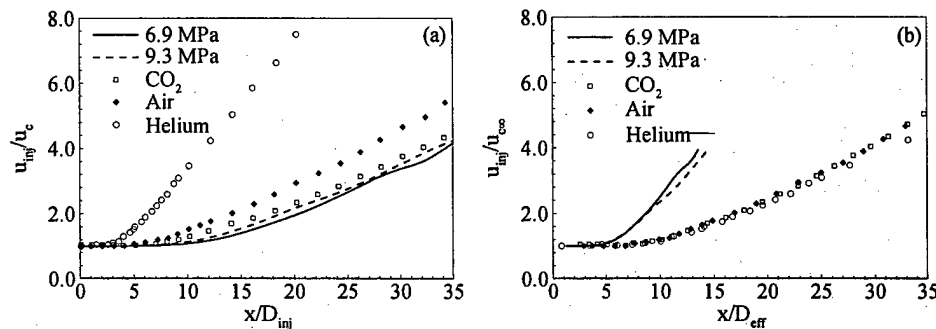


Fig. 5.10: Effect of initial density ratio on velocity decay, a) velocity decay, b) velocity decay normalized using the pseudo-similarity laws suggests by Chen and Rodi (1980).

Following the similarity law proposed by Chen and Rodi (1980) for variable-density incompressible jets, the effect of low velocity co-flow on the velocity decay in the experiments were taken into account by subtracting it from mean flow using  $u_{inj}/u_{\infty} = u_{inj}/(u_c^2 - u_{\infty}^2)$  instead of  $u_{inj}/u_c$ . In addition, an effective diameter considering the initial density ratio  $D_{eff} = D_{inj}(\rho_{inj}/\rho_{\infty})^{1/2}$  is introduced. A negative virtual origin  $x_o$  is needed in Fig. 5.10b to collapse the data. This virtual origin is directly associated with the potential core length, which is

longer for the denser jets. Based on Amielh et al. (1996),  $x_0$  equals to  $-0.2D_{inj}$ ,  $-2.6D_{inj}$ ,  $-2.9D_{inj}$  for the helium, air, and  $\text{CO}_2$  jet, respectively. The values of  $-3.0D_{inj}$  and  $-4.0D_{inj}$  are chosen for the present jets in Cases 1 and 2, respectively. After transformation, the velocity decays of the three low-pressure variable-density jets collapse together, whereas, two supercritical jets exhibit a totally different trend (see Fig. 5.10b). To investigate the influence of the virtual origin,  $x_0$  is intentionally elongated to  $-6.0D_{inj}$  and  $-5.0D_{inj}$  for Cases 1 and 2, respectively. The large deviations between the low- and high-pressure jets still exist (not shown). Compared with the variable density jets, the cryogenic jet has a much stronger initial density stratification, which gives rise to a wider jet effective diameter ( $D_{eff}$ ). The density ratio, however, abates very quickly in the transition region because of the local volume expansion. Therefore, the effective diameter is over estimated by the definition. Obviously, treating the supercritical fluid jet simply as a variable-density incompressible jet without considering severe property variations could lead to unexpected error in the near field.

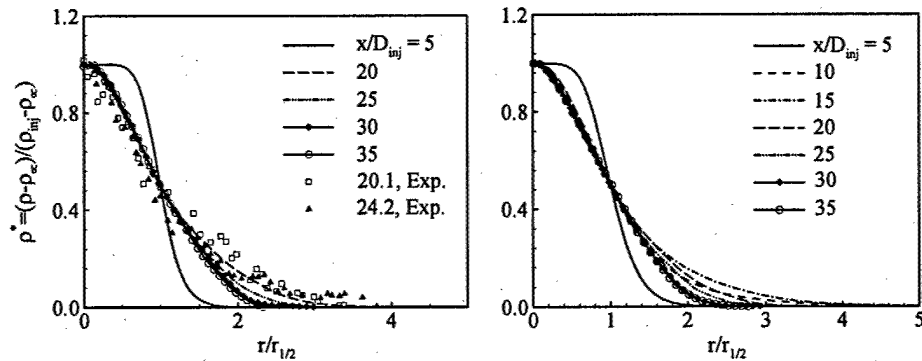


Fig. 5.11: The normalized density distributions in radial direction at different axial locations ( $T_\infty = 300 \text{ K}$ ,  $u_{inj} = 15 \text{ m/s}$ ,  $T_{inj} = 120 \text{ K}$ ,  $D_{inj} = 254 \mu\text{m}$ ).

Figure 5.11 shows the radial distributions of the normalized mean density,  $\rho^+ = (\rho - \rho_\infty)/(\rho_c - \rho_\infty)$  at different axial locations. For comparison purposes, the radial

coordinate is normalized by the FWHM ( $r_{1/2}$ ) based on density at the specified positions. Similarly, there are three distinct regions: a potential core, where a flat-hat distribution around the centerline occurs, a transition region, and a self-similar region. The density profiles at  $x/D_{inj} > 30$  merge to a single distribution for both Cases 1 and 2, manifesting the existence of the self-similarity downstream. Compared with the density field measured using the Raman scattering technique under the same test conditions of Case 1 (Chehroudi and Talley, 2002), the calculated radial density distributions follow exactly the same trend at the two axial locations with a maximum deviation of 8%.

The other quantitative parameter obtained in the experiments is the initial spreading angle of the cryogenic jets. Based on the experimental data, Chehroudi et al. (2002) proposed an empirical model for pure nitrogen injection into different environments, including gaseous nitrogen, helium, and air. Since the jets exhibit distinct features at sub- and supercritical pressures, their model combines the correlation for the isothermal liquid spray (Reitz and Bracco, 1979) and the relationship for the incompressible variable-density turbulent jet (Papamoschou and Roshko, 1988). It takes the following form.

$$\theta = 0.27[F(\varepsilon(\rho_\infty / \rho_{inj})) + (\rho_\infty / \rho_{inj})^{1/2}] \quad (5.4)$$

where

$$F(\varepsilon(\rho_\infty / \rho_{inj})) = \frac{\tau_b}{\tau_b + \tau_g} = 5.325(\rho_\infty / \rho_{inj}) + 0.0288 \quad \rho_\infty / \rho_{inj} < 0.0885 \\ = 0.5 \quad \rho_\infty / \rho_{inj} \geq 0.0885. \quad (5.5)$$

The coefficient  $\varepsilon$  is equal to 1.0, 0.2 and 1.2 for nitrogen, helium, and air environment, respectively.  $\tau_b$  and  $\tau_g$  are the droplet or bugle formation and the gasification times, respectively. Their influences are modeled by the density ratio in Eq. 5.4. In the present simulation,  $\rho_\infty / \rho_{inj}$  is larger than 0.0885, and a constant of 0.5 is adopted for function  $F$ .

Compared with this constant, the second term is smaller and plays a minor role in determining the jet growth rate. In Fig. 5.12, the angle calculated from two times the FWHM of density profile at the axial location  $x/D_{inj} = 30$  and the predicted jet spreading angles are compared. A fairly good agreement is obtained.

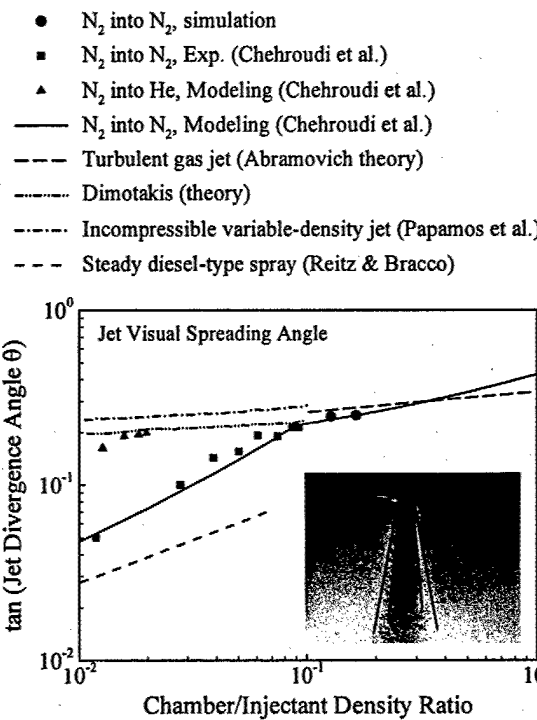


Fig. 5.12: Tangent of the jet visual spreading angle versus the ambience to injectant density ratio.

The normalized mean axial velocities  $\bar{u}^* = (\bar{u} - \bar{u}_\infty)/(\bar{u}_{inj} - \bar{u}_\infty)$  versus the universal self-similarity coordinate  $\eta = r/(x - x_0)$  are presented in Fig. 5.13. The experimental data shown on this figure include the incompressible jets of Panchapakesan and Lumley (1993), Hussein et al. (1993), Wygnanski and Fiedler (1967), and the variable density Helium and CO<sub>2</sub> jets of Amielh et al. (1996). Most of the experimental data were acquired from the far downstream ( $x/D_{inj} > 40$ ), except the two variable density ones, in which only the velocity profiles at  $x/D_{inj} = 20$  are available. To be consistent, the velocity profiles of high-pressure

jets are obtained at the location of  $x/D_{inj} = 35$ , a position where the influence from outflow boundary could be excluded. The range of data acquisition and virtual origin of each experimental dataset are listed in Table 5.4. It should be noted that two virtual origins, which are longer than those employed in Fig. 5.10, have been used here. Since the proximal region and the far-field inherently pose different virtual origins, those values are obtained through the best curve fit on the velocity distribution in the self-similarity region ( $25 \leq x/D_{inj} \leq 35$ ). After a proper virtual origin is chosen, the data of experiments and simulation collapse together.

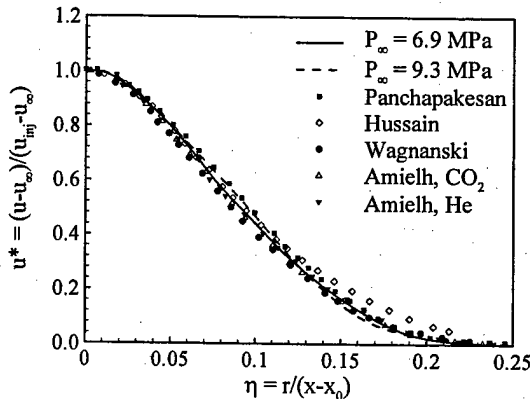


Fig. 5.13: The normalized velocity distributions in radial direction at the axial location  $x/D_{inj} = 35$  ( $T_\infty = 300$  K,  $u_{inj} = 15$  m/s,  $T_{inj} = 120$  K,  $D_{inj} = 254$   $\mu\text{m}$ ).

Figure 5.14 shows the non-dimensionalized Reynolds stress components versus the universal self-similarity coordinate  $\eta$ . Those values are obtained by averaging the nondimensional profiles over the region  $30 \leq x/D_{inj} \leq 35$ . Reasonable agreements are obtained for all components. The measurements of the  $\text{CO}_2$  jet in the experiments of Amielh et al. are smaller than the results of the other experiments and those of the present simulation, because their data are acquired at a relative upstream location ( $x/D_{inj} = 20$ ), where both the turbulent intensity components and Reynolds shear stress are still developing and do not reach a constant level. It was reported that among the four Reynolds stress components, the shear stress

term  $\langle u'v' \rangle$  reaches the self-similarity faster than the other three terms (Boersma et al., 1998).

The same observation is obtained in the present simulation.

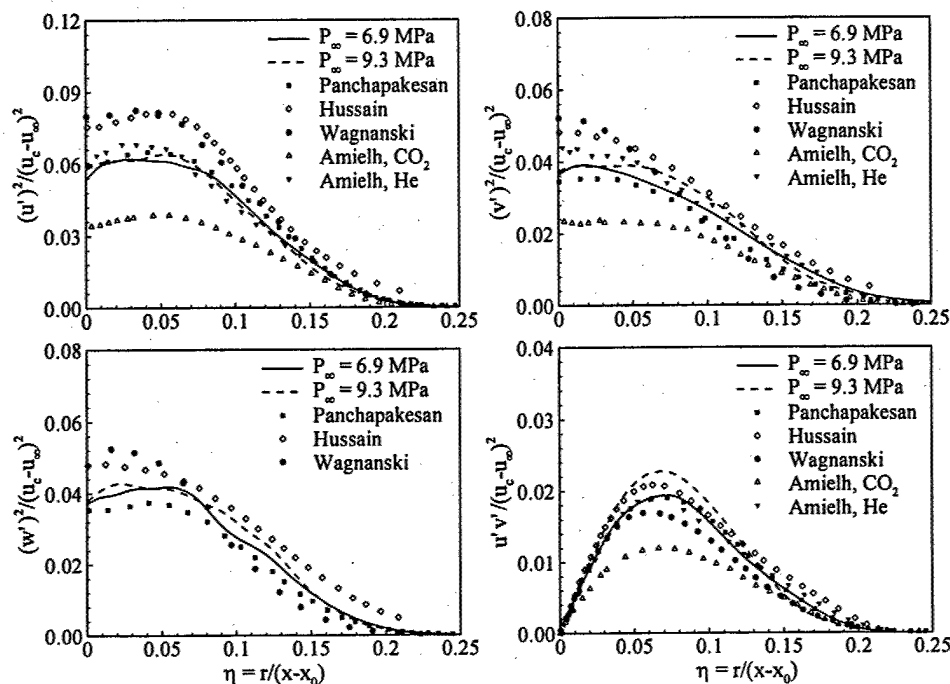


Fig. 5.14: The normalized Reynolds stress components distributions in radial direction averaged among the region  $30 < x/D_{inj} < 35$  ( $T_\infty = 300$  K,  $u_{inj} = 15$  m/s,  $T_{inj} = 120$  K,  $D_{inj} = 254$   $\mu\text{m}$ ).

Based on the experimental observation of gaseous helium, methane, and propane injected into the quiescent air environment at standard temperature and pressure, Richards and Pitts (1993) stated that due to the entrainment and mixing, the density difference between the injected and environmental flows ceases in far-field, where the variable density jet behaves like a constant density jet. The near-field effects (i.e. density ratio, velocity profile) can be included into the far-field flow description through a properly chosen virtual origin  $x_0$ . Presently, the strong density stratification and severe property variations exist only near the injector and disappear as a result of volume expansion in the transition region (as shown in Fig. 5.9). It is reasonable to see that both the axial velocity and Reynolds stress components are comparable with that of the low-pressure counterpart in the far-field.

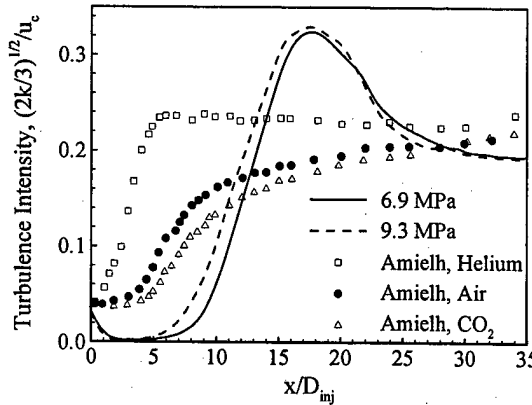


Fig. 5.15: The normalized turbulence intensity distributions along jet centerline ( $T_\infty = 300\text{K}$ ,  $u_{inj} = 15 \text{ m/s}$ ,  $T_{inj} = 120 \text{ K}$ ,  $D_{inj} = 254 \mu\text{m}$ ).

The centerline turbulent intensities are compared with the variable density jets data (Amielh et al., 1996) in Fig. 5.15. In the experiments, the increase of turbulent kinetic energy is slower for the heavier  $\text{CO}_2$  jet near the injector. A similar trend is observed for cryogenic jets. Due to the strong initial density stratifications, turbulent intensity starts to level off at the relative downstream positions. Its value, however, increases suddenly after the potential core and reaches a peak value of 32% around the axial location  $x / D_{inj} = 18$  in Case 2. This value is much greater than the highest point of the variable density incompressible jets. After the peak, turbulent intensity decreases and approaches a constant level close to its low-pressure counterpart. A similar kinetic energy peak off was observed by Zhou et al. (2001) in their numerical simulation on turbulent buoyant jets, where it was attributed to the secondary instability induced by buoyancy force. Presently, the injected fluid is much heavier than the surrounding flow and no buoyant effect is included. Compared with the velocity decay of the variable density jets, that of the cryogenic jet is slower in the transition region (as shown in Fig. 5.10). Therefore, the rapid increase of turbulent intensity could not be resultant from an underestimated centerline velocity. It is noted that the region where turbulent kinetic energy intensely increases is visually correlated with the density dropping-off region in Fig. 5.9. The evidence, so far, indicates that the vigorous

enhancement of turbulence kinetic energy in the transition region might partially be induced by the local volume expansion as the injected cold fluid is heated.

### 5.3.5 Proper Orthogonal Decomposition Analysis

The jet dynamics is further explored using the proper orthogonal decomposition technique, which extracts energetic coherent structures from the calculated flowfield. For a given flow property,  $f(x,t)$ , the POD analysis can determine a set of orthogonal functions  $\varphi_j$ ,  $j = 1, 2, \dots$ , such that the projection of  $F$  onto the first  $n$  functions

$$\hat{f}(x,t) = \bar{f}(x) + \sum_{j=1}^n a_j(t)\varphi_j(x) \quad (5.6)$$

has the smallest error, defined as  $E(\|f - \hat{f}\|^2)$ . Here,  $a_j(t)$  represents the temporal variation of the  $j$ th mode, and  $E(\cdot)$  and  $\|\cdot\|^2$  denote the time average and a norm in the  $L^2$  space, respectively. A more complete discussion of this subject can be found in Berkooz et al. (1993).

Because of the limitation of data storage for the calculated flowfields over an extended time period, the POD analysis is conducted only for the first twelve computational blocks near the injector, which measure approximately  $3D_{inj}$  and  $8D_{inj}$  in radial and axial direction, respectively. A total of 225 three-dimensional snapshots spanning over a time period of 0.45 ms are recorded for both the Cases 1 and 2. The temporal resolution is  $2 \times 10^3$  ms, and the corresponding cutoff frequency is  $5 \times 10^4$  Hz.

Figure 5.16 shows the energy distributions of the POD modes with pressure norm in the near field. The energy of the  $j$ th mode,  $E_j$ , is defined as

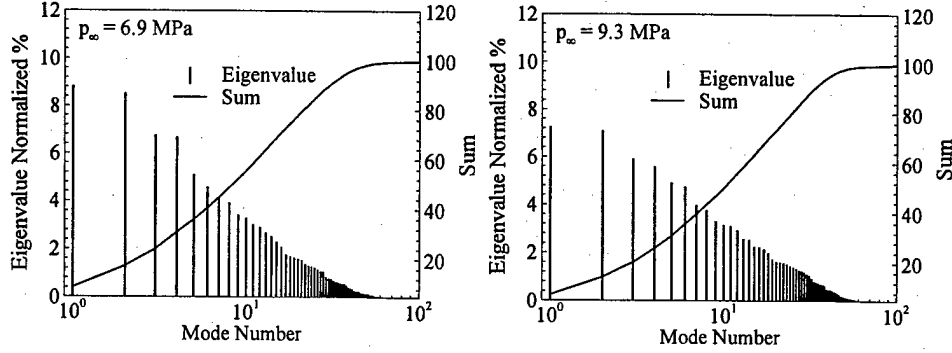


Fig. 5.16: Energies of POD modes in the near field ( $T_\infty = 300\text{K}$ ,  $u_{\text{inj}} = 15 \text{ m/s}$ ,  $T_{\text{inj}} = 120 \text{ K}$ ,  $D_{\text{inj}} = 254 \mu\text{m}$ ).

$$E_j = E \left( \frac{\|a_j(t)\varphi_j(x)\|^2}{2} \right) \quad (5.7)$$

Because of the large characteristic Reynolds numbers of the present jets, even the higher-order modes contain a considerable proportion of flow energy, which is consistent with the presence of smaller scales motions in the flowfield. To capture 90% of the total energy, the first 30 and 32 modes are required for Cases 1 and 2, respectively. For Case 1, the first POD mode accounts only for around 8.8% of the velocity fluctuation energy in the near field. Its spatial distribution (i.e., mode shape,  $\varphi_j(x)$ ) is visualized by the iso-surface of pressure in Fig. 5.17, which bears the axisymmetric ring shape near the injector and is slightly curled in streamwise after  $x/D_{\text{inj}} > 6$ , where the interaction of vortex becomes important. A very similar mode shape is observed for mode 2, which has almost the same energy level (8.5%) as mode 1. The phase differences between those two modes are  $\pi/2$  in both time and space. The local mean streamwise velocity, wavelength, and frequency are consistent and suggest the existence of well-organized vortical waves around the jet core. The dominant frequency of those two modes is

$2.6 \times 10^4$  Hz, between the most amplified frequency of the shear-layer ( $3.5 \times 10^4$ ) and the frequency of the jet prefer mode ( $1.8 \times 10^4$ ). The third and fourth modes also exhibit a vortical wave-like behavior, but the size of the wave structures decreases. Their mode shapes have a mixed axisymmetric and helical distribution, which shows the competing of helical and axisymmetric instability waves near the injector. The dominant frequencies of their time-varying coefficients are  $3.2 \times 10^4$ , close to the most amplified frequency of the shear-layer instability.

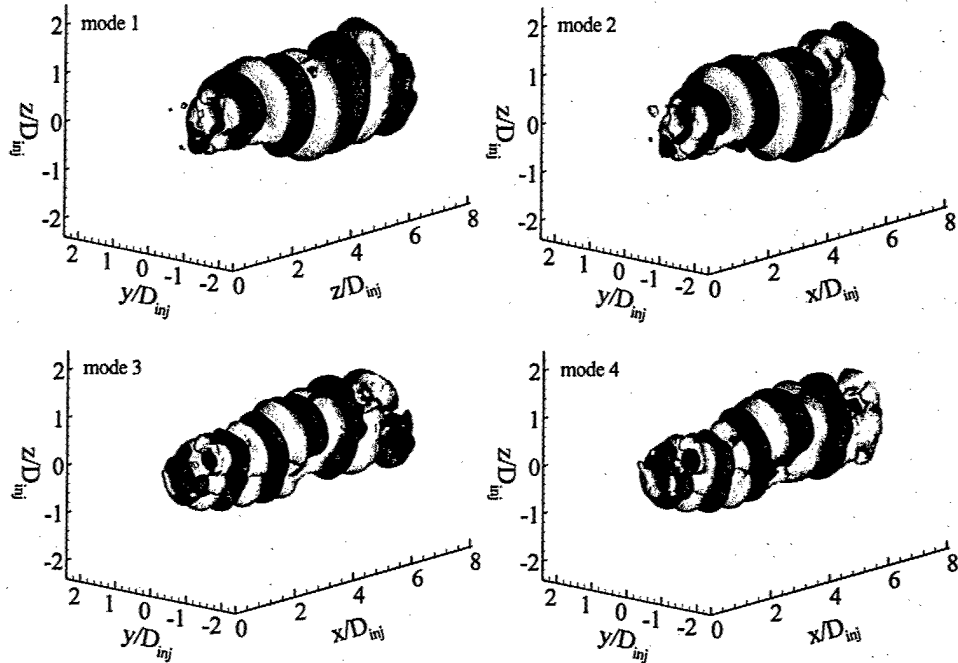


Fig. 5.17: Most energetic pressure POD modes visualized with iso-surfaces of pressure ( $p_\infty = 6.9 \text{ MPa}$ ,  $T_\infty = 300 \text{ K}$ ,  $u_{inj} = 15 \text{ m/s}$ ,  $T_{inj} = 120 \text{ K}$ ,  $D_{inj} = 254 \mu\text{m}$ ).

Compared with Case 1, the energy is more evenly distributed into each mode in Case 2. The first two modes account for only 7.2% and 7.1% of the total energy, respectively (see Fig. 5.16). The most energetic mode shapes are presented in Fig. 5.18. Similarly, the first two modes represent the well organized vortical wave around the jet core because they share the same mode shape, dominant frequency, wave length, and the phase differences are  $\pi/4$  in both time and space. The spatial distributions mainly bear the axisymmetric ring, but are stretched in the

streamwise due to the vortex interactions. The growth and decay spatial distributions observed by Arndt et al. (1997) in the pressure fluctuation adjacent to a constant-density turbulent jet are repeated. Unlike that of Case 1, the flow structures in the third and fourth modes of this case have a relatively longer length scale. A streamwise doubling is presented at the axial location  $x/D_{inj} = 5$  and is consistent with a pairing phenomenon. The dominant frequencies of their time varying coefficients,  $a_j(t)$ , are around 19000 Hz, very close to the passage frequency after the first paring. It seems the vortical motions after paring possesses an important portion of energy in Case 2.

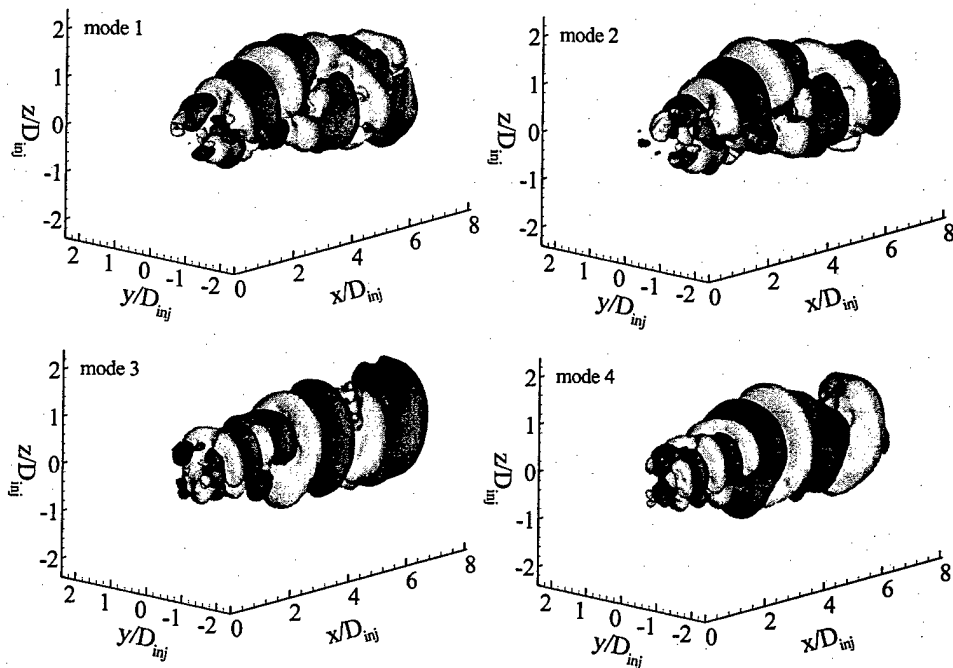


Fig. 5.18: Most energetic pressure POD modes visualized with iso-surfaces of pressure ( $p_\infty = 9.3 \text{ MPa}$ ,  $T_\infty = 300 \text{ K}$ ,  $u_{inj} = 15 \text{ m/s}$ ,  $T_{inj} = 120 \text{ K}$ ,  $D_{inj} = 254 \mu\text{m}$ ).

Those observations, so far, indicate that the stronger initial density stratification could prohibit the instability wave growth and delay the vortex paring. Therefore, the initial helical and axisymmetric instability waves are relative stable and pose a considerable portion of energy in

Case 1. As the density stratification abates with an elevated pressure in Case 2, both vortex shedding and paring are strengthened and become the most energy containing flow motion.

#### 5.4 Summary

A three-dimensional large-eddy-simulation has been conducted to investigate cryogenic fluid jet evolution at supercritical conditions. The near-field dynamics of the turbulent jet is well captured, and the influences of real-fluid thermodynamics on the jet evolutions in terms of mean and high-order turbulence properties are identified. The major results are summarized below.

1. The jet dynamics is largely dictated by the local thermodynamic state. The fluid layer with intense properties variations tends to separate the injected fluid from the hot ambience. The jet core is surrounded by a string of large-density-gradient regions, which exerts a stabilization effect on the large-scale wave motions. Both the instability-wave growth and vortex paring are inhibited.
2. The underlying mechanism of hydrodynamic instability is analyzed by examining the vorticity and vorticity magnitude transport equations. It is found that the stretching and titling is dominant in the vorticity production. Baroclinic torque rivals in magnitude with stretching term at the upstream. Its influence decays with the reduction of density stratification.
3. A local volume expansion occurs in the transition region as the injected fluid is heated by the hot ambience, which has considerable influence on both the mean and turbulence properties. Treating the supercritical fluid jet simply as a variable-density incompressible jet without considering the severe property variations could lead to unexpected error in the near field.
4. The density stratification and volume expansion decay as fluid is convected downstream. Their effects on the far-field flow evolution could be simplified by choosing a proper virtual

origin. In the downstream region ( $30 < x / D_{inj} < 35$ ), both the velocity and Reynolds Stress components match that of the incompressible turbulent jets.

5. POD analysis is employed to identify the detail jet dynamics in the near field. The results indicate that the strong initial density stratification could prohibit the instability wave growth and delay the vortex paring.

## Chapter 6

### High-pressure LOX and Methane Mixing

#### **6.1 Problem Description**

Extensive experimental and theoretical studies have been conducted to provide detailed understanding of cryogenic propellant mixing and combustion under both trans- and supercritical conditions. Most of those studies were focused on the LOX/GH<sub>2</sub> system. For future development of high-performance reusable liquid rocket engines, the mixing and combustion of LOX and methane have recently attracted considerable interest. The key issues of concern include injector performance, combustion efficiency, stability, and soot formation.

In this chapter, the numerical model developed and validated above is employed to explore various fundamental physiochemical mechanisms associated with injection and mixing of LOX and methane under supercritical pressure. Results not only enhance the basic understanding of the subject problem, but also provide a quantitative basis to identify the key design parameters and flow variables that exert strong influence on this process.

A schematic diagram of the model injector employed in the study is illustrated in Fig. 6.1. Co-flowing methane (outer) and oxygen (inner) streams are injected at the inlet and separated by a 0.3 mm thick LOX post. The inner diameter of the LOX post is 1.2 mm, and that of the methane duct is 2.4 mm. The injector is the same as that employed by Gurliat et al. (2003) to study LOX/GH<sub>2</sub> combustion. To simplify the problem, the computational domain starts from the faceplate of the injector and includes only part of the combustion chamber. Fully developed turbulent pipe flow velocity profiles are assumed for the injected streams at the injector outlet.

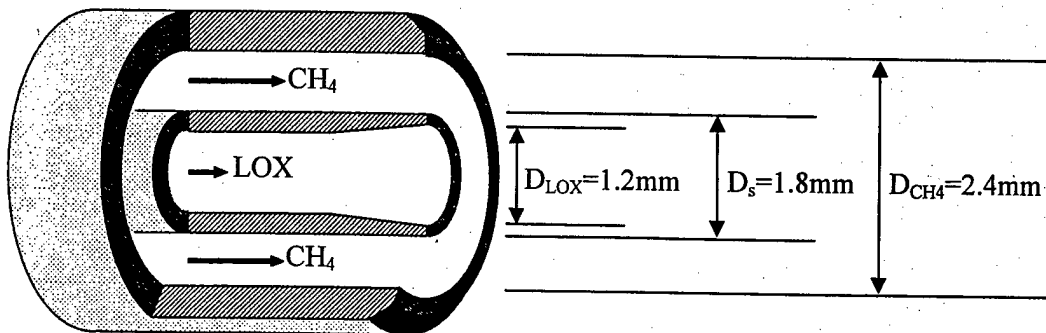


Fig. 6.1: Schematic of shear co-axial injector employed in the simulation.

In the cases considered, the combustion chamber is preconditioned with gaseous methane at 300 K and a reference pressure of 100 atmospheres. The injection temperature and velocity of the streams are varied to obtain a representative and comparable set of thermophysical and fluid dynamic characteristics. Case 1 provides subcritical conditions within the two streams, where the methane and oxygen injection temperatures of  $T_1 = T_2 = 150\text{K}$  are specified. In Case 2, the temperature of the methane stream is set at a supercritical value  $T_2 = 220\text{K}$ , and that of oxygen is fixed at  $T_1 = 150\text{K}$ . As a result, the two streams are mixing in a transcritical state. For reference, the critical points of the propellants are listed in Table 6.1. Since thermo-physical properties play a significant role in determining the flow evolution at high-pressure, their variations are plotted over the fluid state of concern in Fig. 6.2 and Fig. 6.3 for methane and oxygen, respectively.

Table 6.1: The critical points of methane and oxygen.

	$P_c$ (atm)	$T_c$ (K)	$V_c$ (L/mol)
Methane	46	190	0.099
Oxygen	50	154	0.076

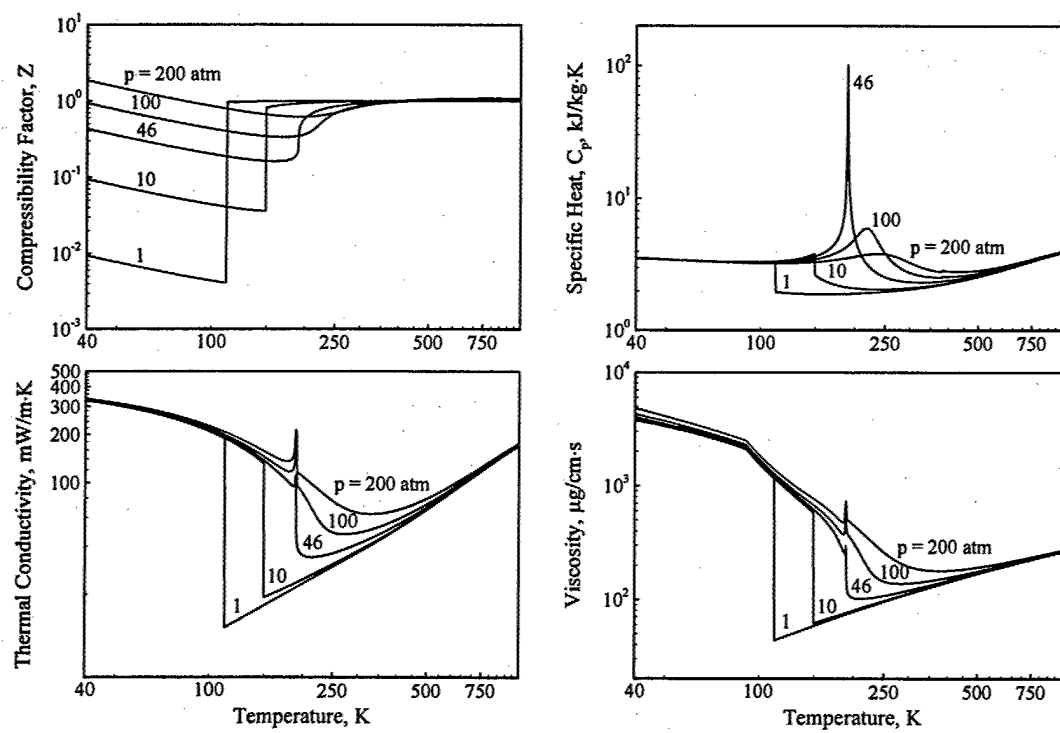


Fig. 6.2: Thermo-physical properties of methane as functions of pressure and temperature.

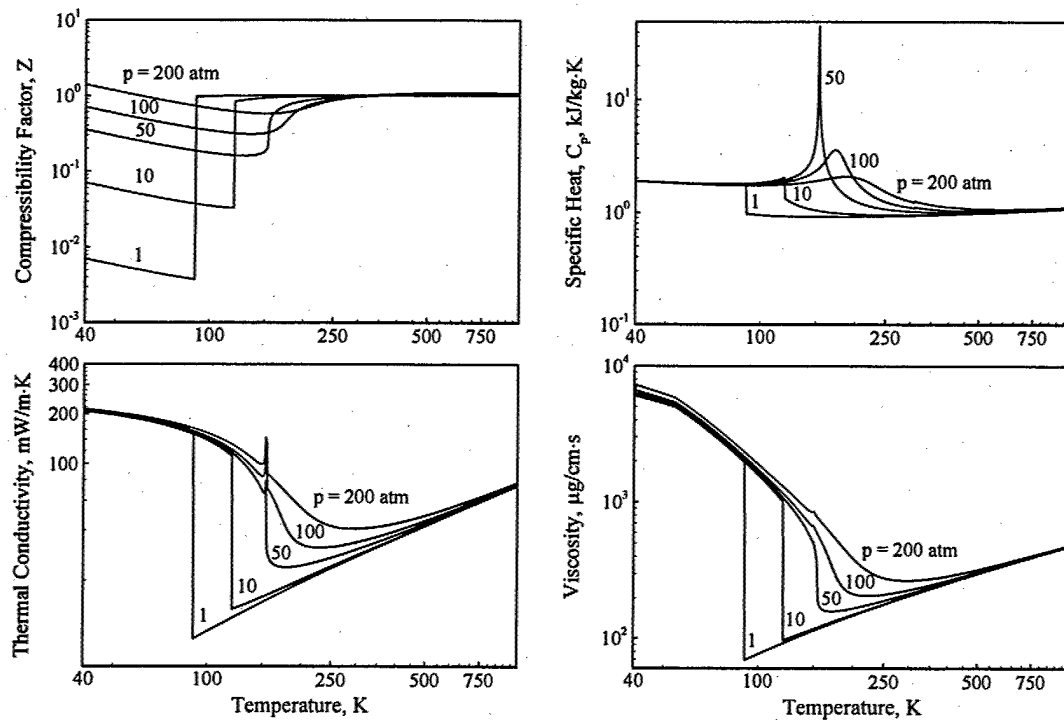


Fig. 6.3: Thermo-physical properties of oxygen as functions of pressure and temperature.

Three factors should be considered when selecting the injection velocities of methane and oxygen: 1) it is desirable to specify mass flow rates typically employed in practical system; 2) it is desirable to minimize respective Reynolds numbers due to the stringent requirement to resolve the characteristic turbulence scales; and 3) it is desirable to maximize the velocity ratio of the streams. Presently, the injection velocities of the two streams are chosen to match the mass ratio of the experiments conducted by Singla et al. (2004). The relevant parameters associated with simulation conditions are summarized in Table 6.2.

Table 6.2: Simulation conditions for the analysis of high-pressure LOX/methane injection and mixing process. Subscript 1 denotes the oxygen stream, and subscript 2 denotes the methane stream.

	Case 1	Case 2
p (atm)	100 atm	100 atm
$T_1$ (K)	150	150
$T_2$ (K)	150	220
$T_\infty$ (K)	300	300
$\rho_1$ (kg/m <sup>3</sup> )	800	800
$\rho_2$ (kg/m <sup>3</sup> )	360	180
$\rho_\infty$ (kg/m <sup>3</sup> )	75	75
$\rho_1/\rho_2$ , $\rho_1/\rho_\infty$	2.2, 10.6	4.4, 10.6
$u_1$ (m/s)	10	10
$u_2$ (m/s)	30	60
$u_1/u_2$	0.33	0.17
$\rho_1 u_1 / \rho_2 u_2$	0.74	0.74
$a_1$ (m/s)	461	461
$a_2$ (m/s)	1070	390
$M_1$	0.022	0.022
$M_2$	0.028	0.154
$Re_1$	$14.6 \times 10^4$	$14.6 \times 10^4$
$Re_2$	$4.9 \times 10^4$	$16.4 \times 10^4$

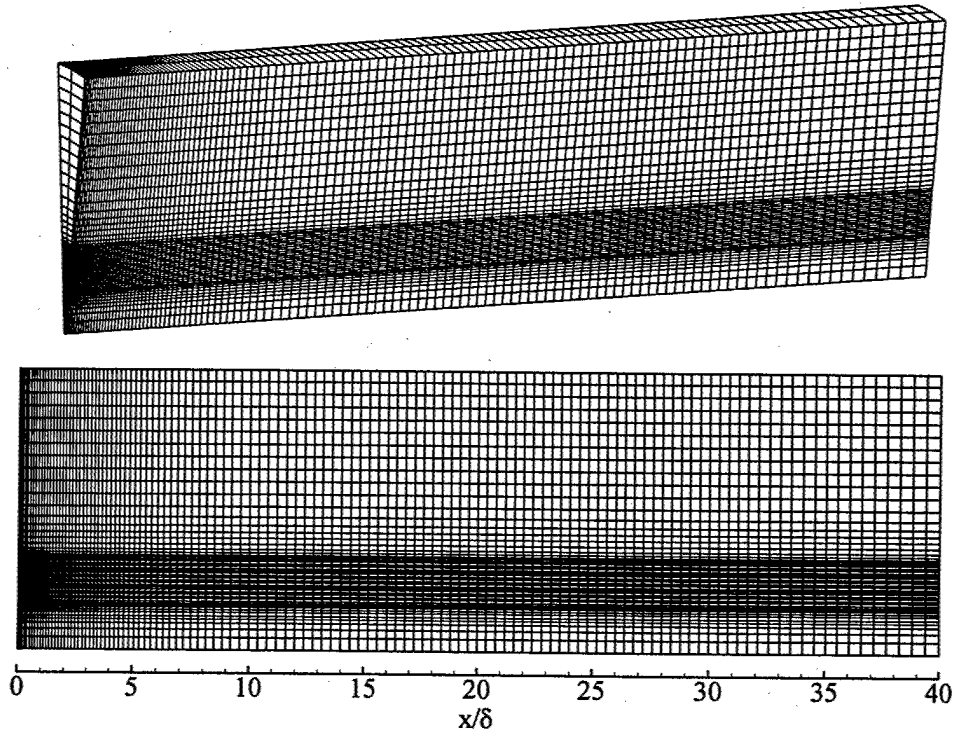


Fig. 6.4: Grid system employed in the simulation (at one-fourth original grid density).

The computational domain downstream of the injector measures a length of  $40 \delta$  and a radius of  $12\delta$ , where  $\delta$  is the thickness of the LOX post. The dimensions are sufficient to minimize the effect of the far-field boundary conditions on the near-injector flow evolution. Because of the enormous computational efforts required for calculating the three-dimensional flowfield, only a cylindrical sector with period boundary conditions specified in the azimuthal direction is treated herein (see Fig. 6.4). The entire grid system consists  $360 \times 200$  points along the axial and radial directions, respectively. The grid size falls in the inertial sub-range of the turbulent kinetic energy spectrum estimated based on the inlet Reynolds number of the LOX stream. To resolve the wake region and the vortical structures which shed off the LOX post tip, 40 radial points are used to cover the splitter. The grids are clustered in the shear-layers and near the solid walls to resolve the predominant processes and large property gradient. The computational domain is divided into 36 blocks, with each calculated on a single processor of a

distributed-memory parallel computer. The physical time step is  $0.5 \times 10^{-3}$  ms, and the maximum CFL number for the inner-loop pseudo-time integration is 0.7. For each case, simulation is conducted for 12 flow-through times (i.e., 10 ms) to obtain statistically meaningful data.

Fully developed turbulent pipe flow velocity profiles are assumed for the injected streams. Turbulence properties at the inlet are specified by superimposing broadband disturbances onto the mean velocities. The disturbances are generated by a Gaussian-random number generator with an intensity of 10% of the mean quantity. The temperature and species distributions are specified with top-hat profiles. The extrapolate boundary condition with a fixed back pressure is imposed at the outlet and the radial boundaries. The no-slip adiabatic condition is employed for the solid wall connected to the injector.

## 6.2 Presentation of Results

### 6.2.1 Instantaneous Flow Dynamics

Figure 6.5 presents the vorticity and oxygen mass fraction fields near the injector faceplate. Three shear-layers are formed at the beginning. The weakest one is generated around the LOX jet, and the other two emerge from the inner and outer boundaries of the high-speed annular methane stream. A large scale vortex sheds from the upper tip of the LOX post. As it grows up, the two shear-layers separated by the post merge together at the axial location  $1.0\delta$  to  $1.5\delta$  away from the injector faceplate. After that, only the inner vortex string and the outer shear-layer exist. The coaxial injection of water without a splitter between the two streams is studied by Rehab et al. (1997). They reported that the evolution of the outer layer is dominant over the inner one. Presently, the inner vortex string is stronger and influences the dynamics of

the outer layer. Those vortices seem to preserve the same wave-length until paring or interaction with the outer layer. Since mass diffusion is inhibited at supercritical pressure, the mixing of the two streams is mainly resultant from the entrainment effect of those large eddies, which occurs during both their initial growth stage and interactions. For both two cases, the methane stream pinches the LOX jet at the end of the potential core.

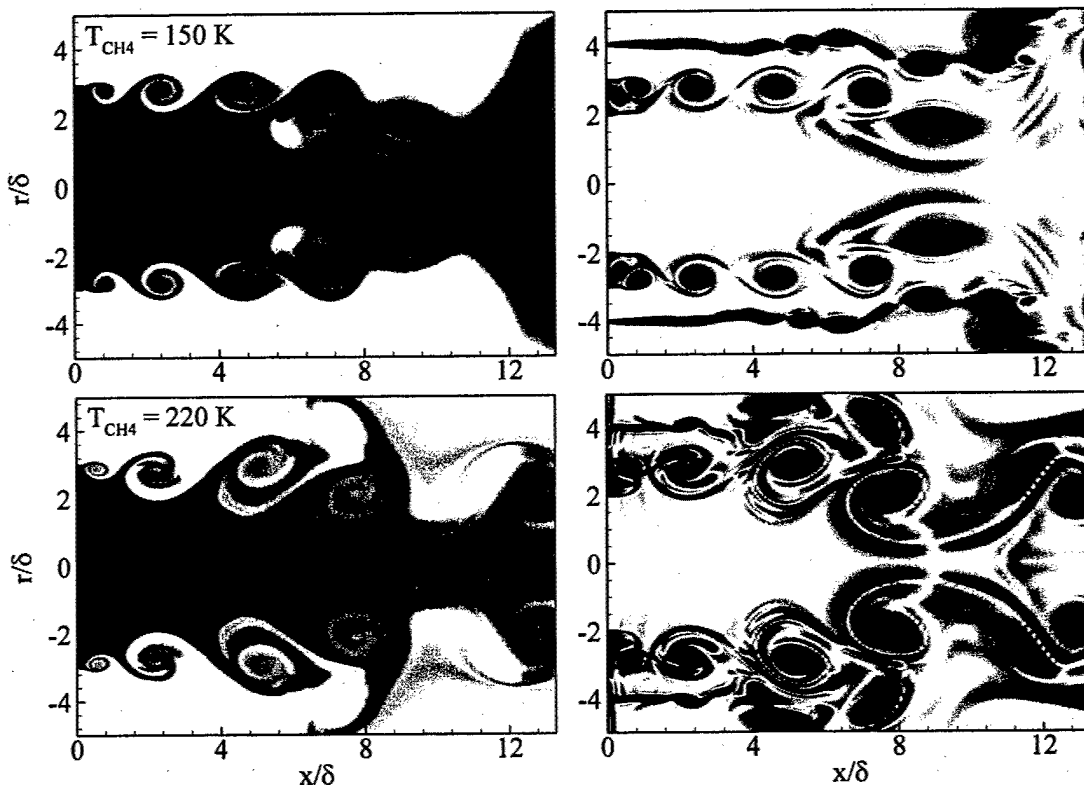


Fig. 6.5: Snapshots of oxygen mass fraction and vorticity fields of co-axial injection of LOX and methane at conditions 1 and 2 in Table 6.2.

Although the mass ratio is kept the same as that of Case 1, the acceleration of the methane stream in Case 2 has substantial influence on the flow evolution. The vortices formed behind the LOX post are stronger with enlarged length scales. They spread the oxygen much wider and pinch the central stream earlier. The outer-shear layer becomes unstable, and the associated vortex shedding starts at an upstream location. The nonlinear interactions among

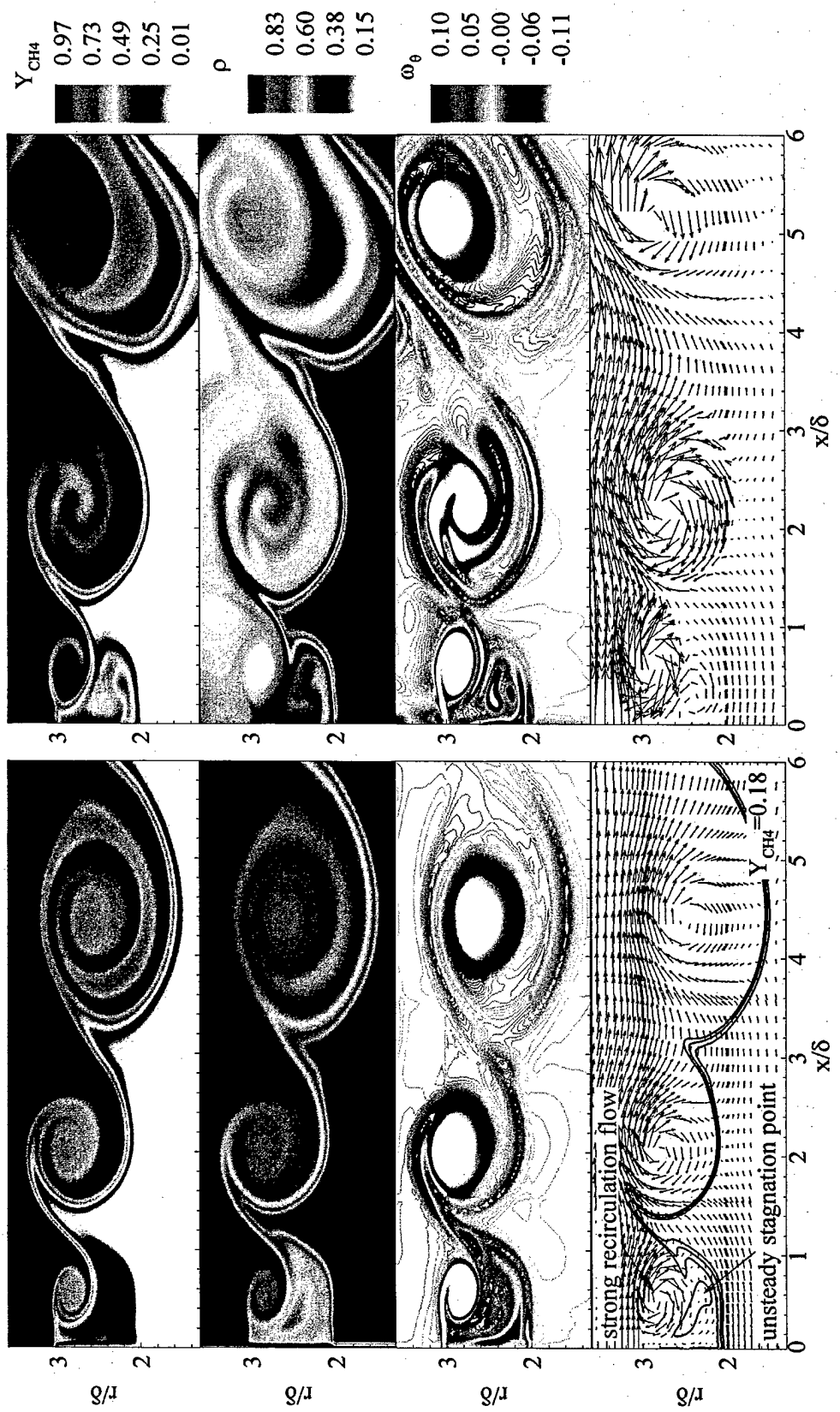


Fig. 6.6: Mass fraction, density, vorticity, and velocity vector fields in the region near the LOX post for Cases 1 and 2 in Table 6.2.

vortices make the flowfield much more complicated with the emergence of small structures.

Both the inner and outer potential cores are reduced in Case 2.

Figure 6.6 presents methane mass-fraction, density, normalized vorticity, and velocity vector fields in the regime downstream of the splitter. Mixing of two propellants occurs immediately behind the LOX post. A vortex sheds from the intermediate shear-layer in a manner analogous to that produced at a backward facing step. Its growth downstream gives rise to the merge of two shear layers separated by the LOX post. Due to the density stratification, the energy-containing flow motions are concentrated in the lighter methane stream and entrain the denser oxygen into it. The near-field flow evolutions are further illustrated in the vorticity and velocity vector fields, in which the large scale vortices and the wake region are manifested. In the LOX/GH<sub>2</sub> system, those vortices play a crucial flame-holding role in the combustor. They consist of partly preburned hydrogen rich gas. After the evaporating LOX mixes and reacts with hydrogen in these eddies, the hot product again mixes with the incoming high-speed stream and circulates back. Since the flow velocity approaches stagnation conditions in those regions, stationary turbulent combustion is possible. More effort is required to quantify the effect of those structures and the associated transport for LOX and methane combustion.

As the velocity of the methane stream increases in Case 2, the length and strength of the large eddies are enhanced; however, the wake region is slightly reduced. Since density of methane decreases at the supercritical temperature, the stratification effect becomes more influential in the near field. Large-scale vortices are more apt to concentrate in the light fluid. Severe velocity variation occurs between the inner and outer streams. As a result, a large strain rate emerges around the LOX jet boundary.

Besides the initial growth of the large-scale vortices, their interaction is another important mechanism governing the entrainment and mixing (Ho and Huerre, 1984). The evolution of the vorticity field over one cycle of vortex paring in Case 1 is illustrated in Fig. 6.7. At the beginning

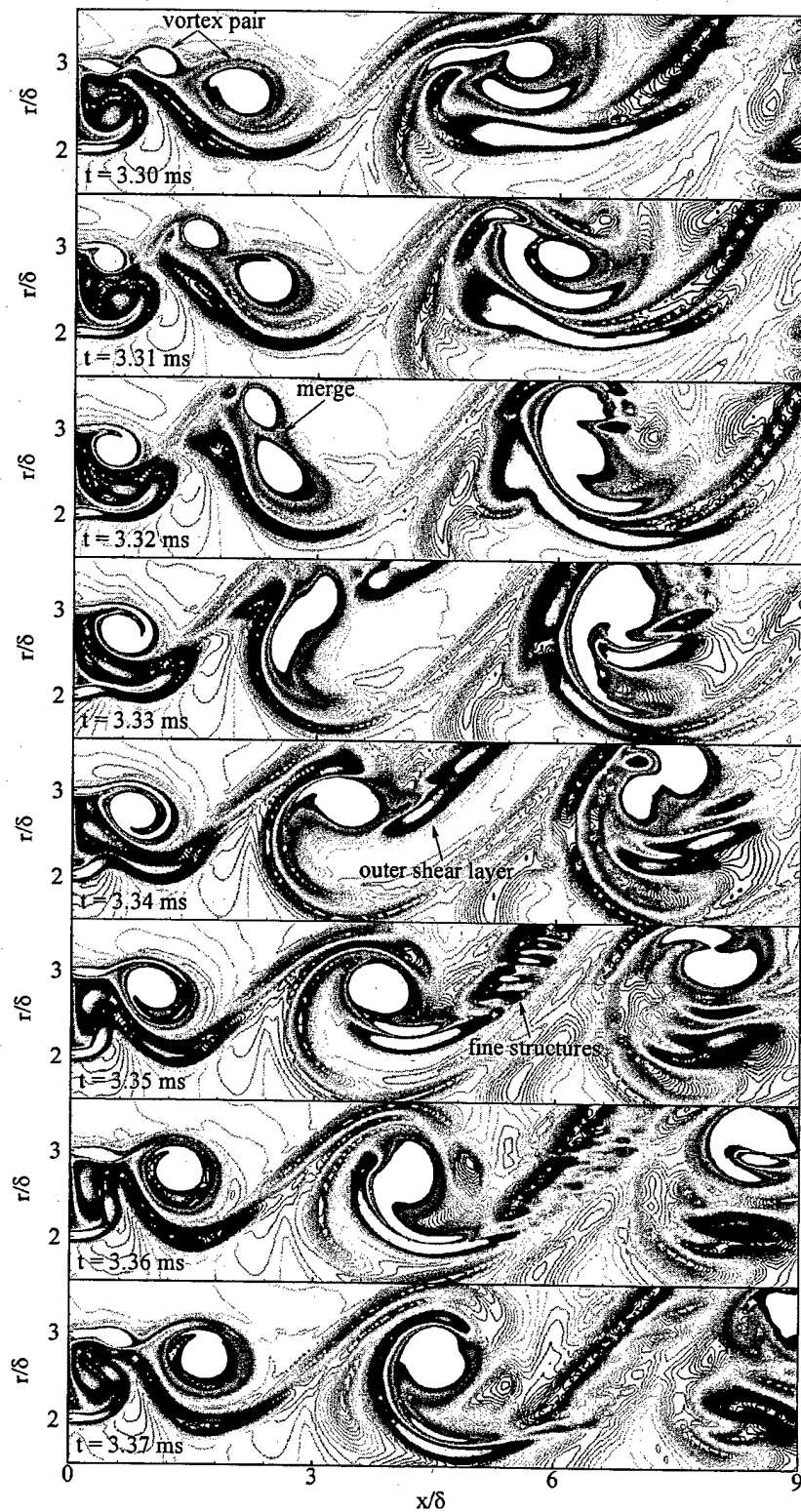


Fig. 6.7: Time evolution of vorticity field over one cycle of vortex pairing of Case 1 in Table 6.2 .

the vortices emerge from the LOX post tip and are displaced to different radial locations due to their phase difference. Owing to the radial velocity gradient, the two vortices will acquire different speeds, and the later vortex could catch the earlier one. They finally merge into a single structure by kinematic induction. During the merging, the outer shear-layer is engulfed into the center. The nonlinear interaction between the vortices and the outer shear-layer causes it break into a series of fine structures. Large strain rates occur, and the interface between the two fluids are enhanced due to the vortex pairing. Since a greater interfacial area could provide more space for the short range molecular diffusion, the total yield of mixing increases.

### 6.2.2 Spectral Analysis

In order to check whether the outer and inner shear-layers evolve according to the fundamental mechanism of Kelvin-Helmholtz instability, the power spectral density of the radial velocity oscillations at the different axial locations are calculated for each case.

The results of Case 1 along the inner and outer shear-layers are presented in Fig. 6.8 and Fig. 6.9, respectively. In this case, the vortex shedding switches between two modes intermittently. The first mode is illustrated in the snapshot of the vorticity field in Fig. 6.8. A string of discrete vortex sheds from the LOX post tip at the dominant frequency of 18.4 kHz. Those vortices tend to keep the same length scale until they merge or interact with the outer shear-layer. In the second mode (see the snapshot of the vorticity field in Fig. 6.9), a strong vortex forms at 18.4 kHz, and is followed by a weaker one with a smaller length scale. The oscillation at 11.9 kHz, which appears at probe locations 2 and reaches the maximum at location 3, is resultant from their paring. Based on Ho and Huerre (1984), the location 3, where two vortices are aligned cross stream, is defined as the paring location. The oscillations at discrete frequency

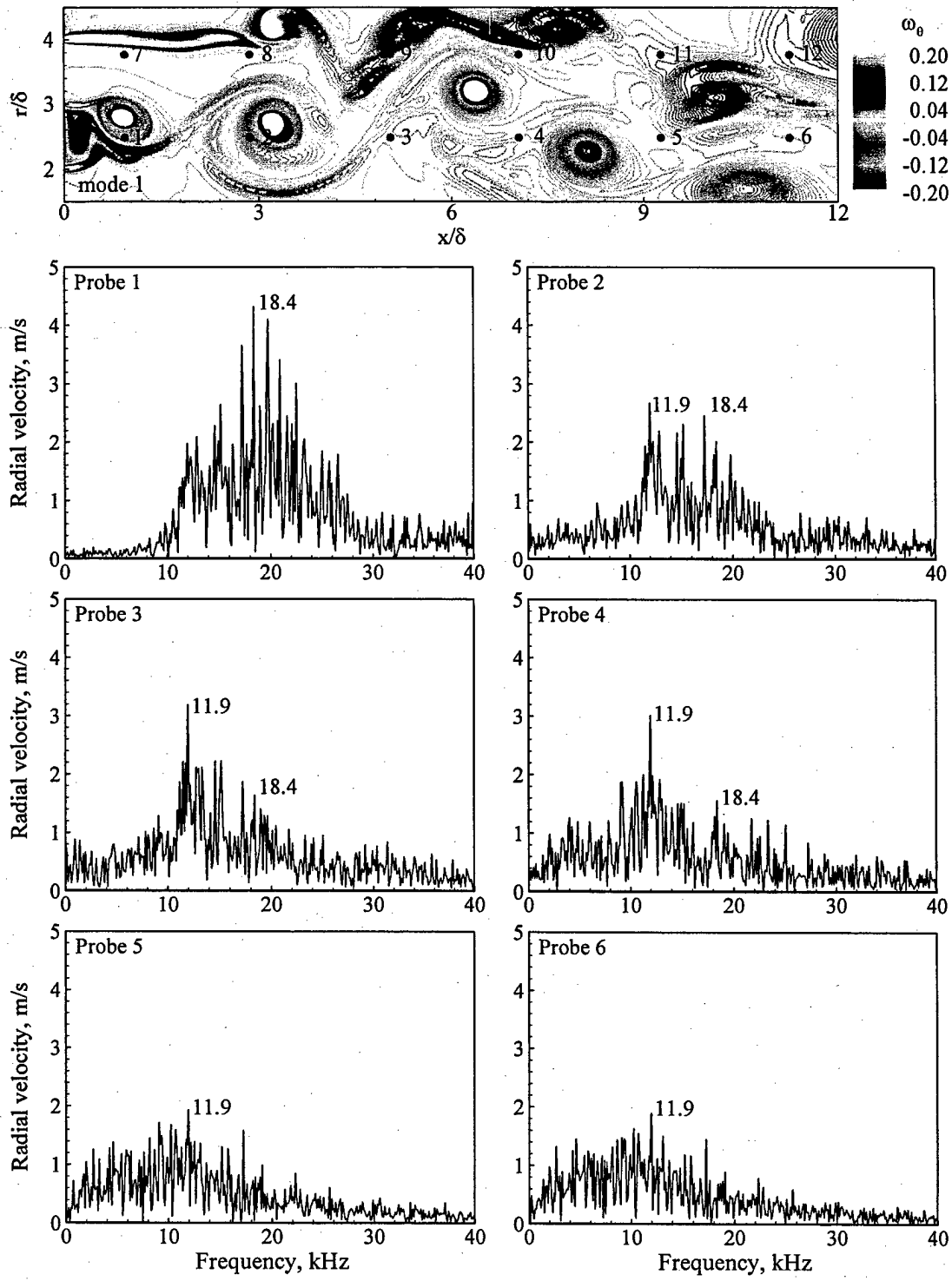


Fig. 6.8: Frequency spectra of the radial velocity oscillations along the inner shear-layer, Case 1 in Table 6.2.

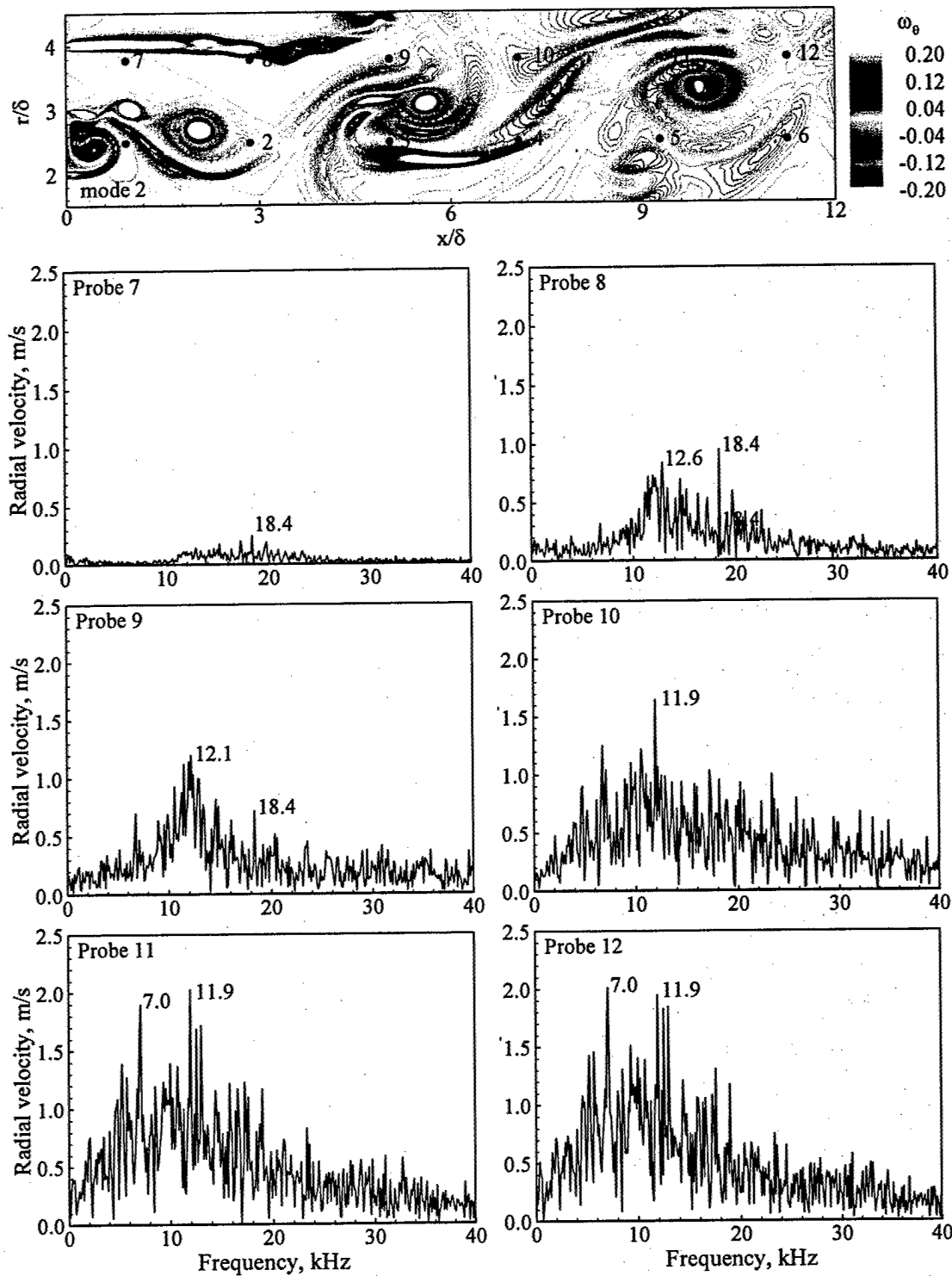


Fig. 6.9: Frequency spectra of the radial velocity oscillations along the outer shear-layer, Case 1 in Table 6.2.

decay downstream along the inner shear-layer. The spectra frequencies become broadband at probe locations 5 and 6.

Although the outer shear-layer is forced by the oscillation generated from the inner vortex string, it is relatively stable upstream. Sinuous wave structures appear at location 8, where both the initial vortex shedding frequency of the inner layer (18.4 kHz) and an oscillation close to 11.9 kHz are dominant. Since the dynamics of the outer shear-layer is coupled with that of the inner one, the passage frequency at 11.9 kHz is dominant through locations 9 to 12, accompanied with broad band spectral.

The characteristic frequency of the coaxial jet without splitter between two streams was studied by Rehab et al.(1997) and Carlos et al.(2003). They reported that the outer shear-layer dynamics is dominant over the inner one, and its most amplified frequency can be predicted by the correlation proposed by Schadow and Gutmark (1992) for the shear-layer instability. Based on the same correlation, the most unstable frequency and its first subharmonics of each shear-layer in Case 1 are estimated and presented in Table 6.3. The momentum thickness used in the correlation is estimated based on the inlet velocity profile. None of those predictions match the present simulation results. The existence of the second length scale (i.e. LOX post thickness) in the current shear coaxial injector significantly changes the flow dynamics. The vortices shed from the LOX post tip in a manner analogous to the vortex generating behind a backward facing step, where the eddy formation frequency is of order  $o(0.1)$  in terms of Strouhal number defined based on the bulk velocity of the outer stream and the step thickness (Wee et al., 2004).

Table 6.3: The predicted initial vortex shedding frequency ( $f_1$ ) and its first sub-harmonics ( $f_2$ ) of each shear-layer in Case 1.

	outer layer	intermediate layer	inner layer
$f_1$	45 kHz	45 kHz	3.7 kHz
$f_2$	22.5 kHz	22.5 kHz	1.85 kHz

Because the methane stream is accelerated in Case 2, the inner vortex shedding frequency increases to 22.1 kHz (see Fig. 6.10 and Fig. 6.11). This frequency, again, dose not match any predictions based on the hydrodynamic instability mechanism (see Table 6.4), but falls into the frequency range of vortex shedding off the backward facing step. The second mode of vortex shedding observed in Case 1 is inhibited. Only the discrete vortices shed from the LOX post tip. The first and the second paring of those eddies occur relatively upstream. The initial shedding oscillation decays rapidly, and its first and second sub-harmonics emerge at the probes 3 and 4, respectively. The dynamics of the outer shear layer becomes more complicated. Although the oscillations from the inner mixing layer still act as the forcing on it, the associate vortex shedding frequency exhibits a relatively smaller value. The vortices formed from the outer layer are strong and induce the inner vortex string to move upward. Therefore, their initial shedding frequency and passage frequency after the first paring appear at the probes 10 to 12.

Table 6.4: The predicted initial vortex shedding frequency ( $f_1$ ) and its first sub-harmonics ( $f_2$ ) of each shear-layer in Case 2.

	outer layer	intermediate layer	inner layer
$f_1$	105 kHz	105 kHz	3.7 kHz
$f_2$	52.5 kHz	52.5 kHz	1.85 kHz

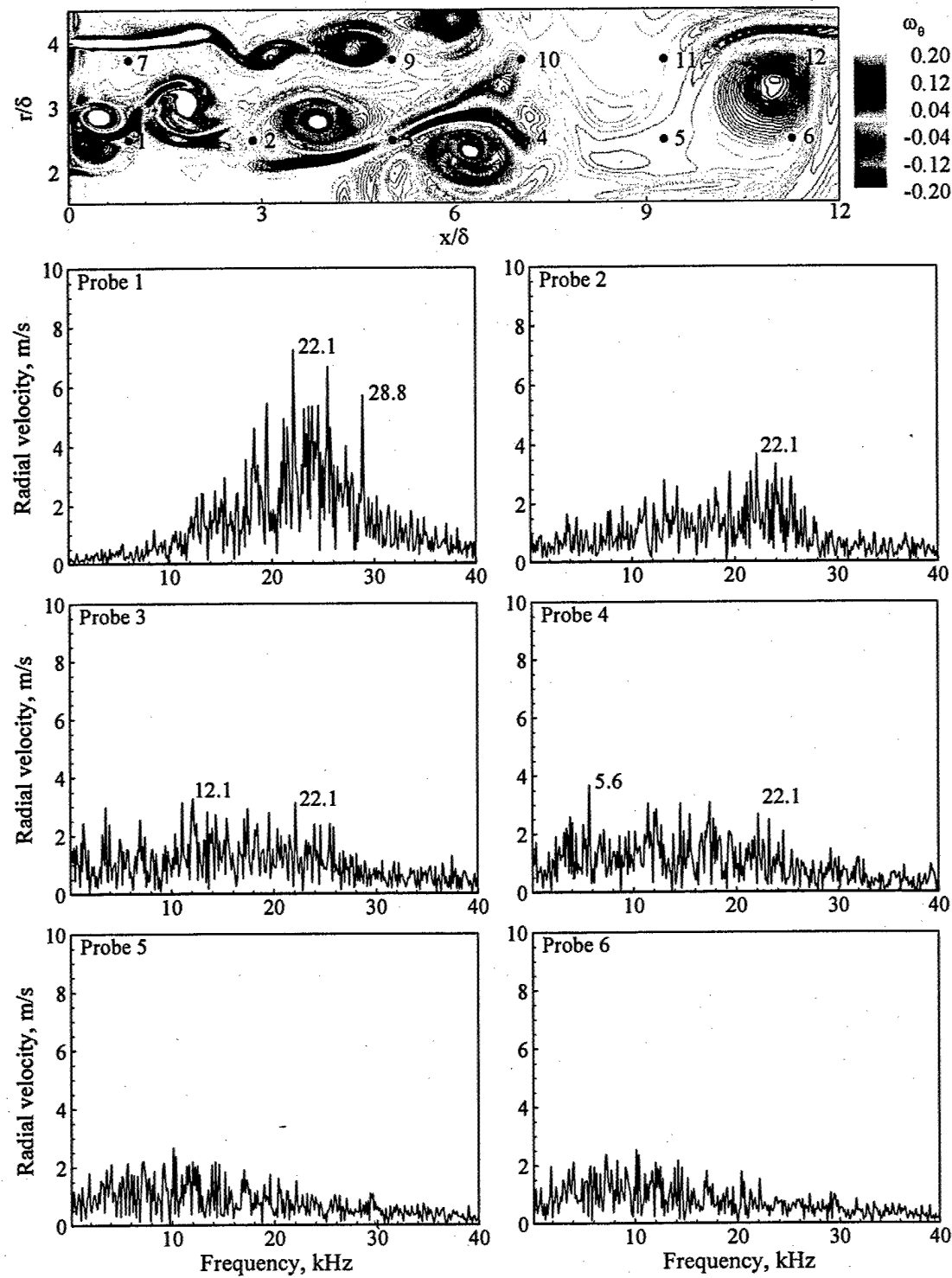


Fig. 6.10: Frequency spectra of the radial velocity oscillations along the inner shear-layer, Case 2 in Table 6.2.

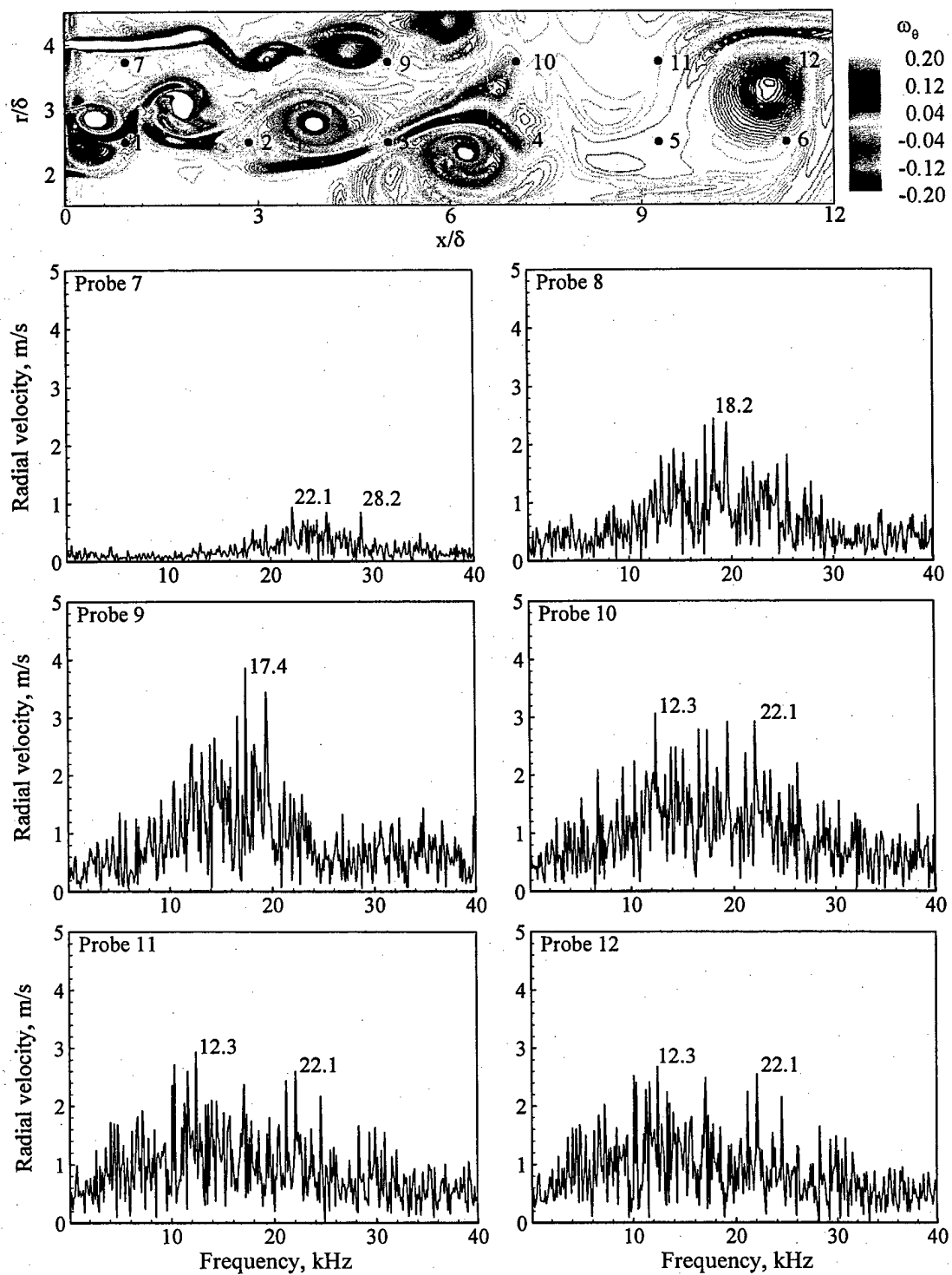


Fig. 6.11: Frequency spectra of the radial velocity oscillations along the outer shear-layer, Case 2 in Table 6.2.

### 6.2.3 Statistical Data Analysis

The statistical data are obtained by taking the long-time average of the instantaneous quantities over 8 ms (about 12 flow-through times) after the calculated flowfield has reached its stationary state. Figure 6.12 presents the time averaged axial velocity, turbulent kinetic energy (TKE), and oxygen mass fraction fields of two cases. For comparison purposes, the axial velocity and TKE are non-dimensionalized by the injection velocity of the LOX jet.

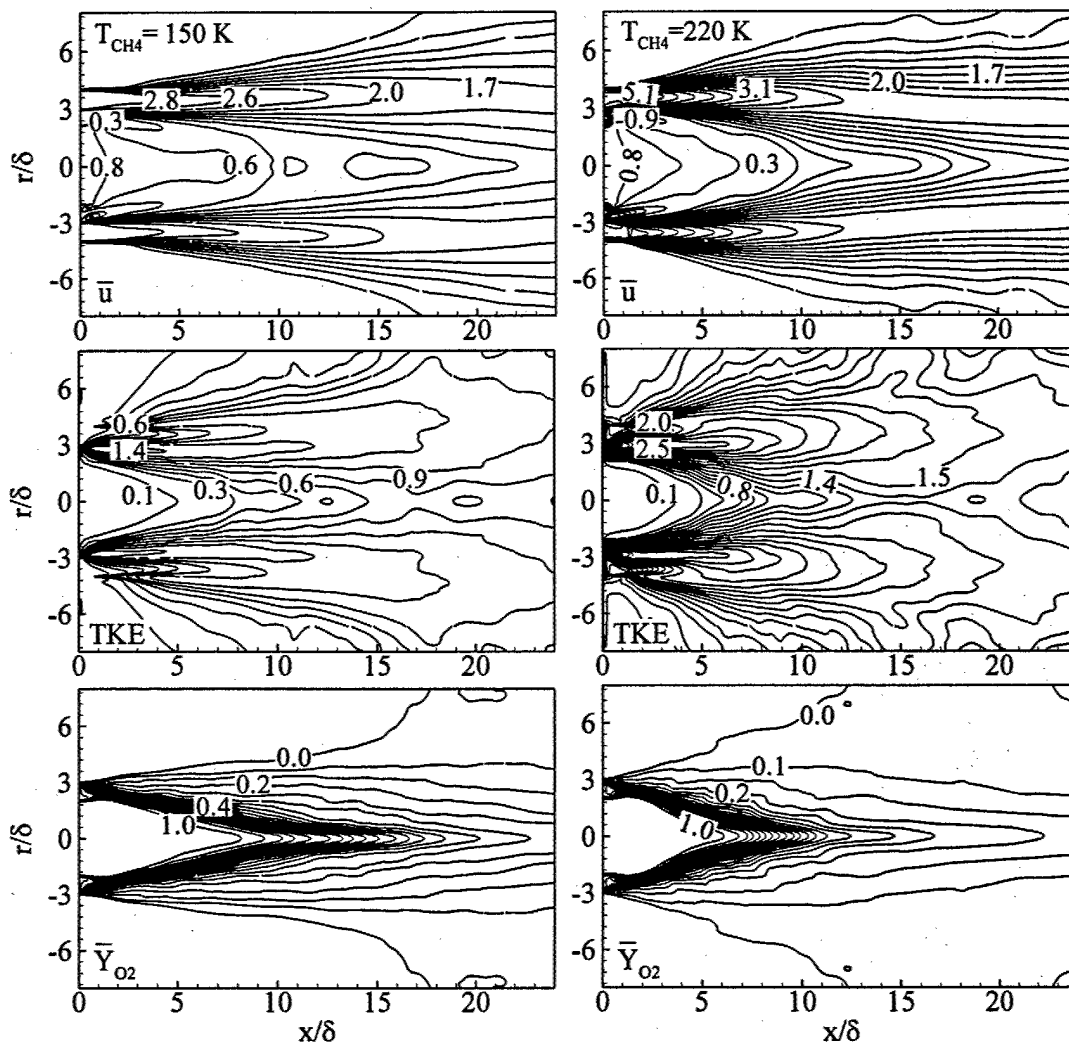


Fig. 6.12: Time averaged axial velocity, turbulent kinetic energy (TKE), and oxygen mass fraction fields of Cases 1 and 2 in Table 6.2.

Since the outer stream is faster, it is dominant in the velocity field and spreads both outward and inward. A wake with negative axial velocity is generated behind the LOX post. It has been reported that if the velocity ratio between the inner and outer streams is greater than a critical value, the wake may extend to the central region to form a recirculation zone. Although no recirculation is observed, the velocity of the LOX jet decays rapidly in Case 2 due to the influence from the stronger wake. The turbulent kinetic energy (TKE) is low in the LOX jet core and readily increases along the centerline. The intensive vortical flow motions in the inner and outer shear-layers give rise to the highest TKE concentration. The two regions merge downstream after the outer layer is engulfed into the center. The vigorous turbulent motion in Case 2 enhances the mixing process. Thus, the core of the LOX jet is reduced, and the oxygen mass fraction is distributed wider.

Figure 6.13 compares the radial distributions of the mean oxygen mass fraction, density, axial velocity, and turbulent kinetic energy at various axial locations, where  $r = 0$  corresponds to the centerline of the chamber. The top-hat mass fraction profiles close to the injector indicate the potential core of the LOX jet. A similar annular methane stream core is manifested by the staged density distributions. Both the inner and outer cores are reduced in Case 2. In addition, its relatively flatter oxygen mass fraction distributions imply a better mixing downstream.

The high speed annular stream and the wake with negative axial velocity are indicated in the axial velocity distribution at  $x/\delta = 2$ . As the wake extends into the center, the centerline velocity decays ( $x/\delta = 6$ ). The inner and outer shear-layers could be revealed by the peaks of the TKE distributions. They merge together at the axial locations  $x/\delta = 10$  and 6 for Cases 1 and 2, respectively.

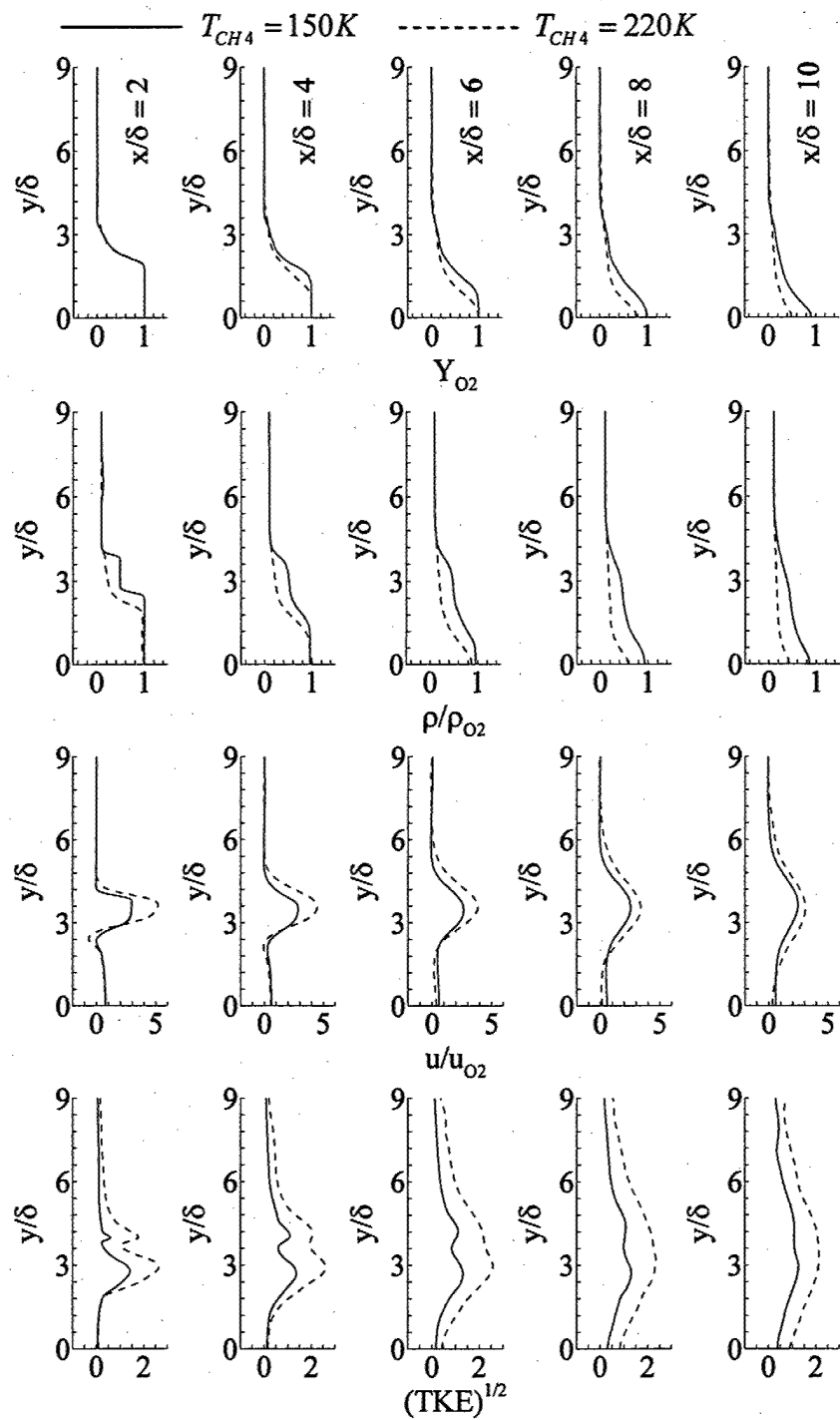


Fig. 6.13: Comparison of the radial distributions of the time averaged density, oxygen mass fraction, axial velocity, and turbulent kinetic energy at the different axial locations for Cases 1 and 2 in Table 6.2 .

Figure 6.14 compares the time-averaged velocity vector distributions near the LOX post. For clarity, the vectors are specified with the uniform length. A recirculation zone forms right behind the LOX post and extends  $2\delta$  downstream in Case 1. Its end is roughly indicated by the circular mark in the flowfield. As the outer stream velocity increases in Case 2, two counter rotating bubbles are generated in the wake, and the length of the recirculation zone is elongated to  $4\delta$ . The detail mechanisms of those structures on the flame stabilization will be quantitatively studied in the subsequent works.

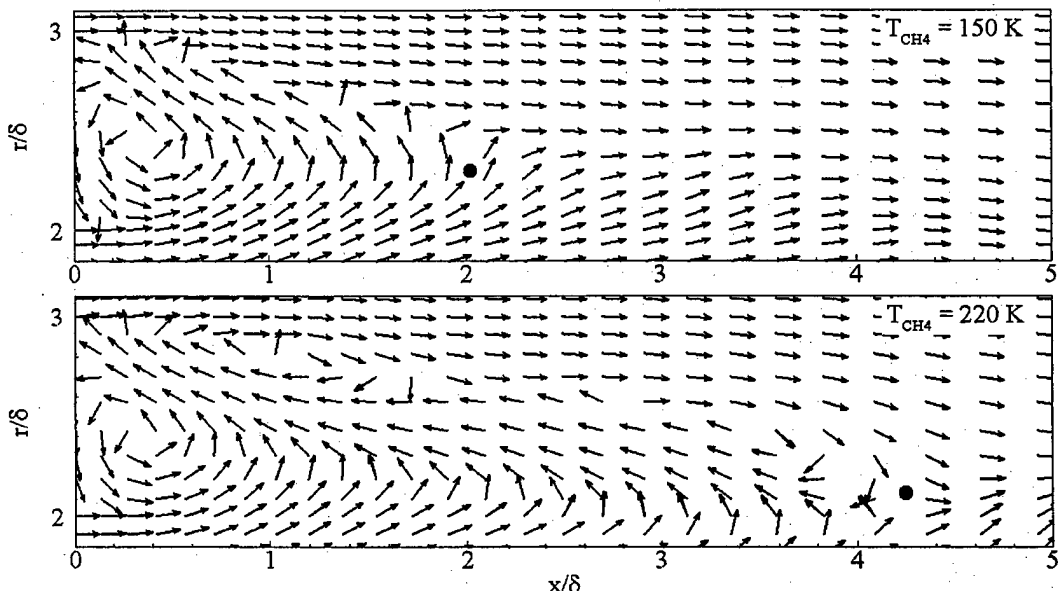


Fig. 6.14: Time-averaged velocity vector distributions near the LOX post of Cases 1 and 2 in Table 6.2.

The axial distributions of density, mass fraction, velocity, and turbulent kinetic energy along the centerline of the inner stream ( $r/\delta = 0$ ) are presented in Fig. 6.15. In the density and mass fraction distributions, their values remain unchanged until  $x/\delta = 9$  and  $x/\delta = 6$  for Cases 1 and 2, respectively, highlighting the existence of the potential cores. After the core, fluid density and oxygen mass fraction decrease rapidly and finally reach a steady level. Since the wake region extends into the center, centerline velocity decreases rapidly. The inner stream

almost reaches stagnation at  $x/\delta = 9$  in Case 2. After the outer stream pinches the inner one, the axial velocity is recovered.

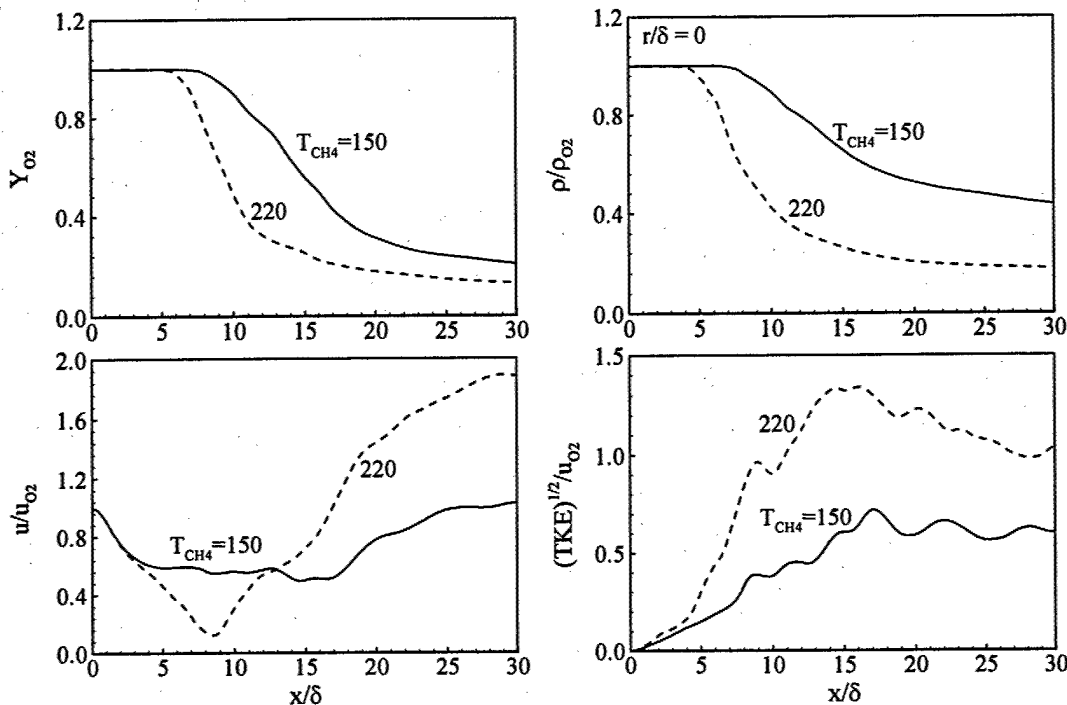


Fig. 6.15: Comparison of axial distributions of the time-averaged density, oxygen mass fraction, axial velocity, and turbulent kinetic energy along the centerline of the inner streams.

Based on the co-axial injection of water over a wide range of velocity ratios, Villermaux and Rehab (2000) proposed that the length of the inner potential core is inversely proportional to the velocity ratio

$$L/D = A \cdot \left(\frac{u_2}{u_1}\right)^{-1} \quad (6.1)$$

where the constant A ranges from 6 to 8. To take into account the density difference between two streams, the velocity ratio in Eq. 6.1 could be replaced by the square root of the momentum ratio

$M^{1/2} = (u_2/u_1)(\rho_2/\rho_1)^{1/2}$ . The resultant correlation takes the form

$$L/D = A \cdot M^{-1/2} \quad (6.2)$$

Based on this equation, the estimated potential core lengths are  $12\delta$  and  $9\delta$  for Cases 1 and 2, respectively. Those values are greater than those obtained from the numerical simulation. It should be noted that the correlation (i.e. Eq. 6.2) does not include the influence from the wake behind the LOX post because the thickness of the splitter is two order's smaller than the diameters of the streams in their experiments. Presently, the thickness of the splitter and the diameters of the jets are the same order. The existence of the wake region significantly changes the flow dynamics. The large energetic eddies shedding from the LOX post tip and their interactions facilitate the entrainment of the inertial dominant annular stream and give rise to a shorter inner potential core.

### 6.3 Discussion

Based on the results obtained, the near field of coaxial injection of LOX and methane could be characterized in Fig. 6.16. The two shear-layers generated from the upper and lower tips of the LOX post merge after the wake and form the inner mixing layer. This layer is dominant in the flowfield. The vortex shedding from the LOX post tip does not follow the hydrodynamic instability mechanism, but is in a manner analogous to the vortices produced at a backward facing step. The oscillations generated from the vortex shedding serve as a forcing on the outer mixing layer.

Compared with Case 1, methane is injected at a supercritical temperature in Case 2. To keep the same mass ratio, the outer stream velocity is increased. With the increase of the velocity and momentum ratios, turbulent mixing between the two streams is enhanced, and the potential core of the LOX jet is reduced. This agrees with the experimental observations of Singla et al. (2004). If the momentum ratio between the methane and LOX stream further increases, the wake

region may extend to the centerline and generate a recirculation zone. This flow regime helps to efficiently mix the outer and inner streams and stabilize the flame at the hot fire conditions.

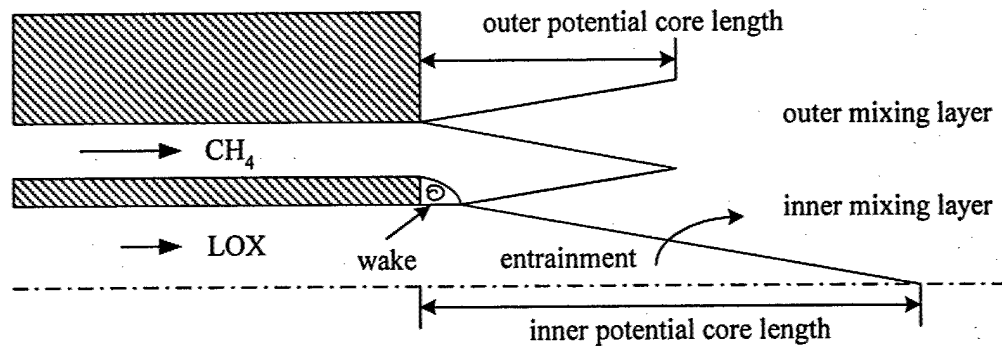


Fig. 6.16: Schematic of the shear coaxial injection of LOX and methane at supercritical conditions.

## Chapter 7

### High-Pressure LOX Swirl Injection

#### 7.1 Problem Description

Compared with a shear coaxial injector, an injector with central LOX swirling (see Fig. 1.6) distinguishes itself in many aspects. First, for the same pressure drop and liquid flowrate, the swirl injector could produce finer droplets, whose median diameter is 2.2 to 2.5-fold smaller than that of the shear injector. Second, a swirl injector is not sensitive to manufacturing errors, such as deviation from prescribed diameter and surface misalignment. In addition, its flow passage area is much larger than that of the shear ones with the same mass flowrate and consequently, the swirl injector is less susceptible to choking or cavitation. Although swirl coaxial injectors have been widely applied in liquid rocket propulsion systems, systematic investigations into their injection and combustion dynamics are lacking.

This chapter presents a series of simulations on the swirl injection of cryogenic fluid under supercritical pressures. Both the internal flow dynamics and the external mixing process of a swirl injector are investigated. Emphasis is placed on the effects of various scaling parameters on the injector performance. To help understand the physical phenomena involved, a theoretical model is established. Its predictions are consistent with the simulation results.

As a beginning, only the central LOX post of a coaxial injector is considered. It can be referred to as a simplex swirl injector, which includes three major parts: a tangential inlet, a vortex chamber, and a discharge nozzle, as shown in Fig. 7.1. The geometrical parameters of the studied injector are listed in Table 7.1. Presently, the diameters of the swirl chamber and the discharge nozzle are set identically. The geometrical characteristic constant ( $K$ ) is defined as

$K = A_n R_{in} / A_{in} R_n$ , where  $R_n$  is the nozzle radius,  $R_{in}$  is the radial location of the inlet passage center,  $A_n$  is the nozzle area, and  $A_{in}$  is the total area of the inlet passages. A swirl injector with the same mass flowrate (0.15 kg/s) and similar geometry has been successfully applied to the RD-0110 liquid rocket engine.

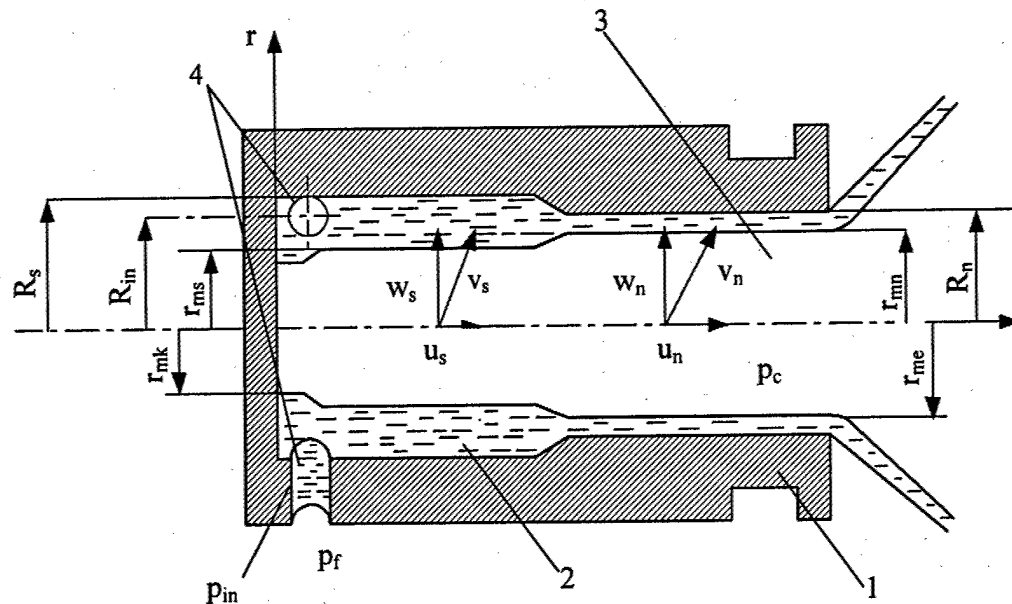


Fig. 7.1: Schematic of simplex swirl injector employed in the present study, 1-injector casing; 2-vortex chamber; 3-discharge nozzle, 4-tangential passages.

Table 7.1: Geometric parameters of the studied swirl injector

$R_s$ (mm)	$R_n$ (mm)	$R_p$ (mm)	$L$ (mm)	$K$	$\dot{m}$ (kg/s)
2.5	2.5	0.85	25	3.2	0.15

The computation domain includes the swirl injector and a portion of the combustion chamber connected to it, as shown in Fig. 7.2. Because of the enormous computational effort required for simulating the flowfield in the entire three-dimensional region, only a cylindrical sector with periodic boundaries specified in the azimuthal direction is treated herein. For a typical simulation, a two-dimensional grid system is generated. A  $50 \times 100$  grid is employed

inside the injector, and a  $150 \times 200$  grid is located outside. The grids are clustered near the wall to resolve the boundary layer and the rapid flow property variations. The mean grid size within the injector is around  $50 \mu\text{m}$ , which can roughly resolve the turbulence length scales in the inertial sub-range of the turbulent energy spectrum. The computational domain is divided into 13 blocks, with each calculated on a single processor of a distributed-memory parallel computer. The physical time step is  $1 \times 10^{-2}$  ms, and the maximum CFL number for the inner-loop pseudo-time integration is 0.7. For each case, simulation is conducted for 10 flow-through times (i.e., 0.1 s) to obtain statistically meaningful data.

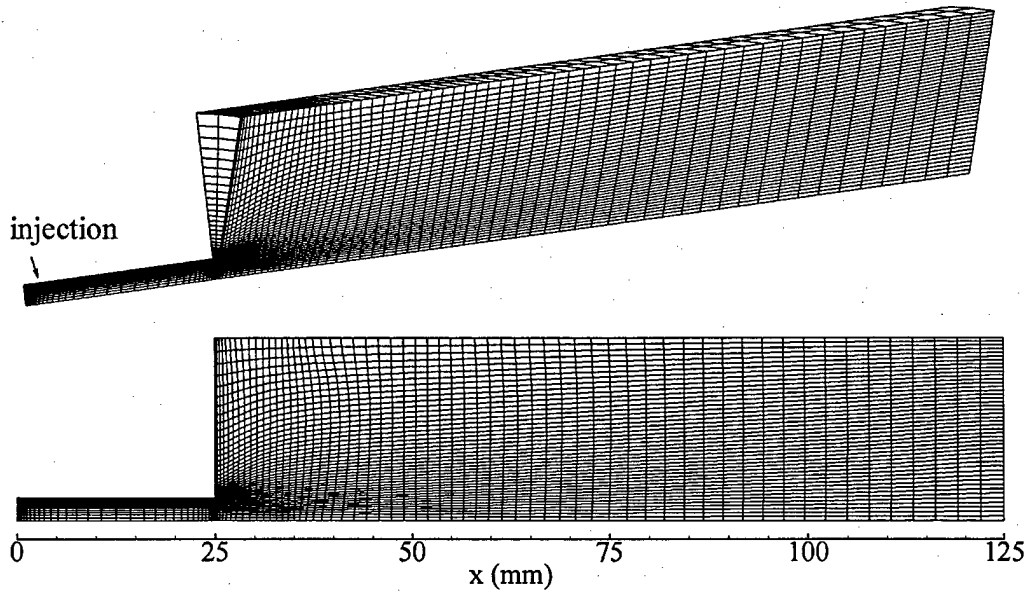


Fig. 7.2: Schematic of 2D axi-symmetric grid system at one-third of the original grid density.

Since it is impossible to simulate a round hole on the surface of the LOX post in an axisymmetric space, the tangential passage is modified as a slit. At the inlet boundary, the mass flowrate and temperature are specified. The pressure is extrapolated from the inner flowfield. The radial and azimuthal velocities are determined from the tangential inlet injection angle. Turbulence properties at the inlet are specified by superimposing broad-band disturbances with an intensity of 3% of the mean quantity onto the mean velocity profiles. The nonreflecting boundary

conditions are applied at the exit boundary, along with the specification of a back-pressure. At the radial direction, a second order extrapolation with a fixed pressure is adopted. Finally, the non-slip adiabatic conditions are enforced to the inner surface of the injector and the solid wall connected to it.

## 7.2 Simulation Results

Since surface tension vanishes and no droplet is formed at supercritical conditions, the parameters that can characterize the LOX swirling jets are the liquid film thickness ( $h$ ) and the spray cone angle ( $\alpha$ ) at the injector exit. Other physical variables needed to describe the flow evolution include the injector geometric constant ( $K$ ), the injector length ( $L$ ) and diameter ( $D$ ), the axial and azimuthal velocities of the swirling flow, and the thermodynamic properties of the injected and ambient fluids. Based on the *Buckingham Pi theorem*, two dimensionless equations can be obtained:

$$h/D = g(\rho_{inj}/\rho_\infty, \mu_{inj}/\mu_\infty, Re_L, K) \quad (7.1)$$

$$\alpha = \tan^{-1} u_n / w_n = g(\rho_{inj}/\rho_\infty, \mu_{inj}/\mu_\infty, Re_L, K) \quad (7.2)$$

The spreading angle can be calculated as the ratio of the axial velocity ( $u_n$ ) to the azimuthal velocity ( $w_n$ ) at the injector exit.  $\rho$  and  $\mu$  are the density and viscosity of the fluid, respectively. The subscript  $inj$  and  $\infty$  denote the injected and ambient conditions, respectively. The Reynolds number is defined as  $Re_L = \rho_{inj} u L / \mu_{inj}$ . Among those parameters, density and viscosity ratios are determined by the operating conditions. Other parameters are related to the geometry of a swirl injector. Their influences on the injector performance will be studied in detail.

Table 7.2: Test Conditions\*

Cases	$Re_L$	$\dot{m}$ (kg/s)	$K$	L (mm)	$\Delta L$ (mm)
1	$5.4 \times 10^6$	0.15	3.2	25	2.0
2	$3.8 \times 10^6$	0.10	3.2	25	2.0
3	$7.6 \times 10^6$	0.20	3.2	25	2.0
4	$5.7 \times 10^6$	0.15	3.2	25	0.5
5	$4.9 \times 10^6$	0.15	3.2	25	4.5
6	$1.1 \times 10^7$	0.15	3.2	50	2.0
7	$1.6 \times 10^7$	0.15	3.2	75	2.0
8	$2.2 \times 10^7$	0.15	3.2	100	2.0
9	$5.8 \times 10^6$	0.15	4.2	25	2.0

\*  $p_\infty = 10 \text{ MPa}$ ,  $\rho_{\text{inj}}/\rho_\infty = 7.6$

Liquid oxygen at a temperature of 120 K is injected into the swirl injector through the tangential passage. The temperature and pressure of the ambient gaseous oxygen remain at 100 atm and 300K, respectively. The pressure is below the combustion chamber pressure (200 atm) of the Space Shuttle Main Engine (SSME) but much higher than the critical pressure of oxygen (54 atm). The important scaling parameters studied are oxygen mass flowrate, LOX post length, tangential passage position, and swirl strength. The detail simulation conditions are presented in Table 7.2 , where  $\Delta L$  is the distance between the inlet center and the injector head end.

Two important definitions should be clarified before we present the simulation results and compare them with the theoretical predictions.

Unlike most of the cold flow experiments that were conducted at standard pressure using water as oxidizer simulant, the chamber pressure of the present simulation is chosen close to the operating pressure of the SSME, which is well above the critical point of oxygen. Although the injected dense fluid still possesses liquid-like density and characteristics, there is no distinction between the injected fluid and the ambience due to the vanishment of surface tension and enthalpy of vaporization. This leaves us freedom to define the injected fluid boundary. In the early works regarding convective high-pressure droplet vaporization, Meng et al. (2000) argued that the critical temperature and critical mass fraction of oxygen-hydrogen mixture are not located

at the same position without phase equilibrium, rendering the critical mixing state meaningless. Only the droplet boundary defined at the critical temperature of oxygen is physically meaningful and unique state. However, because part of the injected fluid is heated and the temperature could exceed the critical value, this definition becomes inaccurate in characterizing the liquid film thickness. Then, another definition based on mass conservation is introduced. The dense fluid boundary is defined at the radial position, where mass flowrate equals the initial value at the inlet.

In the classical inviscid theory, the spray cone angle is defined as twice the apex angle of the asymptotic cone to the hyperboloid of revolution corresponding to the profile of the spray (Tanasawa and Kobayasi, 1955). It can be calculated as the ratio of the circumferential to the axial velocities ( $\tan \alpha = \frac{w_n}{u_n}$ ) at the exit. In the experiments, the spray cone has curved boundaries because the ambience gas was entrained into the injected fluid, which imposes a major difficulty in its measurement. The cone angle is generally quoted as the angle formed by two straight lines drawn from the discharge orifice to cut the spray contours at some specified distance from the injector exit (Ortman and Lefebvre, 1985). Presently, the angle is computed directly from its definition.

### 7.2.1 Flow Structures

The characteristics of a typical swirl injector flowfield are presented in Fig. 7.3. Cold liquid oxygen is introduced tangentially into the injector through circular holes or slots. Since the injected fluid has only the azimuthal velocity, a swirling liquid film forms and moves downstream along the inner wall. The strong radial pressure gradient resultant from centrifugal force prevents the injected fluid from penetrating into the central region, where a whirling air core, called cavity, is formed. Because the chamber pressure (100 atm) is higher than the critical

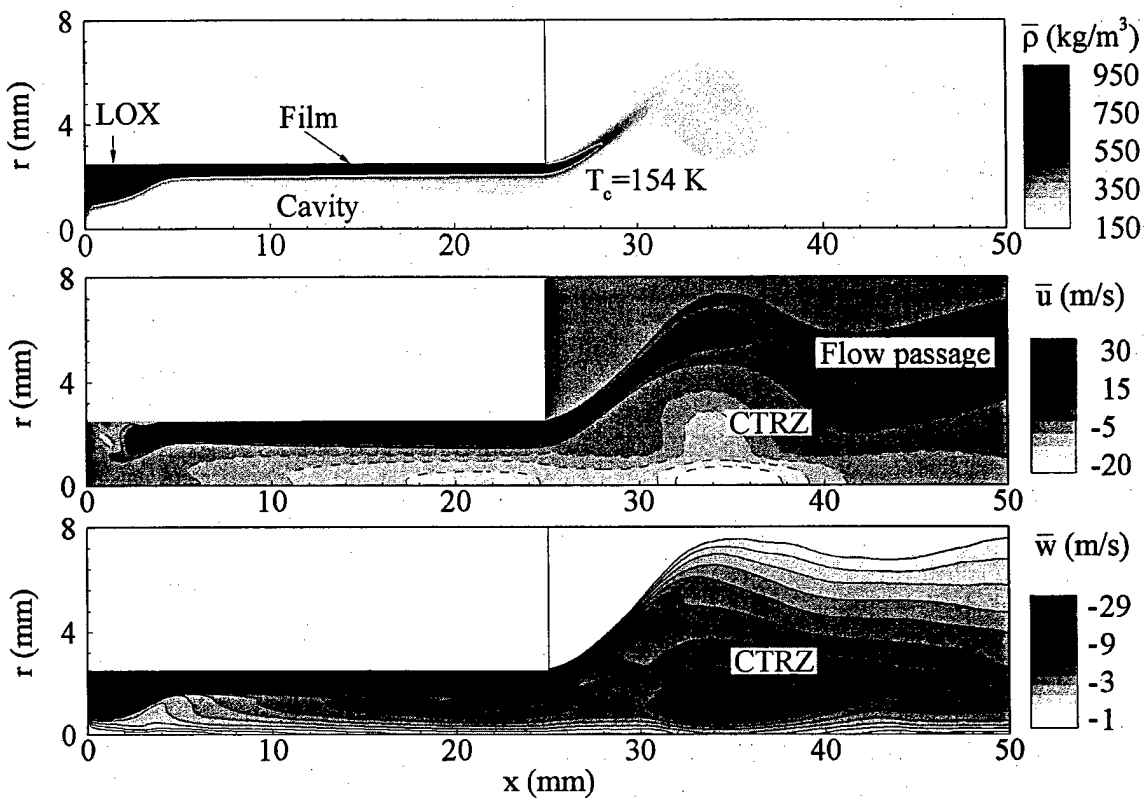


Fig. 7.3: Mean density and velocity components fields ( $p_{\infty} = 10 \text{ MPa}$ ,  $T_{inj} = 120 \text{ K}$ ,  $T_{\infty} = 300 \text{ K}$ ,  $\dot{m} = 0.2 \text{ kg/s}$ ,  $K = 3.2$ ).

pressure of oxygen (54 atm), no obvious boundary between the injected fluid and the air core is observed. The solid line on the density field is the critical isothermal ( $T = 154.6 \text{ K}$ ), which roughly represents the boundary between the injected fluid and the ambience. As the cold oxygen fluid discharges into the combustion chamber, the swirling fluid film spreads away from the exit. Since the hot ambience is entrained into the injected fluid, the fluid density decreases during the mixing and heating process, and its value exhibits a sudden drop across the critical isothermal. The azimuthal velocity and centrifugal force decrease simultaneously. Then, the flow passage shrinks toward the centerline. Near the injector exit, a slowly swirling gaseous region forms. The adverse pressure gradient in this region gives rise to recirculation flow and finally produces a central tornado recirculation zone (CTRZ). Presently, the recirculation flow even penetrates into

the LOX post. The extension of the recirculation region (wake region) into the discharge nozzle was also observed by Panda and McLaughlin (1994) in the experimental study on swirling jet instabilities at high swirl and large Reynolds numbers. They attributed it to the earlier burst of vortices. In the combustion chamber, the CTRZ could serve as a flame stabilization region, where the hot products are mixed with the incoming fuel and oxidizer mixture.

Figure 7.4 presents the mean velocity components, temperature, density, and compressibility distributions in radial direction at various axial locations. Based on the different evolution patterns observed, the flow motions inside the LOX post could be divided into three stages. At the developing stage ( $0 \leq x \leq 6\text{ mm}$ ), the injected fluid with strong swirling fills more than half of the tube, and the azimuthal velocity reaches the maximum magnitude at the dense fluid boundary. Compared with it, the axial velocity is smaller. The injected fluid shrinks to the wall promptly due to the centrifugal force. Meanwhile, the momentum transfers from its azimuthal component to the axial one. A balance is reached in the stable region ( $6 \leq x \leq 23\text{ mm}$ ), where the radial distributions of flow properties (i.e., velocity, film thickness, and thermo-physical properties) vary slowly along the axial direction. For example, only slightly variations of the axial velocity profiles can be observed at the axial positions  $x = 10\text{ mm}$  and  $18\text{ mm}$ . Inside the fluid layer, a thin boundary layer is generated, where the velocity components increase quickly from zero at the wall to a relative flat profile in the film. Since the length to diameter ratio (L/D) of the injector is much greater than that of the conventional swirl atomizer, viscous loss, which has been ignored in the classical theory, influences the axial and azimuthal velocity distributions, and should be included in an improved analytical model. Because the static pressure at the outlet equals the ambient pressure, the overpressure resultant from centrifugal force is transformed into the momentum flux, which gives rise to an acceleration of axial velocity with a decreasing in the film thickness near the injector ( $23 \leq x \leq 25\text{ mm}$ ).

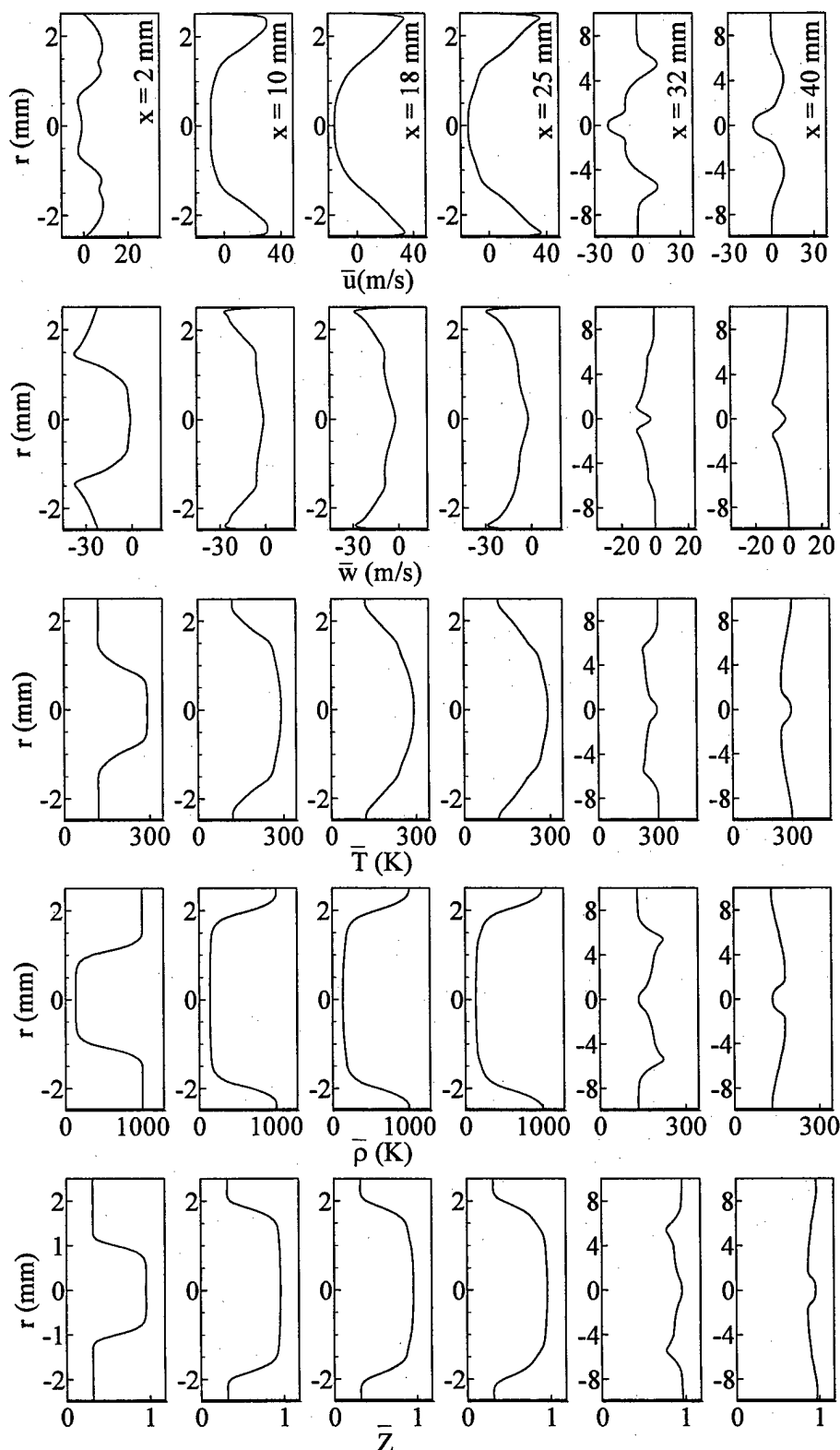


Fig. 7.4: Radial distributions of mean velocity components, temperature, density, and compressibility factor at various axial locations ( $\dot{m} = 0.2 \text{ kg/s}$ ,  $K = 3.2$ ).

The injected fluid discharges into the chamber as a hollow-cone sheet. After it interacts and mixes with the ambient gaseous oxygen, both the axial and the azimuthal velocities decay. At the axial position  $x = 40 \text{ mm}$ , the velocity distributions become flat with a recirculation region appearing in the chamber center, as indicated in Fig. 7.3.

In those profiles, no distinct boundary between the injected fluid and the ambient gas is observed. The thermo-physical properties of oxygen, including density, temperature, and compressibility factor, vary continuously in radial direction. The axial and azimuthal velocities change smoothly, too. In classical theory, the interaction between liquid and gas is neglected, and a solid body rotation with zero axial velocity is assumed for the core. To accurately model the swirl injector behavior at high-pressure, the transient fluid property variations and the interaction between the dense fluid and gaseous oxygen should be considered.

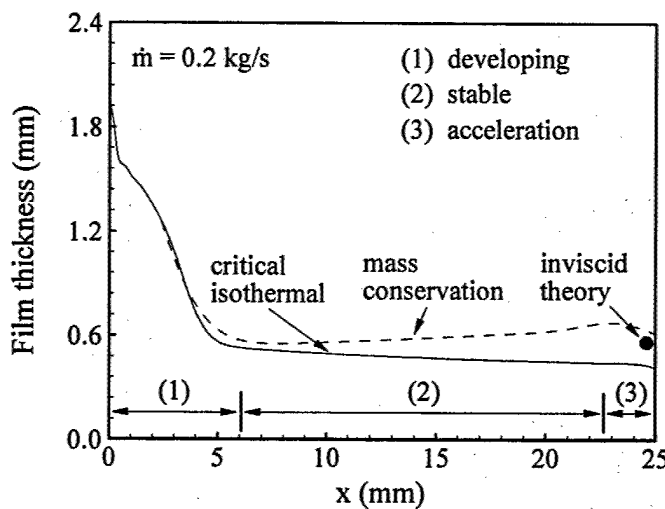


Fig. 7.5: The dense fluid film thickness along the injector inner wall ( $p_{\infty} = 10 \text{ MPa}$ ,  $T_{m_j} = 120 \text{ K}$ ,  $T_{\infty} = 300 \text{ K}$ ,  $\dot{m} = 0.2 \text{ kg/s}$ ,  $K = 3.2$ ).

The existence of the three different flow patterns again is illustrated in Fig. 7.5, in which the liquid film thickness along the wall is presented. Close to the head end, the flow motion in

the azimuthal direction is dominant. The dense fluid with strong swirling penetrates deeply into the center. The film thickness reaches the maximum right at the head end. The fluid shrinks to the wall until a minimum thickness is achieved at  $x=6\text{mm}$ . After that, the film thickness starts a monotonic increase with the boundary layer development. It drops promptly at the injector exit because the centrifugal over pressure transfers to the dynamic pressure, and the axial velocity is accelerated.

The differences between the critical isothermal and the injected fluid boundary based on the mass conservation are also manifested in Fig. 7.5. Because the cold fluid is heated by the hot ambience and its temperature could exceed the critical value (154.6 K), the critical isothermal always tends to move toward the inner wall of the LOX post, whereas, the film thickness increases along the wall. The critical isothermal could not accurately represent the injected fluid boundary. To fully take into account the transient fluid property variations and the viscous loss, only the thickness defined based on mass conservation is proper. The predictions from the viscous correction, obviously, are smaller than the numerical simulation results since the model does not accommodate the transient fluid property variations in the radial direction.

The temporal evolution of the temperature fields within one cycle of the vortex shedding is plotted in Fig. 7.6. Excited by the initial turbulence input at the tangential inlet, a succession of wavy structures with small amplitude forms and is convected downstream around the dense fluid boundary. In a rocket system, those waves are generated due to the presence of intense oscillation inside the combustion chamber or propellant feed-line (Bazarov and Yang, 1998). As the cold oxygen is discharged into the chamber, a sinuous spanwise Kelvin-Helmholtz billows develop along the outer boundary of the fluid cone. As these billows are carried downstream, a hairpin vortice appears and grows up. This vortice then interacts and merges together with other vortices. The flow oscillations are transferred back to the upstream location through the central recirculation zone and provide the feedback necessary for the onset of the next series of

instability waves. A self-sustained instability phenomenon exists. Its frequency is locked by the characteristic length and velocity of the recirculation zone. In Case 3, the length scale of the CTRZ is around 10 mm, and its characteristic velocity is order of tenth. The frequency is approximated as  $f = \frac{10}{0.01} \approx 1.0 \times 10^3 \text{ Hz}$ . Figure 7.7 presents the power spectral densities of the pressure fluctuations at six different locations for Case 3. A pressure oscillation at 836 Hz, which is the same order as the value estimated, is observed both outside and inside the injector.

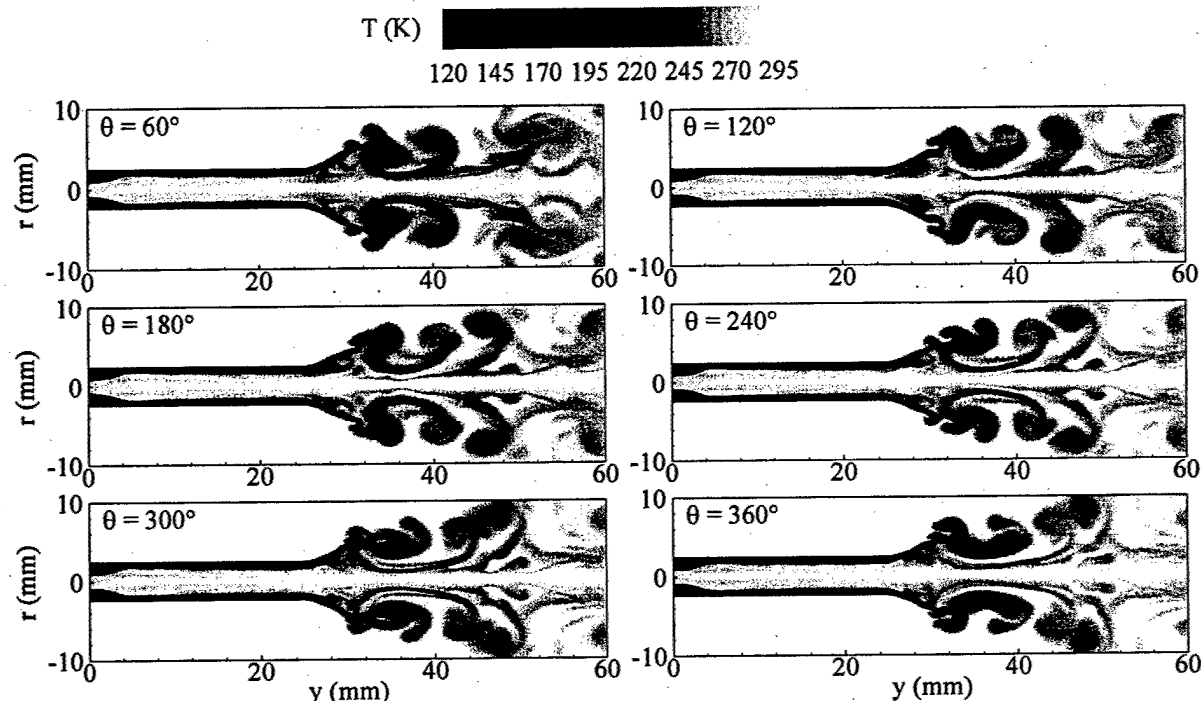


Fig. 7.6: Temporal evolution of temperature field over one cycle of the dominant vortex shedding process ( $p_\infty = 10 \text{ MPa}$ ,  $T_{inj} = 120 \text{ K}$ ,  $T_\infty = 300 \text{ K}$ ,  $\dot{m} = 0.2 \text{ kg/s}$ ,  $K = 3.2$ ).

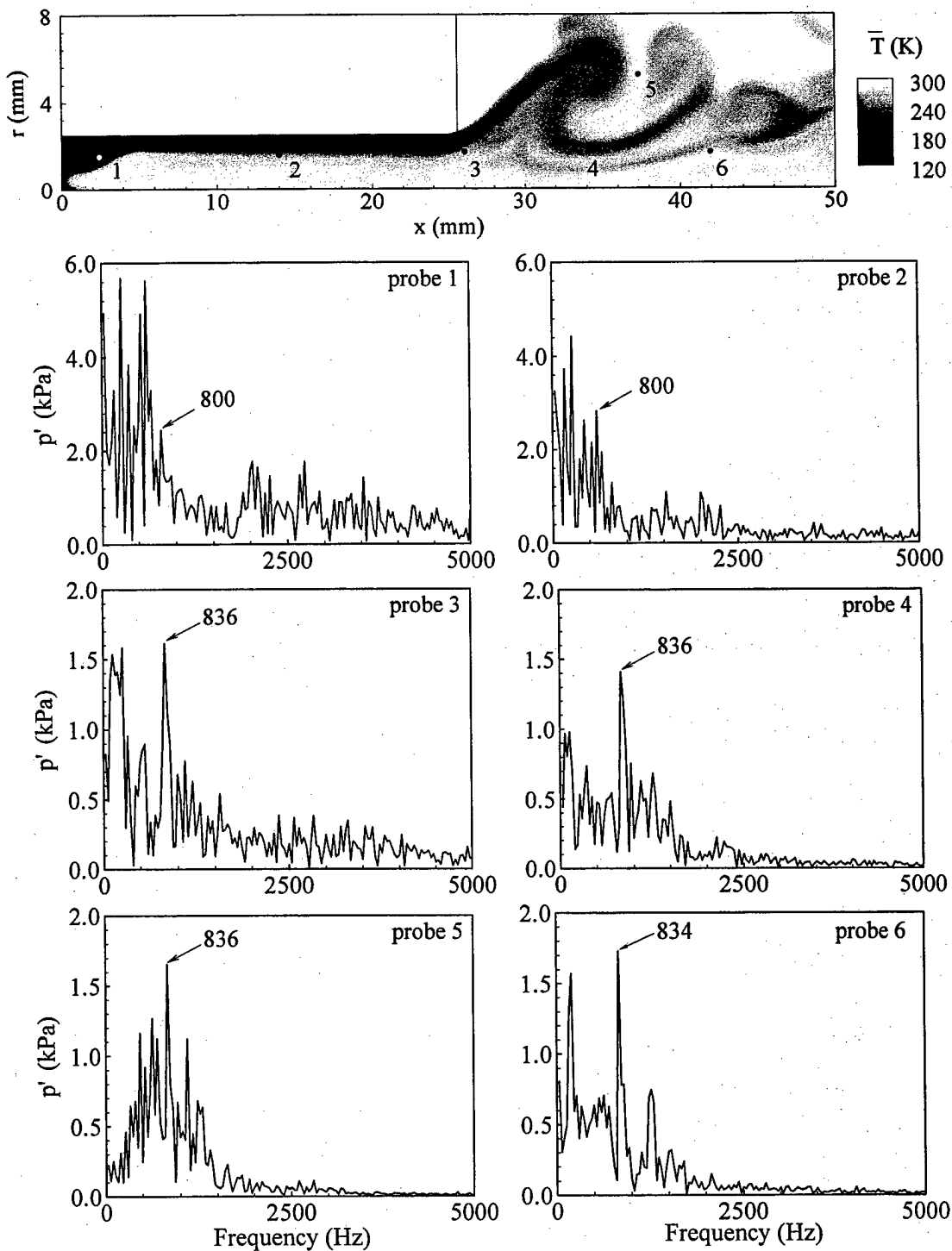


Fig. 7.7: Power spectral densities of the pressure fluctuations at six different axial locations ( $p_{\infty} = 10 \text{ MPa}$ ,  $T_{inj} = 120 \text{ K}$ ,  $T_{\infty} = 300 \text{ K}$ ,  $\dot{m} = 0.2 \text{ kg/s}$ ,  $K = 3.2$ ).

### 7.2.2 Effects of Important Design Parameters on the Swirl Injector Performance

#### 7.2.2.1 Mass Flowrate

Figure 7.8 shows the effect of mass flowrate on the axial distribution of the film thickness. The trends are almost the same. At the beginning, the injected fluid fills more than half of the tube. It, then, shrinks to the wall until reaching a minimum. With the development of the boundary layer, the thickness increases as the fluid moves downstream. It suddenly drops near the exit. Based on the classical inviscid theory (Bazarov et al., 2004), the liquid film thickness at the injector exit is independent of the mass flowrate. This assumption has been re-examined by several researchers in the cold flow experiments at standard pressure. It is reported that mass flowrate has only moderate influence on the film thickness. The differences among three cases are small in the present simulation. The liquid film thickness at the injector exit decreases with the increasing of mass flowrate, a trend consistent with the boundary layer theory.

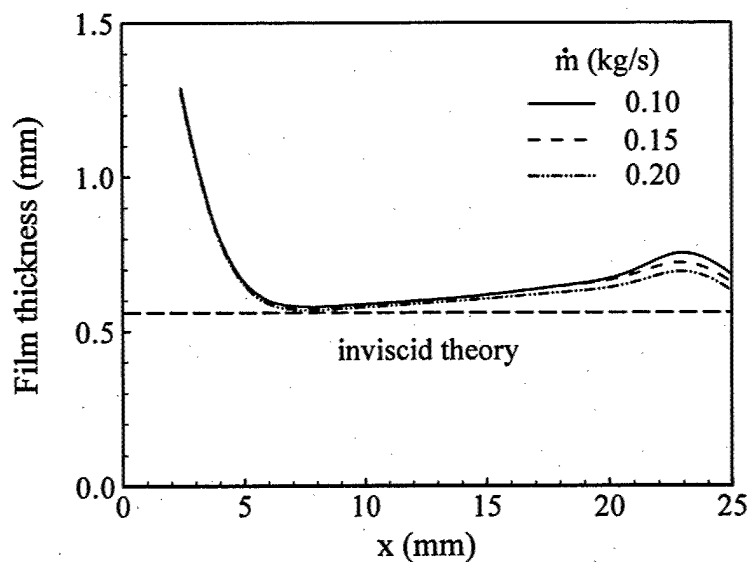


Fig. 7.8: Effect of mass flowrate on the film thickness.

Table 7.3: Effect of mass flowrate on dense fluid film thickness and spray cone angle.

	$\dot{m}$ (kg / s)	$h$ (mm)	$h_{inv}$ (mm)	$h_{vis}$ (mm)	$\tan \alpha / 2$	$(\tan \alpha / 2)_{inv}$
Case 1	0.10	0.686	0.56	0.631	0.752	1.04
Case 2	0.15	0.660	0.56	0.627	0.749	1.04
Case 3	0.20	0.632	0.56	0.625	0.744	1.04

The thicknesses and the spray cone angles at the injector exit are listed in Table 7.3. The subscripts *vis* and *inv* represent the prediction using classical inviscid theory and that of the viscous correction model derived in the next section, respectively. All the three liquid film thicknesses are greater than the predictions with viscous correction because present model does not take into account the transient density variations. In the classical inviscid theory, the cone angle is only a function of the injector geometry. Our simulation results indicate that it is weakly dependent on mass flowrate. The calculated angles are much smaller than those predicted by inviscid theory. This discrepancy was also noted by Rahman et al. (1995) and Dombrowski and Hasson (1969) in the cold flow experiments at low pressure, which was attributed to the more rapid decay of the tangential velocity than the axial one due to the viscous loss along the wall.

Figure 7.9 presents the snapshots of temperature fields of Cases 1 to 3. As the mass flowrate increases, the vortex rolls up relatively later, and the flow pattern becomes more complicated downstream. Figure 7.10 shows the power spectral density of the pressure oscillations at two axial locations for three cases. Since vortex shedding frequency at the injector exit is locked by the length of the recirculation zone, which is enlarged with enhanced mass flowrate, the characteristic frequency is slightly reduced.

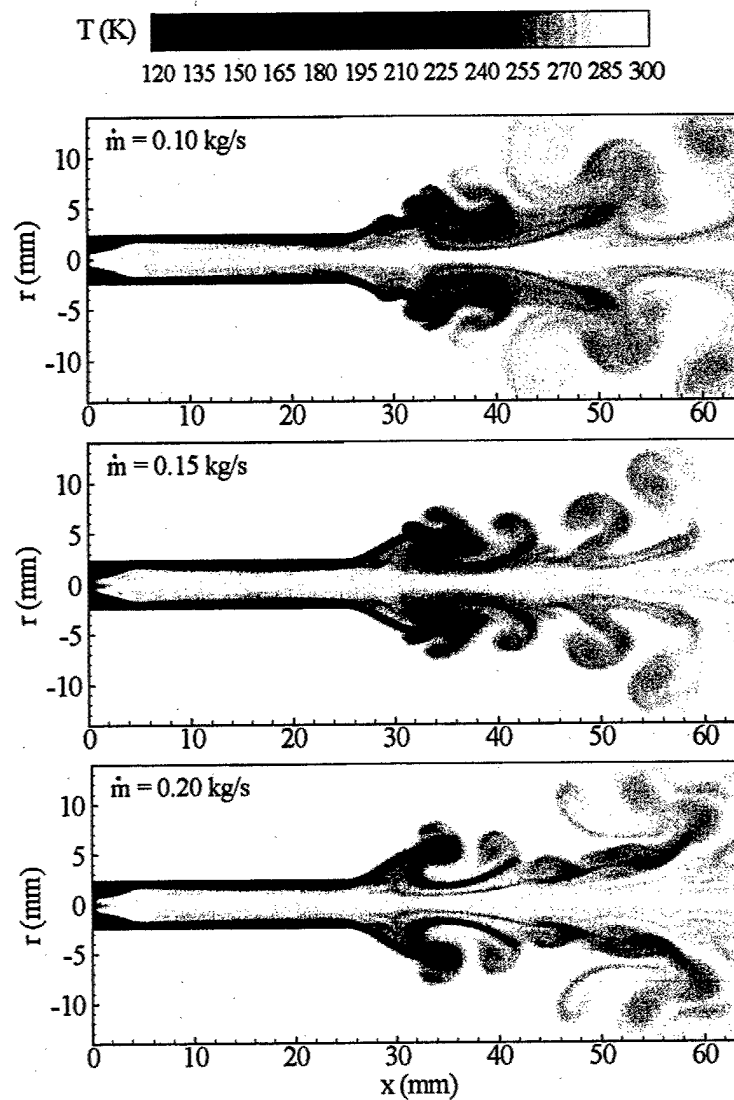


Fig. 7.9: Effect of mass flowrate on the temperature fields.

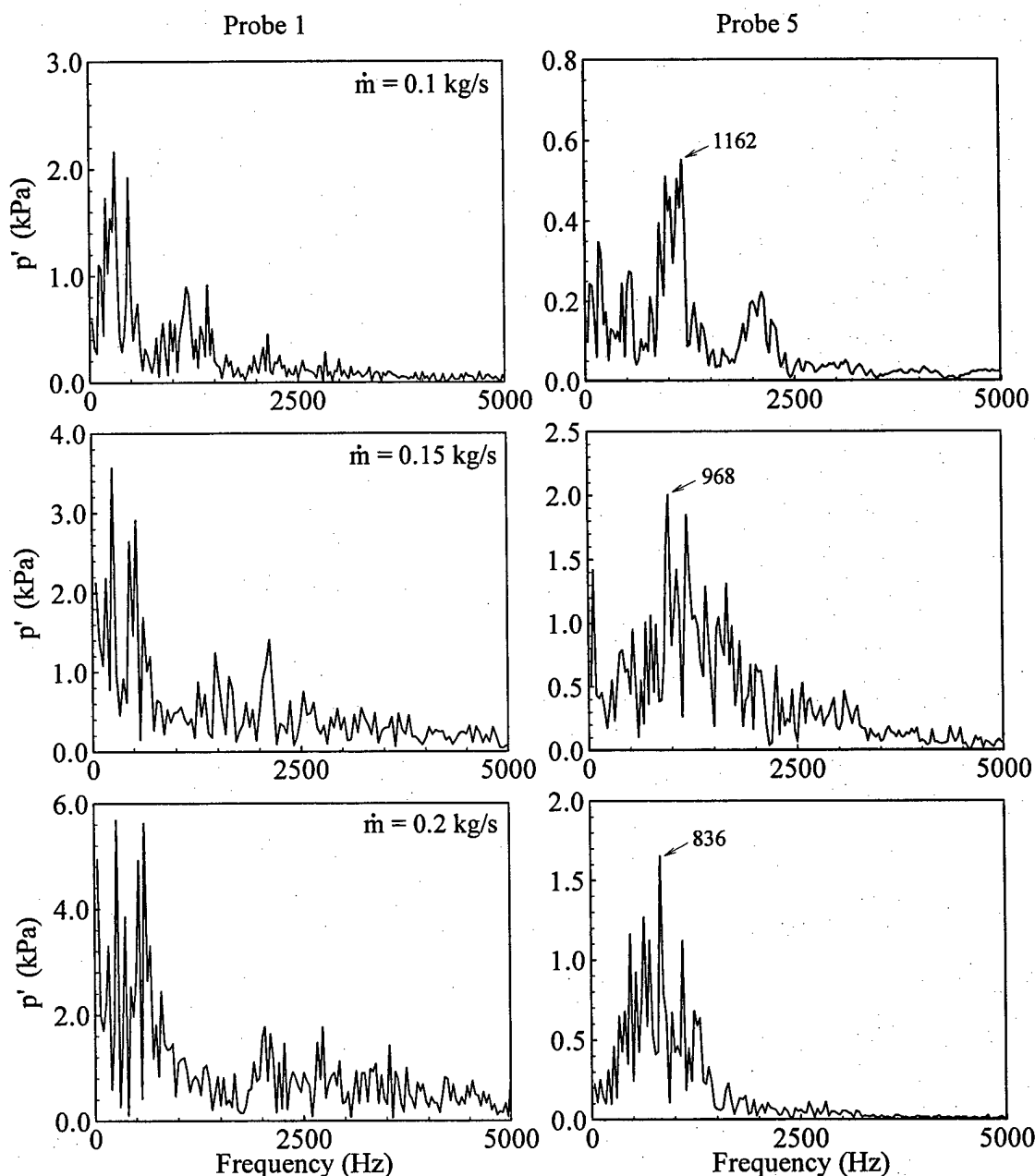


Fig. 7.10: Effect of mass flowrate on the power spectral density of the pressure oscillations.

### 7.2.2.2 Slit Position

Figure 7.11 presents the effect of the tangential slit position on the dense fluid boundary. The film thickness slightly increases as the distance between the tangential slit and the head end increases. It is contradictory to the boundary layer theory. Basically, as the slit position moves downstream, the displacement thickness decreases at the injector exit, and so does the film thickness. The reason is examined in Fig. 7.12, in which the streamline patterns near the head end are presented. In Case 7, part of the injected fluid moves upstream to fill the volume between the tangential slit and the head end. This filling process causes an extra momentum loss and renders the film thickness thicker at the upstream than that of Case 6. In both two cases, a portion of streamlines originating from the dense fluid passes across the critical isothermal, which illustrates that the cold fluid is heated and its temperature exceeds the critical value.

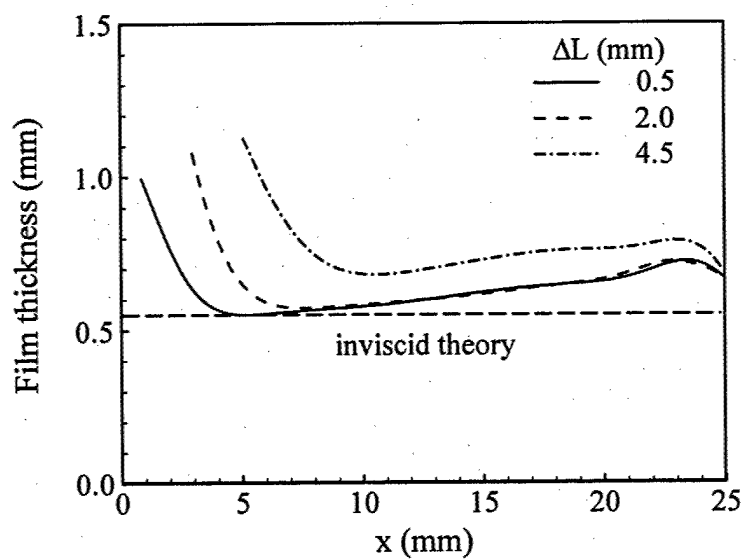


Fig. 7.11: Effect of slit position on the film thickness.

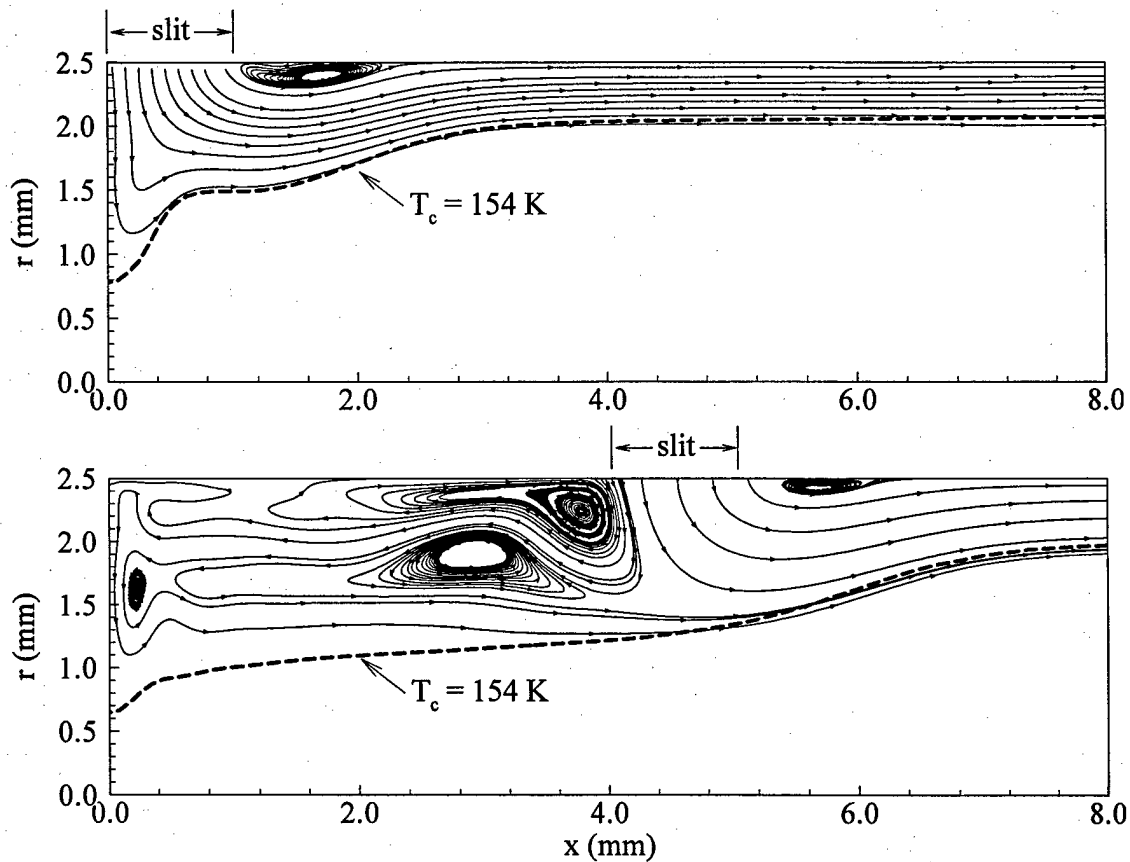


Fig. 7.12: Effect of slit position on the pseudo streamline patterns near the head end.

In Table 7.4 , the maximum spray cone angle is obtained when the slit is placed very close to the head end. Since the film thickness also reaches the minimal value at this position, an optimal injector performance could be obtained. However, a constant mass flowrate is specified at the inlet in the present simulation. In the application, if the tangential inlet is placed very close to the head end, a greater pressure drop between the feed line and the combustion chamber should be employed to overcome the viscous loss at the head end and to maintain the same mass flowrate. The inlet location should be chosen based the following rules: 1) stable flow motion at the injector exit; 2) a minimal momentum loss; 3) wide spreading angle and thin liquid film.

Table 7.4: Effect of slit position on film thickness and spray cone angle

	$\Delta L(\text{mm})$	$h (\text{mm})$	$h_{\text{inv}} (\text{mm})$	$h_{\text{vis}} (\text{mm})$	$\tan \alpha / 2$	$(\tan \alpha / 2)_{\text{inv}}$
Case 4	0.5	0.660	0.56	0.63	0.781	1.04
Case 2	1.5	0.660	0.56	0.627	0.749	1.04
Case 5	4.5	0.672	0.56	0.62	0.760	1.04

### 7.2.2.3 LOX Post Length

Owing to the propellant supply manifolding considerations, the length to diameter ratio of the liquid rocket swirl injector is much greater than that of the conventional swirl atomizer. As a result, the viscous loss along the wall affects the injection process and hence alters the spray distribution and atomization efficiency. Inamura et al. (2003) investigated the effect of viscous loss on the liquid fluid film thickness at the standard pressure. A two-dimensional theoretical model was constructed based on the flat plate boundary layer theory. Figure 7.13 compares their results with the viscous corrections given in section 2. The present model, which is derived for a circular duct, gives more accurate result than Inamura's theory does. However, the predictions are still smaller than those obtained from numerical simulation since only the viscous loss is taken into account in our model. To include the density variations in the radial direction, a reasonable density profile is needed in the mass and momentum conservation integrations. This requires tremendous numerical or experimental efforts, which is beyond the scope of this paper. The spray cone angles are listed in Table 7.5 . They reduce as the injector length increases. Since the friction force along the wall retards both the axial and azimuthal velocities, the obtained information indicated that the axial momentum decays relatively slower than does the swirling motion. The elongation of injector damages its performance in two aspects: (1) momentum loss

along the wall with the growth of film thickness; (2) decrease of the spreading angle and the reduction in the spatial distribution of the injected fluid.

Table 7.5: Effect of LOX post length on the dense fluid film thickness and spray cone angle.

	$L$ (mm)	$h$ (mm)	$h_{inv}$ (mm)	$h_{vis}$ (mm)	$\tan \alpha / 2$	$(\tan \alpha / 2)_{inv}$
Case 2	25	0.660	0.56	0.627	0.749	1.04
Case 6	50	0.709	0.56	0.681	0.747	1.04
Case 7	75	0.738	0.56	0.717	0.727	1.04
Case 8	100	0.796	0.56	0.744	0.698	1.04

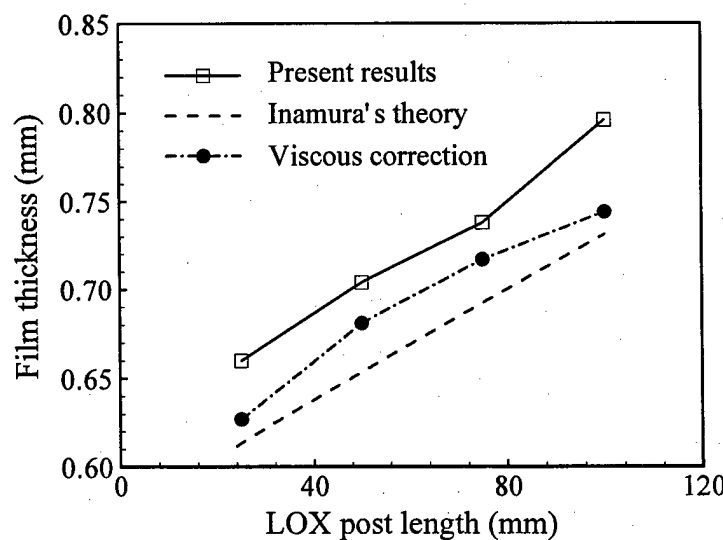


Fig. 7.13: Comparison of liquid film thickness predicted from different theoretical models and the simulation results.

#### 7.2.2.4 Geometric Characteristic Number

The characteristic number “ $K$ ” of a swirl injector is defined as  $K = A_n R_{in} / A_{in} R_n$ . A large “ $K$ ” is obtained when the tangential inlet area is small and the discharge nozzle is wide.

Such a swirl injector could produce stronger swirling motion, which finally gives rise to the thinner liquid film thickness and the wider spray cone angle. Corresponding to the increase of  $K$ , either the inlet area or discharge nozzle should be modified. In the present simulation, this is achieved by changing the radial to azimuthal velocity ratio at the inlet.

Figure 7.14 presents the variations of the film thickness along the injector wall. The strong swirling motion in Case 9 results in a greater radial pressure gradient, which pushes the dense fluid film closer to the wall. Due to the increase in the azimuthal velocity, the spray cone angle enlarges from 0.75 to 0.95 (see Table 7.6). Since a thinner film determines the finer spray droplet and a wider spray cone angle enhances the intraelement mixing efficiency, a better injector performance could be achieved by increasing  $K$ .

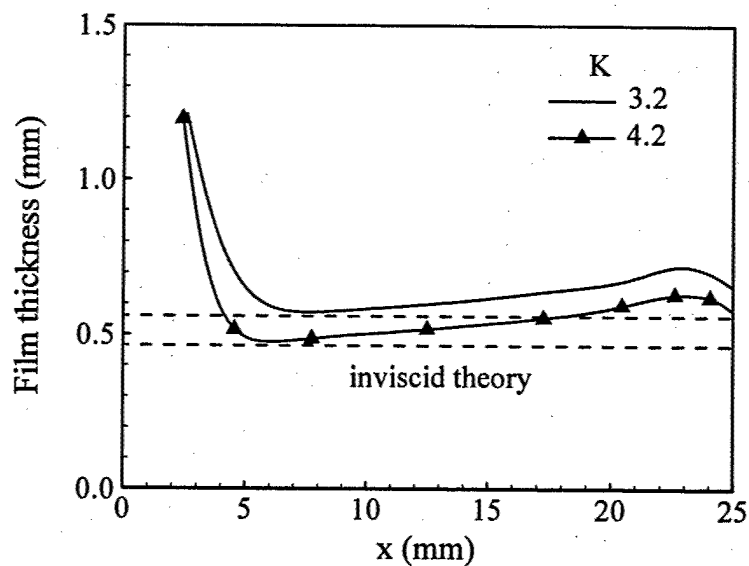


Fig. 7.14: Effect of the swirl strength on the film thickness.

Enhancing the swirl strength has enormous effects on the flow dynamics both inside and outside the injector. Figure 7.15 compares the mean streamline patterns between Cases 2 and 9. As the characteristic number increases, the central recirculation zone elongates in both the radial and axial directions. The recirculation flow penetrates even into the swirl injector. The flow

passage of injected fluid is partly blocked by the recirculation flow, which makes the dense fluid distribute wider. Fig. 7.16 presents the power spectral density of pressure oscillation of Case 9 at Probes 1 and 5. Though the length scale of the recirculation zone is longer than that of Case 2, the characteristic velocity associated with this case is also enhanced. Therefore, the dominant vortex shedding frequency increases. Furthermore, appearing of broad-band spectral both up and downstream implies that more small scale vortices are generated.

Table 7.6: Effect of swirl strength on the dense fluid film thickness and spray cone angle.

	$K$	$h$ (mm)	$h_{inv}$ (mm)	$h_{vis}$ (mm)	$\tan \alpha / 2$	$(\tan \alpha / 2)_{inv}$
Case 2	3.2	0.660	0.56	0.627	0.749	1.04
Case 9	4.2	0.595	0.5	0.564	0.950	1.27

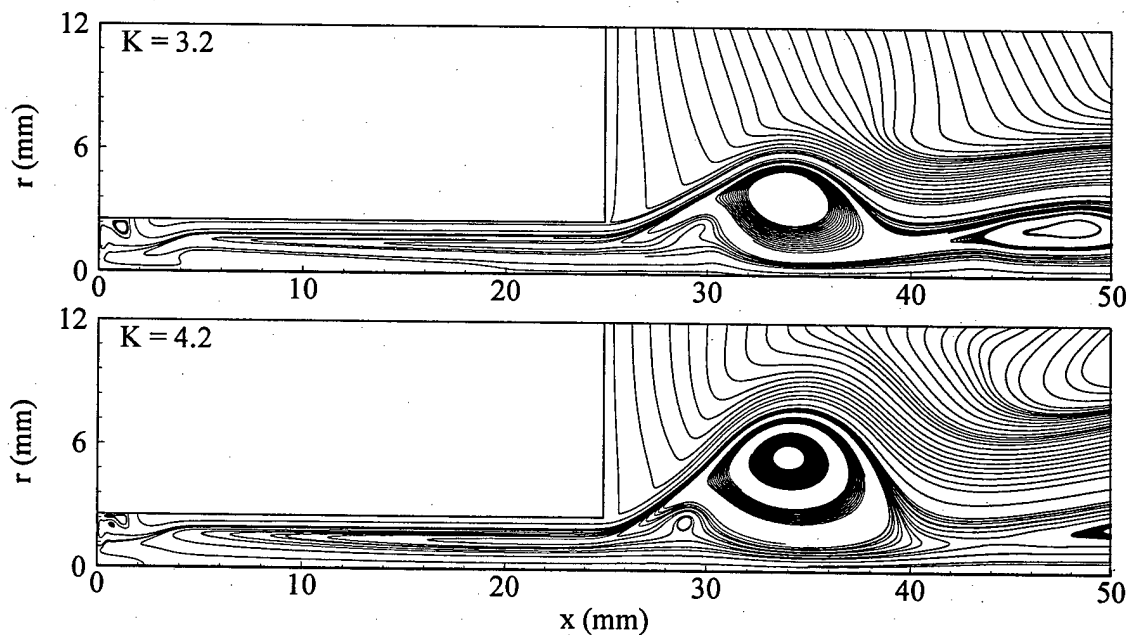


Fig. 7.15: Effect of swirl strength on the pseudo streamline patterns.

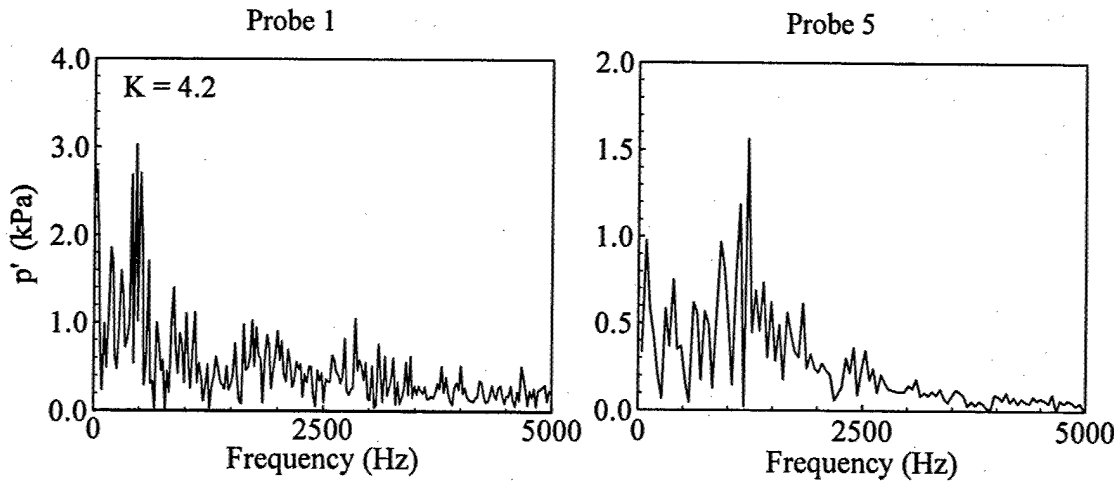


Fig. 7.16: The power spectral density of pressure oscillations at different axial locations ( $p_{\infty} = 10 \text{ MPa}$ ,  $T_{inj} = 120 \text{ K}$ ,  $T_{\infty} = 300 \text{ K}$ ,  $\dot{m} = 0.2 \text{ kg/s}$ ,  $K = 4.2$ ).

### 7.3 A Viscous Correction on Classical Swirl Injector Theory

The fundamentals of swirl injector theory were established more than 60 years ago by Abramovich in 1944 and independently by Taylor in 1947. The up to date discussion of the classical theory, which is particularly easy of implementation, was presented by Bazarov et al. (2004) and Bayvel and Orzechowski (1993).

Although the classical theory is straightforward, it has two intrinsic limitations (Yule and Chinn, 1994). First, it ignores axial momentum conservation. If axial momentum balance is combined with mass and energy conservation, a more rigorous approach could be derived. Second, viscous effect is totally neglected. Compared with a conventional swirl atomizer, a liquid rocket swirl injector is featured for its large length to diameter ratio. Then, the viscous loss along the wall could result in considerable deviation.

Inamura et al. (2003) investigated the effect of viscous loss on the liquid film development at standard pressure. A two-dimensional theoretical model was constructed based

on the flat-plate boundary layer theory. In the present work, their method is extended to accommodate axisymmetric injector configuration. The displacement effect of the boundary layer in a swirl injector is indicated in Fig. 7.17.

If only flow motion in the axial direction is considered, the mass conservation for the boundary layer inside the liquid film is

$$2\pi \int_{R_s-h_0'}^{R_s} \rho u_s r dr = 2\pi \int_{R_s-\delta(x)}^{R_s} \rho u(r) r dr \quad (7.3)$$

where  $\delta(x)$  is the displacement thickness and  $h_0'$  is the thickness of the fluid where the first streamline out of the shear layer started. This equation can be rearranged as

$$2\pi \int_{R_s-h_0'}^{R_s} \rho u_s^2 r dr = 2\pi \int_{R_s-\delta(x)}^{R_s} \rho u_s u(r) r dr \quad (7.4)$$

Momentum conservation is

$$2\pi \int_{R_s-h_0'}^{R_s} \rho u_s^2 r dr - 2\pi \int_{R_s-\delta(x)}^{R_s} \rho u^2(r) r dr = D \quad (7.5)$$

where  $D$  is the friction force along the wall. Substitute Eq. 7.4 into Eq. 7.5

$$D = 2\pi \int_{R_s-\delta(x)}^{R_s} \rho u(r) (u_s - u(r)) r dr \quad (7.6)$$

Following the boundary layer theory, a momentum thickness,  $\theta$ , is defined for the liquid film inside the circular injector

$$D = 2\pi R_n \rho u_s^2 \theta \quad (7.7)$$

Equating Eq. 7.6 and Eq. 7.7, then,  $\theta$  can be written as

$$\theta = \frac{1}{R_n} \int_{R_s-\delta(x)}^{R_s} \rho \frac{u(r)}{u_s} \left(1 - \frac{u(r)}{u_s}\right) r dr \quad (7.8)$$

The friction force along the wall also can be expressed as

$$D = 2\pi R_n \int_0^x \tau_w(x) dx \text{ or } \frac{dD}{dx} = 2\pi R_n \tau_w(x) \quad (7.9)$$

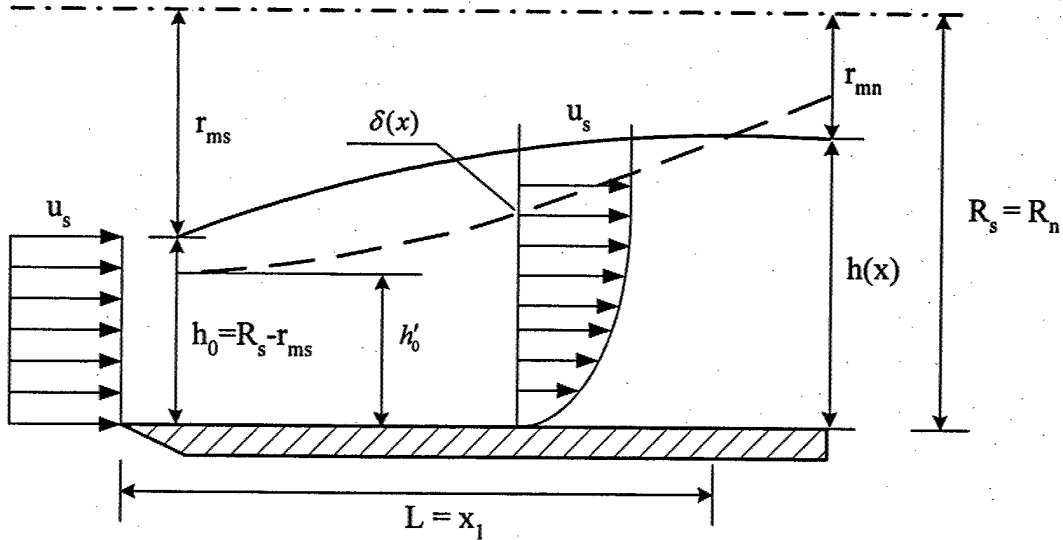


Fig. 7.17: Schematic of displacement effect in a swirl injector.

Equating Eq. 7.7 to Eq. 7.9, the relation of  $\theta$  and  $\tau_w$  is established

$$\frac{d\theta}{dx} = \frac{\tau_w(x)}{\rho u_s^2} = \frac{1}{2} c_f \quad (7.10)$$

where  $c_f$  is the skin friction coefficient. For high-pressure supercritical fluid, the fluid Reynolds number is much higher than its counterpart at low pressure. As a result, turbulent boundary layer starts at a short distance (around 1-2 mm) away from the tangential inlet. Based on Prandtl's power law suggestion for turbulent flow, we have  $c_f = 0.02 Re_\delta^{1/2}$ . The one-seventh power law velocity profile is adopted for the axial velocity distribution.

$$\frac{u}{u_s} = \left( \frac{R_n - r}{\delta(x)} \right)^{1/7} \quad (R_n - r \geq \delta(x)) \quad (7.11)$$

Substituting Eq. 7.11 into Eq. 7.8, the momentum thickness  $\theta$  can be integrated, which is

$$\theta = \frac{7}{72} \delta(x) - \frac{7}{240} \frac{\delta^2(x)}{R_n} \quad (7.12)$$

Inserting Eq. 7.12 into Eq. 7.10, a formulation related displacement thickness  $\delta(x)$  and the injector length  $x$  is obtained

$$\frac{d\delta}{dx} = \frac{0.02 \text{Re}_\delta^{-1/6}}{\left(\frac{7}{72} - \frac{7}{120} \frac{\delta}{R_n}\right)} \quad (7.13)$$

Since  $\delta = 0$  at  $x = 0$ , Eq. 7.13 can be integrated from 0 to  $x$ . If  $\delta(x)$  is known, the liquid film thickness can be solved based on the mass conservation. However, if the tube is long enough, the displacement thickness  $\delta(x)$  may exceed the liquid film thickness  $h(x)$ . In order to accommodate this situation, the axial position  $x_i$ , where  $\delta(x) = h(x)$ , can be calculated based on the momentum conservation.

$$2\pi \int_{R_s-h_0}^{R_s} \rho u_s^2 r dr - 2\pi \int_{R_s-\delta(x)}^{R_s} \rho u^2 r dr = 2\pi r_s \int_0^x \tau_w(x) dx \quad (7.14)$$

Because  $\delta(x)$  and  $\tau_w(x)$  are only function of  $x$ ,  $x_i$  can be solved iteratively from Eq. 7.14.

Finally, when  $L \geq x_i$

$$r_{mn} = \sqrt{(R_n - \delta)^2 + 2[\frac{7}{8} R_n \delta - \frac{7}{15} \delta^2] - \frac{Q}{\pi u_s}} \quad (7.15)$$

when  $L < x_i$ ,  $r_{mn}$  can be iteratively solved by the Newton-Raphson method through equation 7.16

$$[R_n^2 - (R_n - h_0)^2] - 2\delta^{-1/7} \left[ \frac{7}{8} R_n r_{mn}^{8/7} - \frac{7}{15} r_{mn}^{15/7} \right] = 0 \quad (7.16)$$

The original liquid film thickness  $h_0$  and velocity  $u_s$  are evaluated by the classical inviscid theory.

#### 7.4 Summary

The flow evolution inside and outside a swirl injector is investigated numerically. The effects of mass flowrate, tangential slit position, injector length, and geometrical characteristic number on the injector performance are studied. The major results are summarized below:

1. The present analysis allows for a detailed investigation into the temporal and spatial evolution of the flowfield both inside and outside the swirl injector under supercritical conditions. The features which distinct high-pressure swirling injection from its counterpart at low-pressure are noted.
2. The parametric study illustrates that both the dense fluid film thickness and the spray cone angle weakly depend on the mass flowrate. Therefore, a larger oxidizer swirl element with greater mass flowrate than that of the shear coaxial injector still can obtain the required intraelement mixing efficiency.
3. The tangential inlet position has significant influence on the flow evolution. If the slit is located away from the head end, part of the injected fluid will move upstream to fill the gap between the slit and the end wall, which impairs the injector performance.
4. Increasing the geometric characteristic number of the injector results in a thinner film thickness and a wider spray cone angle. This suggests that a better injector performance could be achieved by enlarging the discharge nozzle exit or reducing the tangential inlet area.

## Chapter 8

### Summary and Recommendations

#### 8.1 Summary

The present research addresses a wide variety of basic and practical issues related to the modeling and simulation of cryogenic fluid propellant injection and combustion processes under supercritical conditions. A comprehensive numerical analysis has been established based on a large-eddy-simulation technique. The model accommodates full conservation laws and real-fluid thermodynamics and transport phenomena. All of the thermophysical properties are determined directly from fundamental thermodynamics theories, along with the use of the corresponding state principles. In addition, a unified treatment of general fluid thermodynamics is developed and incorporated into a density-based, preconditioning scheme, which results in a robust and self-consistent numerical method valid for fluid flows at all speeds and over the entire thermodynamic regime of concern. The theoretical and numerical framework established has been validated against a wide range of flow problems in order to establish its creditability and accuracy.

After validation, the analysis was first applied to study the dynamics of a nitrogen fluid jet over a broad range of ambient pressures. Both two- and three-dimensional simulations were conducted, simulating the experiments conducted by Chehroudi et al. (2002). Good agreement was obtained between the numerical and experimental results in terms of the mean density distribution and the jet spreading angle. The jet dynamics is largely dictated by the local thermodynamic state through its influence on the fluid thermophysical properties. When the fluid temperature transits across the inflection point on an isobaric density-temperature curve, the resultant rapid property variations may qualitatively modify the jet behavior. Owing to the

differences of fluid states and flow conditions between the jet and surroundings, a string of strong density-gradient regimes is generated around the jet surface and exerts a stabilizing effect on the flow development. It acts like a solid wall that transfers the turbulent kinetic energy from its axial to radial component. The spatial growth rate of the surface instability wave is inhibited by the density stratification. The frequency of the most unstable mode exhibits a weak pressure dependence at high pressures. It, however, decreases significantly in the near-critical regime due to the enhanced effect of density stratification and increased mixing-layer momentum thickness. The result agrees well with a linear stability analysis. A suddenly volume expansion occurs in the transition region when the injected fluid is heated by the hot ambience, which significantly affects both the mean and turbulence flow properties. The supercritical fluid jet could be characterized by three different regimes: a potential core with uniform density, a transition region accompanied with severe volume expansion, and a variable density gaseous jet in the downstream region. Any realistic treatment of a supercritical fluid jet must accommodate those unique features.

The analysis was then applied to examine the key phenomena associated with the coaxial injection of LOX and methane. The near field dynamics can be characterized by the evolution of the inner and outer mixing layers, because the two shear layers originating from the upper and lower tips of the LOX post merge downstream of the wake and form an inner vortex string. This layer plays a dominant role in the flowfield. The flow oscillations associated with the vortex shedding provides the driving force in the outer mixing layer. The formation of those vortices does not follow the hydrodynamic instability mechanism, but occurs in a manner analogous to that produced at a backward facing step. The dominate effects of the momentum flux ratio on the flow evolution were also demonstrated. As the injection velocity of the methane stream increases, turbulent mixing was enhanced, and the potential core of the LOX stream was reduced. This agrees with the experimental observations of Singla et al. (2004). If the velocity ratio

between the outer and inner streams further increases, the wake region may extend to the centerline and generate a recirculation zone.

The last part of the thesis presents a parametric study on the swirl injection of cryogenic oxygen under supercritical conditions. The influences of various injector geometric parameters and flow conditions, including mass flow rate, tangential slit position, injector length, and swirl strength, on the injector dynamics and performance were investigated systematically. In general, the mass flow rate plays a minor role in dictating the performance of a swirl injector in terms of the liquid film thickness and spray cone angle. A long injector causes a large momentum loss in the azimuthal direction and a reduction in the spray cone angle. Increasing the swirl strength, which could be achieved by changing the injector geometrical constant ( $K$ ), results in a decrease in the liquid film thickness and an increase in the spray cone angle. A companion theoretical model was also established to help understand the underlying physics obtained from numerical calculations.

## 8.2 Recommendation for Future work

One of the primary objectives of the present study was to develop a comprehensive and efficient numerical model capable of treating fluid behavior over a broad range of thermodynamic states. The real fluid equation of state, however, could not be solved in a complete coupled manner. Extensive iterations at each grid point and time step were required to calculate thermophysical properties. The procedure represented an over taxing, especially for three dimensional simulation, and prohibited the analysis from engineering applications. In order to overcome this difficulty, a fully explicit solution technique is needed. The effective approach is an accurate curve-fit methodology in the state space which could determine the density explicitly

as a function of the temperature, pressure, and mass fractions. The method was recently tested and would be implemented in the future.

Although the non-equilibrium thermodynamic effects, such as the Soret and Dufour effects, have unnoticeable influence on large scale energy-containing flow motions, they may be important for transport processes at subgrid scales. The subgrid scale model adopted in the present work (i.e.), the static Smagorinsky model for compressible turbulent flows, however, neglects cross diffusion effect. Further development of a subgrid scale model that accommodates general fluid mixture under supercritical conditions appears to be required.

In the present combustion model, the resolved-scale chemical source terms were treated using resolved field quantities, and the effects of subgrid-scale fluctuations were neglected. Such an approximation is valid only for cases in which reactions are slow relative to the decay of species fluctuations, a situation rarely encountered in contemporary combustors. The problem becomes more severe with increasing pressure. The use of gradient diffusion terms to model turbulence species transport is also questionable due to the effect of heat release on the subgrid-scale turbulence field. The issue of turbulent combustion models deserves significant attention and should be properly addressed in the future work.

## Bibliography

Abramovich, G. N., *Applied Gas Dynamics*, Nauka, Moscow, Russia, 1976.

Abramovich, G. N., *The Theory of Turbulent Jets*, MIT Press, Cambridge, Massachusetts, 1963.

Amielh, M., Djeridane, T., Anselmet, F., and Fulachier, L., "Velocity near Field of Variable Density Turbulent Jets," *International Journal of Heat and Mass Transfer*, 39, 2149, 1996.

Anderson, T. J., Woodward, R. D., and Winter, M., "Oxygen Concentration Measurements in a High Pressure Environment Using Raman Imaging," AIAA Paper No. 95-0140, 1995.

Apte, S. and Yang, V., "Unsteady Flow Evolution in Porous Chamber with Surface Mass Injection, Part 1: Free Oscillation," *AIAA Journal*, 39, 557, 2001.

Apte, S. and Yang, V., "Unsteady Flow Evolution in Porous Chamber with Surface Mass Injection, Part 1: Free Oscillation," *AIAA Journal*, 39, 1577, 2001.

Arndt, R. E. A., Long, D. F., and Glauser, M. N., "The Proper Orthogonal Decomposition of Pressure Fluctuations Surrounding a Turbulent Jet," *Journal of Fluid Mechanics*, 340, 1, 1997.

Atsavapranee, P. and Gharib, M., "Structures in Stratified Plane Mixing Layers and the Effects of Cross-Shear," *Journal of Fluid Mechanics*, 342, 53, 1997.

Barata, J. M. M., Gökalp, I., and Silva, A. R. R., "Numerical Study of Cryogenic Jets under Supercritical Conditions," *Journal of Propulsion and Power*, 19, 142, 2003.

Bardina, J., Ferziger, J. H., and Reynolds, W. C., "Improved Subgrid Scale Models for Large-Eddy Simulation," AIAA Paper No. 80-1357, 1980.

Batchelor, G. K., *The Theory of Homogenous Turbulence*, Cambridge University Press, 1953.

Baum, M., Poinsot, T., and Thevenin, D., "Accurate Boundary Conditions for Multicomponent Reactive Flows," *Journal of Computational Physics*, 116, 247, 1994.

Bayvel, L. and Orzechowski, Z., *Liquid Atomization*, Taylor & Francis, Washington D.C., 1993.

Bazarov, V. and Yang, V., "Liquid-Propellant Rocket Engine Injector Dynamics," *Journal of Propulsion and Power*, 14, 797, 1998.

Bazarov, V., Yang, V., and Puri, P., "Design and Dynamics of Jet and Swirl Injectors," *Liquid Rocket Thrust Chambers: Aspects of Modeling, Analysis, and Design*, Progress in Astronautics and Aeronautics, eds., V. Yang et al., Vol. 200, 2005.

Bellan, J., "Supercritical (and Subcritical) Fluid Behavior and Modeling: Drops, Streams, Shear and Mixing Layers, Jets and Sprays," *Progress in Energy and Combustion Science*, 26, 329, 2000.

Berkooz, G., Holmes, P., and Lumley, J. L., "The Proper Orthogonal Decomposition in the Analysis of Turbulent Flows," *Annual Review of Fluid Mechanics*, 25, 539, 1993.

Boersma, B. J., Brethouwer, G. and Nieuwstadt, F. T. M., "A Numerical Investigation on the Effect of the Inflow Conditions on the Self-Similar Region of a Round Jet," *Physics of Fluids*, 10, 899, 1998.

Branam, R. and Mayer, W., "Characterization of Cryogenic Injection at Supercritical Pressure," *Journal of Propulsion and Power*, 19, 342, 2003.

Brasseur, J., "Lecture Notes on Homogeneous Turbulence," The Pennsylvania State University, University Park, PA., 2002.

Buelow, P. E. O., "Convergence Enhancement of Euler and Navier-Stokes Algorithms," Ph.D thesis, The Pennsylvania State University, 1995.

Buelow, P. E. O., Venkataswaran, S., and Merkel, C. L., "Effect of Grid Aspect Ratio on Convergence," *AIAA Journal*, 32, 2401, 1994.

Buelow, P. E. O., Venkataswaran, S., and Merkel, C. L., "Effect of Grid Aspect Ratio on Convergence," *AIAA Journal*, 32, 2401, 1994.

Calhoon, W. and Menon. S., "Subgrid Modeling for Reacting Large Eddy Simulations," *AIAA Paper No. 96-0561*, 1996.

Candel, S., Herding, G., Synder, R., Scouflaire, P., Rolon, C., Vingert, L., Habiballah, M., Grisch, F., Pealat, M., Bouchardy, P., Stepowski, D., Cessou, A., and Colin, P., "Experimental Investigation of Shear Coaxial Cryogenic Jet Flames," *Journal of Propulsion and Power*, 14, 826, 1998.

Carlos, B., Guillaume, B., Patrick, B., and Olivier, M., "Instability and Transition in High Velocity Ratio Coaxial Jets: A Numerical Study," the 3<sup>rd</sup> International Symposium on Turbulence and Shear Flow Phenomena, Sendai, Japan, 2003.

Chehroudi, B. and Davis, D., "The Effects of Pressure and Acoustic Field on A Cryogenic Coaxial Jet," *AIAA Paper No. 04-1330*, 2004.

Chehroudi, B. and Talley, D., "Interaction of Acoustic Waves with a Cryogenic Nitrogen Jet at Sub- and Supercritical Pressures," *AIAA Paper No. 02-0342*, 2002c.

Chehroudi, B., Cohn, R., and Talley, D., "Cryogenic Shear Layers: Experiments and Phenomenological Modeling of the Initial Growth Rate under Subcritical and Supercritical Conditions," *International Journal of Heat and Fluid Flow*, 23, 554, 2002b

Chehroudi, B., Cohn, R., Talley, D., and Badakhshan, A. "Raman Scattering Measurements in the Initial Region of Sub- and Supercritical jets," *AIAA Paper No. 00-36609*, 2000.

Chehroudi, B., Talley, D., and Coy, E., "Fractal Geometry and Growth Rate Changes of Cryogenic Jets near the Critical Point," AIAA Paper No. 99-31260, 1999.

Chehroudi, B., Talley, D., and Coy, E., "Visual Characteristics and Initial Growth Rates of Round Cryogenic Jets at Subcritical and Supercritical Pressures," Physics of Fluids, 14, 850, 2002a.

Chehroudi, B., Talley, D., Mayer, W., Branam, R., Smith, J. J., Schik, A., and Oschwald, M., "Understanding Injection into High Pressure Supercritical Environments," 5th International Conference on Liquid Space Propulsion, Chattanooga, TN, 2003.

Chen, C. J. and Rodi, W., "Vertical Turbulent Buoyant Jets : A Review of Experimental Data," Pergamon Press, Oxford, 1980.

Choi, Y. H. and Merkle, C. L., "The Application of Preconditioning in Viscous Flows," Journal of Computational Physics, 105, 207, 1993.

Cox, G.B., "Rocket Engine Injection Element Characterization," AIAA Paper No. 88-3135, 1988.

Crow, S. C. and Champagne, F. H., "Orderly Structure in Jet Turbulence," Journal of Fluid Mechanics, 48, 547, 1971.

Deardorff, J. W., "A Numerical Study of 3-D Turbulent Channel Flow at Large Reynolds Numbers," Journal of Fluid Mechanics, 41, 453, 1970.

Delplanque, J. P. and Sirignano, W. A., "Boundary-Layer Stripping Effects on Droplet Transcritical Convective Vaporization," Atomization and Sprays, 4, 325, 1994.

Dombrowski, N. and Hasson, D., "The Flow Characteristics of Swirl (Centrifugal) Spray Pressure Nozzles with Low Viscosity Liquids," AIChE Journal, 14, 604, 1969.

Elam, S. K., "Subscale LOX/Hydrogen Testing with a Modular Chamber and a Swirl Coaxial Injector," AIAA Paper No. 91-1874, 1991.

Ely, J. F. and Hanley, H. J., Prediction of Transport Properties. 1. Viscosity of Fluids and Mixtures, Industrial and Engineering Chemistry Fundamentals, 20, 323, 1981.

Ely, J. F. and Hanley, H. J., Prediction of Transport Properties. 2. Thermal Conductivity of Pure Fluids and Mixtures, Industrial and Engineering Chemistry Fundamentals, 22, 90, 1983.

Erlebacher, G., Hussaini, M. Y., Speziale, C. G., and Zang, T. A., "Toward the Large Eddy Simulation of Compressible Turbulent Flows," Journal of Fluid Mechanics, 238, 155, 1992.

Flynn, M. J., "Some Computer Organizations and Their Effectiveness," IEEE Transactions on Computers, 21, 948, 1972.

Fureby, C. and Grinstein, F.F., "Monotonically Integrated Large Eddy Simulation of Free Shear Flows," AIAA Journal, 37, 544, 1999.

Fureby, C. and Grinstein, F.F., "Recent Progress on MILES for High Reynolds-Number Flows," AIAA Paper No. 02-0134, 2002.

Germano, M., "Turbulence: the Filtering Approach," *Journal of Fluid Mechanics*, 238, 325, 1992.

Germano, M., Piomelli, U., Moin, P., and Cabot, W. H., "A Dynamic Subgrid-Scale Eddy Viscosity Model," *Physics of Fluids*, 3, 1760, 1991.

Gilbert, A. D., "Spiral Structures and Spectral in Two-Dimensional Turbulence," *Journal of Fluid Mechanics*, 193, 475, 1988.

Glaze, D. J. and Frankel, S. H., "Stochastic Inlet Conditions for Large-Eddy Simulation of a Fully Turbulent Jet," *AIAA Journal*, 41, 1064, 2003.

Graboski, M. S. and Daubert, T. E., "A Modified Soave Equation of State for Phase Equilibrium Calculation, 1. Hydrocarbon Systems," *Industrial and Engineering Chemistry Process Design and Development*, 17, 443, 1978a.

Graboski, M. S. and Daubert, T. E., "A Modified Soave Equation of State for Phase Equilibrium Calculation, 2. Systems Containing CO<sub>2</sub>, H<sub>2</sub>S, N<sub>2</sub>, and CO," *Industrial and Engineering Chemistry Process Design and Development*, 17, 448, 1978b.

Grinstein, F. F., Young, T. R., Li, G. G., Gutmark, E. J., Hsiao, G., and Mongia H. C., "Computational And Experimental Analysis of the Flow Dynamics in a Multi-Swirler Combustor," AIAA Paper No. 02-1006, 2002.

Gurliat, O., Schmidt, V., Haidn, O. J., and Oschwald, M., "Ignition of Cryogenic H<sub>2</sub>/LOX Sprays," *Aerospace Science and Technology*, 7, 517, 2003.

Gutmark, E. and Ho, C. M., "Preferred modes and the spreading rates of jets," *Physics of Fluids*, 26, 2932, 1983.

Han, P. G., Seol, J., Hwang, S., and Yoon, Y., "The Spray Characteristics of Swirl Coaxial Injectors," AIAA Paper No. 03-0490, 2003.

Hannoun, I. A., Fernando, H. J. S., and List, E. J., "Turbulence Structure near a Sharp Density Interface," *Journal of Fluid Mechanics*, 189, 189, 1988.

Herding, G., Snyder, R., Rolon, C., and Candel, S., "Investigation of Cryogenic Propellant Flames Using Computerized Tomography of Emission Images," *Journal of Propulsion and Power*, 14, 146, 1998.

Ho, C. M. and Huerre, P., "Perturbed Free Shear Layers," *Annual Review of Fluid Mechanics*, 16, 365, 1984.

Hsieh, K. C. and Shuen, J. S., "Droplet Vaporization in High-Pressure Environments I: Near Critical Conditions," *Combustion Science and Technology*, 76, 111, 1991.

Hsieh, S.Y., and Yang, V., "A Preconditioning Flux-Difference Scheme for Chemically Reacting Flows at All Mach Numbers", International Journal of Computational Fluid Dynamics, 8, 31, 1997.

Hulka, J. and Makel, D., "Liquid Oxygen/Hydrogen Testing of a Single Swirl Coaxial Injector Element in a Windowed Combustion Chamber," AIAA Paper No. 93-1954, 1993b.

Hulka, J. and Schneider, J. A., "Performance and Stability of a Booster Class LOX/H<sub>2</sub> Swirl Coaxial Element Injector," AIAA Paper No. 91-1877, 1991.

Hulka, J. and Schneider, J. A., "Single Element Injector Cold Flow Testing for STME Swirl Coaxial Injector Element Design," AIAA Paper No. 93-2161, 1993a.

Hussein, H. J., Capp, S. P., and George, W. K., "Velocity Measurements in a High-Reynolds-Number Momentum-Conserving, Axisymmetric, Turbulent Jet," Journal of Fluid Mechanics, 258, 31, 1994.

Inamura, T., Tamura, H., and Sakamoto, H., "Characteristics of Liquid Film and Spray Injected from Swirl Coaxial Injector," Journal of Propulsion and Power, 19, 632, 2003.

Ivancic, B. and Mayer, W., "Time and Length Scales of Combustion in Liquid Rocket Thrust Chambers," Journal of Propulsion and Power, 18, 247, 2002.

Ivanici, B. and Mayer, W., "Time and Length Scales of Combustion in Liquid Rocket Thrust Chambers," Journal of Propulsion and Power, 18, 247, 2002.

Jacobsen, R. T. and Stewart, R. B., "Thermodynamic Properties of Nitrogen Including Liquid and Vapor Phases from 63K to 2000K with Pressure to 10000 Bar," Journal of Physical and Chemical Reference Data, 2, 757, 1973.

Jameson, A., "The Evolution of Computational Methods in Aerodynamics," Journal of Applied Mathematics, 50, 1052, 1983.

Jorgenson, P. and Turkel, E., "Central Difference TVD Schemes for Time Dependent and Steady State Problems," Journal of Computational Physics, 107, 297, 1993.

Juniper, M. and Candel, S., "Edge Diffusion Flame Stabilization behind a Step over a Liquid Reactant," Journal of Propulsion and Power, 19, 332, 2003.

Juniper, M., Darabiha, N., and Candel, S., "The Extinction Limits of a Hydrogen Counterflow Diffusion Flame above Liquid Oxygen," Combustion and Flame, 135, 87, 2003.

Juniper, M., Tripathi, A., Scouflaire, P., Rolon, J. C., and Candel, S., "Structure of Cryogenic Flames at Elevated Pressures," Proceedings of Combustion Institute, 28, 1103, 2000.

Kendrick, D., Herding, G., Scouflaire, F., Rolon, C., and Candel, S., "Effects of a Recess on Cryogenic Flame Stabilization," Combustion and Flame, 118, 327, 1999.

Kordulla, W. and Vinokur, M., "Efficient Computation of Volume in Flow Predictions," AIAA Journal, 21, 917, 1983.

Lafon, P., Yang, V., and Habiballah, M., "Pressure-Coupled Vaporization and Combustion Responses of Liquid Oxygen (LOX) Droplets in Supercritical Hydrogen Environments," AIAA Paper No. 95-2432, 1995.

Leonard, A., "Energy Cascade in Large-Eddy Simulation of Turbulence," Advances in Geophysics, 18a, 237, 1974.

Levelt Senger, J. M. H., "Thermodynamics of Solutions near the Solvent's Critical Point," *Supercritical Fluid Technology*, eds., T. J. Bruno and J. F. Ely, Chapter 1, CRC Press, Inc, Boca Raton, Florida, 1991.

Lilly, D. K., "A Proposed Modification of the Germano Subgrid-Scale Closure Model," Physics of Fluid A, 4, 633, 1992.

Liu, T., "Temporal and Spatial Stability of Real-Fluid Mixing Layer with Density Stratification," M.S. Dissertation, Dept. of Mechanical and Nuclear Engineering, Pennsylvania State Univ., University Park, PA, 2004.

Manrique, J. A. and Borman, G. L., "Calculations of Steady State Droplet Evaporation in a High Temperature and High Pressure Environment," International Journal of Heat and Mass Transfer, 15, 831, 1969.

Mayer, W. and Tamura, H., "Propellant Injection in a Liquid Oxygen Gaseous Hydrogen Rocket Engine," Journal of Propulsion and Power, 12, 1137, 1996.

Mayer, W., Ivancic, B., Schik, A., and Hornung, U., "Propellant Atomization and Ignition Phenomena in Liquid Oxygen/Gaseous Hydrogen Rocket Combustors," Journal of Propulsion and Power, 17, 794, 2001.

Mayer, W., Schik, A., Vielle, B., Chauveau, C., Gokalp, I., Talley, D. G., and Woodward, R. D., "Atomization and Breakup of Cryogenic Propellants under High-Pressure Subcritical and Supercritical Conditions," Journal of Propulsion and Power, 14, 1998.

Mayer, W., Schik, A., Schaffler, M., and Tamura, H., "Injection and Mixing Processes in High-Pressure Liquid Oxygen/Gaseous Hydrogen Rocket Combustors," Journal of Propulsion and Power, 16, 823, 2000.

Meneveau, C. and Katz, Joseph, "Scale-Invariance and Turbulence Models for Large-Eddy Simulation," Annual Review of Fluid Mechanics, 32, 1, 2000.

Meng, H. and Yang, V., "A Unified Thermodynamics Treatment of General Fluid Mixtures and Its Application to a Preconditioning Scheme," Journal of Computational Physics, 189, 277, 2003.

Meng, H., "Liquid-Fuel Droplet Vaporization and Cluster Behavior at Supercritical Conditions," Ph.D Thesis, The Pennsylvania State University, 2000.

Miller, R. S., Harstad, K. G., and Bellan, J., "Direct Numerical Simulations of Supercritical Fluid Mixing Layers Applied to Heptane-Nitrogen," Journal of Fluid Mechanics, 436, 1, 2000.

Moin, P. and Kim, J., "Numerical Investigation of Turbulent Channel Flow," *Journal of Fluid Mechanics*, 118, 341, 1982.

Moin, P., Squires, K., Cabot, W., and Lee, S., "A Dynamic Subgrid-Scale Model for Compressible Turbulence and Scalar Transport," *Physics of Fluids A*, 3, 2746, 1991.

Moran, J. M. and Shapiro, N. H., "Fundamentals of Engineering Thermodynamics," 4th edition, John Wiley & Sons, 1999.

Newman, J. A. and Brzustowski, T. A., "Behavior of a Liquid Jet near The Thermodynamic Critical Region," *AIAA Journal*, 19, 1595, 1971.

Oefelein, J. C. and Yang, V., "Modeling High-Pressure Mixing and Combustion Processes in Liquid Rocket Engines," *Journal of Propulsion and Power*, 14, 843, 1998.

Okong'o, N. A., and Bellan, J., "Direct Numerical Simulation of a Transitional Supercritical Binary Mixing Layer: Heptane and Nitrogen," *Journal of Fluid Mechanics*, 464, 1, 2002.

Okong'o, N. A., Harstad, K. G., and Bellan, J., "Direct Numerical Simulation of O<sub>2</sub>/H<sub>2</sub> Temporal Mixing Layers under Supercritical Conditions," *AIAA Journal*, 40, 914, 2002.

Ortman, J. and Lefebvre, A. H., "Fuel Distributions from Pressure-Swirl Atomizer," *Journal of Propulsion*, 1, 11, 1985.

Oschwald, M. and Schik, A., "Supercritical Nitrogen Free Jet Investigated by Spontaneous Raman Scattering," *Experiments in Fluids*, 27, 497, 1999.

Panchapakesan, N. R. and Lumley, J. L., "Turbulence Measures in Axisymmetric Jets of Air and Helium. Part 1. Air Jet," *Journal of Fluid Mechanics*, 246, 197, 1993.

Panda, J. and McLaghlin, D.K., "Experiments on the Instabilities of a Swirling Jet," *Physics of Fluids*, 6, 263, 1994.

Papamoschou, D. and Roshko, A., "The Compressible Turbulent Shear Layer: An Experimental Study," *Journal of Fluid Mechanics*, 197, 453, 1988.

Peng D. and Robinson, B. D., "A New Two Constant Equation of State," *Industry Engineering Chemical Fundamentals*, 1976.

Piomelli, U., "Large-Eddy Simulation: Achievements and Challenge," *Progress in Aerospace Sciences*, 35, 335, 1999.

Piomelli, U., Zang, T. A., Speziale, C. G., and Hussaini, M. Y., "On the Large-Eddy Simulation of Transitional Wall-Bounded Flows," *Physics of Fluids*, 2, 257, 1990.

Poinsot, T. J. and Lele, S. K., "Boundary Conditions for Direct Simulation of Compressible Viscous Flows," *Journal of Computational Physics*, 101, 104, 1992.

Pope, S. B., *Turbulent Flows*, Cambridge University Press, 2000.

Prausnitz, J., Lichtenthaler, R., and de Azevedo, E., "Molecular Thermodynamics for Fluid-Phase Equilibrium," 2nd edition, Prentice-Hall, Englewood Cliffs, NJ, 1986.

Rahman, S. A., Pal, S., and Santoro, R. J., "Swirl Coaxial Atomization: Cold-Flow and Hot-fire Experiments," AIAA Paper No. 95-0381, 1995.

Rai, M. M. and Chakravarthy, S., "Conservative High-Order Accurate Finite Difference Methods for Curvilinear Grids," AIAA Paper No. 93-3380, 1993.

Rehab, H., Villermaux, E., and Hopfinger, E. J., "Flow Regimes of Large-Velocity-Ratio Coaxial Jets," Journal of Fluid Mechanics, 345, 357, 1997.

Reid, R. C., Prausnitz, J. M., and Poling, B. E., *The Properties of Gases and Liquids*, 4<sup>th</sup> edition, McGraw-Hill, 1986.

Reitz, R. D. and Bracco, F. V. "On the Dependence of Spray Angle and Other Spray Parameters on Nozzle Design and Operating Condition," SAE Paper no. 790494, 1979.

Richards, C. D. and Pitts, W. M., "Global Density Effects on the Self-Preservation Behaviour of Turbulent Free Jets," Journal of Fluid Mechanics, 254, 417, 1993.

Rudy, D. H. and Strikwerda, J. C., "A Nonreflecting Outflow Boundary Condition for Subsonic Navier-Stokes Calculations," Journal of Computational Physics, 18, 376, 1980.

Sasaki, M., Sakamoto, H., Takahashi, M., Tomita, T., and Tamura, H., "Comparative Study of Recessed and Non-recessed Swirl Coaxial Injectors," AIAA Paper No. 97-2907, 1997.

Schadow, K. C. and Gutmark, E., "Combustion Instability Related to Vortex Shedding in Dump Combustors and Their Passive Control", Progress in Energy Combustion Science, 18, 117, 1992.

Schetz, J. A., "Injection and Mixing in Turbulent Flow", AIAA Prog. Aeronautics and Astronautics, 68, 19, 1980.

Shuen, J. S., Chen, K. H., and Choi, Y. H., "A Coupled Implicit Method for Chemical Non-equilibrium Viscous Flows at All Speeds," Journal of Computational Physics, 106, 306, 1993.

Singla, G., Scouflaire, P., Rolon, C., and Candel, S., "Transcritical Oxygen/Transcritical or Supercritical Methane Combustion," the 30<sup>th</sup> International Symposium on Combustion, Chicago, U.S.A, 2004.

Smagorinsky, J., "General Circulation Experiments with the Primitive Equations. I. The Basic Experiment," Monthly Weather Review, 91, 99, 1963.

Snyder, R., Herding, G., Rolon, J. C., and Candel, S., "Analysis of Flame Patterns in Cryogenic Propellant Combustion," Combustion Science and Technology, 124, 331, 1997.

Soave, G., "Equilibrium Constants from a Modified Redlich-Kwong Equation of State," Chemical Engineering Science, 27, 1197, 1972.

Soteriou, M. C. and Ghoniem, A., "Effects of the Free-Stream Density Ratio on Free and Forced Spatially Developing Shear Layers," *Physics of Fluids*, 7, 2036, 1995.

Sterling T. L., Salmon J., and Becker D., "How to Build a Beowulf -A Guide to the Implementation of PC Clusters," The MIT Press, Cambridge, Massachusetts, London, 1993.

Strakey, P. A., Talley, D. G., and Hutt, J. J., "Mixing Characteristics of Coaxial Injectors at High Gas/Liquid Momentum Ratios," *Journal of Propulsion and Power*, 17, 402, 2001.

Swanson, R. C. and Turkel, E., "On Central-Difference and Upwind Schemes," *Journal of Computational Physics*, 101, pp.292, 1992.

Takahashi, S., "Preparation of a Generalized Chart for the Diffusion Coefficients of Gases at High Pressures," *Journal of Chemical Engineering (Japan)*, 7, 417, 1974.

Tamura, H., Sakamotot, H., Takahashi, M., Sasaki, M., Tomita, T., and Nagao, R., "LOX/LH<sub>2</sub> Subscale Swirl Coaxial Injector Testing," *AIAA Paper No. 97-2906*, 1997.

Tanasawa, Y. and Kobayasi, K., "A Study on Swirl Atomizer," *Technical Report of Tohoku University*, 20, 27, 1955.

Taylor, G., "The Mechanism of Swirl Atomizers," *Proceedings of 7<sup>th</sup> International Congress for Applied Mechanics*, Vol. 2, London, 1948.

Turkel, E., "Review of Preconditioning Methods for Fluid Dynamics," *Technique Report, 92-47, ICASE*, 1992.

Van Driest, E. R., "On the Turbulent Flow near a Wall," *Journal of Aeronautics Science*, 23, 1007, 1956.

Venkateswaran, S. and Merkel, C. L., "Dual Time Stepping and Preconditioning for Unsteady Computations," *AIAA Paper No. 95-0078*, 1995.

Vesovic, V. and Wakeham, W. A., "Transport Properties of Supercritical Fluids and Fluids Mixtures," *Supercritical Fluid Technology*, eds., T. J. Bruno and J. F. Ely, Chapter 6, CRC Press, Inc, Boca Raton, Florida, 1991.

Villermaux, E. and Rehab, H., "Mixing in Coaxial Jets," *Journal of Fluid Mechanics*, 425, 161, 2000.

Wang, S. W., "Vortical Flow Dynamics and Acoustic Response of Gas Turbine Swirl-Stabilized Injector", Ph.D thesis, The Pennsylvania State University, 2002.

Wee, D., Yi, T., Annaswamy, A., and Ghoniem, A. F., "Self-sustained Oscillations and Vortex Shedding in Backward-Facing Step Flows: Simulation and Linear Instability Analysis," *Physics of Fluids*, 16, 3361, 2004.

Wygnanski, I., and Fiedler, H., "Some Measurements in the Self-Preserving Jet," *Journal of Fluid Mechanics*, 38, 577, 1967.

Yang, V., "Modeling of Supercritical Vaporization, Mixing, and Combustion Processes in Liquid-Fueled Propulsion Systems," Proceedings of Combustion Institute, 28, 925, 2000.

Yu, M. H. and Monkewitz, P.A., "The Effect of Nonuniform Density on the Absolute Instability of Two-Dimensional Inertial Jets and Wakes," Physics of Fluids A, 2, 1175, 1990.

Yule, A. J. and Chinn, J. J., "Swirl Atomizer Flow: Classical Inviscid Theory Revisited," International Conference on Liquid Atomization and Spray Systems, ICLASS-94, Rouen, France, 1994.

Zang, Y., Street, R. L., and Koseff, J., "A Dynamic Mixed Subgrid-Scale Model and Its Application to Turbulent Recirculating Flows," Physics of Fluids A, 5, 3186, 1993.

Zhou, X., Luo, K. H., and Williams, J. J. R., "Study of Density Effects in Turbulent Buoyant Jets Using Large-Eddy-Simulation," Theoretical and Computational Fluid Dynamics, 15, 95, 2001.

Zong, N., Meng, H., Hsieh, S. Y., and Yang, V., "A Numerical Study of Cryogenic Fluid Injection and Mixing under Supercritical Conditions," Physics of Fluids, 16, 4248, 2004.

## Appendix A

### Properties of the Favre Average (Based on Reynolds Average)

The Favre average is defined as

$$\tilde{f} = \frac{\overline{\rho f}}{\bar{\rho}} \quad (\text{A.1})$$

then,

$$\overline{\rho f} = \overline{\rho(\tilde{f} + f')} = \overline{\rho\tilde{f}} + \overline{\rho f'} = \overline{\rho}\overline{\rho\tilde{f}}/\bar{\rho} + \overline{\rho f'} = \bar{\rho}\overline{\rho\tilde{f}}/\bar{\rho} + \overline{\rho f'} = \overline{\rho\tilde{f}} + \overline{\rho f'}$$

thus,

$$\overline{\rho f'} = 0 \quad (\text{A.2})$$

in the mean time,

$$\tilde{f} = \frac{\overline{\rho f}}{\bar{\rho}} = \frac{(\bar{\rho} + \rho')(\bar{f} + f')}{\bar{\rho}} = \frac{\bar{\rho}\bar{f} + \bar{\rho}f' + \rho'\bar{f} + \rho'f'}{\bar{\rho}} = \bar{f} + \frac{\rho'f'}{\bar{\rho}} \quad (\text{A.3})$$

on the other hand,  $\overline{\rho f} = \overline{\rho\tilde{f}} + \overline{\rho f'} = \overline{\rho\tilde{f}}$

then,

$$\overline{\rho\tilde{f}} = \overline{\rho\tilde{f}} \quad (\text{A.4})$$

by definition, we have,  $\overline{\rho\tilde{f}} = \tilde{\tilde{f}} = \overline{\rho\tilde{f}}$ ,

$$\tilde{\tilde{f}} = \tilde{f} \quad (\text{A.5})$$

another important relation is:

$$\overline{\rho fg} = \overline{\rho(\tilde{f} + f')(\tilde{g} + g')} = \overline{\rho\tilde{f}\tilde{g}} + \overline{\rho\tilde{f}g'} + \overline{\rho f\tilde{g}} + \overline{\rho f'g'} = \overline{\rho\tilde{f}\tilde{g}} + \overline{\rho f'g'} \quad (\text{A.6})$$

## Appendix B

### Thermodynamic Relationship

Based on the Soave-Redlich-Kwong equation of state, the following derivative expressions, which are used extensively in property evaluations and numerical Jacobians, can be directly written as

$$\left( \frac{\partial p}{\partial T} \right)_{\rho_j} = \frac{\rho R_u}{(M_w - b\rho)} - \frac{1}{M_w} \left[ \frac{\partial}{\partial T} (a\alpha) \right]_{\rho, Y_j} \frac{\rho^2}{(M_w + b\rho)} \quad (\text{B.1})$$

$$\left( \frac{\partial p}{\partial \rho} \right)_{T, Y_j} = \frac{M_w R_u T}{(M_w - b\rho)^2} - \frac{a\alpha}{M_w} \frac{\rho(2M_w + b\rho)}{(M_w + b\rho)^2} \quad (\text{B.2})$$

$$\begin{aligned} \left( \frac{\partial p}{\partial \rho_i} \right)_{T, \rho_j \neq i} &= \frac{M_w R_u T}{M_{w_i} (M_w - b\rho)^2} [M_w + \rho(b_i - b)] \\ &\quad - \frac{2\rho \sum_j x_j a_{ij} \alpha_{ij}}{M_{w_i} (M_w + b\rho)} + \frac{a\alpha \rho^2 b_i}{M_{w_i} (M_w + b\rho)^2} \end{aligned} \quad (\text{B.3})$$

where the indexes  $i, j = 1 \dots N$ , and the derivative  $\frac{\partial}{\partial T} (a\alpha)$  is given in Appendix C.

It should be noted that these derivatives could be derived based on any equation of state following the fundamental thermodynamics.

The partial density internal energy ( $\tilde{e}_i$ ) of species  $i$  will then be derived. We first need to find the expression for the internal energy ( $e$ ). From the fundamental thermodynamic theory, we have

$$e(T, \rho) = e_0(T) + \int_0^\rho \left[ \frac{P}{\rho^2} - \frac{T}{\rho^2} \left( \frac{\partial p}{\partial T} \right)_\rho \right] d\rho \quad (\text{B.4})$$

where the subscript 0 indicates a reference ideal state at a low pressure.

Utilizing SRK equation of state and the partial derivative relation Eq. B.1, Eq. B.4 is integrated, which leads to the following relationship

$$e(T, \rho) = e_0(T) + \frac{T^2}{bM_w} \left( \frac{\partial a\alpha/T}{\partial T} \right)_{\rho, Y_j} \ln \left( 1 + \frac{b\rho}{M_w} \right) \quad (\text{B.5})$$

where the partial derivative  $\frac{\partial a\alpha/T}{\partial T}$  is presented in Appendix C.

According to the definition for the partial density property, the partial density internal energy ( $\tilde{e}_i$ ) can be expressed as

$$\begin{aligned} \tilde{e}_i &= e_{i,0} + \frac{2}{bM_{w_i}} \left[ \sum_j x_j \left( T \frac{\partial}{\partial T} (a_{ij}\alpha_{ij}) - a_{ij}\alpha_{ij} \right) \right] \ln \left( 1 + \frac{b\rho}{M_w} \right) \\ &\quad + \frac{b_i}{bM_{w_i}} \left[ T \frac{\partial}{\partial T} (a\alpha) - a\alpha \right] \left[ \frac{\rho}{M_w + b\rho} - \frac{1}{b} \ln \left( 1 + \frac{b\rho}{M_w} \right) \right] \end{aligned} \quad (\text{B.6})$$

In addition, utilizing Eq. B.6, the internal energy of a mixture can be related to the partial density internal energy as

$$e = \sum_i Y_i \tilde{e}_i - \frac{1}{M_w} \left[ T \frac{\partial}{\partial T} (a\alpha) - a\alpha \right] \frac{\rho}{M_w + b\rho} \quad (\text{B.7})$$

Based on thermodynamics,

$$\rho h = \rho e + p \quad (\text{B.8})$$

Following the definition for the partial density property, the following expression can be found by taking derivative of the partial density of the species  $i$  to both sides of the Eq. B.8, and keeping temperature and all the other partial densities constant

$$\left( \frac{\partial \rho h}{\partial \rho_i} \right)_{T, \rho_{j \neq i}} = \left( \frac{\partial \rho e}{\partial \rho_i} \right)_{T, \rho_{j \neq i}} + \left( \frac{\partial p}{\partial \rho_i} \right)_{T, \rho_{j \neq i}} \quad (\text{B.9})$$

It is equivalent to Eq. B.10

$$\tilde{h}_i = \tilde{e}_i + \left( \frac{\partial p}{\partial \rho_i} \right)_{T, \rho_j \neq i} \quad (\text{B.10})$$

The following thermodynamic expression exists, which relates a partial density property to a partial mass property

$$\tilde{\phi}_i = \bar{\phi}_i + \rho \left( \frac{\partial \phi}{\partial p} \right)_{T, Y_j} \left( \frac{\partial p}{\partial \rho_i} \right)_{T, \rho_j \neq i} \quad (\text{B.11})$$

where the parameter  $\phi$  refers to any proper intensive thermodynamic property, such as enthalpy, and internal energy.

Substituting Eq. B.10 into Eq. B.11, and taking use of the fundamental enthalpy expression, which can be found in any thermodynamics textbook, the following relation concerning the partial mass enthalpy ( $\bar{h}_i$ ) can be established

$$\bar{h}_i = \tilde{e}_i + \frac{T}{\rho} \frac{\left( \frac{\partial p}{\partial T} \right)_{\rho_j}}{\left( \frac{\partial p}{\partial \rho} \right)_{T, Y_j}} \left( \frac{\partial p}{\partial \rho_i} \right)_{T, \rho_j \neq i} \quad (\text{B.12})$$

Next, we begin to find the expressions for the constant volume and the constant pressure heat capacities based on the SRK equation of state.

The definition of constant volume heat capacity is

$$C_v = \left( \frac{\partial e}{\partial T} \right)_{\rho, Y_j} \quad (\text{B.13})$$

Utilizing Eq. B.5, it is straightforward to find

$$C_v = C_{v,0} + \frac{T}{bM_w} \frac{\partial^2}{\partial T^2} (a\alpha) \ln \left( 1 + \frac{b\rho}{M_w} \right) \quad (\text{B.14})$$

where the derivative  $\frac{\partial^2}{\partial T^2}(a\alpha)$  is given in Appendix C.

Following fundamental thermodynamic relationships, the constant-pressure heat capacity can be expressed as

$$C_p = C_v + \frac{T}{\rho^2} \left( \frac{\partial p}{\partial T} \right)_{\rho_j}^2 \left/ \left( \frac{\partial p}{\partial \rho} \right)_{T, Y_j} \right. \quad (\text{B.15})$$

In order to find the thermodynamic relationships regarding chemical potential, the partial density and partial mass entropy have to be derived first

$$s(T, \rho) = s_0(T, \rho_0) - \int_{\rho_0}^{\rho} \left[ \frac{1}{\rho^2} \left( \frac{\partial p}{\partial T} \right)_{\rho} \right]_T d\rho \quad (\text{B.16})$$

Based on the definition of partial density entropy, it is found

$$\begin{aligned} \tilde{S}_i &= \int_{T_{ref}}^T C_{p_i, 0} \frac{dT}{T} - \frac{R_u}{M_{wi}} (1 + \ln x_i) - \frac{R_u}{M_{wi}} \ln \frac{\rho \frac{R_u}{M_w} T}{p_{ref}} \\ &+ \frac{R_u}{M_{wi}} \ln \left( 1 - \frac{b\rho}{M_w} \right) - R_u \frac{b_i}{M_{wi}} \frac{\rho}{M_w - b\rho} + \frac{b_i}{M_{wi}} \frac{1}{b^2} \frac{\partial(a\alpha)}{\partial T} \left[ \frac{b\rho}{M_w + b\rho} \right. \\ &\quad \left. - \ln \left( 1 + \frac{b\rho}{M_w} \right) \right] + \frac{2}{bM_{wi}} \left[ \sum_j x_j \frac{\partial}{\partial T} (a_j \alpha_j) \right] \ln \left( 1 + \frac{b\rho}{M_w} \right) \end{aligned} \quad (\text{B.17})$$

The partial mass entropy can be further related to the partial density entropy as

$$\bar{S}_i = \tilde{S}_i + \left( \frac{\partial p}{\partial T} \right)_{\rho, Y_i} \bar{V}_i \quad (\text{B.18})$$

where the partial mass volume is

$$\bar{V}_i = \frac{1}{\rho} \left( \frac{\partial p}{\partial \rho_i} \right)_{T, \rho_{j \neq i}} \left/ \left( \frac{\partial p}{\partial \rho} \right)_{T, Y_j} \right. \quad (\text{B.19})$$

The chemical potential of species i can be calculated as

$$\mu_i = \tilde{f}_i = \tilde{e}_i - T\tilde{s}_i \quad (\text{B.20})$$

Finally, the partial derivatives regarding chemical potential can be expressed as

$$\left( \frac{\partial \mu_i}{\partial p} \right)_{T,Y_j} = \bar{V}_i \quad (\text{B.21})$$

$$\left( \frac{\partial \mu_i}{\partial T} \right)_{T,Y_j} = -\bar{S}_i \quad (\text{B.22})$$

## Appendix C

### Derivative Expressions in Soave-Redlich-Kwong Equation of State

In the Soave-Redlich-Kwong (SRK) equation of state, the terms  $a\alpha$  and  $\alpha_i a_{ij}$  are functions of temperature. The derivative of  $a\alpha$  to temperature is given as

$$\frac{\partial a\alpha}{\partial T} = \sum_{i=1}^N \sum_{j=1}^N x_i x_j \sqrt{a_i a_j} \frac{\partial \sqrt{a_i a_j}}{\partial T} \quad (\text{C.1a})$$

where

$$\frac{\partial \sqrt{a_i a_j}}{\partial T} = \frac{1}{2} \left( \frac{\alpha_i}{\alpha_j} \right)^{\frac{1}{2}} \frac{\partial \alpha_j}{\partial T} + \frac{1}{2} \left( \frac{\alpha_j}{\alpha_i} \right)^{\frac{1}{2}} \frac{\partial \alpha_i}{\partial T} \quad (\text{C.1b})$$

$$\frac{\partial \alpha_i}{\partial T} = -\frac{S_i}{\sqrt{T T_{c,i}}} \left[ 1 + S_i \left( 1 - \sqrt{\frac{T}{T_{c,i}}} \right) \right] \quad (\text{C.1c})$$

$$\frac{\partial a_{ij} \alpha_{ij}}{\partial T} = \sqrt{a_i a_j} \frac{\partial \sqrt{a_i a_j}}{\partial T} \quad (\text{C.2})$$

The second derivative of parameter  $a\alpha$  to temperature is

$$\frac{\partial^2 a\alpha}{\partial T^2} = \sum_{i=1}^N \sum_{j=1}^N x_i x_j \sqrt{a_i a_j} \frac{\partial^2 \sqrt{a_i a_j}}{\partial T^2} \quad (\text{C.3a})$$

where

$$\frac{\partial^2 \sqrt{\alpha_i \alpha_j}}{\partial T^2} = \frac{1}{2} \left( \frac{1}{\alpha_i \alpha_j} \right)^{\frac{1}{2}} \frac{\partial \alpha_i}{\partial T} \frac{\partial \alpha_j}{\partial T} - \frac{1}{4} \left( \frac{\alpha_i}{\alpha_j^3} \right)^{\frac{1}{2}} \left( \frac{\partial \alpha_j}{\partial T} \right)^2 \quad (\text{C.3b})$$

$$- \frac{1}{4} \left( \frac{\alpha_j}{\alpha_i^3} \right)^{\frac{1}{2}} \left( \frac{\partial \alpha_i}{\partial T} \right)^2 + \frac{1}{2} \left( \frac{\alpha_i}{\alpha_j} \right)^{\frac{1}{2}} \frac{\partial^2 \alpha_j}{\partial T^2} + \frac{1}{2} \left( \frac{\alpha_j}{\alpha_i} \right)^{\frac{1}{2}} \frac{\partial^2 \alpha_i}{\partial T^2}$$

$$\frac{\partial^2 \alpha_i}{\partial T^2} = \frac{1}{2} \frac{S_i^2}{T T_{c,i}} + \frac{1}{2} \frac{S_i}{\sqrt{T^3 T_{c,i}}} \left[ 1 + S_i \left( 1 - \sqrt{\frac{T}{T_{c,i}}} \right) \right] \quad (\text{C.3c})$$

The variable  $\alpha_i$  for species H<sub>2</sub> ( $\alpha_{H_2}$ ), is treated differently since hydrogen is a quantum gas. The derivative of this variable is

$$\frac{\partial \alpha_{H_2}}{\partial T} = -\alpha_{H_2} \left[ 0.30228 \frac{1}{T_{c,i}} \right] \quad (\text{C.4})$$

$$\frac{\partial^2 \alpha_{H_2}}{\partial T^2} = \alpha_{H_2} \left[ 0.30228 \frac{1}{T_{c,i}} \right]^2 \quad (\text{C.5})$$

## Appendix D

### Jacobian Matrices

The Jacobian matrices employed in Chapter 3 are defined as follows.

#### D.1 Jacobian of Primitive Variables

The Jacobian of primitive variables  $T = \partial Q / \partial Z$  is given by

$$T = \left( \begin{array}{cccccc} \left( \frac{\partial \rho}{\partial p} \right)_{T, Y_i} & 0 & 0 & -\frac{A_T}{A_p} & -\frac{A_{Y_i}}{A_p} & \dots & -\frac{A_{Y_{N-1}}}{A_p} \\ \tilde{u} \left( \frac{\partial \rho}{\partial p} \right)_{T, Y_i} & \bar{\rho} & 0 & 0 & -\frac{A_T \tilde{u}}{A_p} & -\frac{A_{Y_i} \tilde{u}}{A_p} & \dots & -\frac{A_{Y_{N-1}} \tilde{u}}{A_p} \\ \tilde{v} \left( \frac{\partial \rho}{\partial p} \right)_{T, Y_i} & 0 & \bar{\rho} & 0 & -\frac{A_T \tilde{v}}{A_p} & -\frac{A_{Y_i} \tilde{v}}{A_p} & \dots & -\frac{A_{Y_{N-1}} \tilde{v}}{A_p} \\ \tilde{w} \left( \frac{\partial \rho}{\partial p} \right)_{T, Y_i} & 0 & 0 & \bar{\rho} & -\frac{A_T \tilde{w}}{A_p} & -\frac{A_{Y_i} \tilde{w}}{A_p} & \dots & -\frac{A_{Y_{N-1}} \tilde{w}}{A_p} \\ [h_i + (\sum_{i=1}^N \tilde{Y}_i \hat{e}_i - e - \frac{p}{\rho})] \left( \frac{\partial \rho}{\partial p} \right)_{T, Y_i} & \bar{\rho} \tilde{u} & \bar{\rho} \tilde{v} & \bar{\rho} \tilde{w} & \bar{\rho} B_T - \frac{A_T e_i}{A_p} & \bar{\rho} B_{Y_i} - \frac{A_{Y_i} e_i}{A_p} & \dots & \bar{\rho} B_{Y_{N-1}} - \frac{A_{Y_{N-1}} e_i}{A_p} \\ \tilde{Y}_1 \left( \frac{\partial \rho}{\partial p} \right)_{T, Y_i} & 0 & 0 & 0 & -\frac{A_T \tilde{Y}_1}{A_p} & \bar{\rho} - \frac{A_{Y_1} \tilde{Y}_1}{A_p} & \vdots & -\frac{A_{Y_{N-1}} \tilde{Y}_1}{A_p} \\ \vdots & \vdots & \vdots & \vdots & \vdots & \vdots & \ddots & \vdots \\ \tilde{Y}_{N-1} \left( \frac{\partial \rho}{\partial p} \right)_{T, Y_i} & 0 & 0 & 0 & -\frac{A_T \tilde{Y}_{N-1}}{A_p} & -\frac{A_{Y_{N-1}} \tilde{Y}_{N-1}}{A_p} & \dots & \bar{\rho} - \frac{A_{Y_{N-1}} Y_{N-1}}{A_p} \end{array} \right) \quad \text{D.1}$$

where the coefficients  $A_p$ ,  $A_T$ ,  $A_{Y_i}$ ,  $B_p$ ,  $B_T$ , and  $B_{Y_i}$  are defined in the Chapter 2. The terms  $e_i$  and  $h_i$  denote total energy and total enthalpy, respectively.

$$e_i = e + \frac{1}{2}(\tilde{u}^2 + \tilde{v}^2 + \tilde{w}^2)$$

$$h_i = e_i + \frac{p}{\rho}$$

## D.2 Convective Flux Jacobians

The Jacobian matrix  $A = \partial E / \partial Z$  is given by

$$A = \left( \begin{array}{ccccc} \tilde{u} \left( \frac{\partial \rho}{\partial p} \right)_{T,Y_i} & \bar{\rho} & 0 & 0 & -\tilde{u} \frac{A_T}{A_\rho} \\ 1 + \tilde{u}^2 \left( \frac{\partial \rho}{\partial p} \right)_{T,Y_i} & 2\bar{\rho}\tilde{u} & 0 & 0 & -\tilde{u}^2 \frac{A_T}{A_\rho} \\ \tilde{u}\tilde{v} \left( \frac{\partial \rho}{\partial p} \right)_{T,Y_i} & \bar{\rho}\tilde{v} & \bar{\rho}\tilde{u} & 0 & -\tilde{u}\tilde{v} \frac{A_T}{A_\rho} \\ \tilde{u}\tilde{w} \left( \frac{\partial \rho}{\partial p} \right)_{T,Y_i} & \bar{\rho}\tilde{w} & 0 & \bar{\rho}\tilde{u} & -\tilde{u}\tilde{w} \frac{A_T}{A_\rho} \\ \tilde{u}[\tilde{h}_i + (\sum_{l=1}^N \tilde{Y}_l \hat{e}_l - e - \frac{p}{\rho}) + 1] \left( \frac{\partial \rho}{\partial p} \right)_{T,Y_i} & \tilde{h}_i + \bar{\rho}\tilde{u}^2 & \bar{\rho}\tilde{u}\tilde{v} & \bar{\rho}\tilde{u}\tilde{w} & \tilde{u}(\bar{\rho}B_T - \frac{A_T e_i}{A_\rho}) \\ \tilde{u}\tilde{Y}_1 \left( \frac{\partial \rho}{\partial p} \right)_{T,Y_i} & \bar{\rho}\tilde{Y}_1 & 0 & 0 & -\tilde{u} \frac{A_T \tilde{Y}_1}{A_\rho} \\ \vdots & \vdots & \vdots & \vdots & \vdots \\ \tilde{u}\tilde{Y}_{N-1} \left( \frac{\partial \rho}{\partial p} \right)_{T,Y_i} & \bar{\rho}\tilde{Y}_{N-1} & 0 & 0 & -\tilde{u} \frac{A_T \tilde{Y}_{N-1}}{A_\rho} \\ -\tilde{u} \frac{A_{Y_1}}{A_\rho} & \dots & -\tilde{u} \frac{A_{Y_{N-1}}}{A_\rho} & & \\ -\tilde{u}^2 \frac{A_{Y_1}}{A_\rho} & \dots & -\tilde{u}^2 \frac{A_{Y_{N-1}}}{A_\rho} & & \\ -\tilde{u}\tilde{v} \frac{A_{Y_1}}{A_\rho} & \dots & -\tilde{u}\tilde{v} \frac{A_{Y_{N-1}}}{A_\rho} & & \\ -\tilde{u}\tilde{w} \frac{A_{Y_1}}{A_\rho} & \dots & -\tilde{u}\tilde{w} \frac{A_{Y_{N-1}}}{A_\rho} & & \\ \tilde{u}(\bar{\rho}B_{Y_1} - \frac{A_{Y_1} e_i}{A_\rho}) \dots & \tilde{u}(\bar{\rho}B_{Y_{N-1}} - \frac{A_{Y_{N-1}} e_i}{A_\rho}) & & & \\ \tilde{u}(\bar{\rho} - \frac{A_{Y_1} \tilde{Y}_1}{A_\rho}) \dots & -\tilde{u} \frac{A_{Y_{N-1}} \tilde{Y}_1}{A_\rho} & & & \\ \vdots & \vdots & & & \\ -\tilde{u} \frac{A_{Y_1} \tilde{Y}_{N-1}}{A_\rho} & \dots & \tilde{u}(\bar{\rho} - \frac{A_{Y_{N-1}} Y_{N-1}}{A_\rho}) & & \end{array} \right) \quad (D.2)$$

The Jacobian matrix  $B = \partial F / \partial Z$  is given by

$$B = \begin{pmatrix} \tilde{v} \left( \frac{\partial \rho}{\partial p} \right)_{T,Y_i} & 0 & \bar{\rho} & 0 & -\tilde{v} \frac{A_T}{A_\rho} \\ \tilde{u} \tilde{v} \left( \frac{\partial \rho}{\partial p} \right)_{T,Y_i} & \bar{\rho} \tilde{v} & \bar{\rho} \tilde{u} & 0 & -\tilde{u} \tilde{v} \frac{A_T}{A_\rho} \\ 1 + \tilde{v}^2 \left( \frac{\partial \rho}{\partial p} \right)_{T,Y_i} & 0 & 2 \bar{\rho} \tilde{v} & 0 & -\tilde{v}^2 \frac{A_T}{A_\rho} \\ \tilde{v} \tilde{w} \left( \frac{\partial \rho}{\partial p} \right)_{T,Y_i} & 0 & \bar{\rho} \tilde{w} & \bar{\rho} \tilde{v} & -\tilde{v} \tilde{w} \frac{A_T}{A_\rho} \\ \tilde{v} [\tilde{h}_i + (\sum_{i=1}^N \tilde{Y}_i \tilde{e}_i - e - \frac{p}{\rho}) + 1] \left( \frac{\partial \rho}{\partial p} \right)_{T,Y_i} & \bar{\rho} \tilde{u} \tilde{v} & \tilde{h}_i + \bar{\rho} \tilde{v}^2 & \bar{\rho} \tilde{v} \tilde{w} & \tilde{v} (\bar{\rho} B_T - \frac{A_T e_i}{A_\rho}) \\ \tilde{v} \tilde{Y}_1 \left( \frac{\partial \rho}{\partial p} \right)_{T,Y_i} & 0 & \bar{\rho} \tilde{Y}_1 & 0 & -\tilde{v} \frac{A_T \tilde{Y}_1}{A_\rho} \\ \vdots & \vdots & \vdots & \vdots & \vdots \\ \tilde{v} \tilde{Y}_{N-1} \left( \frac{\partial \rho}{\partial p} \right)_{T,Y_i} & 0 & \bar{\rho} \tilde{Y}_{N-1} & 0 & -\tilde{v} \frac{A_T \tilde{Y}_{N-1}}{A_\rho} \\ -\tilde{v} \frac{A_{Y_1}}{A_\rho} & \dots & -\tilde{v} \frac{A_{Y_{N-1}}}{A_\rho} & & \\ -\tilde{u} \tilde{v} \frac{A_{Y_1}}{A_\rho} & \dots & -\tilde{u} \tilde{v} \frac{A_{Y_{N-1}}}{A_\rho} & & \\ -\tilde{v}^2 \frac{A_{Y_1}}{A_\rho} & \dots & -\tilde{v}^2 \frac{A_{Y_{N-1}}}{A_\rho} & & \\ -\tilde{v} \tilde{w} \frac{A_{Y_1}}{A_\rho} & \dots & -\tilde{v} \tilde{w} \frac{A_{Y_{N-1}}}{A_\rho} & & \\ \tilde{v} (\bar{\rho} B_{Y_1} - \frac{A_{Y_1} e_i}{A_\rho}) & \dots & \tilde{v} (\bar{\rho} B_{Y_{N-1}} - \frac{A_{Y_{N-1}} e_i}{A_\rho}) & & \\ \tilde{v} (\bar{\rho} - \frac{A_{Y_1} \tilde{Y}_1}{A_\rho}) & \dots & -\tilde{v} \frac{A_{Y_{N-1}} \tilde{Y}_1}{A_\rho} & & \\ \vdots & \ddots & \vdots & & \\ -\tilde{v} \frac{A_{Y_1} \tilde{Y}_{N-1}}{A_\rho} & \dots & \tilde{v} (\bar{\rho} - \frac{A_{Y_{N-1}} Y_{N-1}}{A_\rho}) & & \end{pmatrix} \quad (D.3)$$

The Jacobian matrix  $C = \partial G / \partial Z$  is given by

$$C = \left( \begin{array}{ccccc} \tilde{w}\left(\frac{\partial \rho}{\partial p}\right)_{T,Y_1} & 0 & 0 & \bar{\rho} & -\tilde{w}\frac{A_T}{A_\rho} \\ \tilde{u}\tilde{w}\left(\frac{\partial \rho}{\partial p}\right)_{T,Y_1} & \bar{\rho}\tilde{w} & 0 & \bar{\rho}\tilde{u} & -\tilde{u}\tilde{w}\frac{A_T}{A_\rho} \\ \tilde{v}\tilde{w}\left(\frac{\partial \rho}{\partial p}\right)_{T,Y_1} & 0 & \bar{\rho}\tilde{w} & \bar{\rho}\tilde{v} & -\tilde{v}\tilde{w}\frac{A_T}{A_\rho} \\ 1 + \tilde{w}^2\left(\frac{\partial \rho}{\partial p}\right)_{T,Y_1} & 0 & 0 & 2\bar{\rho}\tilde{w} & -\tilde{w}^2\frac{A_T}{A_\rho} \\ \tilde{w}[\tilde{h}_t + (\sum_{i=1}^N \tilde{Y}_i \tilde{e}_i - e - \frac{p}{\rho}) + 1]\left(\frac{\partial \rho}{\partial p}\right)_{T,Y_1} & \bar{\rho}\tilde{u}\tilde{w} & \bar{\rho}\tilde{v}\tilde{w} & \tilde{h}_t + \bar{\rho}\tilde{w}^2 & \tilde{w}(\bar{\rho}B_T - \frac{A_T e_t}{A_\rho}) \\ \tilde{w}\tilde{Y}_1\left(\frac{\partial \rho}{\partial p}\right)_{T,Y_1} & 0 & 0 & \bar{\rho}\tilde{Y}_1 & -\tilde{w}\frac{A_T \tilde{Y}_1}{A_\rho} \\ \vdots & \vdots & \vdots & \vdots & \vdots \\ \tilde{w}\tilde{Y}_{N-1}\left(\frac{\partial \rho}{\partial p}\right)_{T,Y_1} & 0 & 0 & \bar{\rho}\tilde{Y}_{N-1} & -\tilde{w}\frac{A_T \tilde{Y}_{N-1}}{A_\rho} \\ -\tilde{w}\frac{A_{Y_1}}{A_\rho} & \dots & -\tilde{w}\frac{A_{Y_{N-1}}}{A_\rho} & & \\ -\tilde{u}\tilde{w}\frac{A_{Y_1}}{A_\rho} & \dots & -\tilde{u}\tilde{w}\frac{A_{Y_{N-1}}}{A_\rho} & & \\ -\tilde{v}\tilde{w}\frac{A_{Y_1}}{A_\rho} & \dots & -\tilde{v}\tilde{w}\frac{A_{Y_{N-1}}}{A_\rho} & & \\ -\tilde{w}^2\frac{A_{Y_1}}{A_\rho} & \dots & -\tilde{w}^2\frac{A_{Y_{N-1}}}{A_\rho} & & \\ \tilde{w}(\bar{\rho}B_{Y_1} - \frac{A_{Y_1} e_t}{A_\rho}) & \dots & \tilde{w}(\bar{\rho}B_{Y_{N-1}} - \frac{A_{Y_{N-1}} e_t}{A_\rho}) & & \\ \tilde{w}(\bar{\rho} - \frac{A_{Y_1} \tilde{Y}_1}{A_\rho}) & \dots & -\tilde{w}\frac{A_{Y_{N-1}} \tilde{Y}_1}{A_\rho} & & \\ \vdots & \ddots & \vdots & & \\ -\tilde{w}\frac{A_{Y_1} \tilde{Y}_{N-1}}{A_\rho} & \dots & \tilde{w}(\bar{\rho} - \frac{A_{Y_{N-1}} Y_{N-1}}{A_\rho}) & & \end{array} \right) \quad (D.4)$$

### D.3 Chemical Source Jacobian

The Jacobian matrix associated with the chemical reaction source term  $D = \partial H / \partial Z$  is

$$D = \begin{pmatrix} 0 & 0 & 0 & 0 & 0 & \dots & 0 \\ 0 & 0 & 0 & 0 & 0 & \dots & 0 \\ 0 & 0 & 0 & 0 & 0 & \dots & 0 \\ 0 & 0 & 0 & 0 & 0 & \dots & 0 \\ 0 & 0 & 0 & 0 & 0 & \dots & 0 \\ (\frac{\partial \omega_1}{\partial p})_{T,Y_i} & 0 & 0 & 0 & (\frac{\partial \omega_1}{\partial T})_{p,Y_i} & (\frac{\partial \omega_1}{\partial Y_1})_{p,T,Y_{j=1}} & \vdots & (\frac{\partial \omega_1}{\partial Y_{N-1}})_{p,T,Y_{j=N-1}} \\ \vdots & \vdots & \vdots & \vdots & \vdots & \vdots & \ddots & \vdots \\ (\frac{\partial \omega_{N-1}}{\partial p})_{T,Y_i} & 0 & 0 & 0 & (\frac{\partial \omega_{N-1}}{\partial T})_{p,Y_i} & (\frac{\partial \omega_{N-1}}{\partial Y_1})_{p,T,Y_{j=1}} & \dots & (\frac{\partial \omega_{N-1}}{\partial Y_{N-1}})_{p,T,Y_{j=N-1}} \end{pmatrix} \quad (D.5)$$

where

$$\frac{\partial \dot{\omega}_i}{\partial p} = \frac{W_i}{p} \sum_{j=1}^N \left[ (v''_{ij} - v'_{ij}) k_{f_j} (\sum_{l=1}^N \varepsilon_{lj} n_l) \left\{ \left( \sum_{l=1}^N v'_{lj} \right) \prod_{l=1}^N n_l^{v'_{lj}} - \frac{1}{k_{c_j}} \left( \sum_{l=1}^N v''_{lj} \right) \prod_{l=1}^N n_l^{v''_{lj}} \right\} \right] \quad (D.6)$$

$$\begin{aligned} \frac{\partial \dot{\omega}_i}{\partial T} = & \frac{W_i}{T} \sum_{j=1}^N \left[ (v''_{ij} - v'_{ij}) k_{f_j} (\sum_{l=1}^N \varepsilon_{lj} n_l) \left\{ \left[ (m_{f_j} - \sum_{l=1}^N v'_{lj}) + \frac{E_{f_j}}{R_u T} \right] \prod_{l=1}^N n_l^{v'_{lj}} \right. \right. \\ & \left. \left. - \frac{1}{k_{c_j}} \left[ (m_{f_j} - \sum_{l=1}^N v'_{lj}) + \frac{E_{f_j}}{R_u T} - \frac{\Delta G_j^0}{R_u T} \right] \prod_{l=1}^N n_l^{v''_{lj}} \right\} \right] \end{aligned} \quad (D.7)$$

$$\begin{aligned} \frac{\partial \dot{\omega}_i}{\partial Y_k} = & W_i \sum_{j=1}^N \left[ (v''_{ij} - v'_{ij}) k_{f_j} (\sum_{l=1}^N \varepsilon_{lj} n_l) \left\{ \left[ (\frac{v'_{kj}}{Y_k} - \frac{v'_{Nj}}{Y_N}) - (\sum_{l=1}^N v'_{lj}) R_K \right] \prod_{l=1}^N n_l^{v'_{lj}} \right. \right. \\ & \left. \left. - \frac{1}{k_{c_j}} \left[ (\frac{v''_{kj}}{Y_k} - \frac{v''_{Nj}}{Y_N}) - (\sum_{l=1}^N v''_{lj}) R_K \right] \prod_{l=1}^N n_l^{v''_{lj}} \right\} \right] \end{aligned} \quad (D.8)$$

and  $R_K = W(\frac{1}{W_K} - \frac{1}{W_N})$ .